Nitrate aerosol

in the Netherlands



Farhan R. Nursanto

Propositions

1. Organic nitrate is likely to contribute more to the nitrogen deposition in the future than it does today.
   (this thesis)
2. To simplify modeling of nitrate aerosol formation, the diversity of organic nitrate compounds may be represented by one compound.
   (this thesis)
3. Structural data archiving of field campaign data requires more attention to fully exploit research outcomes.
4. We need more scientists that work at the interface of field disciplines.
5. A residence permit for non-EU PhD students of only 4 years does not align with the PhD regulations.
6. Reducing nitrogen emissions requires price incentives in food and travel.
7. Organizing atmospheric chemistry conferences in regions with poor air quality will confront environmental injustice and elevate global awareness.

Propositions belonging to the thesis, entitled

Nitrate aerosol in the Netherlands

F. R. Nursanto
Wageningen, 6 July 2026

Nitrate Aerosol in the Netherlands

F. R. Nursanto

Thesis committee

Promotor:
Prof. Dr M.C. (Maarten) Krol
Professor of Air Quality and Atmospheric Chemistry
Wageningen University & Research

Co-promotor:
Dr J.L. (Juliane) Fry
Associate Professor in Meteorology and Air Quality Group
Wageningen University & Research

Other members:
Prof. Dr *ir.* Wim de Vries, Wageningen University & Research
Dr Steve Brown, University of Colorado, Boulder, United States of America
Dr Jean-Eudes Petit, Université Paris-Saclay, France
Dr Astrid Manders-Groot, Netherlands Organisation for Applied Scientific Research (TNO), Utrecht

This research was conducted under the auspices of the Graduate School for Socio-Economic and Natural Sciences of the Environment (SENSE)

Nitrate Aerosol in the Netherlands

F. R. Nursanto

Thesis
submitted in fulfilment of the requirements for the degree of doctor
at Wageningen University
by the authority of the Rector Magnificus
Prof. Dr C. Kroeze,
in the presence of the
Thesis Committee appointed by the Academic Board
to be defended in public
on 6 July 2026
at 1 p.m. in the Omnia Auditorium.

Farhan R. Nursanto
Nitrate aerosol in the Netherlands
XXXIV+210 pages.

PhD thesis, Wageningen University, Wageningen, the Netherlands (2026)
With references, with summaries in English, French, and Indonesian

https://doi.org/10.18174/681814



Summary

Reactive nitrogen species such as ammonia (NH_3) and nitrogen oxides (NO_x) are essential for sustaining life on Earth, but their excessive concentrations harm ecosystems. With a high nitrogen deposition rate from the atmosphere, the Netherlands faces a nitrogen crisis that degrades its natural habitats. Current methods for studying the fate of nitrogen do not consider the speciation of nitrate between ammonium nitrate (NH_4NO_3) and organic nitrates, nor organic nitrate gas-particle partitioning, both of which determine the lifetimes, transport, and deposition of reactive nitrogen. These missing processes can lead to an inaccurate estimates of nitrogen deposition fluxes and, consequently, inefficient emission reduction strategies.

This thesis investigates the sources, sinks, and atmospheric processing of nitrate in the Netherlands, with a focus on nitrate aerosol formation and gas–particle partitioning. New particle formation and growth events involve the clustering and condensation of low-volatility compounds, including inorganic salts and highly oxidized organic molecules — some including nitrate functional groups — leading to the formation of nitrate-containing aerosol particles. The partitioning of nitrate from the gas-phase to the particle-phase depends on factors such as volatility, molecular weight, oxidation conditions, precursor composition, and temperature.

We identify the physical and chemical properties of nitrates using observations from ambient measurements and chamber experiments, as part of both intensive measurement campaigns and long-term monitoring. The role of different chemical species during new particle formation and growth is examined using a hybrid positive matrix factorization (PMF) analysis **(Chapter 2)**. Nitrate aerosol is further speciated into inorganic and organic components using a NO_x^+ ratio method applied to aerosol mass spectrometry measurements **(Chapter 3)**. The gas–particle partitioning and bulk volatility of organic nitrates are investigated through atmospheric chamber experiments **(Chapter 4)** and ambient observations **(Chapter 5)**.

Chapter 2 focuses on understanding the role of different chemical species during new particle formation and growth events using measurements from the Ruisdael Land–Atmosphere Interactions Intensive Trace-gas and Aerosol (RITA) 2021 campaign in Cabauw, central Netherlands. Aerosol chemical composition measured by aerosol

chemical speciation monitor (ACSM) and particle number size distributions are analyzed together using a hybrid PMF. This approach correlates organic mass spectra and inorganic species with specific particle size ranges and the results are analyzed further to identify their source regions. PMF analyses across spring, summer, and autumn identify four aerosol populations. Nucleation-mode particles are associated with ammonium, sulfate, and less-oxidized organics and are linked to westerly and southwesterly airmasses originating from the Rotterdam port and industrial region. Accumulation-mode particles are characterized by ammonium, nitrate, and hydrocarbon-like organic aerosol and are related to westerly and southerly airmasses rich in NH_3 and NO_x. Two additional aerosol populations are not size-resolved: a mixed inorganic–organic aerosol influenced by multiple sources, and more-oxidized organic aerosol originating from long-range transport over continental Europe. These results show that oxidized organics and ammonium sulfate play a key role in new particle formation, while nitrates play a larger role in particle growth.

Chapter 3 focuses on the speciation of particulate nitrate into NH_4NO_3 and organic nitrate. This has historically been achieved using the NO_2^+/NO^+ ion ratio produced during nitrate fragmentation in the standard vaporizer (SV) of a high-mass-resolution time-of-flight aerosol mass spectrometry (HR-ToF-AMS), known as the NO_x^+ ratio method. While this approach is well established for SV-HR-ToF-AMS, this chapter presents the first adaptation of this method for application to the unit-mass-resolution time of flight ACSM (UMR-ToF-ACSM) with capture vaporizer (CV), which is widely used in atmospheric aerosol monitoring networks as a fine particle ($PM_{2.5}$) composition monitor. The uncertainty of the method is $\sim$30 % for total particulate nitrate concentration $<1\ \mu g \cdot m^{-3}$ and $\sim$10 % for total particulate nitrate concentration $>4\ \mu g \cdot m^{-3}$. The method is validated using co-located CV-ACSM and SV-AMS measurements during the CAINA (Cloud-Aerosol Interactions in a Nitrogen-dominated Atmosphere) AIDA (Aerosol Interaction and Dynamics in the Atmosphere) chamber campaign.

Organic nitrates include a large range of compounds. **Chapter 4** explores the formation, gas–particle partitioning, molecular weight, and yield of organic nitrates under controlled conditions in the SAPHIR (Simulation of Atmospheric PHotochemistry In a large Reaction chamber) conducted during the CHANEL (Household Chemicals Amplifying Urban Aerosol Pollution) 2024 campaign. Typical chamber studies employ single-compound precursors to reduce complexity and study specific chemical mechanisms, which do not represent the complex ambient atmospheric mixture. In contrast, the study presented in **Chapter 4** introduces complex urban emission mixtures under realistic oxidation conditions in an atmospheric chamber, allowing a more accurate characterization of organic nitrate formation in the real-world atmosphere. Emission mixtures are constructed from the fingerprint of source-specific emission profiles, including volatile chemical products (VCPs), cooking emissions, and traffic, as well as more complex scenarios representing present-day and future urban environments. The

reaction products are characterized using a total NO_y monitor, AMS, gas chromatography, and high-mass-resolution chemical ionization mass spectrometry. The results show the importance of unsaturated volatile organic compounds (VOCs) in determining the organic nitrate yield. Enhanced particle phase partitioning is observed under nighttime oxidation by $NO_3^{\bullet}$ compared to daytime oxidation by $OH^{\bullet}$. The average molecular weight of particulate organic nitrate produced under nighttime conditions (331±13 $g \cdot mol^{-1}$) is higher compared to daytime conditions (258±24 $g \cdot mol^{-1}$), driven by a larger contribution from oligomers. Similarly, the mass fraction of organic aerosol mass attributed to particulate organic nitrate is higher by a factor of 2.6 to 4.5 under nighttime conditions compared to daytime conditions, reflecting both increased molecular weight and lower temperatures favoring condensation. Despite differences in precursor mixture complexity and the variability of the average molecular weight of particulate organic nitrates, the bulk gas-particle partitioning coefficients of organic nitrate mixtures are consistent with the modeled volatility of oxidized monoterpene nitrates using the group contribution method SIMPOL.1 (10^{-4} to 10^{-2} $m^3 \cdot \mu g^{-1}$ at 18–40 °C). These findings improve our understanding of the sources, molecular weight, and volatility of bulk organic nitrate from controlled simulations of complex urban emissions mixtures.

The knowledge from **Chapter 4** is subsequently applied in **Chapter 5** to long-term ambient measurements in Cabauw (2023–2025). We examine the seasonal and airmass-dependent variability in nitrate aerosol pollution episodes using gas-phase species and particle-phase species observations, meteorological data, and back trajectory analysis. The adapted NO_x^+ ratio method **(Chapter 3)** is applied to quantify inorganic and organic nitrate fractions, while gas–particle partitioning is evaluated using combined ACSM and total NO_y measurements, similar to **Chapter 4**. These observations are integrated with meteorological data and Copernicus Atmosphere Monitoring Service (CAMS) reanalysis data to characterize nitrate pollution episodes (>0.8 $\mu g \cdot m^{-3}$). Wintertime pollution episodes (October–February) occur more frequently and are associated with lower total organic nitrate mixing ratios (2–4 ppb) and smaller particulate organic nitrate fractions (14–43 %) compared to summertime episodes (March–September; 7–11 ppb; 30–58 %). This contrast is associated with a nitric acid (HNO_3)-dominated regime in winter, where reduced photochemistry limits organic nitrate formation and low temperatures favor condensation of ammonium nitrate and less volatile organic nitrates. In summer, enhanced photochemistry promotes the organic nitrate ($RONO_2$) formation, and higher temperatures reduce particle-phase partitioning. Airmass analysis shows that slightly over half of nitrate pollution episodes (53 %) are associated with urban coastal airmasses, characterized by higher total nitrate concentrations but lower organic nitrate fractions due to proximity to NO_x emission hotspots. These findings demonstrate that the evaluation of nitrate pollution mitigation strategies must account for seasonal chemical regimes, and should consider both inorganic and organic nitrate aerosol.

Chapter 6 synthesizes the key findings of the thesis and identifies remaining knowledge gaps. The results emphasize: 1) the influence of emission source profiles on aerosol composition, 2) the significant contribution of organic nitrate to the aerosol mass in the Netherlands, and 3) the role of seasonal conditions in determining the relative production of HNO_3 and $RONO_2$ production from NO_x oxidation. From these findings, we highlight the lack of accounting for organic nitrates in nitrogen transport and deposition models, which can affect emission reduction strategies. We highlight major areas for improvements including: 1) evaluation of emission reduction strategies taking into account seasonal NO_x sink regimes, 2) observation-constrained chemical transport and deposition modeling from NO_x hotspots to nature areas, and 3) more equipped monitoring site facilities with higher time- and mass-resolution VOC and organic aerosol measurements to better characterize organic nitrates.

Overall, this thesis advances understanding of nitrate sources, sinks, and chemical processes in a nitrogen-dominated atmosphere. By developing tools applicable to long-term monitoring sites, characterizing organic nitrate properties under realistic atmospheric conditions, and elucidating the drivers of nitrate pollution episodes, this work provides a foundation for more accurate representation of inorganic and organic nitrate in chemical transport and nitrogen deposition models.

Résumé

Les espèces réactives de l'azote, telles que l'ammoniac (NH_3) et les oxydes d'azote (NO_x), sont essentielles au maintien de la vie terrestre, mais leurs concentrations excessives sont néfastes pour les écosystèmes. En raison d'un taux élevé de dépôts atmosphériques d'azote, les Pays-Bas font face à une crise de l'azote qui dégrade leurs habitats naturels. Les méthodes actuelles d'étude du devenir de l'azote ignorent la spéciation entre nitrate d'ammonium (NH_4NO_3) et nitrates organiques, ainsi que la partition gaz–particule de nitrates organiques. Pourtant, ces deux espèces chimiques déterminent les durées de vie, le transport et le dépôt d'azote réactif. L'absence de prise en compte de ces processus peut conduire à une estimation imprécise des flux de dépôt d'azote et, par conséquent, à des stratégies de réduction des émissions inefficaces.

Cette thèse étudie les sources, les puits et les transformations atmosphériques du nitrate aux Pays-Bas, en mettant l'accent sur la formation des aérosols nitrés et la partition gaz-particule. La formation et la croissance de nouvelles particules impliquent le regroupement et la condensation de composés à faible volatilité, incluant des sels inorganiques et des molécules organiques fortement oxydées — pouvant contenir des groupes fonctionnels nitrate — conduisant à la formation de particules d'aérosols nitrés. La partition du nitrate entre la phase gazeuse et la phase particulaire dépend de facteurs tels que la volatilité, la masse moléculaire, les conditions d'oxydation, la composition des précurseurs et la température.

Nous identifions les propriétés physiques et chimiques des nitrates à l'aide d'observations issues de mesures ambiantes et d'expériences en chambre atmosphérique, dans le cadre de campagnes de mesures intensives et de mesures à long terme. Le rôle des différentes espèces chimiques lors de la formation et de la croissance des particules est examiné à l'aide d'une analyse par factorisation de matrices positives (PMF) hybride **(Chapitre 2)**. Les aérosols nitrés sont ensuite spéciés en nitrates inorganiques et organiques à l'aide de la méthode du rapport NO_x^+ appliquée aux mesures de spectrométrie de masse des aérosols **(Chapitre 3)**. La partition gaz–particule et la volatilité globale des nitrates organiques sont examinées à l'aide d'expériences en chambre atmosphérique **(Chapitre 4)** et d'observations ambiantes **(Chapitre 5)**.

Le **Chapitre 2** se concentre sur la compréhension du rôle des différentes espèces chimiques lors des événements de formation et de croissance de nouvelles particules à partir des mesures de la campagne « Ruisdael Land–Atmosphere Interactions Intensive Trace-gas and Aerosol (RITA) » 2021 à Cabauw, au centre des Pays-Bas. La composition chimique des aérosols mesurée par un moniteur de spéciation chimique des aérosols (ACSM) et les distributions de taille en nombre de particules sont analysées conjointement à l'aide d'une approche PMF hybride. Cette approche corrèle les spectres de masse organiques et les espèces inorganiques à des granulométries spécifique, et les résultats sont analysés pour identifier leurs régions de provenance. Les analyses PMF réalisées au printemps, en été et en automne identifient quatre populations d'aérosols. Les particules du mode de nucléation sont associées à l'ammonium, au sulfate et à des composés organiques moins oxydés qui sont liées à des masses d'air d'origine ouest et sud-ouest provenant de la zone portuaire et industrielle de Rotterdam. Les particules du mode d'accumulation sont caractérisées par l'ammonium, le nitrate et des aérosols organiques de type hydrocarbure qui sont associées à des masses d'air d'origine ouest et sud riches en émissions de NH_3 et de NO_x. Deux populations supplémentaires ne sont pas corrélées à des tailles spécifiques : un mélange d'aérosols inorganiques et organiques de sources multiples, et des aérosols organiques plus oxydés issus du transport à longue distance depuis l'Europe continentale. Ces résultats montrent que les composés organiques oxydés et le sulfate d'ammonium jouent un rôle clé dans la formation des particules, tandis que le nitrate contribue plutôt à la croissance des particules.

Le **Chapitre 3** se concentre sur la spéciation du nitrate particulaire en NH_4NO_3 et en nitrates organiques. Cette spéciation se base sur le rapport ionique NO_2^+/NO^+ qui se produit lors de la fragmentation du nitrate dans le vaporisateur standard (SV) d'un spectromètre de masse des aérosols à temps de vol et à haute résolution de masse (HR-ToF-AMS), connu sous le nom de méthode du rapport NO_x^+. Bien que cette approche soit bien établie pour les instruments SV-HR-ToF-AMS, ce chapitre présente la première adaptation de cette méthode pour son application aux instruments ACSM à temps de vol et à résolution de masse unitaire (UMR-ToF-ACSM) équipés d'un vaporisateur capteur (CV), largement déployés dans les réseaux de surveillance atmosphérique pour le suivi de la composition des particules fines ($PM_{2,5}$). L'incertitude de la méthode est d'environ 30 % lorsque la concentration totale de nitrate particulaire est inférieure à 1 $\mu g \cdot m^{-3}$, et d'environ 10 % lorsque la concentration totale de nitrate particulaire est supérieure à 4 $\mu g \cdot m^{-3}$. La méthode est validée à l'aide de mesures colocalisées de CV-ACSM et de SV-AMS lors des expériences en chambre atmosphérique de la campagne CAINA (*Cloud–Aerosol Interactions in a Nitrogen-dominated Atmosphere*) AIDA (*Aerosol Interaction and Dynamics in the Atmosphere*).

Les nitrates organiques regroupent une grande diversité de composés. Le **Chapitre 4** explore leur formation, leur partition gaz–particule, leur masse moléculaire et leur

rendement sous des conditions contrôlées dans la chambre atmosphérique SAPHIR (*Simulation of Atmospheric PHotochemistry In a large Reaction chamber*) dans le cadre de la campagne CHANEL (*Household Chemicals Amplifying Urban Aerosol Pollution*) en 2024. Les études classiques en chambre utilisent des précurseurs monocomposants afin de réduire la complexité et d'étudier des mécanismes chimiques spécifiques ; toutefois, ceux-ci ne représentent pas la complexité du mélange atmosphérique ambiant. Au contraire, les études présentées dans le **Chapitre 4** reproduisent des mélanges complexes d'émissions urbaines sous des conditions d'oxydation réalistes dans une chambre atmosphérique, permettant une caractérisation plus précise de la formation des nitrates organiques dans l'atmosphère réelle. Les mélanges d'émissions sont élaborés à partir des empreintes de profils d'émission spécifiques à une source incluant les produits chimiques volatils (VCPs), les émissions de cuisson et le trafic ainsi que de scénarios plus complexes représentant des environnements urbains actuels et futurs. Les produits de réaction sont caractérisés à l'aide d'un moniteur de NO_y total, d'un AMS, d'une chromatographie en phase gazeuse et de spectrométries de masse à ionisation chimique. Les résultats montrent l'importance des composés organiques volatils (COV) insaturés dans la détermination du rendement en nitrates organiques. Une partition accrue vers la phase particulaire est observée lors de l'oxydation nocturne par le radical $NO_3^{\bullet}$ par rapport à l'oxydation diurne par le radical $OH^{\bullet}$. La masse moléculaire moyenne des nitrates organiques particulaires formés dans conditions nocturnes (331 ± 13 g $\cdot$ mol^{-1}) est plus élevée que celle obtenue dans conditions diurnes (258 ± 24 g $\cdot$ mol^{-1}), en raison d'une contribution plus importante des oligomères. De même, la fraction massique de l'aérosol organique attribuée aux nitrates organiques particulaires est 2,6 à 4,5 fois plus élevée sous conditions nocturnes que sous conditions diurnes, reflétant à la fois l'augmentation de la masse moléculaire et l'effet des températures plus basses favorisant la condensation. Malgré la complexité variable des mélanges de précurseurs et la variabilité de la masse moléculaire moyenne des nitrates organiques particulaires, les coefficients de partition gaz–particule globaux des nitrates organiques restent cohérents avec les volatilités des nitrates oxydés de monoterpènes modélisées par la méthode de contribution de groupes fonctionnels SIMPOL.1 (10^{-4} à 10^{-2} m$^3 \cdot \mu$g^{-1} à 18–40 °C). Ces résultats améliorent notre compréhension des sources, de la masse moléculaire et de la volatilité globale des nitrates organiques issus de simulations contrôlées de mélanges complexes d'émissions urbaines.

Les informations acquises au **Chapitre 4** sont ensuite appliquées au **Chapitre 5** à des mesures ambiantes effectuées à Cabauw (2023—2025). Nous examinons la variabilité saisonnière ainsi que celle liée aux origines de masse d'air lors des épisodes de pollution aux aérosols nitrés, en utilisant des observations en phase gazeuse et en phase particulaire, des données météorologiques et une analyse des rétro-trajectoires. La méthode adaptée du rapport NO_x^+ **(Chapitre 3)** est appliquée pour quantifier les fractions de nitrates inorganiques et organiques, tandis que la partition gaz–particule

est évaluée à partir d'observations d'ACSM et de mesures de NO_y total, de manière similaire au **Chapitre 4**. Ces observations sont intégrées aux données météorologiques et aux données de réanalyses du *Copernicus Atmosphere Monitoring Service* (CAMS) afin de caractériser les épisodes de pollution aux nitrate ($>$0,8 $\mu g \cdot m^{-3}$). Les épisodes hivernaux (octobre–février) sont plus fréquents et associés à des rapports de mélange totaux plus faibles de nitrates organiques (2–4 ppb) ainsi qu'à des fractions particulaires plus faibles (14–43 %) que les épisodes estivaux (mars–septembre ; 7–11 ppb ; 30–58 %). Ce contraste est associé à un régime dominé par l'acide nitrique (HNO_3) en hiver, où la photochimie réduite limite la formation des nitrates organiques et où les basses températures favorisent la condensation du nitrate d'ammonium et des nitrates organiques peu volatils. En été, une photochimie renforcée favorise la formation des nitrates organiques ($RONO_2$), mais les températures plus élevées réduisent leur partition vers la phase particulaire. L'analyse des masses d'air montre qu'un peu plus de la moitié des épisodes de pollution aux nitrates (53 %) sont associés à des masses d'air côtières urbaines ; celles-ci se caractérisent par des concentrations totales de nitrate plus élevées mais des fractions de nitrates organiques plus faibles, en raison de la proximité des zones sources de NO_x. Ces résultats démontrent que l'évaluation des stratégies d'atténuation de la pollution aux nitrates doit tenir compte des régimes chimiques saisonniers et devrait intégrer la distinction entre nitrates inorganiques et organiques.

Le **Chapitre 6** synthétise les conclusions clés de la thèse et identifie les lacunes de connaissances subsistantes. Les résultats mettent en évidence : 1) l'influence des profils de sources d'émission sur la composition des aérosols ; 2) la contribution significative des nitrates organiques à la masse des aérosols aux Pays-Bas ; et 3) le rôle des conditions saisonnières dans la détermination de la proportion relative de HNO_3 et de $RONO_2$ produits par l'oxydation des NO_x. À partir de ces résultats, nous soulignons l'absence de prise en compte des nitrates organiques dans les modèles de transport et de dépôt d'azote, ce qui peut affecter les stratégies de réduction des émissions. Nous préconisons plusieurs axes majeurs d'amélioration : 1) l'évaluation des stratégies de réduction des émissions en tenant compte des régimes saisonniers des puits de NO_x ; 2) une modélisation du transport chimique et du dépôt contrainte par les observations, depuis les sources de NO_x vers les zones naturelles; et 3) le déploiement de stations d'observation mieux équipées, permettant des mesures de COV et d'aérosols organiques à plus hautes résolutions temporelles et massiques afin de mieux caractériser les nitrates organiques.

Dans l'ensemble, cette thèse fait progresser la compréhension des sources, des puits et des processus chimiques des nitrates dans une atmosphère saturée en azote. En développant des outils applicables aux réseaux de surveillance à long terme, en caractérisant les propriétés des nitrates organiques dans des conditions atmosphériques réalistes et en élucidant les facteurs déterminants des épisodes de pollution aux nitrates,

ce travail permet d'affiner la représentation des nitrates inorganiques et organiques dans les modèles de transport chimique et de dépôt d'azote.

Rangkuman

Spesies nitrogen reaktif seperti amonia (NH_3) dan oksida nitrogen (NO_x) merupakan zat yang penting bagi keberlangsungan kehidupan di Bumi. Akan tetapi, jika kadarnya yang berlebihan, mereka dapat merusak ekosistem. Akibat laju deposisi nitrogen atmosferik yang tinggi, Belanda menghadapi krisis nitrogen yang menyebabkan degradasi lingkungan alamiahnya. Metode terkini untuk mempelajari alur perubahan nitrogen belum mempertimbangkan spesiasi nitrat menjadi amonium nitrat (NH_4NO_3) dan nitrat organik maupun partisi gas–partikel dari nitrat organik. Padahal, proses-proses tersebut menentukan masa hidup, perpindahan, dan deposisi nitrogen reaktif. Pengabaian proses ini dapat menyebabkan ketakakuratan pada estimasi fluks deposisi nitrogen dan mengurangi efektivitas strategi pengurangan emisi.

Disertasi ini menyelidiki sumber, rosot, dan proses kimia atmosferik nitrat di Belanda, terutama pada pembentukan aerosol nitrat dan partisi gas–partikel. Peristiwa pembentukan dan pertumbuhan partikel baru melibatkan pembentukan rangkaian serta kondensasi senyawa dengan volatilitas rendah seperti garam anorganik dan molekul organik yang sangat teroksidasi (beberapa mengandung gugus fungsi nitrat) sehingga mengakibatkan terbentuknya partikel aerosol yang mengandung nitrat. Partisi nitrat antara fase gas dan fase partikel dipengaruhi oleh berbagai faktor, seperti volatilitas, massa molekul, kondisi oksidasi, komposisi prekursor, dan suhu.

Sifat fisik dan kimia nitrat diidentifikasi dalam disertasi ini menggunakan hasil pengamatan dari pengukuran ambien dan eksperimen di dalam ruang simulasi atmosfer sebagai bagian dari program pengukuran intensif atau pemantauan jangka panjang. Peran berbagai spesies kimia dalam proses pembentukan dan pertumbuhan partikel dianalisis menggunakan pendekatan faktorisasi matriks positif (PMF) hibrida **(Bab 2)**. Aerosol nitrat selanjutnya dispesiasi menjadi komponen anorganik dan organik menggunakan metode rasio NO_x^+ yang diterapkan pada pengukuran spektrometri massa aerosol **(Bab 3)**. Partisi gas–partikel dan volatilitas keseluruhan dari nitrat organik diamati melalui eksperimen ruang simulasi atmosfer **(Bab 4)** serta pengamatan ambien **(Bab 5)**.

Bab 2 berfokus untuk memahami peran berbagai spesies kimia selama peristiwa pembentukan dan pertumbuhan partikel baru menggunakan hasil pengukuran dari kampa-

nye RITA (*Ruisdael Land–Atmosphere Interactions Intensive Trace-gas and Aerosol*) tahun 2021 di Cabauw yang berlokasi di Belanda tengah. Komposisi kimia aerosol yang diukur menggunakan monitor spesiasi kimia aerosol (ACSM) serta distribusi ukuran jumlah partikel digabungkan dan diolah dengan pendekatan PMF hibrida. Pendekatan ini mengaitkan spektrum massa aerosol organik dan komposisi aerosol anorganik dengan kelas ukuran partikel tertentu yang kemudian dianalisis lebih lanjut untuk mengidentifikasi daerah asalnya. Analisis PMF pada pengukuran di musim semi, musim panas, dan musim gugur mengidentifikasi empat populasi aerosol. Partikel mode nukleasi ditemukan berkaitan dengan amonium, sulfat, dan aerosol organik dengan tingkat oksidasi rendah, serta berhubungan dengan massa udara dari arah barat dan barat daya yang merupakan kawasan pelabuhan dan industri Rotterdam. Partikel mode akumulasi ditemukan berkaitan dengan amonium, nitrat, dan wilayah barat dan selatan yang kaya akan emisi NH_3 dan NO_x. Dua populasi aerosol lainnya tidak berkaitan dengan golongan ukuran khusus, yaitu campuran aerosol anorganik dan organik dari berbagai sumber, serta aerosol organik dengan tingkat oksidasi tinggi akibat perpindahan jarak jauh dari daratan benua Eropa. Hasil ini menunjukkan bahwa senyawa organik teroksidasi dan amonium sulfat berperan penting dalam tahapan awal pembentukan partikel, sementara nitrat berkontribusi lebih besar pada proses pertumbuhan partikel.

Bab 3 berfokus pada spesiasi partikulat nitrat menjadi NH_4NO_3 dan nitrat organik. Hal ini dicapai menggunakan perbandingan ion NO_2^+/NO^+ yang dihasilkan selama fragmentasi nitrat di dalam *vaporizer* standar (SV) pada spektrometri massa aerosol waktu-terbang dengan resolusi massa tinggi (HR-ToF-AMS), yang dikenal sebagai metode rasio NO_x^+. Meskipun metode ini telah lama digunakan untuk instrumen SV-HR-ToF-AMS, bab ini menyajikan penerapan pertama metode ini pada instrumen ToF-ACSM dengan resolusi unit massa (UMR-ToF-ACSM) dan *vaporizer* tipe perangkap (CV) yang banyak digunakan di stasiun pengamatan udara untuk memantau komposisi partikel halus ($PM_{2,5}$). Metode ini memiliki ketidakpastian sebesar $\sim$30 % untuk total konsentrasi partikulat nitrat <1 $\mu g \cdot m^{-3}$ dan $\sim$10 % untuk total konsentrasi partikulat nitrat >4 $\mu g \cdot m^{-3}$. Metode ini divalidasi menggunakan pengukuran serentak CV-ACSM dan SV-AMS dalam ruang simulasi atmosfer dalam program CAINA (*Cloud–Aerosol Interactions in a Nitrogen-dominated Atmosphere*) AIDA (*Aerosol Interaction and Dynamics in the Atmosphere*).

Nitrat organik mencakup beragam senyawa kimia. **Bab 4** membahas pembentukan, partisi gas–partikel, massa molekul, dan rendemen dari nitrat organik dengan kondisi terkontrol dalam ruang simulasi atmosfer SAPHIR (*Simulation of Atmospheric PHotochemistry In a large Reaction chamber*) yang dilakukan selama program CHANEL (*Household Chemicals Amplifying Urban Aerosol Pollution*) pada tahun 2024. Studi ruang simulasi atmosfer pada umumnya hanya menggunakan satu senyawa prekursor untuk menyederhanakan sistem dipelajari serta mengisolasi suatu mekanisme reaksi tertentu.

Padahal, atmosfer tersusun atas campuran yang kompleks, sehingga penyederhanaan ini kurang merepresentasikan kondisi atmosfer secara nyata. Atas dasar itu, studi pada **Bab 4** menggunakan campuran emisi perkotaan yang kompleks dalam kondisi oksidasi yang realistis di dalam ruang simulasi atmosfer, sehingga meningkatkan akurasi karakterisasi pembentukan nitrat organik layaknya atmosfer di dunia nyata. Campuran emisi yang digunakan disusun berdasarkan sidik jari emisi yang spesifik berasal dari sumber tertentu, meliputi produk kimia volatil (VCP), emisi aktivitas memasak, dan emisi lalu lintas, dengan turut memperhitungkan skenario kompleks yang merepresentasikan lingkungan perkotaan kini dan di masa depan. Produk reaksi dikarakterisasi berdasarkan hasil pengukuran dari monitor NO_y total, spektrometri massa aerosol, kromatografi gas, dan spektrometri massa dengan ionisasi kimia dan resolusi massa tinggi. Hasil penelitian menunjukkan besarnya pengaruh senyawa organik volatil (VOC) tak jenuh terhadap rendemen pembentukan nitrat organik. Kecenderungan partisi menuju fase partikel yang lebih kuat dibanding fase gas diamati dalam kondisi oksidasi malam hari yang melibatkan radikal $NO_3^{\bullet}$ dibanding dalam kondisi oksidasi siang hari yang melibatkan radikal $OH^{\bullet}$. Massa molekul rata-rata partikulat nitrat organik yang terbentuk pada malam hari (331 ± 13 g $\cdot$ mol^{-1}) ditemukan lebih tinggi dibanding siang hari (258 ± 24 g $\cdot$ mol^{-1}) akibat kontribusi oligomer yang lebih besar. Fraksi massa aerosol organik yang merupakan partikulat nitrat organik juga meningkat sebesar 2,6 hingga 4,5 kali pada kondisi malam hari dibanding siang hari. Ini mencerminkan terjadinya peningkatan massa molekul serta suhu yang lebih rendah yang mendukung terjadinya kondensasi. Terlepas dari perbedaan kompleksitas campuran prekursor dan variabilitas massa molekul rata-rata nitrat organik, koefisien partisi gas–partikel dari nitrat organik yang diperoleh konsisten dengan volatilitas dari nitrat monoterpena teroksidasi yang diprediksi menggunakan metode kontribusi gugus SIMPOL.1 (10^{-4} hingga 10^{-2} $m^3 \cdot \mu g^{-1}$ pada 18–40 °C). Temuan ini meningkatkan pemahaman mengenai sumber, massa molekul, dan volatilitas nitrat organik secara keseluruhan dalam campuran emisi perkotaan yang kompleks.

Informasi yang diperoleh dari **Bab 4** kemudian diterapkan pada **Bab 5** pada hasil pengukuran jangka panjang di Cabauw (2023–2025). Variabilitas musiman dan variabilitas terkait asal massa udara selama episode polusi aerosol nitrat dikaji menggunakan pengamatan spesies kimia pada fase gas dan partikel, data cuaca, dan analisis lintasan balik. Metode rasio NO_x^+ yang telah diadaptasi **(Bab 3)** diterapkan untuk menentukan fraksi nitrat anorganik dan organik. Sementara itu, partisi gas–partikel dievaluasi menggunakan kombinasi hasil pengukuran ACSM dan monitor NO_y total, serupa dengan **Bab 4)**. Pengukuran ini diintegrasikan dengan data meteorologi serta data analisis-ulang dari *Copernicus Atmosphere Monitoring Service* (CAMS) untuk mengkarakterisasi episode polusi nitrat ($>0{,}8$ $\mu g \cdot m^{-3}$). Selama musim dingin (Oktober–Februari), episode polusi lebih sering terjadi dan dikaitkan dengan perbandingan campuran total nitrat organik yang lebih rendah (2–4 ppb) serta fraksi partikulat nitrat organik yang

lebih kecil (14–43 %) dibanding musim panas (Maret–September; 7–11 ppb; 30–58 %). Perbedaan ini terkait dengan musim dingin yang didominasi oleh rezim asam nitrat (HNO_3); fotokimia yang terbatas menghambat pembentukan nitrat organik, sementara suhu rendah mendukung kondensasi amonium nitrat dan nitrat organik dengan volatilitas rendah menuju fase partikel. Selama musim panas, reaksi fotokimia yang lebih intensif mendorong pembentukan nitrat organik ($RONO_2$), namun suhu yang lebih tinggi mengurangi kecenderungan partisi menuju fase partikel. Analisis massa udara menunjukkan bahwa sekitar setengah dari seluruh episode polusi nitrat (53 %) terkait dengan massa udara perkotaan di pesisir, yang ditandai oleh konsentrasi nitrat total yang lebih tinggi dan fraksi nitrat organik yang lebih rendah. Ini diakibatkan oleh kedekatan lokasi pengukuran dengan pusat emisi NO_x. Temuan ini menunjukkan bahwa evaluasi dari strategi mitigasi polusi nitrat harus mempertimbangkan rezim kimia musiman dan kedua jenis aerosol nitrat (anorganik dan organik).

Bab 6 merangkum temuan utama disertasi ini dan mengidentifikasi kekurangan yang masih ada. Hasil penelitian ini menekankan: 1) pengaruh profil sumber emisi terhadap komposisi kimia aerosol, 2) kontribusi signifikan nitrat organik terhadap massa aerosol total di Belanda, serta 3) peran musim dalam menentukan perbandingan relatif dari produksi HNO_3 dan $RONO_2$ melalui oksidasi NO_x. Dari hasil temuan ini, kurangnya representasi nitrat organik dalam model perpindahan dan deposisi nitrogen yang dapat memengaruhi strategi pengurangan emisi perlu digarisbawahi. Beberapa hal utama yang dapat dikembangkan lebih lanjut juga layak disorot, antara lain: 1) evaluasi strategi pengurangan emisi yang mempertimbangkan rezim rosot NO_x yang berubah secara musiman; 2) pemodelan transpor kimia dari sumber emisi NO_x menuju kawasan alam berbasis hasil pengamatan; dan 3) peningkatan kapabilitas stasiun pengamatan dalam pengukuran VOC dan aerosol organik dengan resolusi waktu dan massa yang lebih tinggi, agar dapat mengarakterisasi nitrat organik secara lebih komprehensif.

Secara keseluruhan, disertasi ini memperluas pemahaman mengenai sumber, rosot, dan transformasi nitrat dalam atmosfer kaya dengan nitrogen. Melalui pengembangan metode yang dapat diterapkan pada stasiun pengamatan jangka panjang, karakterisasi nitrat organik dalam kondisi atmosfer yang realistis, serta penentuan penggerak utama episode polusi nitrat, penelitian ini menyediakan dasar yang kuat untuk meningkatkan akurasi representasi nitrat anorganik dan organik dalam model transpor kimia dan deposisi nitrogen.

Contents

	Page
Summary	**XI**
Résumé	**XV**
Rangkuman	**XXI**
Contents	**XXV**
List of chemical formulas	**XXVII**
List of abbreviations and notations	**XXIX**
Chapter 1 Introduction	**1**
Chapter 2 Chemical species responsible for new particle formation and growth in the Netherlands	**17**
Chapter 3 NO_x^+ ratio method to separate inorganic and organic nitrate signal from aerosol mass spectrometry measurements	**43**
Chapter 4 Gas-particle partitioning, molecular weight, and yield of organic nitrate in chamber-simulated urban atmospheres	**73**
Chapter 5 Influence of the emission signature and meteorology on nitrate aerosol formation in the Netherlands	**107**
Chapter 6 Synthesis and outlook	**143**
References	**159**
Authorship statement	**195**
List of publications	**197**

Acknowledgements **199**

About the cover **205**

List of chemical formulas

Br^-	bromide
$C_3H_7NH_2$	propylamine
$C_3H_7NH_2^+$	propylamine ion
C_5H_8	isoprene
C_6H_6	benzene
$C_6H_6^+$	benzene ion
$C_{10}H_{16}$	monoterpenes
$Ca(NO_3)_2$	calcium nitrate
CO^+	carbon monoxide ion
CO_2^+	carbon dioxide ion
Cl	chloride (species in AMS/ACSM are referred to as functional groups without charge)
Cl^-	chloride
HNO_3	nitric acid
HONO	nitrous acid
H_2SO_4	sulfuric acid
I^-	iodide
Mo	molybdenum
N	nitrogen
N_2	dinitrogen
N_2O_5	nitrogen pentoxide
$NaNO_3$	sodium nitrate
NaCl	sodium chloride
NH_3	ammonia
NH_4	ammonium (species in AMS/ACSM are referred to as functional groups without charge)
NH_4^+	inorganic ammonium (in the particle phase)
NH_4HSO_4	ammonium bisulfate
NH_4NO_3	ammonium nitrate

$(NH_4)_2SO_4$	ammonium sulfate
NH_x	reduced nitrogen
NO	nitrogen monoxide
NO^+	nitrogen monoxide ion (in the vaporizer)
NO_2	nitrogen dioxide
NO_2^+	nitrogen dioxide ion (in the vaporizer)
NO_3	nitrate (species in AMS/ACSM are referred to as functional groups without charge)
NO_3^-	inorganic nitrate (in the particle phase)
$NO_3^\bullet$	nitrate radical
NO_x	nitrogen oxides = NO+NO_2
NO_x^+	nitrogen oxide ions
NO_y	oxidized nitrogen, or total oxidized nitrogen species (= NO_x+NO_z)
NO_z	nitrogen reservoir species; e.g., $RONO_2$, RO_2NO_2, HNO_3, N_2O_5 (= NO_y−NO_x)
$OH^\bullet$	hydroxyl radical
O_3	ozone
$RO_2^\bullet$	organic peroxy radical
$RONO_2$	alkyl nitrate (also refers to organic nitrate in general)
RO_2NO_2	peroxy nitrate
$RO_x^\bullet$	organic radicals (= $RO^\bullet + RO_2^\bullet$)
SO_2	sulfur dioxide
SO_4	sulfate (species in AMS/ACSM are referred to as functional groups without charge)
SO_4^{2-}	sulfate
SO_x	sulfur oxides

List of abbreviations and notations

ACSM	Aerosol Chemical Speciation Monitor
ACTRIS	Aerosol, Clouds and Trace Gases Research Infrastructure
AEROMMA	Atmospheric Emissions and Reactions Observed from Megacities to Marine Areas
AIDA	Aerosol Interaction and Dynamics in the Atmosphere (chamber at Karlsruhe Institute of Technology)
amine-ToF	amine-reagent chemical ionization time-of-flight mass spectrometer
AmN	ammonium nitrate
AMS	aerosol mass spectrometer
AmS	ammonium sulfate
$a_{\mathrm{Org}[x],[i]}$	multiplier for calculating frag_Org[x] based on the relationship between frag_Org[x] and frag_Org[i]
APi	atmospheric pressure inlet
BBOA	biomass burning organic aerosol
BVOC	biogenic volatile organic compound
CAINA	Cloud-Aerosol Interactions in a Nitrogen-dominated Atmosphere (campaign 2025)
CAMS	Copernicus Atmospheric Monitoring Service
CB	Carbon Bond (chemical scheme)
CCOA	coal combustion organic aerosol
$C_{\mathrm{DL,NO^+}}$	detection limit of NO^+ ($\mu g \cdot m^{-3}$)
$C_{\mathrm{DL,NO_2^+}}$	detection limit of NO_2^+ ($\mu g \cdot m^{-3}$)
$C_{\mathrm{DL,pNO_3}}$	detection limit of pNO_3 ($\mu g \cdot m^{-3}$)
CE	collection efficiency
$C_{g,i}$	concentration/mixing ratio of species i in the gas phase
C_{gON}	concentration/mixing ratio of organic nitrate in the gas phase
CHANEL	Household Chemicals Amplifying Urban Aerosol Pollution (campaign 2024)
CI	chemical ionization
CIMS	chemical ionization mass spectrometry

C_{NO^+}	signal of NO^+ ($\mu g \cdot m^{-3}$)
$C_{NO^+,lim}$	signal limit of NO^+ for reliable organic nitrate and ammonium nitrate separation ($\mu g \cdot m^{-3}$)
$C_{NO_2^+}$	signal of NO_2^+ ($\mu g \cdot m^{-3}$)
COA	cooking organic aerosol
C_{OA}	concentration of total organic aerosol ($\mu g \cdot m^{-3}$)
$C_{ON,tot}$	concentration/mixing ratio of total organic nitrate (gas and particle phases)
CPC	condensation particle counter
$C_{p,i}$	concentration/mixing ratio of species i in the particle phase
$C_{p,i}/C_{g,i}$	particle-to-gas ratio of species i
$C_{PM_{2.5}}$	concentration of total $PM_{2.5}$ ($\mu g \cdot m^{-3}$)
C_{pNH_4}	concentration of total particulate ammonium
C_{pNH_4}	concentration of total particulate nitrate
C_{pRONO_2}	concentration of organic nitrate in the particle phase (organic + nitrate moiety)
C_{pON}	concentration/mixing ratio of organic nitrate in the particle phase (nitrate moiety)
C_{pON}/C_{gON}	particle-to-gas ratio of organic nitrate
C_{ns}	near-surface atmospheric concentration ($mol \cdot m^{-3}$)
C_0	initial concentration
cToF	compact time-of-flight
CV	capture vaporizer
C^*	volatility ($\mu g \cdot m^{-3}$)
DEPAC	DEPosition of Acidifying Compounds (deposition model)
-DH	experiment label for daytime high NO condition
-DL	experiment label for daytime low NO condition
-DM	experiment label for daytime medium NO condition
DMA	differential mobility analyzer
dN	particle number concentration (cm^{-3})
$dN/d\log D_p$	particle number size distribution (cm^{-3})
D_p	particle geometric diameter (nm or μm)
dV	cumulative particle volume (nm^3)
D_{va}	particle vacuum aerodynamic diameter (nm or μm)
EHN	2-ethylhexyl nitrate
ELVOC	extremely low-volatility organic compound
EU	European Union
F	deposition flux ($mol \cdot m^{-2} \cdot s^{-1}$)
FID	flame ionization detector

f_{om}	absorptive organic fraction of the particulate matter
f_{pAmN}	mass fraction of particulate ammonium nitrate to the total nitrate
f_{peak}	rotationality in positive matrix factorization solution
f_{pON}	mass fraction of particulate organic nitrate to the total nitrate
frag_NO_3[x]	total nitrate fragments in nominal m/Q x
frag_Org[x]	total organic fragments in nominal m/Q x
F0AM	Framework for 0-D Atmospheric Modeling
FZJ	*Forschungszentrum Jülich* (Jülich Research Centre)
f_{28}	mass fraction of m/Q 28 in the organic mass spectrum
f_{43}	mass fraction of m/Q 43 in the organic mass spectrum
f_{44}	mass fraction of m/Q 44 in the organic mass spectrum
GC	gas chromatography
gON	gas-phase organic nitrate
H^*	effective Henry's law constant ($\mathrm{mol \cdot L^{-1} \cdot atm^{-1}}$)
HOA	hydrocarbonlike organic aerosol
HOM	highly oxygenated molecule
HR	high (mass) resolution
HR-ToF-AMS	high-mass-resolution time-of-flight aerosol-mass-spectrometer
HYSPLIT	Hybrid Single-Particle Lagrangian Integrated Trajectory
IA	inorganic aerosol
IE	ionization efficiency
IMK	*Institut für Meteorologie und Klimaforschung* (Institute for Meteorology and Climate Research)
IPL	intermediate pressure lens
KIT	Karlsruhe Institute of Technology
KNMI	*Koninklijk Nederlands Meteorologisch Instituut* (Royal Netherlands Meteorological Institute)
$K_{\mathrm{p},i}$	gas-particle partitioning coefficient of species i ($\mathrm{m^3 \cdot \mu g^{-1}}$)
$K_{\mathrm{p,ON}}$	gas-particle partitioning coefficient of organic nitrates ($\mathrm{m^3 \cdot \mu g^{-1}}$)
LML	*Landelijk Meetnet Luchtkwaliteit*
LO-OOA	less-oxidized oxygenated organic aerosol
LOTOS-EUROS	LOng-Term Ozone Simulation - EURopean Operational Smog
LVOC	low-volatility organic compounds
m_{ν}	mass concentration of ν ($\mathrm{\mu g \cdot m^{-3}}$)
m/Q	mass-to-charge ratio
MCM	Master Chemical Mechanisms
minErr	minimum error for positive matrix factorization input
MO-OOA	more-oxidized oxygenated organic aerosol
$m_{\mathrm{Org}}/m_{\mathrm{IA}}$	organic-to inorganic aerosol mass ratio
MPSS	mobility particle size spectrometer

MR-CIMS	multi-reagent chemical ionization mass spectrometer
MR-CIMS-$C_6H_6^+$	MR-CIMS with benzene-reagent ions
MR-CIMS-I^-	MR-CIMS with iodide-reagent ions
m_{tot}	total absorptive mass of particulate matter ($\mu g \cdot m^{-3}$)
MW_{om}	average molecular weight of the organic matter ($g \cdot mol^{-1}$)
MW_{pRONO_2}	molecular weight of bulk particulate organic nitrate as $pRONO_2$ ($g \cdot mol^{-1}$)
$m/\Delta m$	mass resolution
-N	experiment label for nighttime conditions or $NO_3^\bullet$ chemistry
-N-DO	experiment label for nighttime conditions with NO_2+O_3 injections at multiple times
NH_4_bal	ammonium balance
NH_4^+-Vocus	ammonium-reagent Vocus chemical ionization mass spectrometer
NO_2R	reactivity of NO_2 towards $OH^\bullet$ (s^{-1})
n_ν	molar concentration of species ν
$NO_2R/VOCR$	ratio of NO_2 reactivity to total volatile organic compound reactivity towards $OH^\bullet$
NOAA	National Oceanic and Atmospheric Administration
NO_x^+ ratio	NO_2^+-to-NO^+ signal ratio
NPF	new particle formation
OA	organic aerosol
obs	observed data (ambient or chamber)
ODR	orthogonal distance regression
ON	organic nitrate
OOA	oxygenated organic aerosol
OPS	Operational Priority Substance
Org	organic species in AMS/ACSM
p	number of factors in PMF solution
PAH	polycyclic aromatic hydrocarbon
pAmN	particulate ammonium nitrate
PAS	*Programmatische Aanpak Stikstof* (Nitrogen Approach Program)
PEEK	polyetheretherketone
PET	PMF Evaluation Tool
PIKA	Peak Integration by Key Analysis
$p^o_{L,i}$	pure liquid vapor pressure of compound i (atm)
PM	particulate matter
$PM_{2.5}$	particulate matter with size $<$2.5 μm
PM_{10}	particulate matter with size $<$10 μm
PMF	Positive Matrix Factorization
pNH_4	particulate ammonium
pNO_3	particulate nitrate

PNSD	particle number size distribution (cm^{-3})
POA	primary organic aerosol
pON	particulate organic nitrate (only nitrate moiety)
$pRONO_2$	particulate organic nitrate (organic and nitrate moiety)
PTFE	polytetrafluoroethylene
Q/Q_{exp}	local minima of PMF solution
Q-ACSM	quadrupole ACSM
R	ideal gas constant ($= 0.082\ L \cdot atm \cdot K^{-1} \cdot mol^{-1}$)
r^2	coefficient of determination
R_a	aerodynamic resistance ($s \cdot m^{-1}$)
R_b	boundary layer resistance ($s \cdot m^{-1}$)
R_c	surface resistance ($s \cdot m^{-1}$)
RH	relative humidity (%)
$RH_{eq,avg}$	relative humidity at equilibrium (%)
RIE	relative ionization efficiency
RIVM	*Rijksinstituut voor Volksgezondheid en Milieu* (Dutch National Institute for Public Health and the Environment)
R_{obs}	NO_x^+ ratio of observed data
RoR	ratio of ratios
R_{pAmN}	NO_x^+ ratio of particulate ammonium nitrate
R_{pON}	NO_x^+ ratio of particulate organic nitrate
RUG	*Rijksuniversiteit Groningen* (University of Groningen)
SAPHIR	Simulation of Atmospheric PHotochemistry In a large Reaction chamber (at Forschungszentrum Jülich)
s_f	uncertainty of function f
$s_{f_{pON}}$	uncertainty of particulate organic nitrate fraction to the total nitrate
SIA	secondary inorganic aerosol
SMPS	Scanning Mobility Particle Sizer
SOA	secondary organic aerosol
Squirrel	Sequential Igor Data Retrieval
SV	standard vaporizer
SVOC	semi-volatile organic compound
s_{x_i}	standard error
t	time step
T	temperature (K or ^oC)
$T_{eq,avg}$	average chamber temperature at equilibrium (K or ^oC)
TNO	Netherlands Organisation for Applied Scientific Research (*Nederlandse Organisatie voor toegepast-natuurwetenschappelijk onderzoek* in Dutch)
ToF	time-of-flight

UMR	unit mass resolution
UU	Utrecht University
VBS	volatility basis set
VCP	volatile chemical product
V_d	deposition velocity ($m \cdot s^{-1}$)
VOC	volatile organic compound
VOCR	reactivity of volatile organic compounds towards $OH^{\bullet}$ (s^{-1})
WALL-E	Wall-Free Particle Evaporator
WAM	Washington Aerosol Module
WRF-Chem	Weather Research and Forecasting model coupled with Chemistry
-X	experiment label for limonene precursor injection at multiple times
x_i	measurand or measured value
ΔC_{OA}	concentration of total organic aerosol formed (Org+pON) ($\mu g \cdot m^{-3}$)
$\Delta C_{ON,tot}$	total concentration of organic nitrate formed (gas and particle phases)
$\Delta C_{ON,tot} / \Delta C_{VOC,tot}$	molar yield of organic nitrate to the total consumed VOCs
ΔC_{pRONO_2}	concentration of particulate organic nitrate (organic+nitrate moiety) formed ($\mu g \cdot m^{-3}$)
$\Delta C_{pRONO_2} / \Delta C_{OA}$	mass fraction of $pRONO_2$ to the total organic aerosol formed
$\Delta C_{VOC,tot}$	total concentration/mixing ratio of consumed VOCs
ΔD	wet deposition flux ($\mu g \cdot m^{-2}$)
Δz	height of a grid cell (m)
$\delta f / \delta x_i$	partial derivative of the function f
Λ	scavenging coefficient (s^{-1})
ζ	activity coefficient



Chapter 1

Introduction

1.1 Motivation and background

The post-industrial revolution era has been characterized by an increase in human population, globalized trade, and industrial output. This acceleration has profoundly altered the Earth's biogeochemical cycles, notably through the large-scale conversion (fixation) of non-reactive nitrogen (N_2) into reactive nitrogen species. While nitrogen fixation occurs naturally via biological processes and lightning, anthropogenic activities now dominate the global reactive nitrogen budget. These reactive nitrogen species are broadly categorized into reduced nitrogen (NH_x), primarily ammonia (NH_3), and oxidized nitrogen (NO_y), primarily nitrogen oxides (NO_x=NO+NO_2). The two most significant drivers of the increase in reactive nitrogen species are intensive agriculture and fossil fuel combustion for transport and industry, contributing mainly to NH_3 and NO_x, respectively. As these sectors have expanded to meet global resource demands, it has led to excessive nitrogen emission with implications for air quality and ecosystem health.

The atmosphere over the Netherlands may serve as an example for environments with excessive emission of reactive nitrogen due to its unique position as a high-productivity agricultural country and transport/shipping hub. Despite its small land area and human population of around 17.5 million, the country supports a livestock population of approximately 116 million individuals (including pigs, cattle, sheep, dairy goats, and chickens) (CBS, 2022). This intensive agricultural sector makes the Netherlands the world's second-largest exporter of agricultural products by value after the United States, contributing approximately 17.5 % of total Dutch exports (Voort et al., 2012). Consequently, NH_3 emissions remain exceptionally high, totaling 100 $\mathrm{Gg(N)} \cdot \mathrm{y}^{-1}$ in 2022, with 87 % of the emissions attributed to agricultural activities (CBS, 2024; Staats et al., 2025). At the same time, the Netherlands functions as a primary gateway for European trade. The Netherlands remains the top maritime freight hub in the European Union (EU), handling 545 million tonnes of cargo in 2023 (Eurostat, 2022), where 13.82 millions TEU (twenty-foot equivalent unit, representing one 6.1-m shipping container) are shipped through the port of Rotterdam in 2024 (Rotterdam, 2025). Schiphol Airport also consistently ranks among the top European hubs for both passenger traffic and cargo movements, with 66.8 million passengers (fourth position in Europe) and 1.49 million tonnes of cargo (fifth position in Europe) according to Schiphol (2025). These ports contribute substantially to NO_x emissions (Valastro et al., 2023; Tokaya et al., 2024). In 2022, NO_x emissions reached 49 $\mathrm{Gg(N)} \cdot \mathrm{y}^{-1}$, with the transport sector responsible for 57 % of the emissions (CBS, 2024; Staats et al., 2025). The combination of intensive agriculture practice and high-volume logistics results in nitrogen deposition rates averaging at 1315 $\mathrm{mol(N)} \cdot \mathrm{ha}^{-1}$ in 2023, where 29 % of the deposition is contributed by NO_y and 71 % by NH_x (see Fig. 1.1). Fig. 1.2 from Erisman et al. (2015) shows that the total nitrogen deposition modeled using LOTOS-EUROS model (LOng-Term Ozone

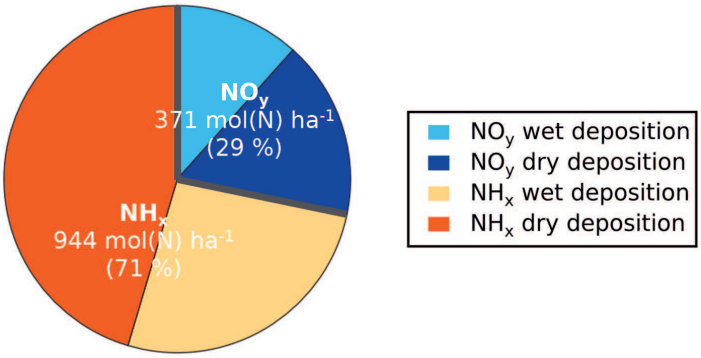


Figure 1.1: Share of oxidized nitrogen (NO_y) and reduced nitrogen (NH_x) deposition (wet and dry) in the Netherlands in 2023 according to the Dutch National Institute for Public Health and the Environment (*Rijksinstituut voor Volksgezondheid en Milieu* or RIVM in Dutch), obtained from CLO (2025).

Simulation - EURopean Operational Smog) for 2009 in the Netherlands is relatively high compared to other European countries given its size, with similar nitrogen deposition observed in other agricultural and/or industrial centers like Northern Belgium, Brittany, Po Valley in Italy, Northern Switzerland, and Western Germany.

While international and national regulations have successfully reduced sulfur dioxide (SO_2) emissions over the past decades, reactive nitrogen emissions have been shown to be more resistant to change. Due to the ubiquity of nitrogen-emitting activities in modern society, NH_x and NO_y are increasingly central to atmospheric chemistry. Specifically, nitrate aerosols have emerged as a major component of the particulate matter (PM) globally and regionally (Adams et al., 1999; Metzger, 2002; Liao et al., 2003; Rodriguez and Dabdub, 2004; Feng and Penner, 2007; Bauer et al., 2007; Paulot et al., 2016; Bian et al., 2017; Vasilakos et al., 2018; Drugé et al., 2019; Lu et al., 2021). Projections suggest that by 2100, nitrate will surpass sulfate as the primary driver of aerosol radiative forcing globally (Adams et al., 2001).

Understanding the properties and formation mechanisms of nitrate aerosols is of increasing importance due to their diverse impacts. Continental nitrate aerosols are largely associated with fine particles, whose efficient light scattering leads to a direct cooling effect and climate forcing across Europe (Schaap et al., 2003; Erisman et al., 2011). Through new particle formation (NPF) events, condensation of low-volatility compounds, including nitrate, contribute to over 50 % of cloud condensation nuclei, thereby influencing cloud albedo and lifetime (Bianchi et al., 2016; Gordon et al., 2016; Haywood, 2016; Dall'Osto et al., 2018; Lee et al., 2019). These phenomena physically affect ecosystems by altering radiation diffusion, temperature, and precipitation (Grantz et al., 2003; Haywood, 2016; Lee et al., 2019). Aerosols also chemically affect ecosystems

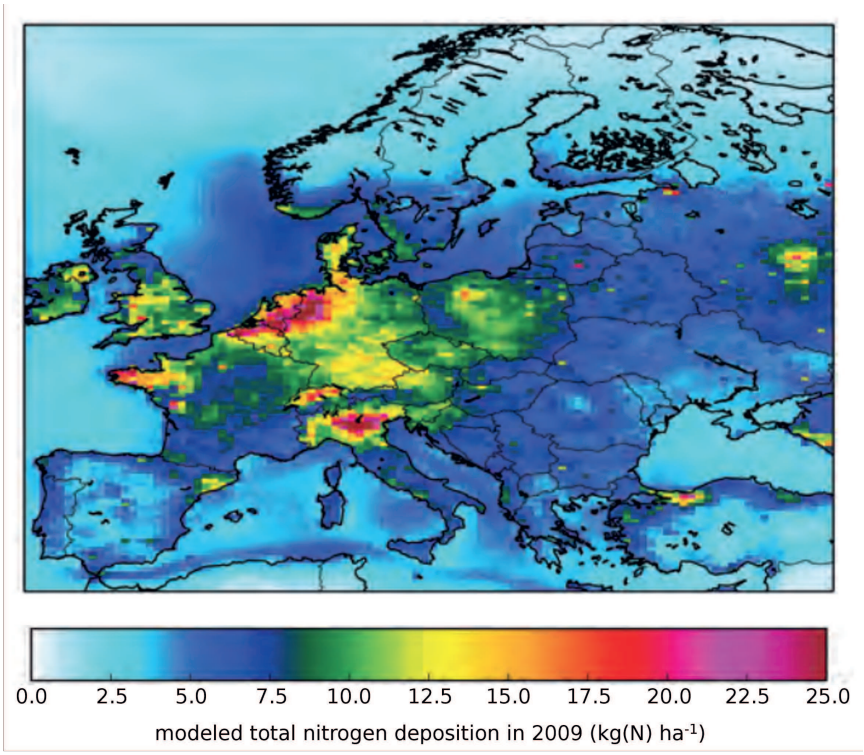


Figure 1.2: Modeled total nitrogen deposition ($\mathrm{kg(N)} \cdot \mathrm{ha}^{-1}$) for 2009 (adapted from figure in Erisman et al. (2015)).

by altering the spatial patterns of nitrogen deposition (Swaluw et al., 2011; Wamelink et al., 2013) and influencing oxidative processes (Xing et al., 2017). Excessive nitrogen deposition leads to soil acidification, eutrophication of aquatic systems, and a significant loss of biodiversity, representing a key obstacle to the conservation and long-term sustainability of natural habitats (Erisman et al., 2011; Wamelink et al., 2013; Heer et al., 2017). NO_x, in the presence of sunlight and volatile organic compounds (VOCs), facilitates the formation of secondary pollutants: ground-level ozone and fine particulate matter ($PM_{2.5}$). These particulates are associated with elevated cardiovascular and pulmonary morbidity (Ayala et al., 2012; Pope et al., 2020).

These negative impacts call for a reduction in nitrogen emission in the EU. Through the Habitats Directive (92/43/EEG) and Birds Directive (2009/147/EG) from the EU, they classify the network of protected natural habitats as Natura 2000. To address the problem, the Dutch government implemented the Nitrogen Approach Program (*Programmatische Aanpak Stikstof* or PAS in Dutch) in 2015 to cut nitrogen emissions and apply restoration measures in Natura 2000 areas while facilitating economic devel-

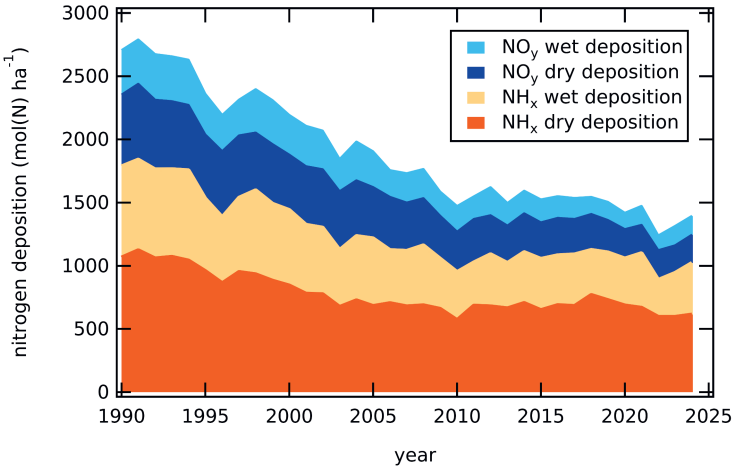


Figure 1.3: Annual trend of wet and dry deposition of NO_y and NH_x ($mol(N) \cdot ha^{-1}$) in the Netherlands from 1990–2024 according to RIVM (CLO, 2025).

opment within strict limits. Through another EU Directive on the National Emission reduction Commitments (2016/2284), the Netherlands is obliged to commit to reduce its national NO_x emission by 45 % and national NH_3 emission by 13 % before 2030 (in comparison to emissions in 2005). In response, policies required emissions reductions from various sectors in the country, mainly agriculture and industries. We have observed a reduction in nitrogen deposition as an impact of nitrogen emission reduction efforts since 1990, as shown by RIVM in Fig. 1.3. However, between 2013 and 2017, total nitrogen deposition remained roughly stable due to a limited decrease in emissions (CLO, 2025). In May 2019, the Dutch Administrative Court of the Council of State (*Raad van State* in Dutch) ruled that the PAS was not sufficient to reduce excess nitrogen in vulnerable natural areas. The persistent failure to mitigate nitrogen levels has led to a regulatory and political impasse in recent years (De Vries, 2021), known as the "Dutch nitrogen crisis."

A primary obstacle to effective policy is the scientific uncertainty surrounding the non-linear relationship between precursor emissions and final deposition, which leads the emission reduction approach to be insufficient (Lohle, 2021). Current models often struggle to capture the complex source-to-sink pathway of nitrogen, including the airborne dispersion of reactive nitrogen species and the chemical transformations that occur during transport. A deeper investigation into the atmospheric chemical processes, specifically the sources and sinks of reactive nitrogen, is essential to improve the situation. This thesis aims to address these knowledge gaps by providing the scientific knowledge about the chemical reactions pathways of reactive nitrogen in the Netherlands for future emission reduction strategies.

1.2 Chemical and physical processes related to nitrate

1.2.1 Atmospheric chemistry

Reactive nitrogen species undergo complex atmospheric transformations influenced by meteorological conditions and the presence of co-pollutants. NO_x is primarily introduced via high-temperature combustion (transport and industry), while NH_3 stems predominantly from agricultural activities, specifically urea hydrolysis in manure and synthetic fertilizers. Other processes, including waste management, biomass burning, and exhaust from catalytic converters, also contribute to NH_3 emissions.

The chemical reactions occurring in the atmosphere involving NO_x and NH_3 are summarized in Fig. 1.4. The atmospheric transformation of these precursors follows two primary pathways: the formation of inorganic nitrates and organic nitrates (ON). In the Netherlands, ammonium nitrate (NH_4NO_3) is the dominant inorganic species (Schaap et al., 2004), rather than ammonium sulfate ($(NH_4)_2SO_4$) due to the abundance of nitrogen emission. NH_4NO_3 is formed through the reaction between nitric acid (HNO_3) and NH_3. HNO_3 is generated via NO_2 oxidation by the hydroxyl radical ($OH^\bullet$) during the day or nitrogen pentoxide (N_2O_5) hydrolysis at night. Meanwhile, ONs are typically formed at first in the gas phase through different channels (Kiendler-Scharr et al., 2016; Zare et al., 2018). During daytime conditions, the oxidation of NO_x by organic peroxy radicals ($RO_2^\bullet$), which are produced through reactions between VOCs and $OH^\bullet$, represents the dominant pathway for ON formation (Sobanski et al., 2017). By contrast, the oxidation of VOCs by nitrate radicals ($NO_3^\bullet$) primarily occurs at night due to the absence of $NO_3^\bullet$ photodissociation (Kiendler-Scharr et al., 2016; Ng et al., 2017).

The dominant NO_x sink, whether it is inorganic nitrate through HNO_3 formation, or organic nitrate, is governed by the ratio of NO_2 reactivity to total VOC reactivity towards $OH^\bullet$ ($NO_2R/VOCR$) (Romer Present et al., 2020). High ratios ($>> 1$) favor HNO_3 production and subsequent inorganic nitrate formation. In contrast, low ratios (< 1) promote the formation of organic nitrates. Because ONs possess atmospheric multiphase lifetimes of 2–97 h (González-Sánchez et al., 2023), longer than the NO_x lifetime, 2–29 h (Singh, 1987; Ryerson et al., 1998; Nunnermacker et al., 2000; Valin et al., 2013; Romer et al., 2016; Kenagy et al., 2018; Lange et al., 2022), the seasonality of NO_x sink pathways significantly alters the spatial distribution and deposition patterns of reactive nitrogen, thus its impact on ecosystems.

1.2.2 Gas-particle partitioning of organic nitrates

The condensation of organic nitrates from the gas phase to the particulate phase facilitates the formation of secondary organic aerosol (SOA), which can lengthen atmospheric lifetimes as stated above. Gas-particle partitioning is an equilibrium process governed by the compound's volatility, which is a function of its functional groups, oxidation

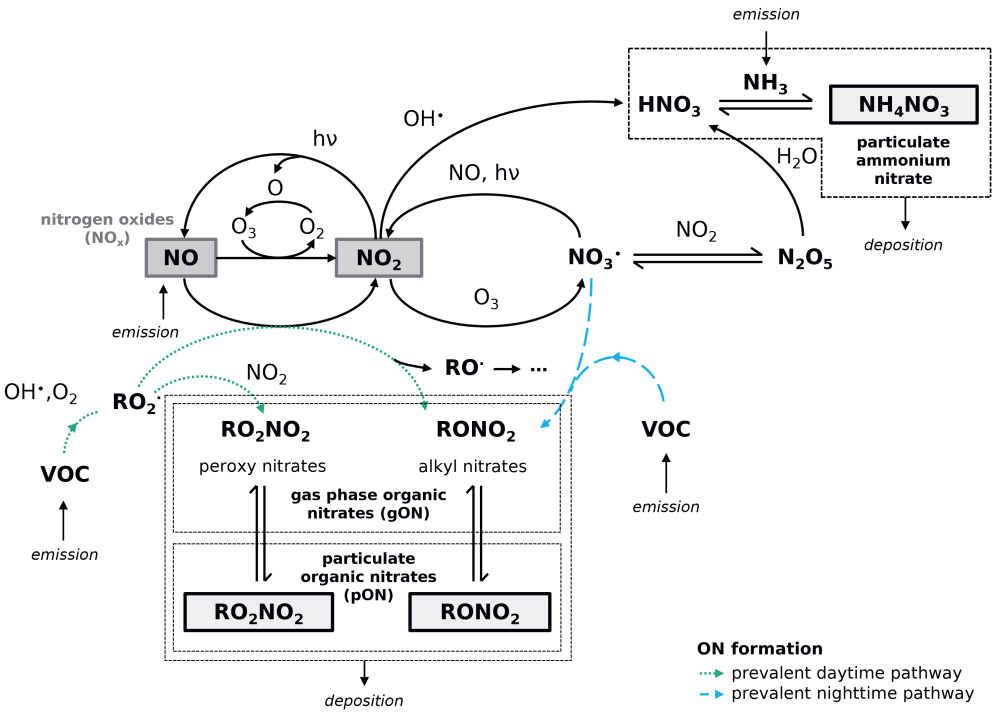


Figure 1.4: Formation of reactive nitrogen species in the troposphere through emissions of NO_x, NH_3, and VOCs and their subsequent reactions with atmospheric oxidants (e.g., $OH^\bullet$ and $NO_3^\bullet$). The reactions lead to the production of particulate ammonium nitrate (NH_4NO_3) and organic nitrates (ONs) in equilibrium between the gas phase ON (gON) and particulate ON (pON). Dashed blue arrows indicate the $NO_3^\bullet$-initiated ON formation pathway dominant at night, while dotted green arrows represent the $OH^\bullet$-initiated pathway prevalent during the day.

level, temperature, and relative humidity (Kroll and Seinfeld, 2008). The partitioning of a compound i between the gas and particle phases occurs via sorption onto pre-existing particles, leading to the condensation of low-volatility organic compounds (LVOCs). This process is described by the gas-particle partitioning coefficient ($K_{p,i}$ in $m^3 \cdot \mu g^{-1}$) based on the volatility of i as expressed in Eq. 1.1 (Pankow, 1994; Pankow and Asher, 2008). $K_{p,i}$ is proportional to the particle-to-gas concentration ratio ($C_{p,i}/C_{g,i}$) and inversely proportional to the total absorptive mass (m_{tot} in $\mu g \cdot m^{-3}$),

$$K_{p,i} = \frac{C_{p,i}}{C_{g,i}} \cdot \frac{1}{m_{tot}} \tag{1.1}$$

When expressed thermodynamically in Eq. 1.2, $K_{p,i}$ depends on the temperature (T in K), the pure liquid vapor pressure of i at that temperature ($p^o_{L,i}$ in atm), and the

properties of the organic matter, including its molecular weight (MW_{om} in $\mathrm{g \cdot mol^{-1}}$), the absorptive organic fraction of the PM (f_{om}), and the activity coefficient in the organic fraction (ζ). The ideal gas constant $R = 0.082\ \mathrm{L \cdot atm \cdot K^{-1} \cdot mol^{-1}}$) is used. By estimating $p^o_{L,i}$ for a given MW_{om} and ζ, $K_{\mathrm{p,i}}$ can be theoretically calculated for a specific chemical structure using group contribution methods such as SIMPOL.1 (Pankow and Asher, 2008). The resulting theoretical $K_{\mathrm{p,i}}$ values (Eq. 1.2) can then be compared with observed bulk value of $K_{\mathrm{p,i}}$ (Eq. 1.1) to infer the average volatility of the organic compounds, providing insights into their possible chemical structures, and to characterize the bulk properties of the SOA mixture (Brownwood et al., 2021).

$$K_{\mathrm{p,i}} = \frac{760 \cdot R \cdot T \cdot f_{\mathrm{om}}}{10^6 \cdot MW_{om} \cdot \zeta \cdot p^o_{L,i}} \tag{1.2}$$

While sulfuric acid (H_2SO_4) has been considered the primary driver of new particle formation together with other species such as highly oxidized molecules (HOMs), HNO_3, organic acids and bases (Zhang et al., 2012; Zhang et al., 2015; Kulmala et al., 2013; Wagner et al., 2017; Lehtipalo et al., 2018; Kürten, 2019; Lee et al., 2019; Brean et al., 2021; Olin et al., 2022), the recent decline in SO_2 emissions has increased the relative importance of HNO_3 and organonitrogen compounds in aerosol nucleation and growth. Studies have shown that the particulate organic nitrate contribution to total particulate nitrate mass is substantial (Ng et al., 2017), with an average fraction of 17–31 % in China (Yu et al., 2024) and 34–44 % in Europe (Kiendler-Scharr et al., 2016) and large differences between urban and rural areas (Fisher et al., 2016; Schlag et al., 2016; Romer Present et al., 2020; Yu et al., 2024), underscoring its critical role in regional aerosol budgets.

1.3 Measurement techniques

Reactive nitrogen species relevant to nitrate aerosol formation are observed primarily using an aerosol mass spectrometer (AMS) and an aerosol chemical speciation monitor (ACSM), which measure aerosol-phase composition, including nitrate. A total NO_y monitor, together with a NO_x monitor, AMS/ACSM, and auxiliary measurements, is used to quantify total oxidized nitrogen (NO_y) and to determine the concentration of gas-phase nitrates.

1.3.1 Aerosol mass spectrometer (AMS) and aerosol chemical speciation monitor (ACSM)

The high-resolution time-of-flight aerosol mass spectrometer (HR-ToF-AMS, or simply AMS) with a standard vaporizer (SV) is an instrument used to measure non-refractory submicron aerosol particles. AMS is able to quantitatively speciate aerosol components into organic components (Org), ammonium (NH_4), nitrate (NO_3), sulfate (SO_4) and

chloride (Cl) in the aerosol phase by mass fragment identification. The operating principles of AMS, including the aerodynamic lens system, vaporizer, electron impact ionization, and time-of-flight mass analyzer, are described in detail by Canagaratna et al. (2007). Inorganic and organic nitrate are separated using the NO_x^+ ratio method (Farmer and Jimenez, 2010; Day et al., 2022a; Takeuchi et al., 2024), which has been widely validated for the analysis of organic nitrate (Fry et al., 2013; Pye et al., 2015; Kiendler-Scharr et al., 2016; Ng et al., 2017; Fry et al., 2018; Huang et al., 2019a; Huang et al., 2019b; Brownwood et al., 2021; Day et al., 2022a).

The unit-mass-resolution time-of-flight aerosol chemical speciation monitor (UMR-ToF-ACSM) is similar to the AMS but optimized for air quality monitoring (Fröhlich et al., 2013). The ACSM employs a capture vaporizer (CV) instead of SV to enhance particle collection efficiency (CE) (Jayne and Worsnop, 2016), which enables $PM_{2.5}$ measurements (Xu et al., 2017). A similar NO_x^+ ratio method is also available for the speciation of inorganic and organic nitrate for CV-UMR-ToF-ACSM as part of this thesis (Nursanto et al., 2025).

1.3.2 NO_y monitor

Total NO_y is measured using a chemiluminescence NO_x analyzer (Thermo 42iQTL) equipped with a modified NO_y inlet, described in detail by Marsavin et al. (2023). Ambient air passes through an external inlet containing a molybdenum (Mo) NO_2-to-NO converter (Thermo 17i) maintained at 350 °C, where NO_y species are thermally reduced to NO via reaction with Mo. The converted NO is then detected and quantified by the chemiluminescence NO_x instrument with 1 min time resolution.

The gas-phase organic nitrate mixing ratio (C_{gON} in ppb) is derived from total NO_y by subtracting simultaneous measurements of NO_x (C_{NO_x} in ppb) and available NO_z species such as HONO, HNO_3, and particulate nitrate (C_{HONO}, C_{HNO_3}, C_{pNO_3}; all in ppb), as shown in Eq. 1.3. While NO_x and particulate nitrate are more commonly measured, other NO_z species (e.g., HONO, HNO_3, N_2O_5, $NO_3^{\bullet}$) are often unavailable. Some of these species also typically have very small mixing ratios (e.g., $NO_3^{\bullet}$). When such measurements are missing, these terms can be neglected if their contributions are negligible relative to dominant NO_z components (e.g., gas-phase organic nitrate and particulate nitrate).

$$C_{gON} = C_{NO_y} - (C_{NO_x} + C_{HONO} + C_{HNO_3} + C_{pNO_3} + ...) \tag{1.3}$$

1.3.3 Other measurement techniques

Gas- and particle-phase measurements can be complemented by additional soft-ionization mass spectrometers, including gas chromatography (GC) and chemical ionization mass spectrometers (CIMS), to provide enhanced molecular speciation. Unlike

electron impact ionization technique where molecules in the sample are fragmented, GC and CIMS enable the characterization of organic component as (nearly) unfragmented compounds. The chromatographic separation or softer ionization techniques enable the determination of individual molecular formulas. Some specific soft-ionization mass spectrometers used in this thesis include GC with a thermal desorption, dual flame ionization, and mass spectrometric detection (GC-TD-FID/MS), multi-reagent CIMS (MR-CIMS), amine-reagent time-of-flight CIMS (amine-ToF), ammonium-reagent Vocus CIMS (NH_4^+-Vocus), and atmospheric pressure CIMS coupled to a Wall-Free Particle Evaporator (WALL-E) interface.

1.4 Representation of nitrate in models

Chemical processes involving reactive nitrogen species are represented in chemical and deposition models to varying degrees. In the Netherlands, the LOTOS-EUROS model is a chemical transport model that has been developed through a collaboration of the Netherlands Organization for Applied Scientific Research (TNO), RIVM, and the Royal Netherlands Meteorological Institute (KNMI), with diverse applications for atmospheric studies (Manders et al., 2017). Its chemical mechanism is based on the CB4 scheme (Whitten et al., 1980) and has been updated over time to CB5 (Yarwood et al., 2005), CB6 (Yarwood et al., 2010), and CB7 (Yarwood et al., 2021) in the current version (v3.0.00), representing 111 species and 230 reactions (Segers et al., 2025). The model simulates typical sulfate formation, heterogeneous N_2O_5 and HNO_3 chemistry, and secondary inorganic aerosols (NH_4NO_3 and $NH_4(SO_4)_2$) using thermodynamic equilibrium modules ISORROPIA II (Nenes et al., 1999; Fountoukis and Nenes, 2007) and EQSAM (Metzger et al., 2002).

LOTOS-EUROS represents organic compounds using a lumped-structure approach for gas-phase photochemistry. Some model species represent single compounds, such as ethene (ETH), isoprene (ISOP), formaldehyde (FORM), acetaldehyde (ALD2); other compounds are lumped into groups with similar structures, such as single-bonded carbons (PAR, from paraffins), double-bonded carbons (OLE, from olefins), ring structures with seven carbons (TOL, from toluene), ring structures with eight carbons (XYL, from xylene), and higher molecular weight aldehydes (ALDX). Six of these families are considered SOA precursors, allowing gas-phase organics to partition into aerosols: two biogenic precursors, isoprene (ISOP) and monoterpenes (TERP); and the anthropogenic precursors xylene (XYL), toluene (TOL), alkanes (PAR), and alkenes (OLE+PAR). SOA formation uses a volatility basis set (VBS) with nine volatility (C^*) bins (10^{-2} to 10^6 $\mu g \cdot m^{-3}$) to describe gas–particle partitioning; an inverse to $K_{p,i}$ ($m^3 \cdot \mu g^{-1}$) described earlier. Each bin undergoes production, volatility modification, gas-particle partitioning, dry deposition, and wet deposition.

Dry deposition is calculated using the DEPAC (DEPosition of Acidifying Compounds) module (Zanten et al., 2010). The DEPAC module simulates dry deposition by representing the transfer of atmospheric species to a surface through a resistance-based framework. In this approach, deposition is treated analogously to an electrical circuit, where aerodynamic resistance (R_a, in $\mathrm{s \cdot m^{-1}}$), boundary layer resistance (R_b, in $\mathrm{s \cdot m^{-1}}$), and surface resistance (R_c, in $\mathrm{s \cdot m^{-1}}$) control the deposition velocity (V_d, in $\mathrm{m \cdot s^{-1}}$) of a given species (Wesely, 1989). By parameterizing these resistances as functions of meteorology, land-use characteristics, and chemical properties (e.g., volatility and solubility), DEPAC provides a method to determine dry deposition fluxes (F, in $\mathrm{mol \cdot m^{-2} \cdot s^{-1}}$) based on V_d and the atmospheric concentration of the species near surface (C_{ns}, in $\mathrm{mol \cdot m^{-3}}$), as shown in Eqs. 1.4 and 1.5. In addition to LOTOS-EUROS, the DEPAC module is also used in the OPS (Operational Priority Substance) model (Sauter et al., 2025) for assessing regulatory compliance.

$$F = -V_d \cdot C_{\mathrm{ns}} \tag{1.4}$$

$$V_d = \frac{1}{R_a + R_b + R_c} \tag{1.5}$$

Wet deposition consists of below-cloud and in-cloud scavenging processes. Wet deposition depends on the scavenging coefficient (Λ in $\mathrm{s^{-1}}$) that describes the mass transfer rate of a species from air into rain droplets (Segers et al., 2025). The contribution of each scavenging to the wet deposition flux (ΔD in $\mathrm{\mu g \cdot m^{-2}}$) at each time step ($t$ in s) is determined using Λ, the initial concentration of the species (C_o in $\mathrm{\mu g \cdot m^{-3}}$) and the height of a grid cell (Δz in m) as shown in Eq. 1.6. The calculation of Λ depends on many parameters for both below-cloud and in-cloud scavenging, which is detailed in the LOTOS-EUROS reference guide (Segers et al., 2025).

$$\Delta D = C_0(1 - e^{-\Lambda t})\Delta z \tag{1.6}$$

DEPAC provides detailed descriptions for the dry deposition of NH_3 and NO_x species as well as their condensed counterparts, NH_4^+ and NO_3^- (which can be considered as NH_4NO_3). The below-cloud scavenging coefficients for HNO_3 and NH_3 are also provided to calculate wet deposition. However, while organic nitrate formation pathways exist in LOTOS-EUROS, gas-phase and particle-phase organic nitrates are not explicitly included in the DEPAC module or wet scavenging processes as part of nitrogen deposition.

A more chemistry-oriented model, such as the Framework for 0-D Atmospheric Modeling (F0AM), is also available. F0AM is a flexible zero-dimensional box model for studying atmospheric chemical mechanisms (Wolfe et al., 2016) in the MATLAB interface. While it omits horizontal and vertical transport, making it suitable for chamber studies, F0AM still supports laboratory, Lagrangian, and steady-state applications. Users

can constrain meteorology and initialize chemical concentrations, allowing species to evolve over time. Common mechanisms include Master Chemical Mechanisms (MCM) v3.2 (Saunders et al., 2003), CB5 (Yarwood et al., 2005), CB6r2 (Hildebrandt Ruiz and Yarwood, 2013), RACM2 (Goliff et al., 2013), and GEOS-Chem v9.02 with isoprene updates (Kim et al., 2025; Fisher et al., 2016; Marais et al., 2016; Travis et al., 2016). Extensions like the Washington Aerosol Module (WAM) introduce Raoult's law-based gas–particle partitioning and dynamic aerosol growth, including a custom isoprene mechanism (D'Ambro et al., 2017; Thornton et al., 2020). However, none of these mechanisms includes reactions in the condensed phase.

In general, these models are developed for different applications. LOTOS-EUROS is more built for regional atmospheric modeling that includes deposition, which is relevant for air quality forecast and regulations. Meanwhile, F0AM-WAM has more detailed chemistry, which enables a more accurate representation of species transformation in both gas phase and particle phase for chemical mechanism studies.

1.5 Knowledge gaps

While the gas-particle partitioning of NH_4NO_3 is well-integrated into current simulations, significant discrepancies remain regarding the total nitrogen budget. Regional models, including LOTOS-EUROS, with incomplete process descriptions for reactive nitrogen species and SOA, consistently exhibit a systematic underestimation of PM by approximately 40 % and particulate nitrate by 20 % in the Netherlands (Kranenburg et al., 2013; Manders et al., 2017). Nitrogen deposition modules mostly treat nitrate exclusively as NH_4NO_3, overlooking the organic nitrate fraction. In Europe, evidence suggests that organic nitrogen contributes substantially to total wet deposition (Cape et al., 2012) within the range of 10–40 % (Cowan et al., 2022), yet it remains absent from routine monitoring and bulk deposition estimates. Furthermore, the capacity for organic nitrates to act as a reservoir species during transport, where up to 52 % of sequestered NO_x can be re-released downwind of emissions sources (Zare et al., 2018), is poorly represented, leading to potential errors in predicting spatial patterns of deposition and resulting strategies for emission reductions.

The change toward a nitrogen-dominated atmosphere, characterized by a shift toward more basic aerosol pH due to excess NH_3, is predicted to alter chemical reactions in the atmosphere. The more alkaline aerosol phase facilitates reactions between organic acids and amines, potentially modifying the formation of organonitrogen compounds. The current knowledge regarding how these aqueous-phase reactions modify the oxidation state, volatility, molecular weight, and yield of organic nitrates is still less known.

Although the important role of H_2SO_4 in new particle formation is well established, there is a lack of ambient observational data exploring the role of nitrate species in particle

nucleation and growth. Understanding the bulk gas-particle partitioning behavior of the nitrate aerosol mixture is essential to characterize its atmospheric lifetime and impact on the climate and ecosystems.

As traditional fossil fuel-related emissions decline further due to regulations, the relative contribution of non-traditional anthropogenic sources is increasing. Volatile chemical products (VCPs) and cooking emissions are emerging as dominant drivers of urban VOC chemistry (McDonald et al., 2018; Coggon et al., 2021; Gkatzelis et al., 2021b; Wernis et al., 2022; Coggon et al., 2024; Rivellini et al., 2024). However, current chemical mechanisms often rely on data from single-compound laboratory experiments, which fail to capture the synergistic effects and chemical complexity of real-world, source-specific mixtures.

The degree to which these emerging precursors participate in SOA and organic nitrate formation remains a major uncertainty. The increasingly more important nitrogen chemistry in the atmosphere represents a growing regulatory and scientific challenge that current models are not equipped to address. Bridging these gaps requires an investigation of the source-specific precursors and their transformation into nitrate aerosols, as well as chemical transformations in the aerosol phase, to fully understand the sources and fates of nitrate aerosol in the atmosphere.

1.6 Research questions and thesis outline

By integrating ambient observations, chamber experiments, and novel analytical techniques, this research aims to provide a comprehensive characterization of the chemical transformation of reactive nitrogen species in the Netherlands. To address the knowledge gaps in reactive nitrogen chemical and physical processes, the main research question of this thesis is:

What are the roles and properties of nitrate aerosols in the reactive nitrogen cycle in the nitrogen-dominated atmosphere of the Netherlands?

To answer this central question, we further breakdown the question into four specific sub-questions:

Q1. What are the major reactive nitrogen sources in the Netherlands and the role of nitrates in secondary aerosol formation?

The production of atmospheric aerosols begins with the new particle formation events and subsequent growth via condensation. While various species contribute to these processes, their roles within the nitrogen-dominated atmosphere of the Netherlands remain poorly characterized. **Chapter 2** uses observations from the Ruisdael Land–Atmosphere Interactions Intensive Trace-gas and Aerosol (RITA) 2021 campaign in Cabauw to answer the first sub-question. By applying a hybrid Positive Matrix Factorization (PMF)

approach to data from an Aerosol Chemical Speciation Monitor (ACSM) and particle number size distributions from a Scanning Mobility Particle Sizer (SMPS), this chapter attributes chemical species to specific size ranges based on temporal covariance. This analysis identifies major reactive nitrogen sources (NO_x and NH_3) and elucidates the role of nitrate condensation in aerosol formation and growth, providing empirical data for modelers and policymakers seeking to mitigate aerosol formation through targeted emission reductions.

Q2. What is the aerosol composition in terms of inorganic and organic nitrates in the Netherlands, and how does it vary temporally?

Inorganic and organic nitrates have different chemical transformation pathways and gas-particle partitioning behaviors. Accurate characterization requires the separation of these species in measurements. **Chapter 3** addresses the technical challenge of applying the NO_x^+ ratio method to the capture-vaporizer unit-mass-resolution time-of-flight ACSM (CV-UMR-ToF-ACSM) commonly used in Dutch and European monitoring networks, as opposed to the standard-vaporizer high-mass-resolution aerosol mass spectrometer (SV-HR-ToF-AMS), for which the original NO_x^+ ratio method was developed. This chapter describes an adapted methodology and its uncertainties, validated through co-located measurements with an SV-HR-ToF-AMS during the CAINA (Cloud-Aerosol Interactions in a Nitrogen-dominated Atmosphere) AIDA (Aerosol Interaction and Dynamics in the Atmosphere) chamber campaign. The validated method is then applied to ambient measurements in Cabauw to quantify the temporal variation of organic nitrate. Further investigation of inorganic/organic nitrate composition during nitrate pollution episodes in Cabauw is detailed in **Chapter 5**.

Q3. How does the nitrate aerosol composition depend on the meteorological conditions, emission sources, and co-emitted species?

Nitrate aerosol composition, especially for organic species, is influenced by precursors and meteorological parameters. **Chapter 4** explores the influence of these factors under controlled conditions in the SAPHIR (Simulation of Atmospheric PHotochemistry In a large Reaction chamber) during the CHANEL (Household Chemicals Amplifying Urban Aerosol Pollution) 2024 campaign. Unlike traditional studies using single-compound precursors, these experiments use realistic urban emission replicas, including VCPs, cooking, traffic, and biogenic emissions. By characterizing reaction products using a total NO_y monitor, AMS, and chemical ionization mass spectrometry (CIMS), this chapter identifies the bulk molecular weights and yields of organic nitrates across varying NO_x levels and oxidation conditions. The findings in **Chapter 4**, as well as the adapted NO_x^+ ratio method described in **Chapter 3** are subsequently applied to long-term ambient datasets in Chapter 5 to study the seasonality of nitrate aerosol composition during nitrate pollution episodes. Using meteorological data, the airmass-dependent variability

of nitrate composition in Cabauw is interpreted using HYSPLIT (Hybrid Single-Particle Lagrangian Integrated Trajectory), an air parcel trajectory computation model.

Q4. What is the volatility of organic nitrate from various emission sources, and how does it vary temporally?

The atmospheric lifetime and deposition flux of organic nitrates are determined by their volatility, quantified via the gas-particle partitioning coefficient. **Chapter 4** investigates these coefficients through chamber experiments, using high-mass-resolution spectrometry and a group contribution method, SIMPOL.1, to associate chemical structures with bulk volatility across various emission profiles. **Chapter 5** brings this knowledge from the chamber studies to the field to interpret the partitioning coefficients observed during nitrate pollution events in Cabauw. By linking the bulk volatility related to source-specific emission profiles in the atmospheric chamber to emission profiles downwind of the ambient observations through back trajectory analysis, both chapters characterize the real-world behavior of organic nitrate sinks.

This thesis concludes with **Chapter 6**, which synthesizes the results from the preceding chapters. The final discussion presents an integrated perspective on nitrate precursors, transformations, and sinks, highlighting novel contributions to atmospheric chemistry. These results provide insights to evaluate emission reduction strategies and introduce simplified yet empirically based parameters that can be readily implemented in chemical transport models to improve nitrogen deposition assessments. Finally, the remaining knowledge gaps are identified and recommendations for future measurement strategies and studies are discussed. These recommendations call for the improvement of monitoring facilities (e.g., more measurements of reactive nitrogen and VOC composition), modeling studies (e.g., plume transect studies constrained by observation), and combined data analysis to further advance understanding of atmospheric reactive nitrogen processes.



Chapter 2

What chemical species are responsible for new particle formation and growth in the Netherlands?

A hybrid positive matrix factorization (PMF) analysis using aerosol composition and size

This chapter is based on a peer-reviewed journal publication:

F. R. Nursanto, R. Meinen, R. Holzinger, M. C. Krol, X. Liu, U. Dusek, B. Henzing, and J. L. Fry (2023). "What chemical species are responsible for new particle formation and growth in the Netherlands? A hybrid positive matrix factorization (PMF) analysis using aerosol composition (ACSM) and size (SMPS)". *Atmospheric Chemistry and Physics* 23 (17), 10015–10034. DOI: 10.5194/acp-23-10015-2023

Figures, tables, and additional discussion referred to as part of the Supplement of Nursanto et al. (2023) are available at the following link: https://doi.org/10.5194/acp-23-10015-2023-supplement

Abstract

Aerosol formation acts as a sink for gas-phase atmospheric species that controls their atmospheric lifetime and environmental effects. To investigate aerosol formation and evolution in the Netherlands, a hybrid positive matrix factorization (PMF) analysis was conducted using observations from May, June, and September 2021 collected in the rural site of Cabauw in the central part of the Netherlands. The hybrid input matrix consists of the full organic mass spectrum acquired from a time-of-flight aerosol chemical speciation monitor (ToF-ACSM), ACSM inorganic species concentrations, and binned particle size distribution concentrations from a scanning mobility particle sizer (SMPS). These hybrid PMF analyses discerned four factors that describe aerosol composition variations: two size-driven factors that are related to new particle formation (NPF) and growth (F4 and F3), as well as two bulk factors driven by composition, not size (F2 and F1). The distribution of chemical species across these factors shows that different compounds are responsible for nucleation and growth of new particles. The smallest-diameter size factor (F4) contains ammonium sulfate and organics and typically peaks during the daytime. Newly formed particles, represented by F4, are mainly correlated with wind from the southwesterly–westerly and easterly sectors that transport sulfur oxides (SO_x), ammonia (NH_3), and organic precursors to Cabauw. As the particles grow from F4 to F3 and to bulk factors, nitrate and organics play an increasing role, and the particle loading diurnal cycle shifts from daytime to a nighttime maximum. Greater organics availability makes secondary organic aerosol (SOA) more influential in summertime aerosol growth, principally due to volatility differences produced by seasonal variation in photooxidation and temperature.

2.1 Introduction

Atmospheric aerosols are solid or liquid particles suspended in the air that are formed from natural or anthropogenic sources (Haywood, 2016). To describe the aerosol particle size distribution, four modes are generally distinguished according to the particle geometric diameter (D_p): the nucleation mode ($D_p \leq 20$ nm), Aitken mode (20 nm $< D_p \leq 100$ nm), accumulation mode (90 nm $< D_p \leq 1000$ nm), and coarse mode ($D_p > 1$ μm) (Hussein et al., 2004; Wu et al., 2008). New particle formation (NPF) is identified by a rapid buildup of high atmospheric concentrations of aerosol particles in the nucleation mode. These particles subsequently grow into Aitken-mode particles and further, larger sizes (Maso et al., 2005; Spracklen et al., 2010; Salimi et al., 2015; Kerminen et al., 2018; Lee et al., 2019).

Aerosols directly impact the Earth by absorbing and scattering solar and terrestrial radiation (Andreae and Crutzen, 1997; Grantz et al., 2003; Wong et al., 2017; Marrero-Ortiz et al., 2019) and indirectly by producing or modifying clouds (Lohmann and Feichter, 2005; Mahowald et al., 2011; Fan et al., 2018). NPF plays a prominent role in cloud formation by contributing to over 50 % of cloud condensation nuclei formation, which affects the lifetime and radiative properties of clouds (Bianchi et al., 2016; Gordon et al., 2016; Haywood, 2016; Dall'Osto et al., 2018; Lee et al., 2019). These phenomena affect the ecosystem physically by modifying radiation diffusion, temperature, and precipitation (Grantz et al., 2003; Haywood, 2016; Lee et al., 2019). Aerosols also influence the ecosystem chemically through influencing the spatial patterns of nitrogen deposition (Swaluw et al., 2011; Wamelink et al., 2013) and oxidative processes (Xing et al., 2017), leading to ecological harm such as soil pollution, water acidification, eutrophication, and loss of biodiversity (Erisman et al., 2011; Wamelink et al., 2013). In terms of public health, aerosols exhibit adverse effects on human health due to their size and chemical composition. NPF events are typically followed by air quality degradation, which is consistently associated with elevated pulmonary and cardiovascular morbidity and mortality worldwide (Ayala et al., 2012; Pope et al., 2020).

Sulfuric acid (H_2SO_4) is typically understood to be the most prevalent nucleation-inducing agent in NPF events, together with other airborne chemical species, including nitric acid (HNO_3), bases (e.g., amines), and organic acids (Zhang et al., 2012; Zhang et al., 2015; Kulmala et al., 2013; Wagner et al., 2017; Lehtipalo et al., 2018; Kürten, 2019; Lee et al., 2019; Brean et al., 2021; Olin et al., 2022). Numerous studies have also reported low-volatility organic species, such as terpene oxidation products and organic nitrates, participating in the formation of new particles (Berkemeier et al., 2016; Bianchi et al., 2016; Tröstl et al., 2016; Barsanti et al., 2017; Dall'Osto et al., 2018; Kerminen et al., 2018; Lee et al., 2019; Heinritzi et al., 2020).

In this work, we show that co-located measurements of aerosols' atmospheric composition and particle size distribution can be used to characterize the chemical composition of new particle and aerosol components that facilitate their growth. A time-of-flight aerosol chemical speciation monitor (ToF-ACSM; Aerodyne Inc.) allows the continuous and real-time quantification of non-refractory chemical species in ambient air (Ng et al., 2011; Fröhlich et al., 2013). For particle size distributions, the scanning mobility particle sizer (SMPS) provides real-time measurement of submicron particle number concentrations of different sizes (Amaral et al., 2015; Wiedensohler et al., 2012).

Aerosol mass spectrometry measurements have been used extensively with positive matrix factorization (PMF) as a strategy for aerosol source apportionment, especially regarding the organic components (Lanz et al., 2007; Jimenez et al., 2009; Ulbrich et al., 2009; Ng et al., 2010; Zhang et al., 2011). This chapter combines the organic mass spectrum and chemical species concentrations from ToF-ACSM with particle size distribution from SMPS into a hybrid PMF input matrix in order to study the association between chemical composition and particle size distribution. A similar approach for hybrid ACSM-SMPS PMF analysis was used for a European aerosol dataset comparison (Dall'Osto et al., 2018). Previous studies on aerosol source apportionment in the Netherlands have focused on organic aerosol composition (Mooibroek et al., 2011; Mensah et al., 2012; Schlag et al., 2016). Here, we analyze ACSM-SMPS datasets from Cabauw, the Netherlands, collected as part of the Ruisdael Observatory Land–Atmosphere Interactions Intensive Trace-gas and Aerosol (RITA) campaign in May to September 2021 (`https://ruisdael-observatory.nl`, last access: 21 August 2023), using PMF to characterize the chemical species responsible for new particle formation and growth across several seasons. Several studies have shown NPF events dependent on air mass origin transporting different pollutants (Hamed et al., 2007; Modini et al., 2009; Castro et al., 2010; Asmi et al., 2011; Németh and Salma, 2014; Nieminen et al., 2014; Qi et al., 2015; Mordas et al., 2016; Kolesar et al., 2017; Peng et al., 2017; Kerminen et al., 2018; Pushpawela et al., 2019), and therefore we also explore the relationships between wind direction, wind speed, and factor time series to interpret source apportionment.

2.2 Methods and instrumentation

2.2.1 Cabauw site and meteorological conditions

Measurements were performed at the CESAR tower (51.97 ^{o}N, 4.93 ^{o}E), managed and operated by the Royal Netherlands Meteorological Institute (KNMI; the Netherlands) (see Fig. 2.1a). The tower is located near Cabauw, in the province of Utrecht, the Netherlands, approximately 18 km southwest of Utrecht's city center, 31 km east of the city and port (the largest in Europe) of Rotterdam, 45 km south of Amsterdam,

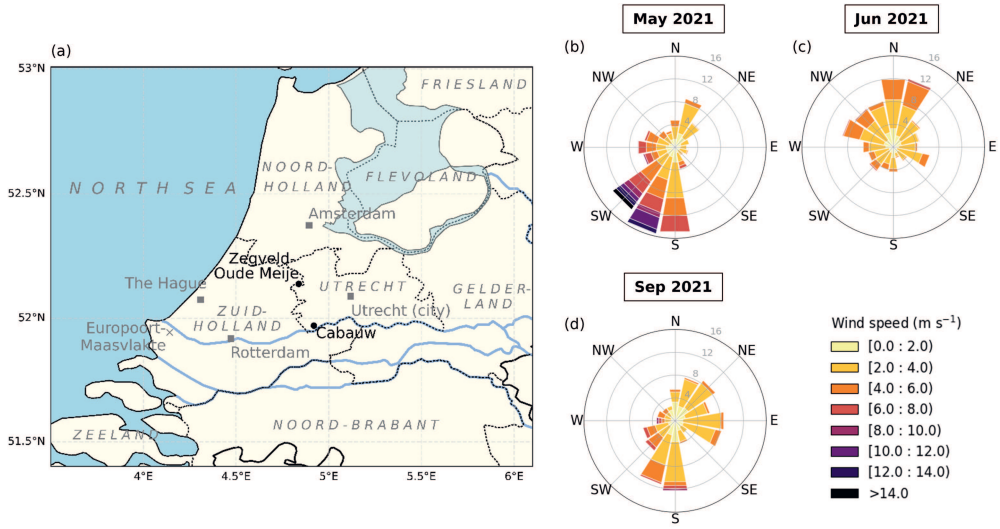


Figure 2.1: (a) Map of a part of the Netherlands showing the locations of the measurement stations Cabauw (main site) and Zegveld-Oude Meije (auxiliary NH_3 measurements). The province, sea, and neighboring country names are indicated in italic and light grey. The big cities in the area, Amsterdam, The Hague, Rotterdam, and Utrecht, collectively known as Randstad, are situated in the Noord-Holland, Zuid-Holland, and Utrecht provinces. The urban and harbor areas of Rotterdam extends as Europoort-Maasvlakte to the mouth of the Maas River. **(b–d)** Wind rose plots for May, June, and September 2021. Winds from the S up to the SW sector were dominant in May. In June, the prevailing winds were from the WNW up to the NNE sector. In September, two major wind directions were from the E and S sectors.

and 45 km southeast of the Dutch North Sea coast. To the east and south of the site are the provinces of Gelderland and Noord-Brabant, which consist mainly of forests; agricultural lands with clay and sand soil types for crops; and animal farms, specifically chicken and pig farms in the south and cattle in the east (CBS, 2022). The Cabauw site itself is rural and is surrounded by agricultural lands. The dataset used in this analysis contains overlapping ACSM and SMPS data split into periods from 11–31 May, 1–22 June, and 1–30 September 2021, providing some seasonal variation. To simplify, in this chapter we refer to these periods as May, June, and September, respectively.

Weather data were retrieved from the Royal Netherlands Meteorological Institute (KNMI; https://www.knmi.nl/home, last access: 21 August 2023). In general, May 2021 was characterized by moderate spring temperatures (11.8 °C on average) with scattered precipitation transitioning into the warmer summer period. June 2021 had the highest temperatures (18.7 °C on average) and was the sunniest of the three periods, reflecting summer weather. September 2021 showed warm temperatures (16.2 °C on average), with less radiation and precipitation compared to May 2021. Winds from

Table 2.1: Meteorological conditions during three periods analyzed (May, June, and September 2021). The periods represent spring, summer, and autumn weather, respectively.

Period	Temperature (°C)	Downward shortwave radiation ($W \cdot m^{-2}$)	Precipitation (mm)
11–31 May 2021	11.8 (mean) 3.5 (low), 23.0 (high)	211.7 (mean) 1032.2 (max)	96.6 (total)
1–22 June 2021	18.7 (mean) 8.1 (low), 29.6 (high)	264.9 (mean) 957.2 (max)	31.2 (total)
1–30 September 2021	16.2 (mean) 5.7 (low), 26.7 (high)	142.0 (mean) 818.9 (max)	24.4 (total)

the south to southwest (180 to 225^o) dominated in spring (May), bringing plumes from the agriculture-heavy province of Noord-Brabant. In summer (June), the prevailing air masses were coming from west–northwest to north–northeast (292.5 to 22.5^o), bringing air from the North Sea and some major cities along the coast and/or in the Randstad, such as Rotterdam, The Hague, Amsterdam, and Utrecht. More diverse wind plumes were observed in September, ranging between easterly (22.5 to 112.5^o), coming from the forested nature and agricultural areas in the province of Gelderland, and southerly (180 to 202.5^o), coming from the province of Noord-Brabant. The meteorological variables for each period are summarized in Table 2.1, and the wind variables are visualized as wind roses in Fig. 2.1b–d.

2.2.2 Chemical species measurements

The ToF-ACSM was the main instrument employed, allowing for the analysis of non-refractory organics, ammonium, nitrate, sulfate, and chloride in the aerosol phase. The instrument has been detailed in other work (Fröhlich et al., 2013). Ambient air was drawn into the instrument through a stainless-steel tubing inlet system equipped with a $PM_{2.5}$ size-cut cyclone (URG-2000-30ED) and a Nafion dryer, sampling at 4.5 m height with a flow rate of 2 $L \cdot min^{-1}$. An intermediate-pressure lens (IPL) is used as an aerodynamic lens, allowing for the transmission of particles in the $PM_{2.5}$ fraction (Xu et al., 2017). The instrument uses a capture vaporizer (CV) to increase the particle collection efficiency (CE) as opposed to a standard vaporizer (SV) (Jayne and Worsnop, 2016). By having a narrow entrance, the CV increases the particle collision events and thus increases the contact with the hot vaporizer surface, minimizing particles that bounce without evaporation (Hu et al., 2017) and resulting in higher CE. Consequently, however, the fragmentation patterns are shifted towards smaller ion masses due to additional thermal decomposition (Hu et al., 2017; Xu et al., 2017; Zheng et al., 2020). The average flow rate in the sample line of the instrument is 1.22 $cm^3 \cdot s^{-1}$ (0.07 $L \cdot min^{-1}$). Combining the $PM_{2.5}$ size-cut cyclone, $PM_{2.5}$ aerodynamic lens, and CV allows the ToF-ACSM to be a $PM_{2.5}$ measurement (Xu et al., 2017).

The ToF-ACSM provides unit mass resolution (UMR) mass spectra with a 10 min time resolution, which are analyzed using Tofware v3.2 in Igor Pro 8. The fractions of measured UMR signals were assigned to individual aerosol species using the fragmentation Table (Allan et al., 2004). On-site calibrations were performed to determine the ionization efficiencies of the chemical species. The calibrations of ionization efficiency (IE) and relative IE (RIE) were performed following the procedures described in previous studies by using 300–350 nm pure ammonium nitrate (NH_4NO_3) and ammonium sulfate ($(NH_4)_2SO_4$) dissolved in aqueous solution. The calibration gives an IE value of 250.0 ions $\cdot$ pg^{-1} for nitrate (NO_3) and RIE values of 1.40, 1.67, 1.30, and 3.35 for organics (Org), sulfate (SO_4), chloride (Cl), and ammonium (NH_4), respectively. The detection limits (measured similarly to Fröhlich et al. (2013)) at a 10 min time resolution for this ToF-ACSM operating at Cabauw (a relatively polluted site in the central Netherlands) are 0.38 $\mu g \cdot m^{-3}$ for Org, 0.12 $\mu g \cdot m^{-3}$ for NH_4, 0.07 $\mu g \cdot m^{-3}$ for NO_3, 0.11 $\mu g \cdot m^{-3}$ for SO_4, and 0.09 $\mu g \cdot m^{-3}$ for Cl.

In addition to the aerosol measurements by the ToF-ACSM, ambient sulfur dioxide (SO_2) concentrations were obtained from the open-source data of *Landelijk Meetnet Luchtkwaliteit* (LML; `https://www.luchtmeetnet.nl`, last access: 21 August 2023), measured at the same location. Ammonia (NH_3) concentrations were obtained from measurements in the Zegveld-Oude Meije station, 20 km to the north of the Cabauw station (see Fig. 2.1a), also acquired from LML.

2.2.3 Particle size distribution measurements

The particle size distribution measurements were conducted using an SMPS instrument developed by the Leibniz Institute for Tropospheric Research (TROPOS-SMPS). The instrument has been detailed in other work (Wiedensohler et al., 2012). Ambient air was sampled using a stainless-steel inlet equipped with a PM_{10} size-cut cyclone and a Nafion dryer at 4.5 m height sampling with a flow rate of 16.7 L $\cdot$ min^{-1}. The SMPS inlet was placed approximately 2 m lateral distance from the ACSM instrument inlet. The instrument consists of a Vienna-type differential mobility analyzer (DMA) and a butanol-based TSI condensation particle counter (CPC) 3750. The flow rate in the instrument is L $\cdot$ min^{-1}. The TSI CPC 3750 has a collection efficiency of 100 % at the first selected and reported size of 10 nm.

The raw dataset was processed using a linear multiple charge inversion algorithm to derive the particle number size distribution (PNSD or $dN/d\log D_p$) (Wiedensohler et al., 2012; Pfeifer et al., 2014). The mobility particle size spectrometer (MPSS) inversion algorithm version 2.13 was utilized to obtain a final PNSD from the raw dataset. The final PNSD has a 5 min time resolution and covers 71 geometric mean diameters (D_p) from 8 to 853 nm. The particle number concentrations (dN) for individual D_p were then calculated by multiplying PNSD by $d\log D_p$ values.

2.2.4 Positive matrix factorization (PMF)

The 10 min average matrices of UMR organic fragment mass spectra with a mass-to-charge ratio (m/Q) of 12 to 120 were combined with the inorganic species average mass concentrations (i.e., ammonium (NH_4), nitrate (NO_3), sulfate (SO_4), and chloride (Cl)) and the 10 min average particle number concentrations (dN) in 18 particle diameter size bins from 71 geometric mean diameters (D_p) to generate hybrid input data matrices for PMF analysis. Each organic fragment m/Q, species concentration, and size-binned particle concentration is treated as an individual variable in the PMF.

The values and errors of organic fragment mass spectra and inorganic mass concentration variables, as well as the minimum error (minErr) of all species, were generated by Tofware v3.2 in Igor Pro 8. The 10 min resolution particle size dataset was obtained from the 5 min resolution particle number concentration described in Section 2.2.3. The particle number concentrations are categorized into 18 size bin variables (8–10, 10–13, 13–16, 16–20, 20–25, 25–32, 32–40, 40–51, 51–65, 65–83, 83–107, 107–140, 140–185, 185–249, 249–342, 342–481, 481–691, and 691–853 nm). Each size bin contains the sum of four concentration points (except for the last bin containing only three concentration points) and is then averaged to 10 min. We use larger bin sizes for the larger diameters because larger particles occur less frequently. The errors in each size bin are taken to be the standard deviation of the raw data.

We performed the analysis using the PMF Evaluation Tool (PET) v3.08 (Ulbrich et al., 2009) in Igor Pro 8. The details of applying PMF to aerosol mass spectrometry datasets have been discussed elsewhere (Paatero and Tapper, 1994; Paatero, 1999; Ulbrich et al., 2009). Prior to analysis before the PMF input matrix preparation, the variable values and errors of species mass concentrations and particle number concentrations were downweighted in reference to the highest average peak of the original organic mass spectrum, m/Q 44 (f_{44}). During PMF input matrix preparation in PET v3.08, the m/Q 44, 28, 18, 17, and 16 signals in the organic mass spectrum are also downweighted as provided by the procedure to account for duplicated information of m/Q 44 in the organic mass spectrum (Ulbrich et al., 2009). The details of the PMF variable downweighting can be found in Section S3 in the Supplement of Nursanto et al. (2023).

The first step of the factor analysis was identifying the optimum number of factors (p) by running unconstrained experiments using two to eight factors and varying the seed value (min = 0, max = 20, delta = 1) to pick different initial values for the PMF algorithm. The optimum p is selected by considering the lowest residuals and local minima (Q/Q_{exp}) of the PMF solutions. Alongside the local minima, we considered whether all the factors are environmentally reasonable and unique, mainly based on their particle size distribution and chemical composition. After the optimum p and seed value are chosen, the rotationality of the best PMF solution is explored by varying the rotation (f_{peak}) value (min = -1, max = +1, delta = 0.2). Bootstrapping runs with 100

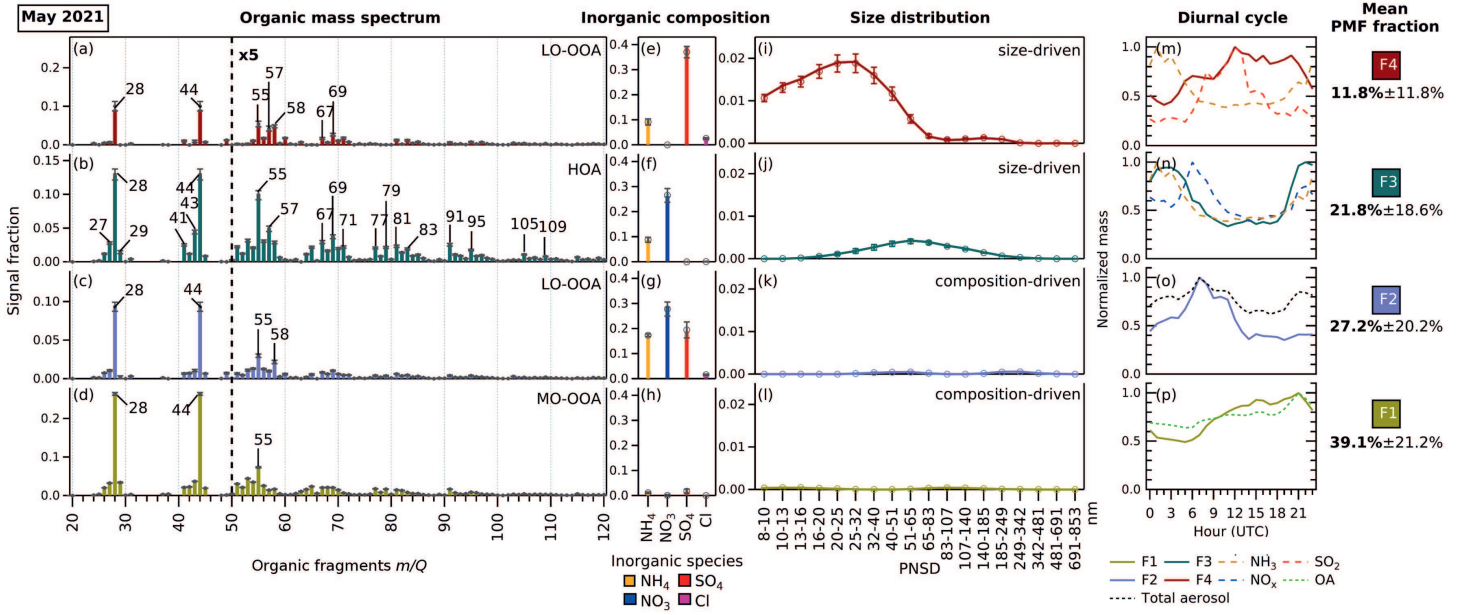


Figure 2.2: The profiles of the four-factor PMF solution from the combined ACSM-–SMPS dataset in May 2021. Each factor is split into 3 matrices with their own rescaled signal fraction axes. The error bars in each variable represent the standard deviation generated by performing a bootstrapped run of the solution. Panels **(a)–(d)** show the organic fragment mass spectrum from m/Q 20 to 120 from ACSM ($m/Q < 20$ not included). Panels **(e)–(h)** show the ACSM standard inorganic aerosol species concentrations (ammonium (NH_4), nitrate (NO_3), sulfate (SO_4), and chloride (Cl)). Panels **(i)–(l)** show the particle size distribution profiles from the SMPS. In panels **(m)–(p)**, the diurnal cycles of the factors and related species are depicted. The mean PMF fractions and their standard deviations are shown, indicating the mean contribution of each hybrid PMF factor to the total variable reconstruction by PMF throughout the period. Note that the standard deviations shown here indicate real variability in the contribution of each factor and not uncertainty. The factors in May 2021 are assigned as (F1) more-oxidized oxygenated organic aerosol (MO-OOA), (F2) NH_4+NO_3+SO_4+less-oxidized OOA (LO-OOA), (F3) size-driven NH_4+NO_3+hydrocarbonlike organic aerosol (HOA), and (F4) size-driven NH_4+SO_4+LO-OOA. Similar figures for June and September 2021 can be found in Figs. S1 and S2 in the Supplement of Nursanto et al. (2023).

iterations on the chosen PMF solution were performed to estimate the uncertainty in the factor profile variables and time series, ensuring the robustness of the solution.

To determine the organic and inorganic composition in each PMF factor, the particle size distributions are removed from the factor profile. The total organic mass fraction is considered to be the sum of the organic fragment fraction from m/Q 12 to 120, while the inorganic mass fractions are upweighted back and taken as NH_4, NO_3, SO_4, and Cl mass fractions. The final fraction of each species is determined by dividing the species mass fraction by the total organic and readjusted inorganic mass fraction.

2.2.5 Wind analysis

To analyze the factors using wind variables, we investigate the prevailing wind for several pollution episodes observed in the dataset. Bivariate polar plots are generated for the factor reconstructed mass concentration derived from PMF analyses and the mass concentration for each ACSM species in each period using the Openair package in the R environment (Carslaw and Ropkins, 2012). The wind parameters are obtained from the co-located measurement of 10 m wind direction data acquired from KNMI.

2.3 Results and discussion

2.3.1 Mean bulk atmospheric chemical composition across periods

We hypothesize that the mean bulk atmospheric chemical composition influences how the chemical species are distributed across the PMF factors. Therefore, we discuss this topic before the PMF solutions. To compare the mean bulk composition among periods, we choose the springtime period (May) as a reference. The mean concentrations of atmospheric species and the species percentages in the bulk atmosphere are summarized in Table S1 in the Supplement of Nursanto et al. (2023). In summer (June), we observe roughly a doubling in aerosol concentration for all inorganic aerosol (IA) and an increase by a factor of 2.6 in organics compared to spring (May). In autumn (September), the particle concentrations decrease again, with a relatively larger decrease for sulfate.

The ion balance ratio, also called ammonium balance (NH_4_bal = $n_{NH_4}/(n_{NO_3} + 2 \cdot n_{SO_4} + n_{Cl})$), is the molar concentration ratio between the measured ammonium (n_{NH_4}) and the total ammonium required to neutralize the major anions ($n_{NO_3} + 2 \cdot n_{SO_4} + n_{Cl}$). The ratio illustrates the excess of atmospheric ammonium (cation) or nitrate (anion) and other possibilities based on aerosol chemistry (see Section S2 for details in the Supplement of Nursanto et al. (2023)). Ambient aerosol is normally charge balanced, meaning that the major cation (NH_4^+) and major anion species (NO_3^-, SO_4^{2-}, and Cl^-) should roughly have a one to one molar ratio (NH_4_bal ~ 1). Among the three periods

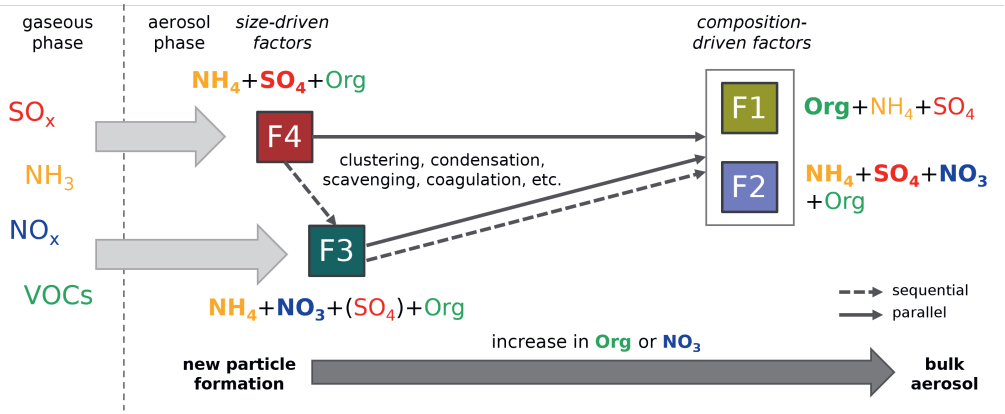


Figure 2.3: Potential relationships between the size-driven factors (F4 and F3, linked to NPF and growth) and the composition-driven factors (F2 and F1, linked to the bulk atmospheric aerosol composition), illustrating multiple possible aerosol growth pathways. From F4 (mainly ammonium sulfate) and F3 (mainly ammonium nitrate), particles can grow into F2 (mixed OA and IA factor) and/or F1 (OA dominant) in a sequential (dashed), parallel (solid), or combined manner. The particle formation and growth occur through condensation of gaseous precursors or particle coagulation. An increase in organics and NO3 in the bulk composition is observed as particles progress along these pathways.

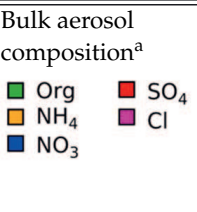
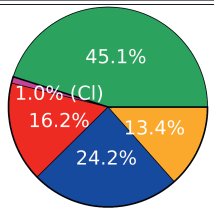
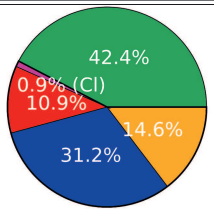
analyzed, the ion balance ratio was found to be close to unity for all periods. This infers that the bulk aerosol charge is fully neutralized.

We introduce the mean organic to inorganic mass ratio ($m_{\mathrm{Org}}/m_{\mathrm{IA}}$) to quantitatively compare the bulk OA and IA composition across seasons. Based on this ratio, in summertime (June), we have a composition richer in organics compared to spring and autumn. This difference is likely due to increasing biogenic emissions of volatile organic compounds (VOCs) in summertime, and higher-temperature-induced increases in anthropogenic VOC concentrations.

2.3.2 Identification of PMF factors

From the unconstrained experiments using the combined ACSM–SMPS matrix, the best PMF solution was found to have four factors for May 2021 (Fig. 2.2), June 2021 (Fig. S1 in the Supplement of Nursanto et al. (2023)), and September 2021 (Fig. S2 in the Supplement of Nursanto et al. (2023)). The determination of the PMF solution is detailed in Section S3 in the Supplement of Nursanto et al. (2023). The resulting hybrid PMF solution matrix is split into organic mass spectrum, species mass concentrations, and particle number concentration bin matrices for ease of presentation. The fragments of m/Q below 20 are included in the PMF analysis but are not shown in the figures, as they do not convey information for the spectrum interpretation. The signal factor axes

Table 2.2: Mean bulk atmospheric chemical composition in the three periods, summarized as the values of the total aerosol mass loading in $\mu g \cdot m^{-3}$, ion balance ratio (NH_{4_bal}) from linear regression, and mean organic to inorganic ratio (m_{Org}/m_{IA}). More detailed information about each chemical species can be seen in Table S1 in the Supplement of Nursanto et al. (2023).

Mean value	May 2021 (spring)	June 2021 (summer)	September 2021 (autumn)
Bulk aerosol composition[a]			
Aerosol mass loading ($\mu g \cdot m^{-3}$)[c]	6.60	14.12	5.15
NH_{4_bal}[b]	0.997±0.001	0.986±0.001	1.006±0.001
m_{Org}/m_{IA}	0.61	0.82	0.74

[a] mass concentration.
[b] molar concentration.
[c] total mass of aerosol detected by ToF-ACSM (m_{Org}+m_{NH_4}+m_{NO_3}+m_{SO_4}+m_{Cl}).

for inorganic composition and particle size distribution are rescaled and fixed to allow a comparison across factors. As each period encompasses around one month of time series data, the factors discerned by the hybrid PMF analyses show typical average aerosol composition during each period rather than individual pollution episode profiles that may vary over time. Similarities and differences between factors across months are discussed further below.

Factor particle size distributions and composition

Two factors have particle size profiles associated with specific diameter subranges, which we interpret as related to NPF and growth. We therefore call these factors "size-driven". The size-driven factors resolved from the analysis possess similarities in composition across months, where the factor associated with the smallest particle sizes is associated with the bulk composition of ammonium sulfate aerosol (F4), while the larger sizes are linked to the bulk composition of ammonium nitrate aerosol (F3). The other two factors are unrelated to specific particle size and are therefore called "composition-driven" factors, consisting of (F2), a mixed OA and IA factor, and (F1), an OA-dominant factor. Both composition-driven factors can be seen as the representatives of the bulk atmospheric aerosol composition. We can summarize that the NPF and growth follow the pathway starting from F4 and F3 into F2 and F1 (bulk aerosol composition), likely through processes such as condensation of gaseous precursors (SO_x, NH_3, NO_x, and

VOCs and their reaction products) or particle coagulation (see Fig. 2.2). We note that this does not imply that all aerosol growth proceeds sequentially through these four factors; a discussion of possible NPF and growth pathways will be detailed at the end of this subsection.

Factor organic profiles

The organic mass spectrum can be used to obtain information regarding the degree of oxidation, which can be related to atmospheric aging of each factor profile. In general, OA can be categorized into two types: primary organic aerosols (POAs) and secondary organic aerosols (SOAs). Oxygenated organic aerosols (OOAs) are often considered to be SOAs, while other OA profiles are generally considered POAs (Chen et al., 2022).

OOAs are characterized by relatively high m/Q 28 (f_{28}) and m/Q 44 (f_{44}) fragment signals, originating primarily from CO^+ and CO_2^+ fragments of carboxylate groups in organic compounds, produced by thermal decomposition inside the ACSM vaporizer (Alfarra, 2004). The f_{44} fragment is often related to a high degree of oxidation and photochemical aging (Alfarra, 2004; Ng et al., 2010). It is also important to note that the ACSM used in this chapter has a CV instead of an SV inlet (see Section 2.2.2), which is known to produce higher f_{44} values due to enhanced thermal decomposition (Hu et al., 2017; Zheng et al., 2020). The m/Q 43 (f_{43}) fragment is characteristic of both oxygenated organic compounds (CH_3CO^+) and saturated hydrocarbon compounds ($C_3H_7^+$). Thus, factors with higher f_{44} and lower f_{43} values are understood to be more oxidized, while lower f_{44} and higher f_{43} values imply that the factor is less oxidized. OOA may appear in more than one factor in a PMF solution, and thus it is common to distinguish between less-oxidized OOA (LO-OOA), typically associated with higher-volatility organics, and more-oxidized OOA (MO-OOA), typically associated with lower-volatility organics. To assess the variation in the OOA oxidation level, the triangle plot (Ng et al., 2010) is normally used to compare f_{44}/f_{43} values among resolved OOA factors in the PMF solution (see Fig. S6 in the Supplement of Nursanto et al. (2023)). OOAs generally increase throughout the afternoon as their formation is photochemically driven (Hu et al., 2016b; Sun et al., 2016), and they accumulate in the evening due to the shallow nocturnal boundary layer. In the morning, the concentration decreases as clean airmasses are introduced into the rising boundary layer, diluting existing aerosol concentrations (Stull, 1988).

POA consists of various sources, which can be identified from the appearance of certain fragmentation patterns in the organic mass spectrum, and has a diurnal cycle as well as correlation with other measurements. Some of the most common POAs from PMF analysis are hydrocarbonlike organic aerosols (HOAs), biomass burning organic aerosols (BBOAs), cooking organic aerosols (COAs), and coal combustion organic aerosol (CCOAs) (Chen et al., 2022). POAs have similar characteristics to alkyl and

alkenyl fragments ($C_nH_{2n+1}^+$: m/Q 29, 43, 57, 71, ... and $C_nH_{2n-1}^+$: m/Q 27, 41, 55, 69, ...). HOA, as a type of POA, is often correlated with anthropogenic combustion pollutants, such as nitrogen oxides (NO_x) and black carbon from vehicular emissions (Alfarra, 2004; Mohr et al., 2009; Zheng et al., 2020). Other POA profiles are distinguished by looking at certain fragments (e.g., m/Q 60 and 73 for BBOA (Schneider et al., 2006; Weimer et al., 2008; He et al., 2010), m/Q 55 for COA (He et al., 2010; Mohr et al., 2012), m/Q of larger fragments related to polycyclic aromatic hydrocarbons (PAHs) for CCOA (Hu

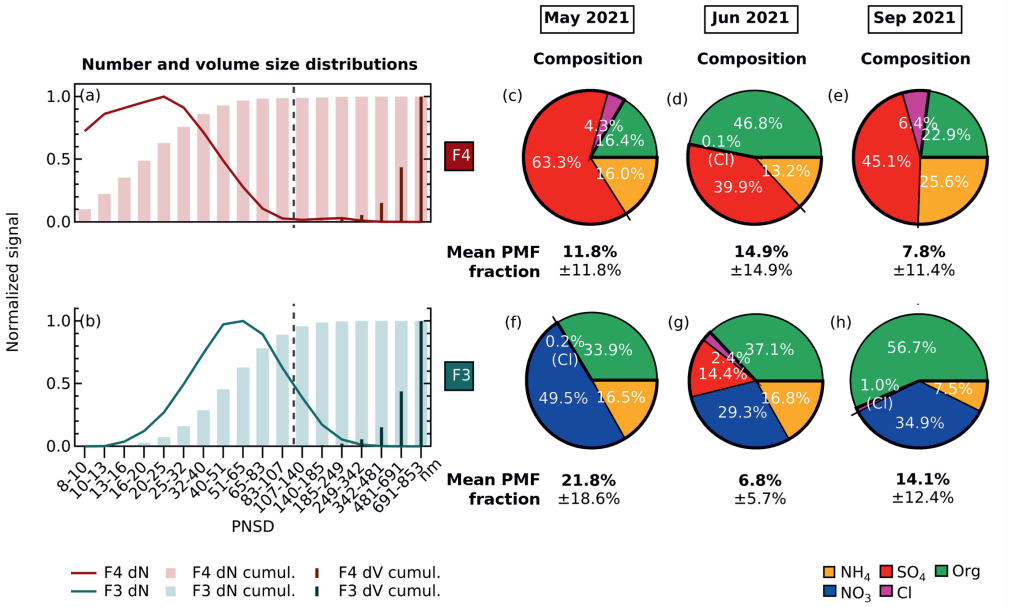


Figure 2.4: (a–b) Normalized average particle size distributions of two size-driven factors of F4 (maroon) and F3 (turquoise) across periods. The line plot shows the particle number concentration (dN) fraction in each size bin. The thick histogram represents the cumulative particle number concentration (dN) fraction as the particle size increases, while the thin histogram represents the cumulative particle volume ($dV = dN \cdot (4/3) \cdot \pi \cdot (D_p/2)^3$) fraction. The vertical dashed dark grey line divides the particle diameters where particles are transmitted with 50 % efficiency on the left (diameter less than ~100 nm) and with at least 50 % efficiency by the $PM_{2.5}$ lens of ToF-ACSM on the right (diameter more than ~100 nm). **(c–h)** Pie charts showing the mass percentage of each aerosol species contributing to each size-driven factor in May 2021, June 2021, and September 2021. Green represents organics (Org), orange represents ammonium (NH_4), dark blue represents nitrate (NO_3), dark red represents sulfate (SO_4), and pink represents chloride (Cl). F4 is dominated by ammonium sulfate, while F3 is dominated by ammonium nitrate. The mean PMF fractions and their standard deviations are shown, indicating the mean contribution of the factor to the total reconstructed PMF mass and its variability over each month-long period.

et al., 2016b)). While CV increases the f_{44} values and smaller organic fragments due to enhanced thermal decomposition, larger fragments become underestimated (Hu et al., 2017; Zheng et al., 2020), and therefore the differences between POA factors become more subtle.

The PMF analyses in this study resolved one POA factor (as an HOA factor) and three SOA factors (two LO-OOA factors and one MO-OOA factor) across periods, where each organic profile has its corresponding IA composition and size distribution. Among size-driven factors, the factor related to the smallest particle sizes (F4) has OA assigned as LO-OOA, while the OA associated with the second size-driven factor (F3) is assigned as HOA. In the composition-driven factors, the OA+IA mixture factor (F2) resolves an LO-OOA profile, while the OA factor (F1) resolves an MO-OOA profile.

2.3.3 Size-driven factors (F4 and F3)

Using the hybrid ACSM–SMPS datasets, two size-driven factors emerge from the PMF analyses as F4 and F3 (see Fig. 2.4). These factors are considered size driven due to the approximately normally distributed particle concentrations in a specific subrange of diameter. The two factors display different particle size clusters increasing in diameter from F4 to F3.

New particle formation (NPF) events are characterized by the rapidly increasing particle number concentration below 20 nm followed by particle growth, creating nearly vertical aligned peaks in particle number concentration plotted against time (Heintzenberg et al., 2007; Kerminen et al., 2018). By comparing the time series of the particle size distribution ($dN/d\log D_p$), total mass loading, and PMF mass fraction (see Fig. 2.5 (May) and Fig. S3 (June and September) in the Supplement of Nursanto et al. (2023)), we can observe that the episodes during which the size-driven factors' fractions increase occur when the total aerosol mass concentration is relatively low. This is to be expected, as during these periods, the condensational sink, which would compete by scavenging low-volatility gases or small particles, is reduced. If we zoom into the time series, the NPF growth shapes appear during episodes that are dominated by F4 and/or F3 (see Fig. S4 in the Supplement of Nursanto et al. (2023)).

The reconstructed PMF masses show the influence of sunlight and temperature on NPF events. The average PMF mass fraction of the size-driven F4 is larger in summertime (June) compared with other periods (see Fig. 2.4) due to higher mean radiation and temperatures (see Table 1). In summer (June), F4 accounts for on average 14.9 % of the total reconstructed PMF mass, while in spring (May) and autumn (September), it only represents 11.8 % and 7.8 %, respectively. The more frequent appearance of NPF growth events during summer can be seen in Fig. S3a–c in the Supplement of Nursanto et al. (2023). Other studies have likewise found that the occurrence of NPF events is generally favored in high radiation (Modini et al., 2009; Peltola et al., 2022) and warmer

temperatures (Jokinen et al., 2022; Peltola et al., 2022). This is because solar radiation provides the UV radiation that promotes the photochemical reactions and turbulent motions needed to form new particles (Wehner et al., 2015; Dada et al., 2017; Kerminen et al., 2018; Sellegri et al., 2019).

Particle size distributions

F4 corresponds to the bulk composition when the particles in the nucleation mode are growing into the Aitken-mode size range, with a modal size of 20–25 nm (see Fig. 2.4a). F3 is characterized by clustered particle sizes in the Aitken and accumulation mode region, with a modal size of 51–65 nm (see Fig. 2.4b). The F4 and F3 mass loading shows a good correlation with the particle number concentration in the size bin of 20–25 and 51–65 nm, respectively, across periods (see Fig. S5 in the Supplement of Nursanto et al. (2023)). The size range differs slightly across months, but F4 always appears as the smallest particle size range among the factors, which we therefore designate as the nucleation-mode factor, while F3 with a larger particle size range is designated as the growth-mode factor.

Some concerns may arise because the ACSM and SMPS measure different particle size ranges, especially the smaller sizes, which are the biggest focus of this study. According to a study conducted using a ToF-ACSM in the same configuration as this study, the $PM_{2.5}$ lens in the ToF-ACSM transmits particles with a vacuum aerodynamic diameter (D_{va}) between 100 nm and 3 μm with efficiency above 50 %, decreasing to around 20 % for D_{va} 55–60 nm (Xu et al., 2017). Meanwhile, the SMPS instrument samples particles with diameters ranging from 10 to 800 nm. As we are mainly interested in elucidating the composition of NPF and growth in sizes finer than 100 nm, we address the influence of this mismatch on the interpretation of our PMF results here.

In Fig. 2.4a, we observe that F4 is mainly related to aerosol with sizes that have a transmission efficiency ∼50 % in $PM_{2.5}$ ToF-ACSM, while in Fig. 2.4b, only the size bins of 107–140 nm in F3 have a transmission efficiency ≥50 %. The small-sized particles will make a negligible contribution to the $PM_{2.5}$ mass, and the larger particles will always dominate the particle volume size distribution, regardless of whether the finer particles are efficiently sampled or not by ACSM. Nevertheless, although the ACSM does not directly measure the finest particle composition, the factor still illustrates the bulk chemical composition that occurs during and favors the formation and growth of new particles. Moreover, the PMF tool does not recognize that the diameter bins are sequential, so the fact that particle diameters cluster in certain ranges in factors F4 and F3 is consistent with their identification as corresponding to NPF and growth.

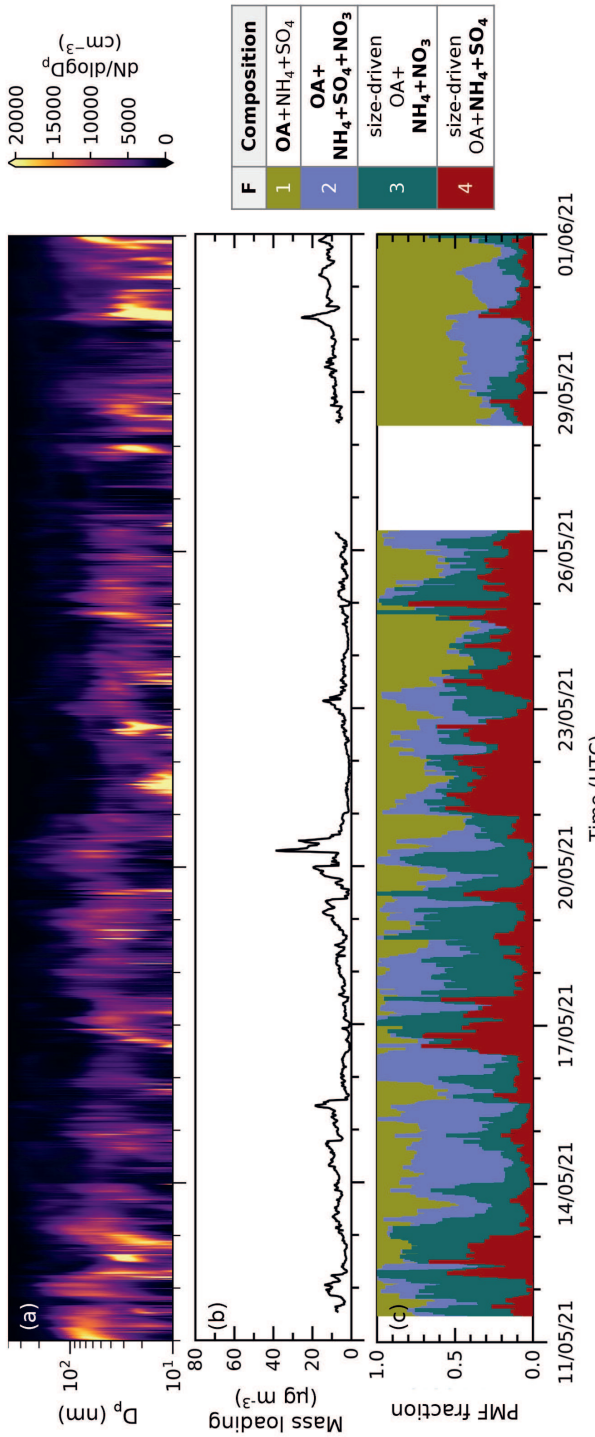


Figure 2.5: Time series of **(a)** particle size distribution ($dN/d\log D_p$) in cm^{-3} with a logarithmic scale in particle size obtained from SMPS measurements, **(b)** total mass loading calculated from the ACSM species concentration (using Tofware) in $\mu g \cdot m^{-3}$, and **(c)** reconstructed PMF fraction (stacked) from analysis in May 2021. Episodes of F4 and F3 coincide with relatively low total aerosol mass conditions and high fine particle concentrations. Similar figures for June and September 2021 can be found in Fig. S3 in the Supplement of Nursanto et al. (2023).

Chemical composition

In all periods, the nucleation-mode F4 has ammonium sulfate as the major component (see Fig. 2.4c–e). The factor further consists of ammonium (13 % to 26 %), sulfate (40 % to 63 %), organic compounds (16 % to 47 %), and traces of chloride (0.1 % to 6.4 %). Organics are known to participate in particle formation and growth (Riipinen et al., 2012; Hodshire et al., 2016), while in this study, the mass percentage share between ammonium, sulfate, and organics of F4 depends on the mean bulk organic composition in each period (see Fig. 2.4c–e). The low mean bulk organic composition in springtime and autumn (May and September) leads to F4 being largely ammonium (16 % and 26 %) and sulfate (63 % and 45 %), followed by OA (16 % and 23 %) and chloride (4.3 % and 6.4 %). The organic-rich regime in summer (June; see Table 2.2) results in the increase in OA in F4 (47 %) and less ammonium, sulfate, and chloride (13 %, 40 %, and 0.1 %, respectively). F4 represents from 9.5 % up to 14.3 % of total reconstructed PMF mass in the solution, with the highest being during summer when there is a higher contribution from organic masses. On the other hand, the growth-mode F3 is mainly composed of ammonium nitrate aerosol (see Fig. 2.4f–h). The factor is further composed of ammonium (8 % to 17 %), nitrate (29 % to 50 %), organic compounds (34 % to 57 %), and traces of chloride (0.2 % to 2.4 %). In contrast to other months, the PMF analysis also resolves variations in F3 containing sulfate (14 %) during summertime (June).

Overall, we interpret these results as indicating that sulfate is a key component of nucleating particles during NPF events. When the mean bulk organic concentration is high and more oxidized (e.g., summertime), it participates more abundantly in particle nucleation. While sulfate is key to nucleation, nitrate plays a more important role in particle growth (see Section S2 in the Supplement of Nursanto et al. (2023)).

Organic profiles

The organic mass spectrum profile of each size-driven factor and their diurnal cycles in each period are shown in Fig. 2.6. Across seasons, LO-OOA is a part of the bulk composition related to nucleation-mode particles. The factors are assigned as LO-OOA due to their f_{44}/f_{43} values compared with other OOA factors (see the triangle plot in Fig. S6 in the Supplement of Nursanto et al. (2023)). The LO-OOA F4 profile resolved in this study is comparable to LO-OOA resolved in other aerosol mass spectrometry studies using CV (Zheng et al., 2020; Joo et al., 2021), although fragments with $m/Q > 50$ are less prevalent. Several aerosol chamber experiments have reported that lower volatility and highly oxygenated organic molecules from biogenic and anthropogenic organic precursors play a dominant role in new particle formation and growth (Schobesberger et al., 2013; Ehn et al., 2014; Riccobono et al., 2014; Tröstl et al., 2016; Mohr et al., 2019; Pospisilova et al., 2020; Zhao et al., 2021). In this study, however, we surprisingly observe LO-OOA rather than MO-OOA associated with nucleation. This could imply

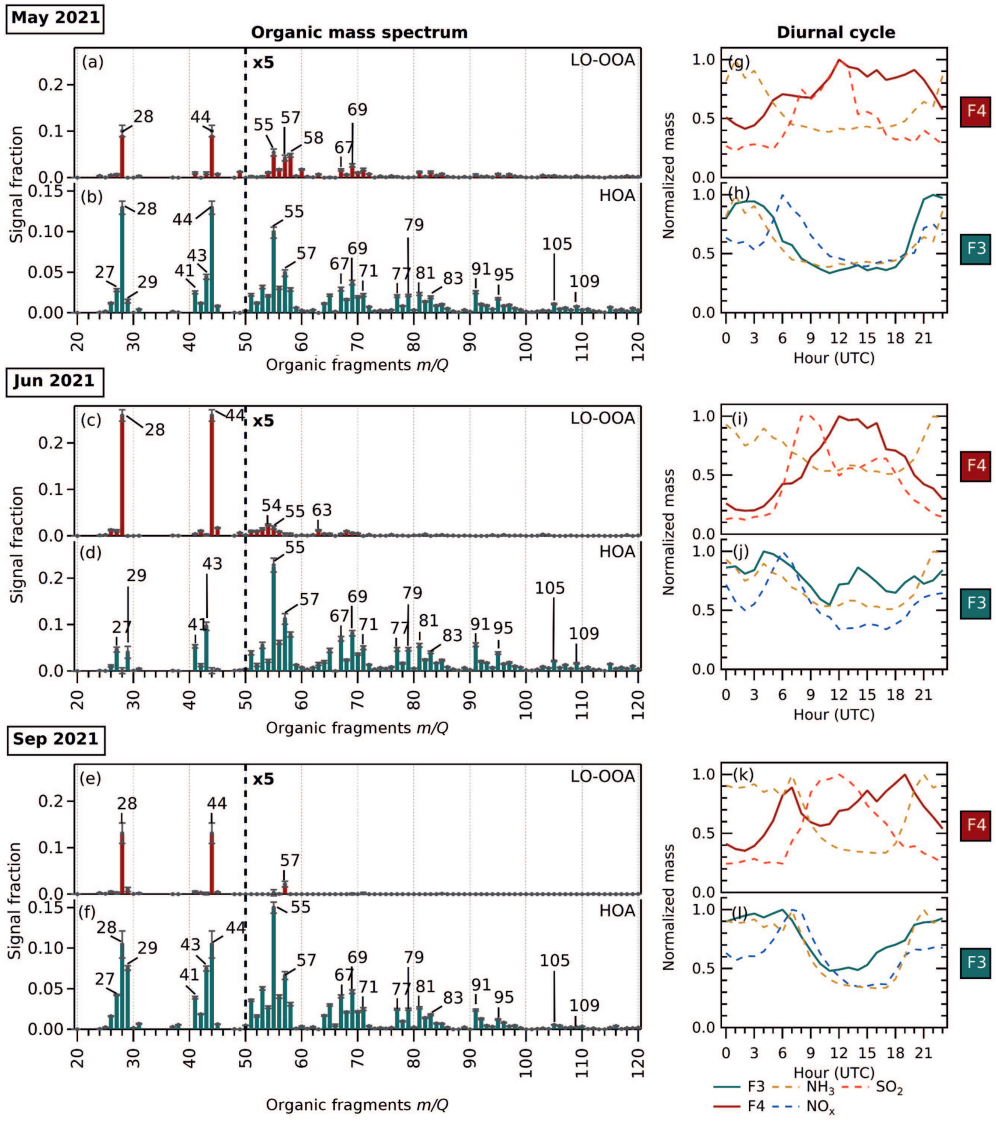


Figure 2.6: (a–f) Organic mass spectrum from m/Q 20 to 120 ($m/Q < 20$ is not included) of F4 (maroon) showing LO-OOA factor profiles and F3 (turquoise) showing HOA factor profiles in May 2021, June 2021, and September 2021. The error bars in each m/Q were generated from a bootstrap run. **(g–l)** Diurnal cycles of corresponding factors and potential precursor gases. The diurnal cycles of F4, mainly composed of ammonium sulfate, are shown together with its precursors, NH_3 and SO_2. The diurnal cycles of F3, mainly composed of ammonium nitrate, are shown together with its precursors, NH_3 and NO_x.

that organic compounds with less oxygenation are more abundant and condense on freshly nucleated particles in this region or that the ToF-ACSM delineation between LO-OOA and MO-OOA does not directly correspond to volatility in this case.

In terms of the diurnal cycle, the F4 mass loading does not follow the typical LO-OOA pattern but rather together with the formation of ammonium sulfate is responsible for the increase in new particle loading during the day, as seen in the diurnal cycles (Fig. 2.6g,i,k). The organic-rich regime in summer (see Table 2.2) combined with a higher mean temperature also favor the abundant production of semi-volatile OA, which can condense onto newly formed particles, leading to an increase in OA to 47 % compared to 16 % in spring and 23 % in autumn (see Fig. 2.4).

F3, seen as the growth-mode factor mainly related to the organic and ammonium nitrate bulk composition, has an HOA-like organic profile. The factor is assigned as HOA due to the alkyl and alkenyl fragments that are abundant (m/Q 27, 29, 41, 43, 55, 57, 69, and 71). The diurnal cycle of F3 in this study shows a similarity with general non-urban HOA diurnal patterns, with increased loading at nighttime (see Fig. 2.6h,j,l), contrary to the typical diurnal pattern of HOA in urban sites with peaks during morning and evening rush hour (Chen et al., 2022). It suggests that the growth-mode F3 may be related to transported vehicular emissions from urban areas and/or local primary organic emissions. Organic nitrates can also be formed from the reaction between NO_x with less-oxygenated VOCs through nitrate radical ($NO_3^{\bullet}$) or organic peroxy ($RO_2^{\bullet}$) radical chemistry (Berkemeier et al., 2016). The diurnal pattern of F3 is consistent with this organic nitrate formation, followed by condensation onto the newly formed particles as the temperature lowers at night. During the summer, a small increase in the F3 mass loading during the daytime can also be observed, hinting at the enhancement of daytime organic nitrate formation in the hottest and sunniest period.

During the summer, the values of f_{28} and f_{44}/f_{43} as oxygenated organic markers in F4 are higher compared to other seasons, while they are almost absent in F3. In the chemical composition discussed previously, sulfate also makes an appearance in F3 in summer, unlike other seasons. We hypothesize that the PMF solution did not resolve the two size-driven factors in summer (June) similarly to other seasons, and therefore the aerosol composition is more mixed between NPF and growth particles. Mathematically, this is reflected in the local minima of the chosen PMF solution. Despite being the lowest minimum in the PMF solution space, Q/Q_{exp} in June scores lower compared to May and September (see Table S3 in the Supplement of Nursanto et al. (2023)).

New particle formation (NPF) and growth pathway

The NPF events shown by the time series of the particle number size distribution and size-driven factor loading reveal that particle formation and growth take around 6 to 12 h (see Fig. S4 in the Supplement of Nursanto et al. (2023)). The high occurrence

of ammonium sulfate and oxidized organic molecules in the aerosol phase observed during nucleation-mode F4 episodes marks the beginning of NPF. This is related to ammonium sulfate formation from the reaction between ammonia and sulfuric acid and the uptake of oxygenated organic compounds. We can consider F3 to be a "sequential" pathway of F4 growing in size (see Fig. 2.3); this sequential nature is observed in some NPF events shown in Fig. S4 in the Supplement of Nursanto et al. (2023), when F3 peaks after F4. F4 grows into F3 when nitric acid and/or organic nitrates and hydrocarbonlike semi-volatile organic compounds are dominant in the aerosol composition.

One might argue that F3 cannot be considered the successor of F4 as it does not contain any sulfate (for May and September), which should remain from the initial nucleation. Another possible explanation is that F3 emerges directly from ammonium nitrate as a "parallel" nucleation pathway (see Fig. 2.3). Other studies have observed this nucleation mode to occur very rarely and only in the free troposphere, at a lower temperature and under very clean air conditions, through the reaction between nitric acid and NH_3 (Höpfner et al., 2019; Wang et al., 2020). In a "combined" hypothesis, F3 emerges from F4, but the particles rapidly favor the pathway of growing by mainly ammonium nitrate condensation to the particle phase. The simultaneous pathway of F4 and F3 growth can be observed in some NPF events in Fig. S4 in the Supplement of Nursanto et al. (2023). This process leads to the negligible amount of sulfate and abundance of ammonium nitrate during particle growth, hence to sulfate mass being unresolved in the F3 composition (for May and September). Chamber experiments and theoretical studies support this interpretation of NPF occurring with only minor involvement of sulfate (Liu et al., 2018; Wang et al., 2020; Wang et al., 2022). The chemistry of ammonium sulfate and nitrate aerosol formation is discussed in more detail in Section S2 in the Supplement of Nursanto et al. (2023).

Relationship between new particle formation and wind variables

To study the relationship between wind variables and new particle formation in the rural site of Cabauw, wind analyses were done using bivariate polar plots of size-driven F4 and F3 by wind speed and wind direction (see Fig. 2.7). We observe that nucleation-mode F4 is mainly correlated with air masses transported from the southwesterly–westerly sector and sometimes from the easterly sector. These wind sectors supply sulfate, ammonium, and organics (Fig. S8 in the Supplement of Nursanto et al. (2023)), as well as their precursor gases that determine the main composition of F4 (see Fig. S9 in the Supplement of Nursanto et al. (2023)). Westerlies represent a source of sulfate, which mainly comes from sulfur oxide (SO_x) emissions along the waterway of Rotterdam's harbor, the busiest port in Europe. The sulfate in the air transported to Cabauw from the northern to the eastern sector may arise from the SO_x precursor from other urban, shipping, and industry centers (e.g., the city and port of Amsterdam, the city of Utrecht), as well as power plants (see Fig. 2.1) (Henschel et al., 2013; Fioletov et al., 2016; Ledoux

et al., 2018). The supply of ammonium for new particle condensation through NH_3 emission comes from the agricultural practices that take place around the Cabauw site, with a tendency of receiving higher NH_3 and ammonium from the southern sector. The easterlies extending to the north are also sources of VOCs coming from the forested nature areas in the provinces Utrecht and Gelderland, which are subsequently transformed into SOA.

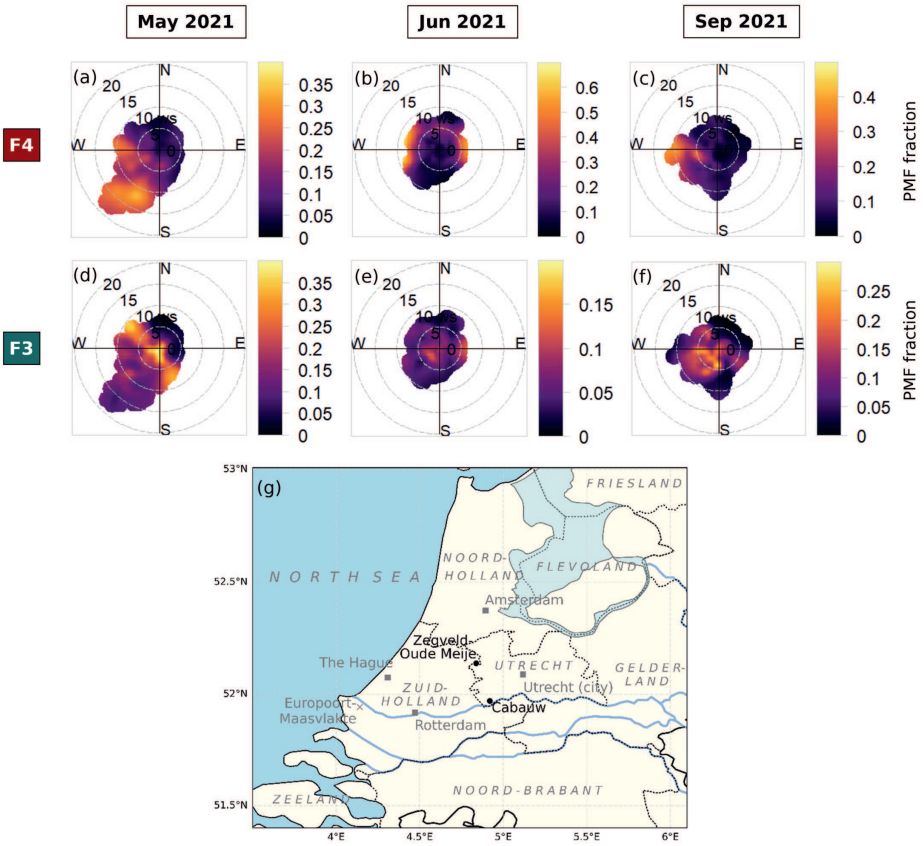


Figure 2.7: (a–f) Bivariate polar plots of size-driven factor mass fractions (F4 and F3) by wind speed and wind direction measured in Cabauw in May, June, and September 2021. We observe that the nucleation-mode particle (F4, **a–c**) fraction is largely correlated with air masses from the southwesterly–westerly sector where the urban and harbor areas of Rotterdam are located. The growth-mode particle (F3, **d–f**) fraction is distributed around the site and is from the southwesterly sector. Similar figures for composition-driven factors can be found in Fig. S7 in the Supplement of Nursanto et al. (2023).

The different prevailing wind also affects the F4 composition and frequency. In spring (May) and autumn (September), new particle formation mainly correlates with winds

from southerly and westerly directions (see Fig. 2.7a,c) and thus has less organic composition. In summer (June), winds coming from the east contribute to NPF events (see Fig. 2.7b), supplying more organics to the site. The abundant organics due to higher radiation and temperatures allow semi-volatile SOA to directly condense onto newly formed particles, increasing NPF events and F4 mass fraction during summer (see Fig. 2.4d).

2.3.4 Composition-driven factors (F2 and F1)

The two composition-driven factors yielded by the PMF analyses are F2 and F1 (see Fig. 2.2 (May), Fig. S1 (June), and Fig. S2 (September) in the Supplement of Nursanto et al. (2023)). We call these factors composition driven because they are found across the size distribution rather than in a specific size range. They collectively account for a large fraction of total reconstructed PMF mass (66 % to 78 %) and can be considered to be the result of size-driven factors' further growth into the bulk aerosol. F2 and F1 are both representative of the mean atmospheric bulk aerosol composition and are split into two different factors by PMF.

F2 is characterized by the presence of a mixture of OA and IA (see Fig. S10m—r in the Supplement of Nursanto et al. (2023)). Based on the organic spectrum, the aerosol mixture can be characterized as LO-OOA, comparable to the LO-OOA profile found in other aerosol mass spectrometry studies using CV (Hu et al., 2018a; Zheng et al., 2020; Joo et al., 2021). It has similar f_{44}/f_{43} to the LO-OOA profile in F4 on average (see triangle plot in Fig. S6 in the Supplement of Nursanto et al. (2023)). In terms of the diurnal cycle, the F2 mass loading does not follow the typical LO-OOA pattern. Normally, LO-OOA would have a higher nighttime concentration and a slight decrease during the day (Chen et al., 2022), but we found the diurnal cycle of F2 to be similar to the diurnal pattern of the total aerosol mass loading in this study (see Fig. S10g,i,k in the Supplement of Nursanto et al. (2023)). This finding suggests that F2 is the result of condensation of available semi-volatile chemical constituents over the course of the day as the continuation of NPF and growth, governed by the availability of both bulk IA and OA composition.

While F2 contains both OA and IA, F1 is dominated by OA (see Fig. S10m—r in the Supplement of Nursanto et al. (2023)). It represents the continuation of NPF and growth enriched by organic compounds. F1 is mainly composed of organics (82 % to 94 %) and a trace amount of ammonium (2 % to 6 %) and sulfate (2 % to 12 %). A trace of nitrate aerosol (2 %) can also be found in F1 in the summer (June). The abundance of m/Q 44 fragments and high f_{44}/f_{43} values (see Fig. S6 in the Supplement of Nursanto et al. (2023)) indicate that the factor F1 represents aged SOA, resembling OOA profiles observed at the same site in previous studies (Mensah et al., 2012; Paglione et al., 2014; Schlag et al., 2016) and MO-OOA profiles observed in aerosol mass spectrometry with

CV (Hu et al., 2018a; Zheng et al., 2020; Joo et al., 2021). F1 exhibits a diurnal pattern consistent with MO-OOA, with the concentration rising slightly across the day. It has a relatively stable concentration throughout the day because the factor is largely driven by long-range transport of aerosol (Kodros et al., 2020; Chen et al., 2022) but with a slightly increasing concentration from the morning to afternoon due to photochemical oxidation. Wind analysis suggests that the bulk SOA in F1 is related to air masses arriving from the easterly sector that span from north ($\sim 0^o$) to south ($\sim 180^o$) (see Fig. S7 in the Supplement of Nursanto et al. (2023)). To the east, the province of Gelderland is mostly covered by agricultural grass land and forested nature areas that emit VOCs, therefore increasing the amount of OA produced. Easterly wind directions may also contain the accumulated pollutants or VOCs from continental Europe and therefore may contain a variety of OA from either biogenic or anthropogenic sources. Considering the organic profile, the high mass loading percentage, and the source regions across periods, we attribute F1 to background regional and continental OA.

2.4 Conclusions

In this work, we have shown that hybrid ACSM-SMPS PMF analysis can be used to determine the bulk chemical composition associated with new particle formation and growth. The analyses of three selected periods enable us to use the seasonality of the factor profiles, representing conditions of spring (sunny and warm) for May, summer (very sunny and hot) for June, and autumn (less sunny and warm) for September, as well as different prevailing winds, to attribute factor sources.

New particle formation episodes appeared when the total aerosol concentration was low, with key contributions from ammonium sulfate and oxygenated organic compounds across seasons, despite the high nitrogen emission in the Netherlands. New particle formation and growth exhibit a diurnal pattern dominated by daytime formation that shifts to nighttime growth as the particle size increases. While sulfate promotes new particle formation, nitrate and semi-volatile organics are more influential in growth. The substantial contribution of nitrate and less-oxidized organic aerosols to F3 and its shift to a nighttime peak in concentration indicate that ammonium and organic nitrate condense during the particle growth when the temperature is lower. The organic-rich regime, higher mean radiation, and higher mean temperature in summer result in a larger contribution of oxygenated organic vapors in new particle formation.

New particle formation is the most pronounced with winds from the southwest–west and sometimes northeast. These directions supply precursor gases, with the westerlies bringing SO_x from the port of Rotterdam, southwesterlies bringing NH_3 from agricultural emissions, and easterlies bringing organic vapors from the forest and nature areas. The influence of the wind direction could be clearly seen during the summer, where instead of southern and western winds, the prevailing winds were from the north and

east and brought abundant organics, resulting in the rapid growth of large amounts of organic aerosol.

In sum, this combination of composition and size information into the statistical method of PMF, augmented by meteorological and gas-phase auxiliary data, provides a powerful tool to assess the factors that control aerosol production in a complex region, heavily influenced by agricultural and industrial activities, alongside biogenic emissions of VOCs.


URG
2.5μm

Chapter 3

Development and validation of a NO_x^+ ratio method for the quantitative separation of inorganic and organic nitrate aerosol

Using a unit-mass-resolution time-of-flight aerosol chemical speciation monitor equipped with a capture vaporizer (CV-UMR-ToF-ACSM)

This chapter is based on a peer-reviewed journal publication:

F. R. Nursanto, D. A. Day, R. Meinen, R. Holzinger, H. Saathoff, J. Fu, J. Mulder, U. Dusek, and J. L. Fry (2025). "Development and validation of a NO_x^+ ratio method for the quantitative separation of inorganic and organic nitrate aerosol using a unit-mass-resolution time-of-flight aerosol chemical speciation monitor equipped with a capture vaporizer (CV-UMR-ToF-ACSM)". *Atmospheric Measurement Techniques* 18 (13). Publisher: Copernicus GmbH, 3051–3072. DOI: 10.5194/amt-18-3051-2025

Figures, tables, and additional discussion referred to as part of the Supplement of Nursanto et al. (2025) are available at the following link: https://doi.org/10.5194/amt-18-3051-2025-supplement

Abstract

Particulate nitrate is a major component of ambient aerosol around the world, present in inorganic form, mainly as ammonium nitrate, and also as organic nitrate. It is of increasing importance to monitor ambient particulate nitrate, a reservoir of urban nitrogen oxides that can be transported downwind and harm ecosystems. The unit-mass-resolution time-of-flight aerosol chemical speciation monitor equipped with capture vaporizer (CV-UMR-ToF-ACSM) is designed to quantitatively monitor ambient $PM_{2.5}$ composition. In this chapter, we describe a method for separating the organic and ammonium nitrate components measured by CV-UMR-ToF-ACSM based on evaluating the NO_2^+/NO^+ ratio (NO_x^+ ratio). This method includes modifying the ACSM fragmentation table, time averaging, and data filtering. By using the measured NO_x^+ ratio of NH_4NO_3 and a plausible range of NO_x^+ ratio for organic nitrate aerosol, the measured particulate nitrate can be split into inorganic and organic fractions. Data pre-treatment filters concentrations of particulate nitrate below 0.6–2.0 $\mu g \cdot m^{-3}$, depending on the time averaging. The method detection limit, when considering ± 10 % absolute uncertainty of organic nitrate fraction, is found to be 2 $\mu g \cdot m^{-3}$ (120 min averaging) to 10 $\mu g \cdot m^{-3}$ (10 min averaging) for total particulate nitrate concentration and 10 % (120 min) to 20 % (10 min) for organic nitrate fraction. We show that this method is able to distinguish periods with inorganic or organic nitrate as major components at a rural site in the Netherlands. A comparison to a high-resolution time-of-flight aerosol mass spectrometer equipped with a standard vaporizer (SV-HR-ToF-AMS) and positive matrix factorization (PMF) method shows similar response of increasing particulate organic nitrate fraction with uncertainties mainly from sensitivity to fragmentation table correction when obtaining the NO_2^+ signal. We propose that researchers use this NO_x^+ ratio method for CV-UMR-ToF-ACSM (adapting the appropriate fragmentation table and data pre-treatment for each specific application) to quantify the particulate organic nitrate fraction at existing monitoring sites in order to improve understanding of nitrate formation and speciation.

3.1 Introduction

In the current age of decreasing sulfur emissions, nitrate is becoming a principal aerosol component globally and regionally (Adams et al., 1999; Metzger, 2002; Liao et al., 2003; Rodriguez and Dabdub, 2004; Feng and Penner, 2007; Bauer et al., 2007; Paulot et al., 2016; Bian et al., 2017; Vasilakos et al., 2018; Drugé et al., 2019; Lu et al., 2021). In addition to an increasing aerosol fraction of ammonium nitrate (NH_4NO_3), ambient organic nitrates (ONs) produced through the oxidation of volatile organic compounds (VOCs) in the presence of nitrogen oxides (NO_x) can condense into the particulate phase or grow new particles (Huang et al., 2019a; Huang et al., 2019b; Song et al., 2024). The particulate organic nitrate (pON) contribution to total particulate nitrate mass (pNO_3) is substantial (Ng et al., 2017), with an average fraction of 17–31 % in China (Yu et al., 2024) and 34–44 % in Europe (Kiendler-Scharr et al., 2016), with large differences between urban and rural areas (Fisher et al., 2016; Schlag et al., 2016; Romer Present et al., 2020; Yu et al., 2024). Improved understanding of pON fraction in different regions can provide insight into chemical mechanisms of secondary aerosol formation (Pye et al., 2015; Lee et al., 2016; Ng et al., 2017; Zare et al., 2018).

Organic nitrogen (i.e., organic nitrates and amines) flux worldwide accounts for ∼25 % of the total nitrogen deposition (Jickells et al., 2013). Zare et al. (2018) estimated, via WRF-Chem (Weather Research and Forecasting model coupled with Chemistry) simulations in the southeast United States, that 60 % of NO_x loss is related to ON chemistry. Similar to inorganic nitrate, ON also can be regarded as a NO_x reservoir, because thermal or photolysis processes can re-release NO_x. The partitioning between gas-phase and particulate ON (Zare et al., 2018) can affect this reservoir lifetime and, thus, the spatial scale of transport of urban nitrogen emissions from their source, determining how far downwind these emissions can harm natural habitats (Fields, 2004; Bobbink and Hicks, 2014; Erisman et al., 2015; Melillo, 2021).

The NO_x^+ ratio method, first described by Farmer et al. (2010), is a robust method to separate the total pNO_3 signal measured by high-resolution aerosol mass spectrometer (AMS) into particulate ammonium nitrate (pAmN) and particulate organic nitrate (pON) using the variation of NO_2^+/NO^+ ion ratios (subsequently referred to as NO_x^+ ratios) in the mass spectra observed. This method has been successfully used to analyze pON composition in several studies (Fry et al., 2014; Fry et al., 2018; Pye et al., 2015; Kiendler-Scharr et al., 2016; Ng et al., 2017; Huang et al., 2019a; Huang et al., 2019b; Brownwood et al., 2021; Day et al., 2022a).

The basis of the NO_x^+ ratio method comes from the different fragmentation patterns of chemical species due to the interaction of the mass spectrometer's vaporizer and ionizer with the analytes. The empirical observation shows that nitrates attached to an organic moiety have different fragmentation patterns compared to nitrate in the form of

NH_4NO_3, as well as other less-volatile inorganic nitrates. Thus, each nitrate will have different NO_x^+ ratios, R_ν, as shown below in Eq. 3.1 (Day et al., 2002; Francisco and Krylowski, 2005; Farmer et al., 2010; Drewnick et al., 2015; Hu et al., 2016b; Day et al., 2022a),

$$R_\nu = \frac{(C_{NO_2^+})_\nu}{(C_{NO^+})_\nu} \tag{3.1}$$

where ν is the nitrate compound or mixture measured, $C_{NO_2^+}$ is the signal intensity of NO_2^+, and C_{NO^+} is the signal intensity of NO^+.

The NO_x^+ ratio of the observed air (R_{obs}) falls between the NO_x^+ ratios of pure pAmN (R_{pAmN}) and pure pON (R_{pON}). The time-varying mass fraction of particulate organic nitrate (f_{pON}, referring to pNO_3 existing as pON), and particulate ammonium nitrate (f_{pAmN}, referring to pNO_3 existing as pAmN) can be extracted from this time-varying R_{obs} using Eqs. 3.2 and 3.3 (Farmer et al., 2010).

$$f_{pON} = \frac{(R_{obs} - R_{pAmN})(1 + R_{pON})}{(R_{pON} - R_{pAmN})(1 + R_{obs})} \tag{3.2}$$

$$f_{pAmN} = 1 - f_{pON} \tag{3.3}$$

The aerosol chemical speciation monitor (ACSM, Aerodyne Inc.) is a unit-mass resolution (UMR) mass spectrometry instrument intended for continuous ambient aerosol monitoring (Ng et al., 2011; Fröhlich et al., 2013), unlike its predecessor, the aerosol mass spectrometer (AMS, Aerodyne Inc.) which is designed primarily for research (Drewnick et al., 2005). In this work, we explored whether the ACSM can be used to determine pAmN and pON in the same way as has been successfully demonstrated for the AMS. ACSMs are used extensively in monitoring networks, such as the sites in the Aerosol, Clouds and Trace Gases Research Infrastructure (ACTRIS) network in Europe (`https://www.psi.ch/en/acsm-stations/overview-full-period`, last access: 6 November 2024) and the Atmospheric Science and Chemistry mEasurement NeTwork (ASCENT) network in the United States (`https://ascent.research.gatech.edu`, last access: 6 November 2024).

For monitoring purposes, a capture vaporizer (CV) and an intermediate pressure lens (IPL) are recommended by Aerodyne for improved quantification of the $PM_{2.5}$ fraction, relative to a standard vaporizer (SV) and standard lens (Zheng et al., 2020). Almost half of the ACSMs in the ACTRIS network in Europe use a CV. The CV is designed to increase particle collision events with the vaporizer surface by having a narrow entrance, resulting in a particle collection efficiency (CE) of 1 and better mass closure of $PM_{2.5}$ monitoring (Jayne and Worsnop, 2016; Hu et al., 2017; Xu et al., 2017; Liu et al., 2024). The enhanced thermal decomposition, however, shifts the fragmentation pattern toward smaller ion fragments (Hu et al., 2017; Hu et al., 2018b; Xu et al., 2017; Zheng

et al., 2020). Therefore, the NO_x^+ ratio is substantially lower with CV compared to SV due to favored NO^+ formation. In consequence, the NO_x^+ ratio method's applicability in CV-based measurements is limited by the NO_2^+ detection limit ($< 0.1\ \mu g \cdot m^{-3}$; Hu et al. (2017)).

While high-resolution mass spectrometers can separate non-NO_x^+ peaks which are detected at the same nominal m/Q (mass-to-charge ratio) as NO_x^+ peaks (30 for NO^+ and 46 for NO_2^+), UMR analysis requires estimations based on related ions at other m/Q. These estimations are incorporated into data workup by the implementation of a fragmentation table, which subtracts an estimated amount of organic at m/Q 30 and m/Q 46, based on the signal at another related organic-only m/Q values. The default fragmentation table typically applied for the analysis of UMR spectra is based on generalized fragment mass composition of ambient aerosol composition measured using SV-based instruments (Allan et al., 2004; Ulbrich et al., 2009) and, thus, is not suitable for CV-UMR-ToF spectra that have different fragmentation patterns. Using a CV-HR-ToF-AMS, Hu et al. (2017) determined the organic fragment interference with NO^+ at m/Q 30 and with NO_2^+ at m/Q 46 for CV-UMR measurements in a biogenically dominated dataset, but no study has yet shown this calculation adapted to general ambient aerosol composition.

This work aims to adapt the NO_x^+ ratio method to separate pAmN and pON signals for CV-UMR-ToF-ACSM measurements. We first provide a revised fragmentation table for m/Q 30 and m/Q 46 that is compatible with CV-UMR-ToF-ACSM measurements with varying composition to better calculate NO^+ and NO_2^+ signal contributions. Second, we show the variation of experimental NO_x^+ ratio for pAmN in CV-UMR-ToF-ACSM instruments and determine the NO_x^+ ratio for pON. Third, we demonstrate the capability of data pre-treatments (filtering and time averaging) to overcome the low and noisy ratio signals produced by CV in ambient measurements. Fourth, the proposed NO_x^+ ratio method is applied to an extended ambient dataset (at the Cabauw site of the Ruisdael Observatory Network) to test its robustness for changing ambient aerosol mixtures. Lastly, the formation of pAmN and pON in a chamber experiment measured using CV-UMR-ToF-ACSM is used for method validation by comparing results with SV-HR-ToF-AMS.

3.2 Instrumentation

3.2.1 Description of ToF-ACSM

A ToF-ACSM (Aerodyne Inc.) is the main instrument used in this study, allowing for the chemical analysis of non-refractory organics (Org), ammonium (NH_4), nitrate (NO_3), sulfate (SO_4), and chloride (Cl) in the aerosol phase (Ng et al., 2011; Fröhlich et al., 2013). In comparison to compact time-of-flight (cToF)-AMS (Drewnick et al., 2005) and

HR-ToF-AMS (DeCarlo et al., 2006), ToF-ACSM is more compact in size, lower in price and operational cost, simpler in analysis, and requires less user intervention, which makes this instrument practical for long-term monitoring but still comparable to the AMS (Fröhlich et al., 2013). ToF-ACSM uses a three-way valve system that allows automatic switching between the sample and filter mode, unlike ToF-AMS, which has a mechanical chopper that physically blocks the particle beam. The lack of a chopper (but with the use of particle time-of-flight chamber) in the ToF-ACSM, however, removes the particle sizing feature, which makes it similar to the quadrupole-ACSM (Q-ACSM) but with better mass resolution and detection limits.

To conduct the various analyses in this chapter, we primarily use data from two ToF-ACSM instruments with identical setup. The instruments are managed by Utrecht University (UU) and University of Groningen (RUG), part of a larger monitoring network of Ruisdael Observatory in the Netherlands (`https://ruisdael-observatory.nl`, last access: 6 November 2024). We label the instruments as ACSM-UU and ACSM-RUG. The instrument setup for ambient measurements uses a combination of a $PM_{2.5}$ size-cut cyclone, an intermediate-pressure lens ($PM_{2.5}$ aerodynamic lens), and a capture vaporizer (CV, temperature $\sim$525 °C, Jayne and Worsnop (2016)) that has been aligned with the particle beam. Together, they configure the ToF-ACSM as a $PM_{2.5}$ monitor (Xu et al., 2017) with unit mass resolution. The instrument provides UMR mass spectra with default 10 min time resolution, analyzed using Tofware v3.3 in Igor Pro 8. The fractions of the UMR signal are assigned to different aerosol species using the fragmentation table.

3.2.2 Ambient measurements with ACSM

We use an ambient dataset measured using ACSM-UU deployed in Cabauw, the Netherlands, for method development and case studies. The ambient data were measured between 18 April 2023 to 15 April 2024 with some gaps (net 205 d of data) as part of the continuous monitoring of the Ruisdael Observatory network. Aerosol measurements were carried out with an inlet height of 4.5 m above the ground at the Cabauw tower (51.97 °N, 4.93 °E), an infrastructure of the Royal Netherlands Meteorological Institute (KNMI, the Netherlands, `https://www.knmi.nl/home`, last access: 9 November 2024). The site is surrounded by agricultural lands in the province of Utrecht, the Netherlands, a relatively nitrogen-polluted rural site.

Ambient air is sampled through a stainless-steel inlet system with a $PM_{2.5}$ size-cut cyclone (URG-2000-30ED) and a Nafion dryer with a sampling flow rate of $\sim$2 $L \cdot min^{-1}$, of which in average 1.23 $cm^3 \cdot s^{-1}$ (0.07 $L \cdot min^{-1}$) is sampled by the ACSM. The calibrations of ionization efficiency (IE) and relative IE (RIE) were performed using 300 nm particles from ammonium nitrate (NH_4NO_3) and ammonium sulfate ($(NH_4)_2SO_4$)) solutions (size-selected with a differential mobility analyzer, model TSI 3081 and co-

sampled with a condensation particle counter, model TSI 3750). The average IE value for the instrument is 169 ions $\cdot$ pg^{-1} for NO_3, and RIE values are 1.40, 1.58, 1.30, and 3.37 for Org, SO_4, Cl, and NH_4, respectively. RIE values used for Org and Cl were not measured and were instead applied as default values, as is common practice. The detection limits at 10 min time resolution are 0.38 $\mu g \cdot m^{-3}$ for Org, 0.12 $\mu g \cdot m^{-3}$ for NH_4, 0.07 $\mu g \cdot m^{-3}$ for NO_3, 0.07 $\mu g \cdot m^{-3}$ for NO^+ (m/Q 30), 0.04 $\mu g \cdot m^{-3}$ for NO_2^+ (m/Q 46), 0.11 $\mu g \cdot m^{-3}$ for SO_4, and 0.09 $\mu g \cdot m^{-3}$ for Cl.

3.2.3 Chamber measurements with ACSM and AMS

ACSM-RUG was deployed to measure aerosol in chamber experiments conducted in the Aerosol Interaction and Dynamics in the Atmosphere (AIDA) chamber, a facility maintained by Karlsruhe Institute of Technology (KIT), Germany. Chamber experiments were conducted in 2023 and 2024 as part of the Cloud-Aerosol Interactions in a Nitrogen-dominated Atmosphere (CAINA) project (`https://sites.google.com/view/cainaproject/`, last access: 6 November 2024).

Chamber air is sampled using stainless-steel tubing equipped with a Nafion dryer and a sampling flow of $\sim$2 L $\cdot$ min^{-1} of which in average 1.44 cm$^3 \cdot$s^{-1} (0.09 L $\cdot$ min^{-1}) is sampled by the ACSM. The average IE value for the instrument is 152 ions $\cdot$ pg^{-1} for NO_3. The ACSM instrument is run with 2 min time resolution unlike the default setting to capture more variation in the aerosol composition. The detection limits at 2 min time resolution for the ACSM-RUG instrument are 0.20 $\mu g \cdot m^{-3}$ for Org, 0.19 $\mu g \cdot m^{-3}$ for NH_4, 0.17 $\mu g \cdot m^{-3}$ for NO_3, 0.17 $\mu g \cdot m^{-3}$ for NO^+ (m/Q 30), 0.03 $\mu g \cdot m^{-3}$ for NO_2^+ (m/Q 46), 0.02 $\mu g \cdot m^{-3}$ for SO_4, and 0.05 $\mu g \cdot m^{-3}$ for Cl.

In addition, a high-resolution time-of-flight aerosol mass spectrometer (HR-AMS, Aerodyne Research Inc.) from KIT is connected to the chamber via a 6 mm (4 mm internal diameter) stainless-steel tube. The instrument is equipped with a $PM_{2.5}$ aerodynamic lens to measure the non-refractory $PM_{2.5}$ components, at a time resolution of 1 min (DeCarlo et al., 2006; Canagaratna et al., 2007; Williams et al., 2013), averaged to 2 min for this comparison. The operation of the AMS is explained in previous publications (Huang et al., 2019a; Song et al., 2022). Briefly, chamber air is sampled with a flow of 1.08 L $\cdot$ min^{-1}, of which on average 84 cm$^3 \cdot$min^{-1} is sampled by the AMS (Gao et al., 2022). The aerosol particles are then focused into a narrow beam by a $PM_{2.5}$ aerodynamic lens with an effective complete transmission for particle sizes ranging from 70 to 2500 nm (vacuum aerodynamic diameter; D_{va}) and heated by a standard vaporizer at 600 °C. The resulting vapors are ionized by electron impact (70 eV) and characterized by a time-of-flight mass spectrometer. The AMS ionization efficiency is calibrated using 300 nm dried NH_4NO_3 aerosol particles to give an average IE for NO_3 of 185.0 ions $\cdot$ pg^{-1}. The AMS data are analysed using the software packages Squirrel 1.66E and PIKA 1.26E in Igor Pro 8. To account for the effect of particle bouncing loss, chemical-composition-

based collection efficiency (0.5) was applied to calculate the particle mass concentration (Middlebrook et al., 2012).

3.3 Development of a fragmentation table for CV-UMR-ToF-ACSM from the AMS spectral database and ACSM chamber experiment spectra

3.3.1 General fragmentation table for typical ambient dataset

In the UMR-ACSM instruments, ions detected at m/Q 30 and m/Q 46 can originate from both nitrate (NO^+ and NO_2^+) and organic fragments. However, it is known that some fragments produced by processes in the vaporizer and ionizer can be related to one another (Allan et al., 2004). For instance, UMR peaks at m/Q 29, m/Q 42, m/Q 43, and m/Q 45 are mainly the product of further fragmentation of fragments at m/Q 30 and m/Q 46 and assumed to be exclusively of organic origin. The aim of the fragmentation table, with respect to the NO_x^+ species, is to predict the signal contribution of organic fragments at m/Q 30 and m/Q 46 based on the masses measured at m/Q 29, m/Q 42, m/Q 43, and m/Q 45 and subsequently to extract the signal that can be attributed to NO^+ and NO_2^+.

Our starting point is the default fragmentation table from Allan et al. (2004) (see Table 3.1). A fragmentation table consists of columns dividing the raw mass spectra into chemical species, with rows denoting entries for different UMR nominal masses. Thus, each entry consists of components which are added up to obtain the species concentration at a specific nominal mass. These components can be the whole peak of an m/Q x, referred to as an integer number (with square brackets in this thesis, "[x]"), or the contribution of a certain species to m/Q x in the fragmentation table, denoted as "frag_species[x]." A multiplier a (positive or negative) is included if the addition or subtraction of the component is fractional. The fragmentation table for ToF-AMS and ToF-ACSM are identical, except that gas-phase species contribution must also be removed in ToF-AMS. For the ACSM, due to the automatic filter sampling cycle and subtraction, gas-phase species are already removed. The fragmentation table developed in this chapter, therefore, is applicable to a CV-UMR aerosol mass spectrometer. Because the training data set incorporated multiple chamber and ambient measurements with different instruments, it should be applicable for a range of typical measurement configurations, but users should be aware of the potential effects of the instrument condition (e.g., vaporizer temperature, particle beam alignment, measurement history).

In the default fragmentation table (which was developed using SV-based instruments), the signal at m/Q 46 is assigned exclusively to NO_2^+, and the relationship of organic signal at m/Q 30 is found to be only 0.022 times the magnitude of organic signal at m/Q

Table 3.1: Excerpt of fragmentation table for Org and NO_3 species at m/Q 30 and m/Q 46. The first three rows show entries originated from the default fragmentation table of Allan et al. (2004) (used in Tofware v3.3). The last three rows show entries proposed to develop a revised CV-UMR-ToF-ACSM fragmentation table in this study.

m/Q	Allan et al. (2004), default fragmentation table	
	Org	NO_3
30	0.022 · frag_Org[29]	[30], -frag_Org[30]
46	-	[46]
m/Q	Proposed for general CV-ToF-ACSM	
	Org	NO_3
30	$a_{Org[30],[i]}$ · frag_Org[i] [a]	[30], -frag_Org[30]
46	$a_{Org[46],[i]}$ · frag_Org[i] [b]	[46], -frag_Org[46]

i represents UMR masses tested against m/Q 30 and m/Q 46 in this study, which includes frag_Org[29], frag_Org[42], frag_Org[43], and frag_Org[45]. See the list in the footnote of Table S3 in the Supplement of Nursanto et al. (2025).

[a] $a_{Org[30],[i]}$ is the multiplier for frag_Org[30] component, obtained from the slope of ODR fit between frag_Org[30] and frag_Org[i].

[b] $a_{Org[46],[i]}$ is the multiplier for frag_Org[46] component, obtained from the slope of ODR fit between frag_Org[46] and frag_Org[i].

29. Switching from SV to CV modifies the signal ratio between organic and inorganic fragments at m/Q 30 and m/Q 46 because of greater organic fragmentation in CV (Hu et al., 2018b). It also leads to greater nitrate fragmentation and consequently smaller NO_2^+ signal, which makes the organic contribution at m/Q 46 more important. For instance, Fry et al. (2018) found larger contributions of organic fragments at m/Q 30 and m/Q 46 than the default fragmentation table in a semi-polluted biogenically influenced air analyzed with an SV-HR-ToF-AMS. Therefore, modifications to frag_NO_3[46] and frag_NO_3[30] entries (later referred to as $C_{NO_2^+}$ and C_{NO^+} to calculate NO_x^+ ratio outside fragmentation table context) must be established for CV-based instruments.

To make a revised fragmentation table applicable for general ambient organic aerosol (OA) mixtures, a variety of organic aerosol profiles is necessary. We use 25 CV-HR-ToF-AMS spectra (including both nitrates and non-nitrate organics) from the AMS spectral database (`http://cires1.colorado.edu/jimenez-group/AMSsd_CV`, last access: 6 November 2024) and 6 CV-UMR-ToF-ACSM spectra from chamber experiments. The CV-HR-ToF-AMS database mass spectra include 3 chamber experiments, 7 factors of positive matrix factorization (PMF) analysis from ambient measurements, and 15 laboratory standards measurements (Hu et al., n.d.; Hu et al., 2017; Carlton et al., 2018; Hu et al., 2018b; Hu et al., 2018a), summarized in Table S1 in the Supplement of Nursanto et al. (2025). The CV-UMR-ToF-ACSM mass spectra were measured from experiments conducted in the AIDA chamber (see Section 3.2.3). These spectra were obtained using

vaporizer temperature ranging from 525 to 600 °C (see Tables S1 and S2 in the Supplement of Nursanto et al. (2025)). Therefore, the revised fragmentation table should be valid for CV-based instruments run in this temperature range.

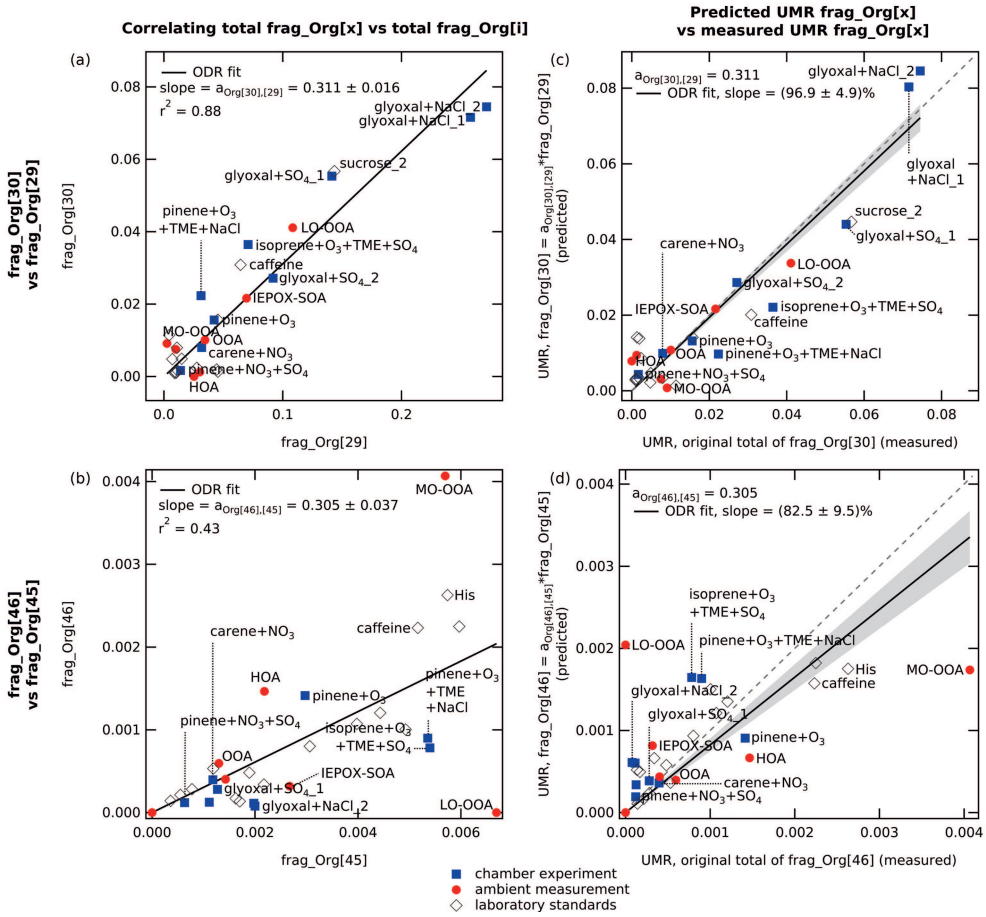


Figure 3.1: The left-hand panels (**a** and **b**) show the best ODR fits (set to zero intercept) which are found in the relationship between the signal contributions of (**a**) frag_Org[30] vs. frag_Org[29], and (**b**) frag_Org[46] vs. frag_Org[45]. The correlations of all mass pairs are summarized in Table S3 in the Supplement of Nursanto et al. (2025). The right-hand panels (**c** and **d**) show the predicted organic contributions (based on the new multipliers) at each m/Q versus the measured amount. Plot **(c)** shows the predicted UMR frag_Org[30] against the measured total Org fragments at m/Q 30, and plot **(s)** shows the predicted UMR frag_Org[46] against the measured total Org fragments at m/Q 46. The figure demonstrates that the predicted frag_Org[x] slightly underestimates (slope = 0.83) but approached the measured frag_Org[x].

Using these data, we determine the multipliers a used in a revised calculation of frag_Org[30] and frag_Org[46] (see Table 3.1, last three rows, and Table S1 in the Supplement of Nursanto et al. (2025)). The new multipliers are determined by performing orthogonal distance regression (ODR) constrained to a zero intercept of mass spectra in UMR. For HR-AMS spectra, the dataset is "degraded" from HR into UMR spectra by summing HR Org fragments to their respective nominal mass in each AMS spectrum. Note that for UMR-ACSM spectra, because we cannot separate species at the same nominal m/Q, we only use chamber experiments that are assumed nitrate-free or to contain negligible nitrate (no seed or precursor for inorganic and organic nitrate). Therefore, all signals at m/Q 30 and m/Q 46 are exclusively organic fragments. We perform ODR fits of frag_Org[30] and frag_Org[46] against a list of chemically related masses (frag_Org[i]). The slope of the ODR fits to determine the multiplier $a_{\mathrm{Org}[30],[i]}$ and $a_{\mathrm{Org}[46],[i]}$ are summarized in Table S3 in the Supplement of Nursanto et al. (2025), alongside the list of fragments of i that contribute to each nominal mass, in the footnote. It is found that frag_Org[30] is best correlated with frag_Org[29] (see Table S3 in the Supplement of Nursanto et al. (2025)), where $a_{\mathrm{Org}[30],[29]} = 0.311 \pm 0.016$ (mean $\pm$ uncertainty, $r^2 = 0.88$, see Fig. 3.1a). On the other hand, frag_Org[46] has the best correlation with frag_Org[45] (see Table S3 in the Supplement of Nursanto et al. (2025)), where $a_{\mathrm{Org}[46],[45]} = 0.305 \pm 0.037$ (mean $\pm$ uncertainty, $r^2 = 0.43$, see Fig. 3.1b). The final revised fragmentation table in CV-UMR-ToF-ACSM is summarized in the conclusions (see Table 3.4).

We apply these new multiplier values to the full dataset and compare the results with those from multipliers described in Allan et al. (2004), the Supplement of Fry et al. (2018), and the Supplement of Hu et al. (2017) (see in Table S4 in the Supplement of Nursanto et al. (2025)). The result suggests that the multiplier $a_{\mathrm{Org}[46],[45]}$ determined here gives the best predicted frag_Org[46] over multipliers from other studies (see Table S4 in the Supplement of Nursanto et al. (2025)). Meanwhile, the multiplier $a_{\mathrm{Org}[30],[29]}$ determined here performs similarly with the multipliers obtained from Hu et al. (2017) (SV and CV) for a dataset dominated by biogenic secondary organic aerosol (SOA). The plot of predicted UMR frag_Org[30] against the measured total Org fragments at m/Q 30 (see Fig. 3.1c) shows that the multiplier determined here is able to estimate on average 96.9 $\pm$ 4.9% of the measured frag_Org[30]. Meanwhile, the similar plot for frag_Org[46] against the measured total Org fragments at m/Q 46 (see Fig. 3.1d) shows that the multiplier determined here estimates on average 82.5 $\pm$ 9.5% of the measured frag_Org[46]. The low signal intensity of both m/Q 46 and m/Q 45 may cause this underestimation and suggests that frag_Org[46] and frag_Org[45] may have a more complicated relationship; their correlation may vary substantially depending on the aerosol mixture. Therefore, it may be appropriate to modify the entry for frag_NO_3[46] according to the type of aerosol mixture analyzed. On the other hand, for complex ambient mixtures, the ensemble composition may produce spectra that are more similar

to the average determined here. Analysis of CV-HR spectra from a variety of ambient samples would be required to determine the actual variation of organic contributions at m/Q 46.

3.3.2 Composition-specific fragmentation table

The multipliers determined in Section 3.3.1 are designated for typical ambient aerosol composition. In some cases, a composition-specific fragmentation table may be more appropriate to use. For instance, from a field study with biogenically-dominated composition, Hu et al. (2017) reported $a_{\mathrm{Org[30],[29]}} = 0.32$ and $a_{\mathrm{Org[46],[45]}} = 0.68$. By using selected chamber experiments in the same dataset, we can explore different multipliers that are compatible for different composition profiles. For chamber experiments that involves glyoxal (and its oligomers), we obtain $a_{\mathrm{Org[30],[29]}} = 0.291 \pm 0.022$ (mean $\pm$ uncertainty, $n = 4$, $r^2 = 0.90$) and $a_{\mathrm{Org[46],[45]}} = 0.082 \pm 0.036$ (mean $\pm$ standard deviation, $n = 4$, $r^2 = 0.35$). For chamber experiments that involve only terpenes (e.g., isoprene, α-pinene), we obtain $a_{\mathrm{Org[30],[29]}} = 0.476 \pm 0.067$ (mean $\pm$ uncertainty, $n = 5$, $r^2 = 0.82$) and $a_{\mathrm{Org[46],[45]}} = 0.204 \pm 0.055$ (mean $\pm$ uncertainty, $n = 5$, $r^2 = 0.33$) which can be applied for chamber experiments with terpene as precursor. The ODR fit plots are given in Fig. S1 in the Supplement of Nursanto et al. (2025). The multipliers to revise the fragmentation table in CV-UMR-ToF-ACSM for specific aerosol composition subsets is summarized in the conclusions (see Table 3.4).

3.4 Determination of NO_x^+ ratios for the CV-UMR-ToF-ACSM

3.4.1 NO_x^+ ratio of pure pAmN

To quantify the inorganic NO_x^+ ratio typical value and variability produced by the CV, we use repeated measurements from regular pAmN calibration from the two ACSM instruments described in Section 3.2. The R_{pAmN} of ACSM-UU is found to be 0.0237 ± 0.0009 (mean $\pm$ uncertainty, $n = 5$), and R_{pAmN} of ACSM-RUG is 0.0115 ± 0.0002 (mean $\pm$ uncertainty, $n = 3$). The values are similar but lower than other studies where R_{pAmN} with CV was found to be 0.04–0.07 (Hu et al., 2016a), and all are $\sim$10 times lower than the typical R_{pAmN} measured with the SV, i.e., 0.3–0.7 (Day et al., 2022b). We found that R_{pAmN} values are very consistent for each instrument over time. A summary of R_{pAmN} values and regression fit parameters from each measurement can be found in Table S5 in the Supplement of Nursanto et al. (2025).

Hu et al. (2017) found that the NO_x^+ ratio is affected by the aerodynamic lens alignment. The influence is greater in the CV since the vaporizer opening diameter is $\sim$2.5 mm (Supplement of Hu et al. (2018a)), smaller than that of SV, which is $\sim$3.8 mm (Drewnick

et al., 2005). For optimum particle detection, the aerodynamic lens must point the particle beam at the center of the vaporizer. Directed into the center, the particles enter the CV cavity and experience augmented thermal decomposition, at which the NO_2^+ signal intensity is at its minimum, while the NO^+ signal intensity is highest. The NO_2^+ signal intensity increases as the particle beam moves closer to the edge of the vaporizer, where the thermal decomposition is not as extensive as in the center, resembling how the SV works. Thus, it is important to consider performing lens alignment to obtain the correct result for the NO_x^+ ratio method. Monitoring the behavior of m/Q 30 and m/Q 46 during pAmN calibration is a good way to determine whether the aerodynamic lens is aligned well. Combining the result of this study and the R_{pAmN} range in Hu et al. (2017), a value of R_{pAmN} in the range of 0.01-0.07 can be used as reference to indicate properly aligned lens. Plotting the profile of the NO_x^+ ratio with movement in both the vertical and horizontal directions obtained during the alignment is the best diagnostic.

3.4.2 NO_x^+ ratio of pure pON

To obtain a NO_x^+ ratio for pON, one would ideally measure pure atmospherically relevant ON, prepared through synthesis or in a chamber experiment. Often, such standards are not available; therefore, experimental R_{pON} cannot be easily determined for each instrument. To overcome this challenge, Day et al. (2022a) used the strategy of a "ratio-of-ratios" ($RoR = R_{pAmN}/R_{pON}$) which can be used to calculate R_{pON} for any arbitrary instrument from its routinely measured R_{pAmN}, and an average value for the RoR measured across many instruments under varying conditions. Day et al. (2022a) found that based on the relationship between R_{pAmN} and R_{pON} over a large range of measurement conditions, SV produces RoR of 2.75 $\pm$ 0.70 (mean $\pm$ 25% uncertainty).

There have not yet been enough studies that determined R_{pON} values in CV-based instruments in order to determine a robust RoR estimate for CV instruments. In the work of Hu et al. (2017), a chamber experiment producing pure pON yielded R_{pON} = 0.0045; with comparison to R_{pAmN} = 0.06 of their instrument, the value RoR = 13.3 is obtained. With R_{pAmN} being 0.01 in CV as found in this study, using this RoR of 13.3, R_{pON} would be 0.0008 (approaching zero).

Similar to the approach of Kiendler-Scharr et al. (2016) that used the minimum measured value of NO_x^+ ratio to set a fixed R_{pON} value, to estimate R_{pON}, we use the lowest measured NO_x^+ ratio from a chamber experiment in which we expected to produce pON, with no inorganic nitrate present. The selected experiment used glyoxal as SOA precursor, NO_2 and O_3 to produce nitrate radical ($NO_3^\bullet$) as the major oxidant, and sodium chloride (NaCl) seed to form SOA containing organic nitrates at 90% relative humidity. This experiment was conducted in the AIDA chamber at IMK KIT, Germany

as part of CAINA project. For the spectrum analysis, we use the fragmentation table specific for glyoxal-related chamber experiment, as described in Section 3.3.2.

While this experiment should produce pure organic nitrate aerosol, during pON formation, we observe an increase in NH_4 which could happen for two reasons. First, ammonium nitrate impurities can be formed from reactions or chamber wall repartitioning. Second, particulate water can be incorrectly assigned as NH_4 through fragmentation table correction at the m/Q 16 and m/Q 17 (see complete fragmentation table in Allan et al. (2004)). Both can result in a higher NO_x^+ ratio than we would have if the total nitrate were purely pON. Therefore, we derive two bounding R_{pON} values from the glyoxal chamber experiment. First, we determine the R_{pON} from the experiment by assuming pure pON formation to obtain an upper limit. Second, to obtain the lower limit of R_{pON}, we assume all observed NH_4 increase is NH_4NO_3 aerosol and subtract this equivalent amount of inorganic nitrate, with the inorganic NO_x^+ ratio, from the total NO_3, in order to obtain a lower limit of pON time series and calculate the R_{pON}. This strategy has been described as the "excess NH_4" method in Takeuchi and Ng (2019). By rearranging the Eq. 3.2, we can obtain R_{pON} using f_{pON}, R_{pAmN}, and R_{obs} for the lower limit experiment (see details in Section S3 in the Supplement of Nursanto et al. (2025)).

The upper limit experiment gives R_{pON} = 0.0035 (see Fig. 3.2a). If we compare to R_{pAmN} = 0.0115 $\pm$ 0.0002 (measured separately with pure AmN), R_{pON} = 0.0035 obtained from the upper limit experiment gives RoR = 3.29 (see Fig. 3.2a). This value is higher than RoR for SV-AMS but lower than RoR obtained from Hu et al. (2017).

On the other hand, the lower limit experiment gives R_{pON} = -0.0033 (see Fig. 3.2b). A negative (or below zero) R_{pON} value is not chemically possible for the ratio. This value indicates an overcorrection, or that R_{pON} is varying around the zero value (small positive and negative) when the air mixture is strictly inorganic nitrate free. Thus, for calculation purposes, we use R_{pON} = 0.0001 to represent the smallest possible NO_x^+ ratio for CV-ACSM measurements.

As the RoR from the experiments (including Hu et al. (2017), RoR = 13.3) are very different, we set the upper limit of R_{pON} to be R_{pON} obtained using RoR = 3.29, and the lower limit to be R_{pON} = 0.0001 in CV. The calculated R_{pON} for two CV-ToF-ACSM deployed in this study are summarized in Table 3.2. These limits are used to determine the uncertainty of the f_{pON} calculation. Since we see a tendency for the m/Q 46 signal intensity (and thus NO_2^+) to be produced in the vaporizer in relatively small quantities compared to NO^+, the tendency of R_{pON}, therefore, is also to approach zero (non-normal distribution). With only limited information about R_{pON} in CV unlike SV, we use the geometric mean instead of arithmetic mean to establish the expected central value of R_{pON}. We note that it is common to use geometric means to eastimate averages of ratios.

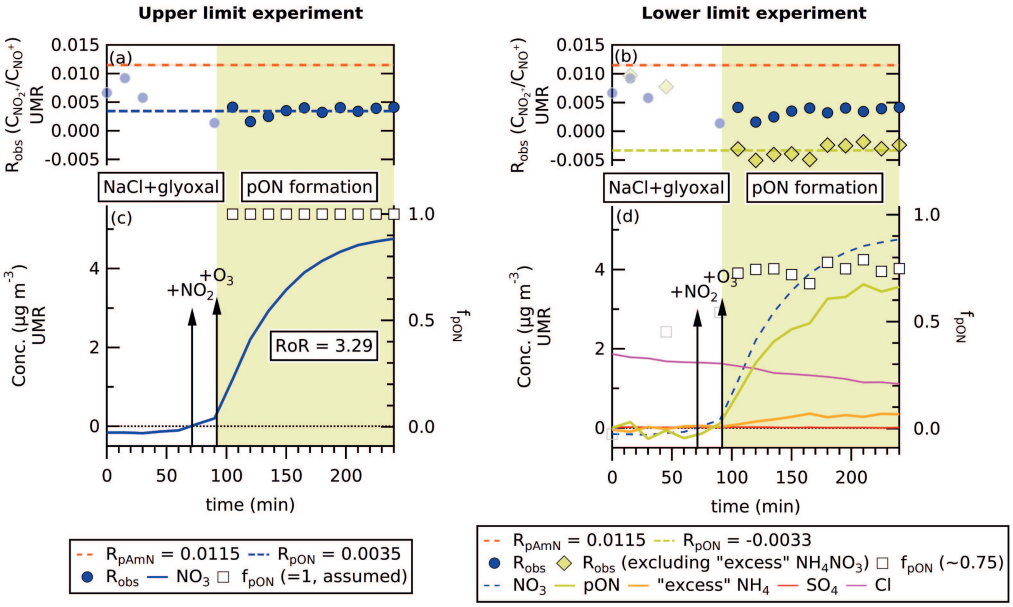


Figure 3.2: The time series of **(a, b)** R_{obs}, **(c, d)** ACSM species concentration (in $\mu g \cdot m^{-3}$, left bottom axis), and f_{pON} (right bottom axis) of glyoxal+$NO_3^{\bullet}$ chamber experiment at 15 min time averaging. The UMR fragmentation table specific for glyoxal is used to obtain C_{NO^+} and $C_{NO_2^+}$. Panels **(c)** and **(d)** shows the progression of NO_3 concentration, compared to panels **(a)** and **(b)** for the NO_x^+ ratio during the formation of pON. By averaging R_{obs} after pON formation started, the left-hand panel shows that R_{pON} = 0.0035 is obtained when assuming f_{pON} = 1. When possible inorganic impurity is removed by assuming "excess" NH_4 species are NH_4NO_3, the average f_{pON} is found to be 0.75. The excess NH_4 concentration is obtained by subtracting total NH_4 concentration by the average NH_4 concentration before the addition of NO_2 and O_3 (to exclude any possible NH_4Cl contribution). By calculating R_{pON} using the obtained f_{pON} from "excess NH_4" method, R_{pAmN} and R_{obs}, the value R_{pON} = -0.0033 is obtained, suggesting an overcorrection (see text). The value R_{pON} = 0.0035 from the lower limit experiment and R_{pAmN} = 0.0115 $\pm$ 0.0002 (mean $\pm$ uncertainty) give a ratio of ratios (RoR = R_{pAmN}/R_{pON}) of 3.29.

Since the R_{pAmN} values are quite different for the two ACSMs used in this study (as we see in Table 3.2), the upper limit R_{pON} are also different by almost a factor of 2. However, since the lower limit of R_{pON} approaches zero, the geometric means of the upper and lower limits for the two instruments differ by only 25 %. While calibrating every instrument with a pure organic nitrate aerosol standard would be a preferable way to establish R_{pON}, we recognize the unlikeliness of that for all monitoring ACSMs. Therefore, we recommend this RoR-based approach. As will be shown in the following section, despite the uncertainties outlined here based on potential impurities in our

"pure pON" chamber experiment, the nitrate splitting performs encouragingly well, with both ACSMs.

Table 3.2: Summary of measured R_{pAmN} (including uncertainties) and calculated R_{pON} (upper and lower limits as determined from pON in glyoxal+$NO_3^\bullet$ chamber experiment). The geometric mean is considered as central value since R_{pON} is likely approaching zero. Values are for ACSM-UU (employed for ambient measurements in Cabauw) and the ACSM-RUG (employed for AIDA chamber experiments).

Instrument	ACSM-UU		ACSM-RUG	
Measurements	Cabauw ambient air		chamber experiment	
Value	R_{pAmN}	R_{pON}	R_{pAmN}	R_{pON}
Upper limit		0.0072[a]		0.0035[b]
Geometric mean	0.0237 ± 0.0009	0.0008[c]	0.0115 ± 0.0002	0.0006[c]
Lower limit		0.0001[d]		0.0001[d]

[a] Calculated using RoR = 3.29. The RoR is obtained using R_{pON} from the upper limit experiment of glyoxal+$NO_3^\bullet$ and measured R_{pAmN}, using ACSM-RUG (see Fig. 3.2).

[b] Experimental NO_x^+ ratio value from the lower limit experiment of glyoxal+$NO_3^\bullet$ using ACSM-RUG (see Fig. 3.2a).

[c] Geometric mean of the upper and lower limits R_{pON}.

[d] Set as the lowest possible NO_x^+ ratio in CV-based instruments, approaching zero.

3.5 Development of the NO_x^+ ratio method for CV-UMR-ToF-ACSM

3.5.1 Challenges in the NO_x^+ ratio method application to the CV-UMR-ToF-ACSM dataset

Applying the NO_x^+ ratio method to separate pAmN and pON in CV-UMR-ToF-ACSM datasets is a greater challenge than with SV, due primarily to the higher detection limit of pNO_3. The detection limit of pNO_3 in CV-UMR-ToF-ACSM is 0.01–0.08 $\mu g \cdot m^{-3}$ (from this work and Zheng et al. (2020) converted), which is around 10–100 times higher compared to those in SV-cToF-AMS ($\sim$0.6 $ng \cdot m^{-3}$ from Drewnick et al. (2009)) and SV-HR-ToF-AMS (0.1–4.0 $ng \cdot m^{-3}$ from DeCarlo et al. (2006)), all converted to 10 min time resolution.

The poor detection limit for NO_x^+ ratios in CV-ToF-ACSM results from the low signal for m/Q 46 relative to m/Q 30 that are used to calculate frag_NO_3[30] (C_{NO^+}) and frag_NO_3[46] ($C_{NO_2^+}$). For instance, using ACSM-UU, the detection limit of NO_2^+ is comparable to the detection limit of NO^+ at pNO_3 concentration near the detection limit of pNO_3 ($C_{DL,NO_2^+} = 0.044$ $\mu g \cdot m^{-3}$; $C_{DL,NO^+} = 0.066$ $\mu g \cdot m^{-3}$; for $C_{DL,pNO_3} = 0.075$ $\mu g \cdot m^{-3}$; all in 10 min time resolution). However, the magnitude of observed NO_2^+ from

ambient measurements is 25–500 times lower than NO^+ in CV-ToF-ACSM. This means the NO_2^+ signal intensity is regularly close to the detection limit, particularly when the total pNO_3 concentration is low. This behavior also leads to noisy R_{obs}, due to a computation of very low or negative NO_2^+ signals, poor baseline, or both.

3.5.2 Data pre-treatment: Time averaging and data filtering

To determine which data points are reliable for R_{obs} calculation in the dataset, we could discard observed NO_2^+ signal intensities that are below the detection limit. However, this would result in removing nearly all the data, including data that, while low and noisy, can still provide quantitative information with adequate averaging. Therefore, we use observed NO^+ signals as the filtering parameter. The NO^+ signal accounts for ~95% of the total concentration of NO_3 species measured by ToF-ACSM (no RIE applied) and thus is a good indicator of when both NO^+ and NO_2^+ signals are too uncertain.

Equation 3.4 describes the NO^+ signal limit ($C_{NO^+,lim}$) which assures reliable separation of f_{pON} and f_{pAmN} calculated using the detection limit of NO_2^+ (C_{DL,NO_2^+}) and R_{pAmN} as filter NO_x^+ ratio. We choose the larger R_{pAmN} value, which is a less strict limit relative to R_{pON} value, but still keeps any data with sufficiently good signal-to-noise ratio. The measured data points with observed NO^+ signal intensity below these criteria are replaced with "nan" (not a number).

$$C_{NO^+,\,lim} = \frac{C_{DL,NO_2^+}}{R_{pAmN}} \tag{3.4}$$

On this basis, we recommend data pre-treatments by time averaging and data filtering using observed NO^+ signal contribution as parameter. Time averaging over longer time periods allows for the reduction of the electronic noise coming from the instrument response and low counting statistics associated with sampling ambient air. Meanwhile, the data filtering serves to determine the minimum pNO_3 concentration at which reliable R_{obs} can be obtained to calculate f_{pON} and f_{pAmN}.

The values of C_{DL,NO_2^+} and $C_{NO^+,lim}$ in different time averaging are evaluated in Table 3.3 for the CV-ToF-ACSM deployed for ambient measurements in Cabauw, the Netherlands. The signal limit is lower as the time resolution increases due to the improvement of detection limit with better statistics. For measurements in this study, the minimum reliable C_{NO^+} for 10 min, 30 min, 60 min, and 120 min time resolutions are 1.88, 1.08, 0.77, and 0.54 $\mu g \cdot m^{-3}$, respectively.

With these $C_{NO^+,lim}$, we performed data filtering to the ambient measurement time series from Cabauw in different averaging of the time series. The time averaging (generated by Tofware v3.3) is applied first before the data filtering to maximize retained data in the concentration average.

Table 3.3: Detection limits of NO_2^+ and signal limits for NO^+ across different time averaging with R_{pAmN} as filter NO_x^+ ratio for the CV-UMR-ToF-ACSM deployed for ambient measurements in the rural site of Cabauw, the Netherlands (ACSM-UU).

Signal intensity ($\mu g \cdot m^{-3}$)	10 min	30 min	60 min	120 min
C_{DL,NO_2^+}	0.044	0.026	0.018	0.013
$C_{NO^+,lim}$ (filter: R_{pAmN} = 0.0237)	1.88	1.08	0.77	0.54

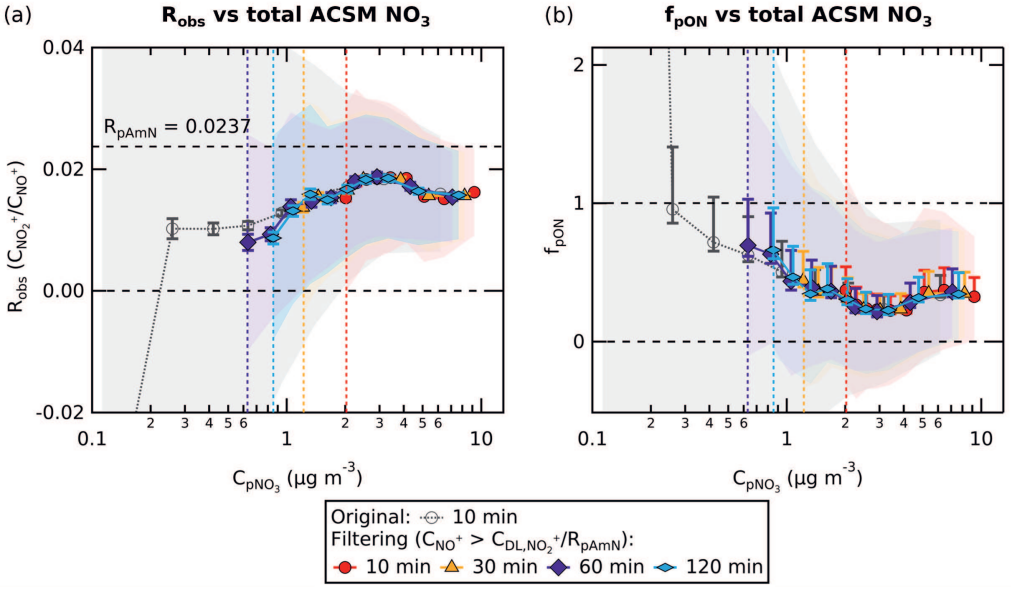


Figure 3.3: Chemical coordinate plots **(a)** between R_{obs} against C_{pNO_3} in Cabauw (net 205 d of data), and **(b)** between the f_{pON} calculated using geometric mean of R_{pON} (R_{pON} = 0.0008) against C_{pNO_3}. The revised fragmentation table for typical ambient dataset is used to obtain C_{NO^+} and $C_{NO_2^+}$. The line and marker traces represent the quantile average. The colored shading represents the standard deviation of each quantile while the whisker is the standard error. The standard deviation and standard error both include the uncertainty of ion counting statistics from measurements and uncertainty from ODR fit slope of fragmentation table correction. For f_{pON} (plot **b**), the standard deviation and standard error also include the uncertainty from lower and upper limit of R_{pON} (R_{pON} = 0.0001; R_{pON} = 0.0072). All analyses were done using the 10 min, 30 min, 60 min, and 120 min averaging of the time series, with data filtering. The original 10 min data without pre-treatment is also included as comparison. The combination of data filtering and time averaging reduces the noise compared to original data and improves the minimum concentration reliable for apportionment calculation (pNO_3 concentration limit for each time average, as indicated with vertical dashed lines).

Chemical coordinate plots of R_{obs} and f_{pON} against the total concentration of particulate nitrate (C_{pNO_3}) are shown in Fig. 3.3. These plots show the quantile average of the

output variable on the y axis (i.e., R_{obs} or f_{pON}) as a function of concentration bins in the x axis (C_{pNO_3}). Figure 3.3a and b show that data filtering removes extreme R_{obs} and f_{pON} values near the detection limit level. The fact that the chemical coordinate trends are consistent across different averaging times indicates that filtering to remove noisy data will not bias the interpretation of the ensemble dataset. The value of treating the data as a chemical coordinate plot is to allow for a robust characterization of the average trend, even using a method with substantial uncertainties. Importantly, the standard errors represent how well the averages are known. Their small uncertainty ranges support that the characterized trend is robust.

The combination of data filtering and time averaging shows different concentration cut-offs for calculation of the NO_x^+ ratio. The concentration cut-off is lower for longer averaging times due to the improvement of C_{DL,NO_2^+}. For measurements in this study, the C_{pNO_3} cut-offs for 10 min, 30 min, 60 min, and 120 min time averaging are 2.0, 1.2, 0.9, and 0.6 $\mu g \cdot m^{-3}$, respectively. Because there is a trade-off between time resolution and the concentration cut-off, for a given dataset, the timescale of typical variations should be assessed in order to determine the appropriate averaging time.

3.5.3 Propagation of uncertainty

We propagated uncertainties from the variables in f_{pON} using simplified propagation of uncertainties as standard error (Day et al. (2023); see Section S4 in the Supplement of Nursanto et al. (2025) for details). The uncertainty of the final function (s_f) is calculated using the standard error (s_{x_i}) and partial derivative of the function ($\frac{\partial f}{\partial x_i}$) of each measurand ($x_i$) using Eq. 3.5.

$$s_{f(x_i,x_{i+1},...)} = \sqrt{\sum_{i=1}^{N} \left(\frac{\partial f(x_i, x_{i+1}, ...)}{\partial x_i} \right)^2 \cdot s_{x_i}^2} \tag{3.5}$$

The uncertainty of f_{pON} arises from three terms: R_{obs}, R_{pAmN}, and R_{pON}. For R_{obs}, the uncertainty is further composed of six components that make up NO^+ and NO_2^+ signals (the uncertainties of m/Q 29, m/Q 30, m/Q 45, and m/Q 46 related to precision uncertainty from electronic noise and ion counting statistics, and the uncertainties of the fragmentation table multipliers, represented by the uncertainty of ODR fit slope). For R_{pAmN}, we propagate the uncertainty of the mean NO_x^+ ratio from repeated NH_4NO_3 measurements using ODR fit to consider the instrument stability in acquiring the NO_x^+ ratio over time. For R_{pON}, the uncertainty is set to zero. Instead, the lower and upper limits of R_{pON} (see Table 3.2) serve to give a range of final propagated uncertainty, which includes R_{obs}, R_{pAmN}, and R_{pON}.

Fig. 3.4a shows that low pNO_3 concentrations produce larger uncertainties in f_{pON} ($s_{f_{pON}}$) compared to higher concentrations. If we compare the analysis with and without

data filtering, we observe that filtering targets data points with high absolute $s_{f_{pON}}$ (above ± 0.5). We avoid removing many data points in the low concentration range by performing time averaging, where the average uncertainty decreases by $\sim \sqrt{N}$ for each N-fold of averaging from 10 min. Meanwhile, the uncertainties from R_{pAmN} and R_{pON} (RoR) remain unaffected by time averaging because the values remain constant in the time series.

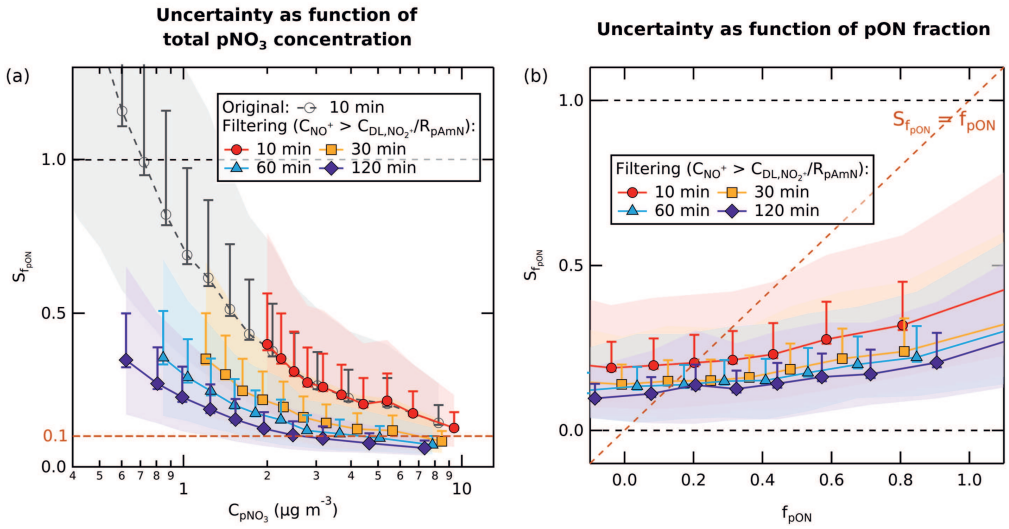


Figure 3.4: The chemical coordinate plot (quantile average) between **(a)** $s_{f_{pON}}$ and C_{pNO_3} (logarithmic scale), and **(b)** $s_{f_{pON}}$ and f_{pON} (linear scale), with R_{pAmN} = 0.0237 as filter NO_x^+ ratio at various averaging of the time series. The line and marker trace represent the average uncertainty produced from the geometric mean of f_{pON}. The uncertainty consists of uncertainties of ion counting statistics from measurements, uncertainty from ODR fit slope of fragmentation table correction, and uncertainty of R_{pAmN}. The colored shading represents the standard deviation of each quantile, while the whisker is the standard error. The shading and whisker both include the uncertainty of R_{pON} coming from the lower and upper limit of R_{pON} (R_{pON} = 0.0001 and R_{pON} = 0.0072), as well as the uncertainty of the average quantile. Uncertainties of $f_{pON} < 0.1$ (absolute value) are reached at pNO_3 concentration $> 10\ \mu g \cdot m^{-3}$ for 10 min time averaging, while at 60 min, it is reached already at $\sim 4\ \mu g \cdot m^{-3}$. In terms of fraction, uncertainties of f_{pON} below the calculated f_{pON} ($s_{f_{pON}} < f_{pON}$) is reached at f_{pON} $\sim$0.2 for 10 min averaging, while at 60 min, it is reached at f_{pON} $\sim$0.17.

Several studies reported f_{pON} lower than 20 %, which occur mainly in urban areas and during a colder period. Yu et al. (2024) observed a lower range of annual average of urban f_{pON} in China to be $\sim$17 %, while Mohr et al. (2012) and Pandolfi et al. (2014) reported $\sim$13 % fraction in Barcelona, Spain, and Xu et al. (2021) reported 9.8 % fraction in wintertime Beijing, China. If we use the lower range of f_{pON} of $\sim$ 10 % as reference for the minimum uncertainty needed to report reliable f_{pON}, we can observe that the

lowest pNO_3 where we obtain below 0.1 absolute uncertainty in f_{pON} decreases along with time averaging as well. Uncertainties below ± 0.1 can only be reached at pNO_3 concentrations higher than 10, 7, 4, 2 $\mu g \cdot m^{-3}$ at 10, 30, 60, and 120 min time averaging, respectively.

Fig. 3.4b shows the relationship between the absolute $s_{f_{pON}}$ and f_{pON}. The limit at which the absolute value of $s_{f_{pON}}$ is below or equal to f_{pON} (minimum uncertainty) is found to be 20 %, 15 %, 14 %, 12 % at 10, 30, 60, and 120 min time averaging, respectively. This result suggests that the NO_x^+ ratio method in CV-UMR-ToF-ACSM is more reliable to analyze nitrate pollution episodes or chamber experiments and not for low background pNO_3 concentrations. By combining both the concentration limit and the fraction limit, we suggest that in the region where pNO_3 concentration is $< 10\ \mu g \cdot m^{-3}$ and/or $f_{pON} <$ 12 %, the method requires a longer time average to calculate f_{pON} to achieve minimum uncertainty.

3.6 Case studies demonstrating the NO_x^+ ratio method for CV-ToF-ACSM

3.6.1 Ambient measurements at a rural site

In order to demonstrate the efficacy of this method, we investigate the trend of f_{pON} and f_{pAmN} in the dataset observed at Cabauw. The ambient concentration time series of pAmN and pON (using $R_{pAmN} = 0.0237$ and $R_{pON} = 0.0008$) are compared with the ACSM-measured Org and NH4 fractions, shown in Fig. 3.5. The time series are averaged to 60 min and filtered using $R_{pAmN} = 0.0237$ (values of $C_{NO^+} < C_{DL,NO_2^+}/R_{pAmN}$ are discarded). We observe that f_{pON} increases with increasing fraction of organic aerosol concentration in total ACSM $PM_{2.5}$ ($C_{OA}/C_{PM_{2.5}}$, from 48 % to 64 %), whereas the f_{pAmN} increases with increasing fraction of particulate ammonium concentration in total ACSM $PM_{2.5}$ ($C_{pNH_4}/C_{PM_{2.5}}$, from 8 % to 15 %). This shows that the organic nitrate fraction is correlated with availability of organics (particularly at high organic fraction), while the inorganic fraction increases with available NH_4 (particularly at low ammonium fraction).

We also investigate specific nitrate episodes to show the composition of pON and pAmN in ambient pollution events. The time series of the NO_x^+ ratios, ACSM species concentrations (OA, pNH_4, pNO_3), and pAmN and pON concentrations are shown in Fig. 3.6. Four nitrate episodes from spring (15 May 2023), summer (23 June 2023), autumn (5–6 September 2023), and winter (11 January 2024) are shown. The uncertainty of the concentration is obtained by combining the uncertainty from the nitrate fraction (f_{pON} or f_{pAmN}), the total ACSM NO_3, and the R_{pON} value range (see Eqs. S14 and S15 in the Supplement of Nursanto et al. (2025)). Note that the reported uncertainties

are only related to precision uncertainty and not to concentration quantification (e.g., ionization efficiency) like the one described by Bahreini et al. (2009) (see details in Section S4 in the Supplement of Nursanto et al. (2025)). We observe that the adapted NO_x^+ ratio method is able to separate contributions of pON and pAmN to the total pNO_3 concentration. In Fig. 3.6i,ii, and iv, we can see that the time series of pON tracks with total OA, while pAmN tracks with pNH_4 in the rural site. In Fig. 3.6iii, no significant trend is observed for pON due to lower mass loading of pNO_3.

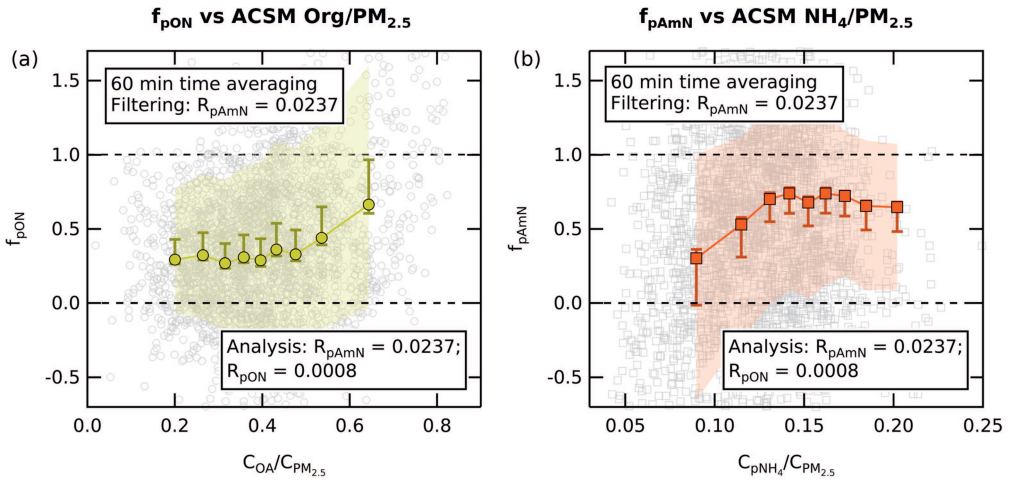


Figure 3.5: (a) The chemical coordinate plot (quantile average) of f_{pON} against $C_{OA}/C_{PM_{2.5}}$ shows an average increase in f_{pON} as OA fraction increases from 48 % to 64 %, where the f_{pON} varies from 33 % to 66 %. **(b)** The chemical coordinate plot (quantile average) of f_{pAmN} against $C_{pNH_4}/C_{PM_{2.5}}$ shows an average increase in f_{pAmN} as pNH_4 fraction increases from 8 % to 15 %, where f_{pAmN} varies from 30 % to 74 %. Note that all quantile averages were calculated using the 60 min averaging of the time series. The colored shading is the standard deviation of each quantile average, while the whiskers represent the standard error. They include the uncertainties of ion counting statistics from measurements, uncertainty from ODR fit slope of fragmentation table correction, and R_{pON} range value.

Unless there are co-located ambient measurements of UMR and HR instruments, the reported concentration of NO_3 in pON depends on the value of R_{pON} and multipliers used to calculate NO^+ and NO_2^+ signal contribution in the fragmentation table. The sensitivity of these variables needs to be assessed to understand which parameter is the most critical in the separation of the inorganic and organic nitrate signal from ACSM.

In Fig. 3.7, we show the sensitivity analysis of R_{pON}, $a_{Org[30],[29]}$, and $a_{Org[46],[45]}$. We varied R_{pON} from zero to R_{pON} = 0.0072 (calculated using RoR = 3.29). Figure 3.7a suggests that for $R_{pON} \leq 10^{-3}$ the reported pON concentrations are not significantly

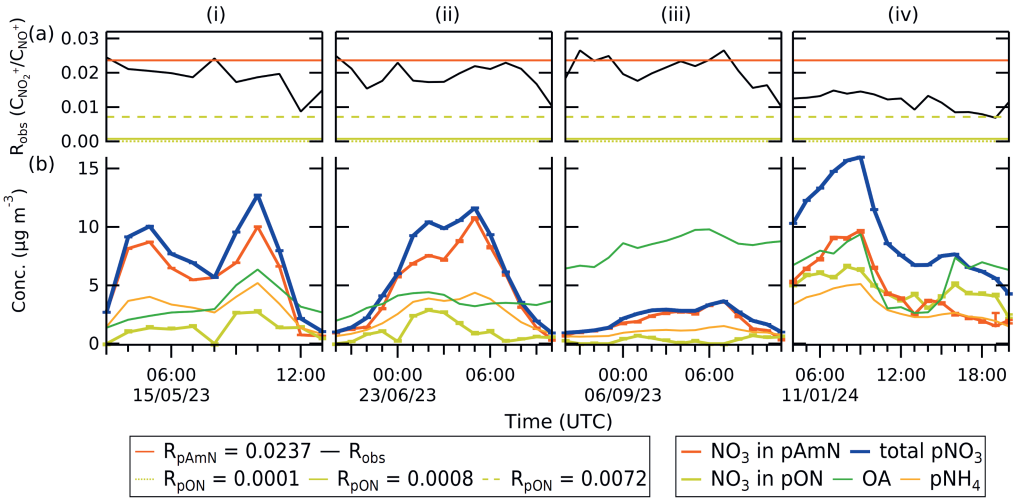


Figure 3.6: The time series for select periods of **(a)** R_{obs}, with horizontal lines indicating the values for R_{pAmN} and R_{pON}, and **(b)** mass concentration of ACSM-measured total OA, pNH_4, and pNO_3, as well as pAmN and in pON. The separation of pAmN and pON is calculated using $R_{pAmN} = 0.0237$ and $R_{pON} = 0.0008$. The whiskers represent the uncertainty from nitrate fraction (f_{pON} or f_{pAmN}), precision uncertainty of total ACSM NO_3 from Tofware v3.3, and the R_{pON} value range. The time series **(i)**, **(ii)**, **(iii)**, **(iv)** represents representative composition in spring, summer, autumn, and winter, all in 60 min time averaging.

different and therefore confirm the lower limit of R_{pON} approaching zero, as established in Table 3.2. The value of R_{pON} calculated using RoR (in this case $R_{pON} = 0.0072$) shows relatively higher pON concentration, which is consistent with its use as the upper limit of R_{pON}.

We also varied $a_{Org[30],[29]}$ and $a_{Org[46],[45]}$ using the values listed in Table S4 and Fig. S1c,d in the Supplement of Nursanto et al. (2025). Fig. 3.7b shows that the calculated pON concentration is sensitive to $a_{Org[46],[45]}$, which is not the case for $a_{Org[30],[29]}$. It further demonstrates that the limitation of this adapted NO_x^+ ratio method is its sensitivity towards $a_{Org[46],[45]}$ to obtain the NO_2^+ signal contribution. Chemically, this suggests that the organic contribution in m/Q 46 can vary and comprises a substantial portion of the total m/Q 46 signal. Therefore, an average correction for m/Q 46 may result in a high uncertainty of calculated f_{pON} using the NO_x^+ ratio method. This was considered in the propagation of uncertainty, where we take into account the changing $a_{Org[46],[45]}$ in the reported f_{pON}, therefore representing a range of the observed organic nitrate contribution.

3.6.2 pAmN and pON formation in chamber experiment

We investigated the pAmN and pON formation in a chamber experiment using limonene precursor, $NO_3^{\bullet}$ oxidant, and with NH_4NO_3 seed aerosol. The experiment was carried out in the AIDA chamber. Alongside CV-UMR-ToF-ACSM (ACSM-RUG), an SV-HR-ToF-AMS managed by IMK KIT was also deployed.

The ACSM data are analyzed using the revised fragmentation table specific for terpene chamber experiments (see Section 3.3.2), while the AMS data are analyzed using Squirrel 1.66E and PIKA 1.26E with the default ion list. Although the time resolution is 2 min,

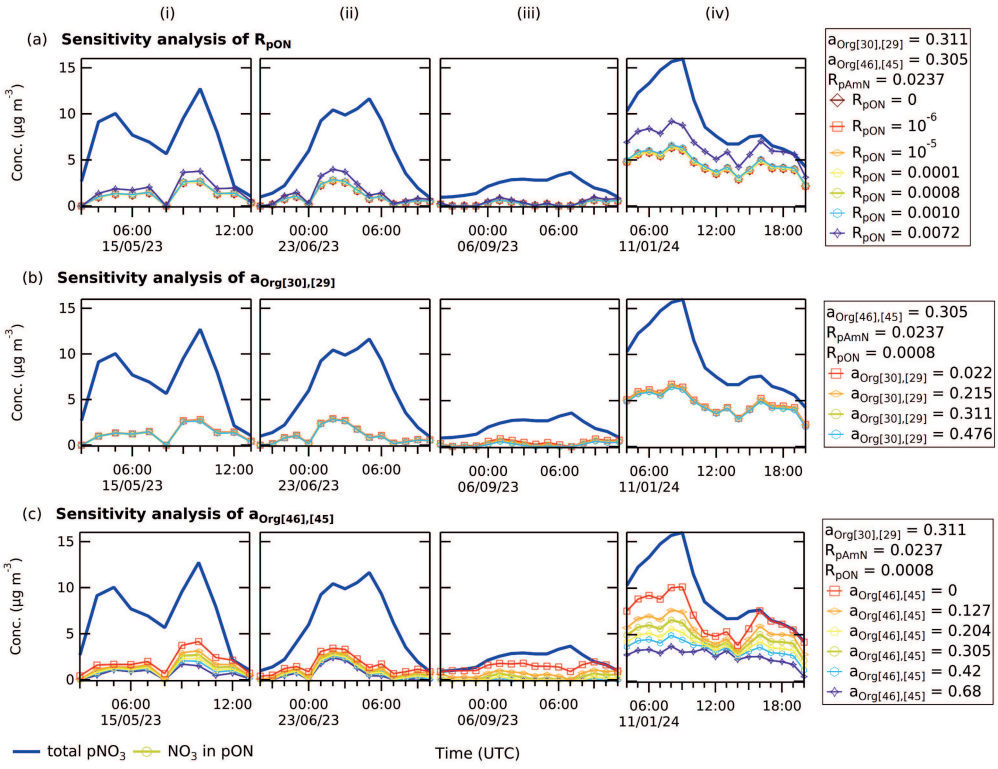


Figure 3.7: Sensitivity analysis of **(a)** R_{pON}, **(b)** $a_{Org[30],[29]}$, and **(c)** $a_{Org[46],[45]}$ to the pON concentration (NO_3 in pON) calculated using adapted NO_x^+ ratio method. The time series in each case is an ambient pollution episode in Cabauw, the Netherlands, during spring, summer, autumn, and winter period **(i-iv)**. The results show that **(a)** $R_{pON} \leq 10^{-3}$ does not show significant differences in reported pON concentration, and (b) the reported pON concentration is not sensitive to the change of $a_{Org[30],[29]}$. In contrast, the results **(c)** show a significant change in reported pON concentration when $a_{Org[46],[45]}$ is varied, showing that this correction is the primary limitation of the NO_x^+ ratio method in CV-ACSM, as it can be highly dependent on the calculation of NO_2^+ signal contributions to m/Q 46.

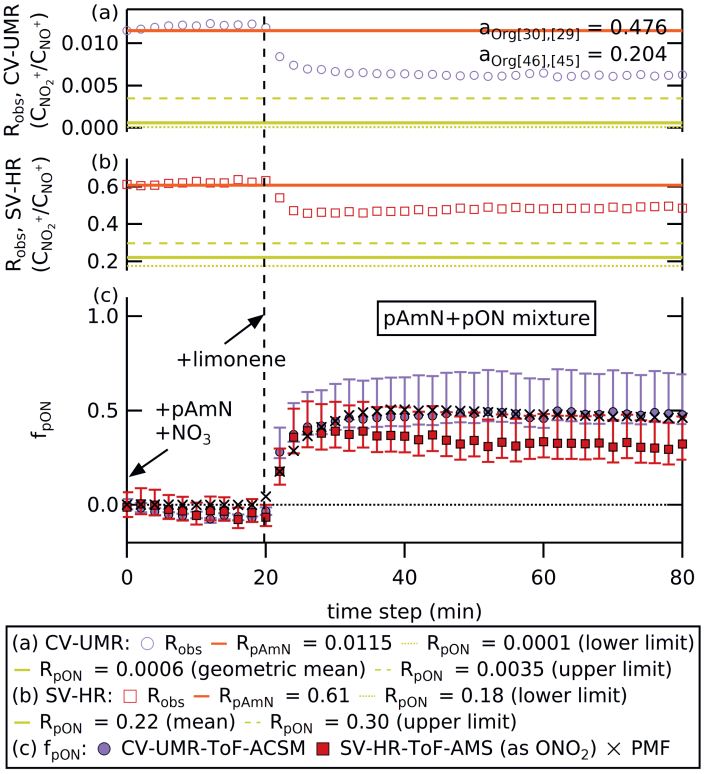


Figure 3.8: (a,b) The time series with 2 min time averaging of R_{obs}, R_{pAmN}, and R_{pON} measured by CV-UMR-ToF-ACSM (top) and SV-HR-ToF-AMS (middle). The fragmentation table specific for terpene is used to obtain the C_{NO^+} and $C_{NO_2^+}$ of the chamber experiment. **(c)** The time series with 2 min time averaging of f_{pON} from NO_x^+ ratio method applied to SV-HR-ToF-AMS and CV-UMR-ToF-ACSM, as well as the PMF method applied to CV-UMR-ToF-ACSM. The markers represent geometric mean for NO_x^+ ratio method applied to CV-UMR-ToF-ACSM (circle), mean for NO_x^+ ratio method of SV-HR-ToF-AMS (square) and for the PMF method of CV-UMR-ToF-ACSM (cross). The whiskers represent the uncertainties from the value range of R_{pON} combined with the uncertainties from electronic noise, ion counting statistics, fragmentation table (for UMR), and R_{pAmN}. The uncertainty from the PMF analysis is not shown for simplicity.

time averaging and data filtering are not necessary since the experiment involves high concentrations. The lower limit, geometric mean, and upper limit of R_{pON} (R_{pON} = 0.0001; 0.0006; 0.0035, respectively) are employed to estimate the uncertainty of f_{pON}, alongside R_{pAmN} = 0.0115 (see Table 3.2). For the AMS instrument, the measurements of pure pAmN give R_{pAmN} = 0.61 ± 0.05 and the R_{pON} value is calculated using RoR =

2.75 ± 0.70 (Day et al., 2022a), which gives R_{pON} = 0.18, 0.22, and 0.30 as lower limit, mean, and upper limit, respectively.

We also performed PMF analysis using the ACSM data including OA, NO_x^+, and NH_x^+ ions, which has been similarly done in other studies (e.g., Day et al. (2022a), and references therein). The 2 min average matrices of UMR organic fragment mass spectra with a m/Q of 12 to 120, fragments of ammonium (NH_4_16 and NH_4_17, two main signals of NH_4 which are NH_2^+ and NH_3^+), and fragments of nitrate (NO_3_30 and NO_3_46, two main signals of NO_3 which are NO^+, NO_2^+) are used as variables in the PMF input matrix. Fragment contributions are calculated using the terpene-related fragmentation table (see Section 3.3.2). We choose a two-factor solution (see Fig. S2 in the Supplement of Nursanto et al. (2025)) because we are interested in splitting the aerosol mass only into inorganic aerosol (pAmN) and organic aerosol (OA mixture, containing pON). From the organic aerosol factor, we calculate the f_{pON} from the factor concentration time series. The details of the PMF method are described in Section S5 in the Supplement of Nursanto et al. (2025), including the statistical summary and the diagnostic plots of the PMF analysis.

The NO_x^+ ratio and f_{pON} time series for the limonene SOA experiment are shown in Fig. 3.8. The whiskers around the mean f_{pON} represent the uncertainties coming from the value range of R_{pON} combined with the uncertainties from ion counting statistics, electronic noise, fragmentation table (for UMR), and R_{pAmN} (see Section 3.5.3). The initial mixture of NH_4NO_3 seed and $NO_3^\bullet$ from NO_2 and O_3 gives a ratio that matches R_{pAmN} from an offline calibration, where f_{pON} is close to zero for both instruments. Although nitric acid (HNO_3) can be formed by nitrogen pentoxide (N_2O_5) hydrolysis under these humid conditions, experiments were run in excess NH_3; therefore, we expect no substantial increase of HNO_3 that can affect NO_x^+ ratio. After the limonene injection, the R_{obs} rose to values in between R_{pAmN} and R_{pON}, indicating the formation of a mixture of pAmN and pON inside the chamber.

Based on observations of Takeuchi et al. (2024), pON measured with the SV-AMS is only quantitatively detected as $-NO_2$ moiety, not $-ONO_2$. The reasoning for this difference in detection of alkyl nitrate ($RONO_2$) and NH_4NO_3 is thought to be due to thermal decomposition of pON producing NO_2 gas in the vaporizer, while NH_4NO_3 would more likely decompose to HNO_3 and thus dominantly ionizing gases of different molecular weights. The "missing oxygen" is generally retained bound to the carbon, and thus accounted as an organic moiety. Thus, f_{pON} needs to be corrected for this phenomenon using molar mass ratio of NO_3/NO_2 (62 g · mol^{-1}/46 g · mol^{-1}) to recalculate the pON mass. There is no study yet assessing the necessity of correcting f_{pON} in CV, and we suggest that it is likely unnecessary due to the more complete thermal decomposition that shifts the fragmentation pattern of both NH_4NO_3 and $RONO_2$ to NO_2 and NO.

Both NO_x^+ ratio methods (SV-AMS and CV-ACSM) and the PMF method (CV-ACSM) show a similar response to the injection of limonene, whereupon f_{pON} increases rapidly from ~0 to 0.3–0.5. The agreement between the two instruments on this initial pON production is encouraging. However, after this initial jump, the trend of f_{pON} seems to vary. While mean f_{pON} calculated using NO_x^+ ratio method from CV-ACSM remains steady after the injection, the other two results show a gradual decrease of f_{pON} as the chamber dilutes.

The NO_x^+ ratio method on CV-ACSM data shows a similar change in f_{pON} relative to the PMF method immediately after limonene injection but then continues to decrease over time (see Fig. 3.8). The PMF method combines the variations of Org, NO_x^+, and NH_x^+ ions to obtain the factor profiles, therefore allowing a more subtle change in the chamber composition to be taken into account. The NO_x^+ratio method in CV-UMR, in contrast, only takes into account fragments that are in m/Q 30 and m/Q 46 using a constant fragmentation table relationship.

Similarly, the SV-AMS also shows a gradual decrease in mean f_{pON} unlike the NO_x^+ ratio method from CV-ACSM (see Fig. 3.8). This suggests that changing contributions of organics at m/Q 30 and m/Q 46 may be taken into account by HR peak fitting and not by the UMR fragmentation table, causing a divergence as the chamber aerosol dilutes. Based on the sensitivity analysis in Fig. 3.7, the signal contribution of NO_2^+ (m/Q 46) is the largest source of uncertainty in the CV-ACSM, since the adapted method is sensitive to the change of $a_{Org[46],[45]}$. On the other hand, the uncertainty of RoR used to calculate R_{pON} accounts for the largest contribution to the uncertainty calculated for SV-AMS. Since the RoR in Day et al. (2022a) relies on the average value of a broad range of organic nitrate, a chamber experiment that uses a specific precursor is likely to have R_{pON} further away from the average value than, for instance, a complex ambient mixture.

Nevertheless, we are encouraged by the match in responses upon formation of organic nitrate, indicating that the NO_x^+ ratio method is similarly sensitive to changing nitrate speciation in both instruments. When considering the propagation of uncertainty, we observe overlaps between the results of CV-ACSM and SV-AMS. Therefore, by considering the uncertainty from $a_{Org[46],[45]}$ in CV-UMR and uncertainty from RoR in SV-AMS, the results for both instruments are comparable. Further investigation of the detailed response of each instrument to changing aerosol composition would be valuable.

3.7 Conclusions and recommendations

We have shown the separation of particulate ammonium nitrate (pAmN) and particulate organic nitrate (pON) signals from the total particulate nitrate (pNO_3) signal

measured using a time-of-flight aerosol chemical speciation monitor equipped with a capture vaporizer with unit mass resolution (CV-UMR-ToF-ACSM), using an adapted NO_x^+ ratio method with a revised fragmentation table and data pre-treatment. The shift of fragmentation pattern towards smaller ion fragments in the capture vaporizer (CV) compared to the standard vaporizer (SV) affects the signals of NO^+ and NO_2^+ fragments and interferences by Org fragments used to calculate the NO_x^+ ratio in UMR. Therefore, we recommend updating the default fragmentation table from Allan et al. (2004) for entries shown in Table 3.4 before applying the NO_x^+ ratio method, according to the aerosol composition. As noted previously, substantial corrections to the fragmentation table for these terms have been shown to be needed for measurements using the SV under some conditions (Fry et al., 2018).

Table 3.4: Proposed m/Q 30 and 46 entries for Org and NO_3 in the revised fragmentation table adapted for the NO_x^+ ratio method in CV-UMR-ToF-ACSM. The multipliers ($a_{\mathrm{Org}[x],[i]}$) are applied according to the aerosol composition. The entries that are not included in this table should follow the fragmentation table of Allan et al. (2004) for AMS and adapted without gas-phase corrections (frag_air) for ACSM.

m/Q	Revised fragmentation table for CV-UMR-ToF-ACSM	
	Org	NO_3
30	$a_{\mathrm{Org}[30],[29]}$*frag_Org[29]	[30], -frag_Org[30]
46	$a_{\mathrm{Org}[46],[45]}$*frag_Org[45]	[46], -frag_Org[46]

m/Q	$a_{\mathrm{Org}[x],[i]}$			
	General	Biogenic[a]	Glyoxal	Terpene
30	0.311	0.32	0.291	0.476
46	0.305	0.68	0.082	0.204

[a]Retrieved from Hu et al. (2017).

The shift of fragmentation pattern in the CV towards more formation of NO^+ fragments and less of NO_2^+ fragments changes the magnitude of the NO_x^+ ratio for both pure pAmN and pure pON. The NO_x^+ ratio in CV is affected by the aerodynamic lens alignment, and therefore we recommend users to align their aerodynamic lens to obtain the correct NO_x^+ ratio.

To separate the pAmN and pON signal from total pNO_3 and calculate the particulate organic nitrate fraction (f_{pON}), the regular ammonium nitrate calibration should be used to obtain the NO_x^+ ratio for pure ammonium nitrate (R_{pAmN}), where a value of 0.01–0.07 is expected. On the other hand, we observed from a chamber experiment that the R_{pON} value approaches zero in the CV. Therefore, we recommend analyzing using three R_{pON} values, to describe the upper limit (R_{pON} calculated using RoR = 3.29), geometric mean, and lower limit (R_{pON} = 0.0001), which also provides the f_{pON}

uncertainty. If possible, we recommend constraining the RoR for more accurate results (e.g., performing chamber experiment to form pure organic nitrate). Through this study, we hope to inspire more research regarding R_{pON} measurement in CV-based instruments to obtain more precision in analyzing organic nitrate concentrations.

The observed NO_x^+ ratio (R_{obs}) tends to have more noise in CV-based measurements compared to SV. Data filtering using the instrument's R_{pAmN} and NO_2^+ detection limit has shown that the adapted NO_x^+ ratio method in the CV-UMR-ToF-ACSM is able to filter unreliable measurements with concentration cut-off ranging from 0.6 to 2.0 $\mu g \cdot m^{-3}$, depending on time averaging. This data pre-treatment filters data points with high fraction uncertainty (above ± 0.5) and decreases the average uncertainty by $\sqrt{N}$ for each N-fold of averaging from 10 min.

With a longer time averaging, the concentration limit and fraction limit improve, which allows more reliable determination of f_{pON} and f_{pAmN}. The method reports absolute uncertainty of particulate organic nitrate $< 10\%$ at the total particulate nitrate concentrations of 2 $\mu g \cdot m^{-3}$ (120 min time averaging) to 10 $\mu g \cdot m^{-3}$ (10 min time averaging) and organic nitrate fraction of 10% (120 min time averaging) to 20% (10 min time averaging). We recommend users to average the time series to 30 or 60 min to retain information about real ambient variation, while improving the reliable nitrate concentration limit. This may also be convenient when comparing to auxiliary data that are typically reported half-hourly or hourly.

In the region where pNO_3 concentration is < 10 $\mu g \cdot m^{-3}$ and/or $f_{\mathrm{pON}} < 12$ %, longer time averaging may be necessary to achieve the absolute uncertainty < 10 %. In studies where noise is not a problem (e.g., chamber experiments with high particle concentration), time averaging may be unnecessary. With a similar approach, this method could be used for SV-UMR-ToF-ACSM observations as well, with a fragmentation table suited for SV-based measurements.

The adapted NO_x^+ ratio method on rural nitrate episodes can distinguish periods with pAmN or pON as the major component, confirmed by relation to the ammonium and organic aerosol composition, respectively. The adapted NO_x^+ ratio method applied to CV-UMR-ToF-ACSM measurements in a chamber experiment is able to replicate the response to precursor injection observed from PMF analysis of the same measurements, as well as a co-located high-resolution time-of-flight aerosol mass spectrometer equipped with standard vaporizer (SV-HR-ToF-AMS). The largest uncertainties in this comparison come from $a_{\mathrm{Org[46],[45]}}$ (CV-UMR-ToF-ACSM) and RoR (SV-HR-ToF-AMS). The adapted NO_x^+ ratio method for CV-UMR-ToF-ACSM demonstrated in this study can be used at monitoring sites to monitor regional f_{pON} and improve understanding of particulate nitrate sources and evolution.



Chapter 4

Gas-particle partitioning, molecular weight, and yield of organic nitrate under different urban VOC, NO_x, and oxidation conditions during SAPHIR-CHANEL campaign

This chapter is based on the submission in the Atmospheric Chemistry and Physics journal currently under review as:

F. R. Nursanto, Q. He, S. Van De Wouw, A. Zanders, T. Hohaus, W. S. J. Kroese, R. Wegener, M. G. Adam, B. Winter, R. Dubus, L. Kesper, F. Rohrer, Y. Wang, E. Matthews, A. Voliotis, T. J. Bannan, G. McFiggans, H. Coe, Y. Wu, M. Roska, M. Canagaratna, M. Alton, M. M. Coggon, C. E. Stockwell, K. H. Bates, E. Y. Pfannerstill, S. R. Zorn, H. Wang, M. Riva, S. Perrier, B. Yang, L. Liu, A. Novelli, M. Färber, H. Fuchs, A. C. Marcillo Lara, A. Grasse, C. Wesolek, R. Tillmann, R. Holzinger, M. C. Krol, G. I. Gkatzelis, and J. L. Fry (2026). *Gas-particle partitioning, molecular weight, and yield of organic nitrate under different urban VOC, NO_x, and oxidation conditions during SAPHIR-CHANEL campaign*. DOI: 10.5194/egusphere-2025-6310

Figures, tables, and additional discussion referred to as part of the Supplement of Nursanto et al. (2026) are available at the following link: https://egusphere.copernicus.org/preprints/2026/egusphere-2025-6310/egusphere-2025-6310-supplement.pdf

Abstract

Oxidation of volatile organic compounds (VOCs) involving hydroxyl radicals ($OH^{\bullet}$), nitrogen oxides (NO_x), or nitrate radicals ($NO_3^{\bullet}$) forms organic nitrates that undergo gas-particle partitioning, changing the lifetime of nitrogen compounds and their deposition on ecosystems. In urban areas, VOC composition is complex, with contributions from traffic, cooking, volatile chemical products (VCPs), and biogenic emissions. Secondary organic aerosol (SOA) formation from urban VOC mixtures was investigated using chamber experiments during the SAPHIR-CHANEL campaign under realistic VOC-NO_x and oxidation conditions. The yield of total organic nitrates is higher for precursor mixtures with a higher percentage of unsaturated VOCs, such as those from traffic and cooking sources (11–21 %), compared to VCPs and complex urban emission replicas (2–7 %). Enhanced particle-phase partitioning is observed under nighttime oxidation (by $NO_3^{\bullet}$) versus daytime oxidation (by $OH^{\bullet}$). Particulate organic nitrates have a higher average molecular weight under nighttime conditions (331 ± 13 g $\cdot$ mol^{-1}) than under daytime conditions (258 ± 24 g $\cdot$ mol^{-1}) due to increased oligomerization. Similarly, the mass fraction of the total organic aerosol that is organic nitrate is 2.6–4.5 times higher under nighttime than daytime conditions, likely due to higher molecular weight and lower temperatures. Although gas-phase organic nitrate composition varies substantially between precursor mixtures, bulk organic nitrate volatility is generally similar to that of modeled oxidized monoterpene nitrates (10^{-4}–10^{-2} m$^3 \cdot \mu$g^{-1} at 18–40 °C). These findings improve understanding of bulk organic nitrate sources and properties in a complex urban environment, allowing better simulations of air quality and nitrate deposition.

4.1 Introduction

As sulfur oxide emissions decrease due to emission controls, reactive nitrogen species are becoming increasingly important atmospheric constituents, in particular for the formation of secondary aerosols. The term NO_y is commonly used to refer to oxidized reactive nitrogen species, which include nitrogen oxides ($[NO_x] = [NO] + [NO_2]$) and reservoir species (NO_z). NO_z includes chemical species such as nitrate radical ($NO_3^{\bullet}$), nitrogen pentoxide (N_2O_5), nitric acid (HNO_3), nitrous acid (HONO), organic nitrates (ON; e.g., alkyl nitrates ($RONO_2$), peroxy nitrates (RO_2NO_2)), and inorganic nitrates (NO_3^-).

Several modeling studies have shown that particulate nitrate is becoming the principal component of continental aerosols on both the global and regional scales (Adams et al., 1999; Metzger, 2002; Liao et al., 2003; Rodriguez and Dabdub, 2004; Feng and Penner, 2007; Bauer et al., 2007; Paulot et al., 2016; Bian et al., 2017; Vasilakos et al., 2018; Drugé et al., 2019; Lu et al., 2021). The climatic impact of nitrates through aerosol radiative forcing modification is predicted to become larger than sulfate in the upcoming century (Adams et al., 2001; Schaap et al., 2003; Liao et al., 2003; Bauer et al., 2007; Erisman et al., 2011; Westervelt et al., 2015). Some regions of Northwestern Europe with relatively higher nitrogen emissions, compared to the rest of Europe, already experience greater importance of nitrate than sulfate aerosol. For instance, in the Netherlands, inorganic nitrate in the form of ammonium nitrate (NH_4NO_3) makes up the majority of aerosol (Schaap et al., 2004; Schlag et al., 2016; Nursanto et al., 2023).

Although inorganic nitrate is prevalent, the contribution of ambient ON is not negligible. With spatial and seasonal variability, the average mass fraction of particulate nitrate in forms of ON varies from 9.8 % in winter Beijing, China (Xu et al., 2021), 13 % in Barcelona, Spain (Mohr et al., 2012; Pandolfi et al., 2014), 17–31 % for annual average in China (Yu et al., 2024), up to 34–44 % in Europe (Kiendler-Scharr et al., 2016) and 20–60 % in the Netherlands during spring and summer (Nursanto et al., 2025). ON can play a significant role in secondary organic aerosol (SOA). Because ONs typically have longer atmospheric multiphase lifetimes, 2–97 h (González-Sánchez et al., 2023), longer than the lifetime of NO_x, 2–29 h (Singh, 1987; Ryerson et al., 1998; Nunnermacker et al., 2000; Valin et al., 2013; Romer et al., 2016; Kenagy et al., 2018; Lange et al., 2022), they can modify the overall atmospheric lifetime of reactive nitrogen species, transport distance, and therefore the natural areas affected by nitrogen deposition. Therefore, it is important to identify ON compounds formed in the atmosphere and to understand their precursor emissions and the chemical processes they undergo to assess their impact on ecosystems.

NO_x is mainly introduced to the atmosphere via combustion emissions, and involved in the oxidation of volatile organic compounds (VOCs) produced from different sources in

the troposphere. The fate of NO_x emissions is illustrated in Fig. 4.1, showing that it can end up in the particulate phase as NH_4NO_3 or ON. ONs are typically formed at first in the gas phase, either by the reaction between organic peroxy radicals ($RO_2^{\bullet}$) and NO_x or between $NO_3^{\bullet}$ and VOCs (the latter is usually considered nighttime chemistry, because the $NO_3^{\bullet}$ photodissociates and reacts with NO rapidly during the day). These species can then condense into the particle phase or undergo further reactions, forming SOA. The condensation of organic compounds depends on many factors, such as the temperature, relative humidity, and oxidation level of the compound (Kroll and Seinfeld, 2008). In urban mixtures with various VOC sources, the variety of produced ON compounds is still largely unknown. Because much ON chemistry is not well understood, this component of SOA is likely to be poorly estimated in models.

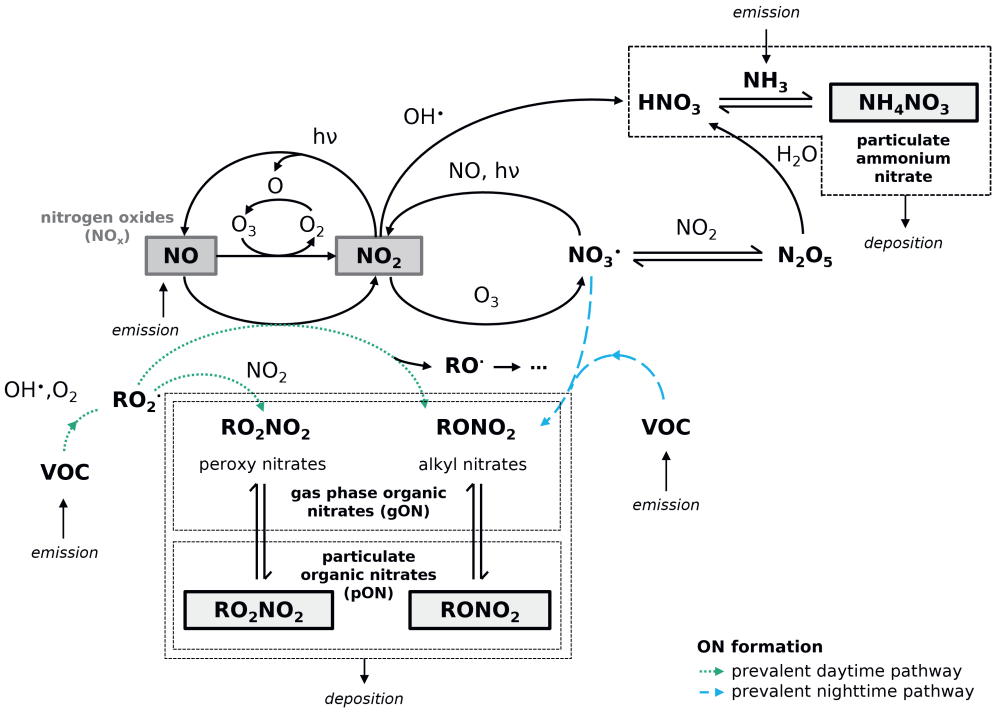


Figure 4.1: Reactive nitrogen species formation in the troposphere involving emissions of NO_x, NH_3, VOCs, and their reactions with oxidants (e.g., $OH^{\bullet}$, and $NO_3^{\bullet}$) to form particulate ammonium nitrate (NH_4NO_3) and ONs that are in equilibrium between gas phase ON (gON) and particulate ON (pON). The dashed blue arrows represent the $NO_3^{\bullet}$ chemistry pathway for ON formation prevalent during nighttime, while the dotted green arrows represent the $OH^{\bullet}$ chemistry pathway for ON formation prevalent during daytime.

Although single VOC precursor experiments are helpful in determining the chemical mechanisms of SOA formation, the interactions between the products of different

precursors can lead to significant differences in particle composition, volatility, and SOA yields (McFiggans et al., 2019; Voliotis et al., 2021; Voliotis et al., 2022; Shao et al., 2022). As the VOCs from fossil fuel-related emissions are decreasing, several studies have shown that non-traffic SOA precursors such as volatile chemical products (VCPs) originating from household cleaning and personal care products as well as cooking emissions are becoming increasingly important in urban VOC chemistry (McDonald et al., 2018; Coggon et al., 2021; Gkatzelis et al., 2021b; Wernis et al., 2022; Coggon et al., 2024; Rivellini et al., 2024). VCPs and cooking VOCs are expected to increasingly dominate SOA formation from anthropogenic VOCs in the urban environment of industrialized countries.

In summer 2024, the SAPHIR (Simulation of Atmospheric Photochemistry in a Large Reaction Chamber) atmospheric simulation chamber at Forschungszentrum Jülich was used during the "Household Chemicals Amplifying Urban Aerosol Pollution" (CHANEL) campaign to replicate complex urban VOC-NO_x chemistry (Wu et al., in progress). This chapter focuses on understanding the differences in the yield, average molecular weight, and gas-particle partitioning of organic nitrate formation from different VOC precursor mixtures under various NO levels and oxidation conditions. We identify the ON compounds and their bulk volatility in the selected urban mixture to fill the knowledge gap and enable modelers to improve the simulation of nitrate aerosol formation, transport, and deposition in real-world atmospheric mixtures.

4.2 Methods

4.2.1 SAPHIR-CHANEL campaign

The SAPHIR-CHANEL 2024 campaign focused on understanding SOA formation from different co-emitted urban VOC precursors under various NO_x emission scenarios and oxidation conditions (Wu et al., in progress). Based on emission inventories from the Atmospheric Emissions and Reactions Observed from Megacities to Marine Area (AEROMMA) 2023 campaign and previous studies (Warneke et al., 2023; Pfannerstill et al., 2024; Stockwell et al., 2025), the major atmospheric chemical conditions in the urban atmospheres of United States and European cities were replicated by oxidizing various VOC mixtures and mixed systems inside the SAPHIR chamber. SAPHIR is an outdoor cylindrical chamber (length = 18 m, diameter = 5 m, and volume = 270 m^3) made of double-wall Teflon film that allows investigation of gas phase species oxidation, aerosol formation and chemical transformation with a minor influence from the chamber wall (Rohrer et al., 2005; Bossmeyer et al., 2006; Wegener et al., 2007; Apel et al., 2008). The chamber is equipped with a shutter roof system that allows exposure or blocking of sunlight to simulate daytime and nighttime chemistry.

Three variables were controlled for the experiments: VOC composition, NO level, and oxidation conditions, as listed in Table 4.1. The VOC precursor mixtures representing different urban emission sources used throughout the campaign are shown in Fig. 4.2 and Tables S1, S2, S3, S4, and S5 in the Supplement of Nursanto et al. (2026). These include biogenic and anthropogenic VOCs, such as single-compound experiments of limonene, multi-injection source-specific experiments of VCP, diesel, gasoline, and cooking emissions, as well as complex urban mixtures. The discussion of the VOC composition for each emission source is detailed in Wu et al. (in progress). A more complex urban VOC-NO_x mixture was represented by the Los Angeles anthropogenic emission profile, which combines VCPs, cooking emissions, traffic emissions (100 % gasoline), and a medium NO condition as a representation of average urban NO_x (Coggon et al., 2024; Stockwell et al., 2025). We further investigated the SOA formation by combining the Los Angeles anthropogenic mixture with biogenic VOC (BVOC) emissions to replicate a real-world emission profile (Pfannerstill et al., 2024). We also replicated a global city scenario where we have different traffic emission profile (50 % gasoline, 50 % diesel) representing European and global cities following Scholz et al. (2025). Lastly, we performed an experimental scenario for future cities, where there is more influence from biogenic emissions and less from traffic (no traffic emissions and low NO) compared to the current day Los Angeles and global city emission profile. The experiments explored in this study do not cover all the experiments performed during the SAPHIR-CHANEL campaign.

The scenario of changing NO_x emissions and oxidation conditions was achieved by changing the NO condition for each VOC precursor mixture, and whether the roof of the SAPHIR chamber was opened or closed. Under daytime conditions, three NO conditions were used. The low NO condition was accomplished by producing NO_x only from the photolysis of HONO produced inside the chamber from the Teflon film (Rohrer et al., 2005). NO concentrations were further suppressed by injecting additional ozone (O_3) up to 100 ppb. This resulted in an average mixing ratio (after the roof was opened until it was closed) of 0.07-0.19 ppb of NO and of 1.03–2.21 ppb of NO_2. The medium NO condition was achieved with no addition of NO and O_3 to the chamber, leading to 0.15–0.31 ppb of NO and 1.08–1.65 ppb of NO_2, only slightly higher NO than for the low NO conditions. To obtain high NO conditions, NO was added before exposing the chamber air to sunlight, reaching mixing ratios of 0.23–1.05 ppb of NO and 2.82–4.29 ppb of NO_2. Under this condition, NO was only enhanced for a short time interval ($\sim$0.5 h) after opening the chamber's roof, since it was converted into NO_2 by the photochemically produced O_3 and $RO_2^{\bullet}$. Lastly, the nighttime oxidation condition was achieved by adding NO_2 and O_3 to the chamber air and keeping the chamber's roof closed to block the sunlight and to favor $NO_3^{\bullet}$ accumulation. The average NO and NO_2 mixing ratios corresponding to each experiment are listed in Table S6 in the Supplement of Nursanto et al. (2026).

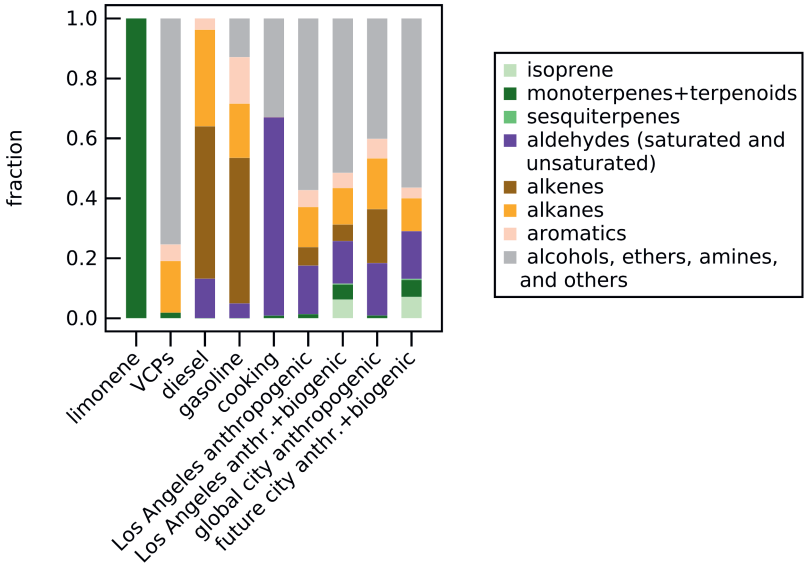


Figure 4.2: Relative VOC composition (calculated using mixing ratios) categorized by compound family for each urban VOC mixture injected into the SAPHIR chamber during the SAPHIR-CHANEL 2024 campaign. The composition is based on the fingerprint compounds in the adjusted emission inventories of urban United States and European emissions (see the details in Tables S1, S2, S3, S4, and S5 in the Supplement of Nursanto et al. (2026).

The typical sequences of SAPHIR-CHANEL chamber experiments are shown in Fig. S1 in the Supplement of Nursanto et al. (2026). A chamber experiment was started by humidifying the air until ∼60 % relative humidity (RH) was reached, except for the limonene experiment under nighttime conditions, where it was ∼20 %. After about an hour, ammonium sulfate ($(NH_4)_2SO_4$) was introduced as particle seeds to encourage condensation into the particle phase. RH and seed type were kept constant to ensure the same initial aerosol conditions. One hour after the introduction of seeds, the different VOC precursors in a given emission profile were added in sequential injections. Subsequently, the desired oxidation conditions were introduced to the chamber (i.e., the addition of NO and O_3 followed by immediately opening the roof, or the addition of NO_2 and O_3 while keeping the roof closed). In the limonene experiments, the oxidation condition was established first, followed by several injections of limonene at three distinct times with 1–1.5 h intervals.

Table 4.1: List of experiments in the SAPHIR-CHANEL 2024 campaign included in this chapter, grouped based on VOC precursors. All experiments were run at initially 60 % relative humidity (RH), unless indicated otherwise.

Date (yyyy.mm.dd)	VOC precursor(s)	Oxidation and NO conditions
Single-compound precursor experiments		
2024.07.01	limonene	daytime, low NO
2024.07.03[a]	limonene	nighttime
Source-specific emission mixture experiments		
2024.07.04	VCPs	daytime, low NO
2024.07.08	VCPs	daytime, medium NO
2024.07.09	VCPs	daytime, high NO
2024.07.05	VCPs	nighttime
2024.07.17	diesel	daytime, medium NO
2024.07.18	diesel	daytime, high NO
2024.07.11	gasoline	daytime, medium NO
2024.07.10	gasoline	daytime, high NO
2024.07.16	cooking	daytime, low NO
2024.07.15	cooking	daytime, medium NO
Complex urban mixture experiments		
2024.07.22	Los Angeles anthropogenic emission	daytime, medium NO
2024.07.23	Los Angeles anthropogenic emission	nighttime
2024.08.05	Los Angeles anthropogenic+biogenic emission ($+O_3$)	daytime, low NO
2024.07.29	Los Angeles anthropogenic+biogenic emission	daytime, medium NO
2024.08.06	Los Angeles anthropogenic+biogenic emission ($+O_3$+NO_2)	daytime, high NO
2024.07.31	Los Angeles anthropogenic+biogenic emission	nighttime
2024.07.30	global city anthropogenic emission	daytime, medium NO
2024.08.02	future city anthropogenic+biogenic emission	daytime, low NO
Background experiments		
2024.07.28	background (no seed)	daytime
2024.08.04	background (with seed)	daytime

[a] Initial RH 20 %.

4.2.2 Instrumentation

Aerosol mass loadings and chemical composition measurements using high-resolution time-of-flight aerosol mass spectrometer (HR-ToF-AMS)

Non-refractory submicron aerosol components speciated into organics (Org), nitrate (NO_3), sulfate (SO_4), ammonium (NH_4), and chloride (Cl) were measured using a high-

resolution time-of-flight aerosol mass spectrometer (HR-ToF-AMS) with a standard vaporizer. The operating principles of the instrument, including the aerodynamic lens system, vaporizer, and electron impact ionization, are described in detail by Canagaratna et al. (2007). Aerosols were sampled through a 5 m long (1/4″ or 6.4 mm outer diameter and 0.065″ or 1.7 mm wall thickness) stainless steel tube at a total flow of 580 mL $\cdot$ min^{-1}. The HR-ToF-AMS was operated in V-mode throughout the campaign, providing chemical composition data at a time resolution of 1 min. The detection limit of the instrument was approximately 3 ng $\cdot$ m^{-3}, with a typical measurement uncertainty of 20 %.

Calibration of the HR-ToF-AMS was performed weekly using size-selected 350 nm dry NH_4NO_3 particles to determine the ionization efficiency (IE). In addition, the relative IE for SO_4 was assessed using $(NH_4)_2SO_4$ particles. For Org, the relative IE was set to the default value of 1.4, while for NH_4 and SO_4, it was determined to be 4.4 and 1.3. The total aerosol mass concentrations are calculated from the sum mass of Org, NO_3, SO_4, NH_4, and Cl species. Data analysis was conducted using the PIKA 1.24 software toolkit, applying high-resolution peak fitting for chemical speciation.

To divide the total nitrate signal measured by AMS into particulate ammonium nitrate (NH_4NO_3) and particulate organic nitrate (pON), the NO_x^+ ratio method was applied (Farmer and Jimenez, 2010; Day et al., 2022a; Takeuchi et al., 2024). This method has been shown to successfully analyze organic nitrate composition in several studies (Fry et al., 2013; Pye et al., 2015; Kiendler-Scharr et al., 2016; Ng et al., 2017; Fry et al., 2018; Huang et al., 2019a; Huang et al., 2019b; Brownwood et al., 2021; Day et al., 2022a). The method is described in Section S2.1 in the Supplement of Nursanto et al. (2026).

Total NO_y measurements

A chemiluminescence NO_x monitor (Thermo 42iQTL) equipped with a modified NO_y inlet was deployed to measure the total NO_y concentration in the experiments. The instrument and the custom inlet setup have been described in detail in previous work (Marsavin et al., 2023). The chamber air is sampled through a 1.6 m long Teflon tube (1/4″ or 6.4 mm outer diameter, 4.0 mm inner diameter), as short as possible to prevent wall losses of adsorbed NO_y species (Neuman et al., 1999). The sampled air then enters the external NO_y inlet box, which consists of a NO_2-to-NO molybdenum converter scavenged from another instrument (Thermo 17i) and a temperature controller (Omega CN616A) to adjust the converter temperature. Through the converter, the NO_y species are reduced to NO by means of heat and reaction with the molybdenum (Mo) before being transported through a longer inlet line to the chemiluminescence detector. The converter is operated at 350 °C, the same as in Marsavin et al. (2023), to maximize the conversion of ONs. The sampled air then goes through the downstream inlet line (approximately 3 m of Teflon tubing) and passes through a filter paper (PTFE, TE 38,

Whatman^{TM}) to avoid any residual particles entering the main instrument. The air at a flow rate of 1 L min^{-1} is drawn into the instrument using an external pump. The chemiluminescence NO_x instrument measures NO_y as NO with 1 min time resolution. The instrument was calibrated with and without the NO_y inlet using a standard NO_x cylinder, where the instrument's sensitivity remains relatively stable ($\pm$7 %). The detection limit of the instrument is $\sim$50 ppt.

The conversion efficiency of NH_4NO_3, $(NH_4)_2SO_4$, and 2-ethylhexylnitrate (an ON compound, González-Sánchez et al. (2021)) to NO by the heated NO_y converter at 350 °C was tested using simultaneous mass spectrometer measurements. The detailed procedure is shown in Section S2.2 in the Supplement of Nursanto et al. (2026). The conversion efficiency was (104 ± 5) % for $RONO_2$, (94 ± 2) % for NH_4NO_3, and (0 ± 1) % for $(NH_4)_2SO_4$. These results are comparable to the numbers reported in other studies (Winer et al., 1974; Baylon et al., 2015) and confirm that the converter decomposes pNO_3 but not NH_3 or NH_4^+. The conversion efficiency of HNO_3 was not characterized, but Baylon et al. (2015) shows 95 % efficiency using the same converter condition. The detection of HNO_3 also depends on the inlet line because the species is often absorbed by the tubing (Neuman et al., 1999; Day et al., 2002; Keehan et al., 2020), which was minimized by making the inlet line as short as possible. We therefore assume that there is negligible loss of HNO_3 in the inlet line.

To extract the gON mixing ratio (C_{gON}) from the total NO_y measurements, we subtracted the total NO_y mixing ratio with the simultaneous measurements of NO_x, HONO, HNO_3, and total pNO_3 (C_{NO_x}, C_{HONO}, C_{HNO_3}, C_{pNO_3}; all in ppb) as expressed in Eq. 4.1.

$$C_{gON} = C_{NO_y} - (C_{NO_x} + C_{HONO} + C_{HNO_3} + C_{pNO_3}) \tag{4.1}$$

The NO_x mixing ratio was measured using the Ecophysics CLD-780 TR, which operates on the principle of chemiluminescence detection, widely used in laboratory and field studies, and long-term monitoring (Clough and Thrush, 1967; Fontijn et al., 1970; Drummond et al., 1985). The HONO measurements were made using the Airyx ICAD $HONO/NO_2$ 200L, which used an iterative cavity-enhanced differential optical absorption spectroscopy (ICAD) method (Platt et al., 1979; Platt et al., 2009; Horbanski et al., 2019). The HNO_3 concentrations were obtained from the multi-reagent chemical ionization mass spectrometer (MR-CIMS) measurements and the total pNO_3 concentrations were from the HR-ToF-AMS. We assume that other NO_z species that are not included in the subtraction are negligible.

Gas and particle phase chemical species measurements using gas chromatography (GC) system and chemical ionization mass spectrometers (CIMS)

An online gas chromatography (GC) system, coupled to a flame ionization detector (FID) and mass spectrometer (MS), and four online chemical ionization mass spectrometers

(CIMS) were deployed to measure chemical compounds during the campaign. Each instrument has the ability to measure different types of compounds in the gas phase and particle phase. The details of how each instrument was operated during the campaign can be found in Section S2 in the Supplement of Nursanto et al. (2026).

The GC system has a thermal desorption unit and is coupled to a dual flame ionization and mass spectrometric detection (GC-TD-FID/MS; Markes TT24-7xr with Kori-xr units, Agilent 8890 GC, Agilent 5977B MS). The system allows for cryogenic preconcentration, chromatographic separation, and dual detection to measure alkanes, alkenes, alkynes, aromatics, and monoterpenes. FID targets the detection of light hydrocarbons and MS for heavier or structurally complex species.

The multi-reagent CIMS (MR-CIMS, Vocus B2, Tofwerk AG, Switzerland) is a newly designed instrument equipped with bipolar ToF, which can simultaneously measure cations and anions without inner interference. MR-CIMS operates with four different reagent ions (i.e., iodide, bromide, acetone dimer, benzene). In this work, we obtain the HNO_3 mixing ratio (sensitivity = 9.3 ncps $\cdot$ pptv^{-1}) from the iodide channel (I^-) and the VOC species measurements such as isoprene, aldehydes, aromatics, and monoterpenes (as signal intensity in ncps) from the benzene channel ($C_6H_6^+$). The design and geometric structure of the ion-molecular reactor of MR-CIMS (i.e., Vocus AIM IMR) has been discussed in detail elsewhere (Riva et al., 2024).

The amine-ToF used an Eisele type inlet for chemical ionization and coupled to an atmospheric pressure interface time-of-flight mass spectrometer (CI-APi-ToF-MS). The precursor for the primary ion in the chemical ionization was propylamine, and the generated $C_3H_7NH_2^+$ reagent ions selectively ionize oxygenated organic compounds by forming adducts with neutral molecules. The operating principles and instrument configuration are detailed in previous works (Eisele and Tanner, 1993; Junninen et al., 2010; Berndt, 2021).

A Vocus long time-of-flight mass spectrometer (Tofwerk AG, Switzerland) was operated with ammonium reagent ions (NH_4^+-Vocus), allowing measurements of VOCs and oxygenated VOCs. The detailed operating principles and instrument setup have been described elsewhere (Krechmer et al., 2018; Xu et al., 2022; Roska et al., in progress).

A Wall-Free Particle Evaporator (WALL-E) interface was coupled to an atmospheric pressure chemical ionization inlet (Riva et al., 2019; Riva et al., 2020) connected to a high-resolution orbitrap mass spectrometer (Q-Exactive, Thermo Fisher Scientific). The system includes a gas-phase denuder, a thermal desorption unit with sheath flow, a ceramic spacer for thermal isolation, and a dilution/cooling unit (Gao et al., 2025). The instrument used bromide ions (Br^-) as reagent ions to measure organic species in the particle phase.

The signal intensities of different organic compounds in the gas phase (±280 species from amine-ToF and ±900 species from NH_4^+-Vocus) and in the particle phase (±1000 species from WALL-E) from various mass-to-charge ratio (m/Q) in the observation were visualized as ON composition profile plots. The ON composition profiles were characterized separately for each instrument, as each detected species may have a different sensitivity in each instrument. The signals were summed from the signal intensity of compounds containing at least one nitrogen and three oxygens ($C_xH_yO_{\geq 3}N_{\geq 1}$). This criterion was chosen because it represents the minimum number of nitrogen and oxygen atoms for an ON species, but is not limited to ONs because it may also include other organic nitrogen compounds such as oxygenated amines and nitro aromatic compounds. The ON composition distribution is an estimate of how the ON species signal is distributed across carbon and oxygen atom numbers, rather than the actual mass distribution of molecular composition.

4.2.3 Determination of organic nitrate yields

The ON molar yield in each chamber experiment was calculated by determining the ratio of the mixing ratio of total ON formed in both the gas phase and the particle phase ($\Delta C_{ON,tot}$) to the mixing ratio of VOC consumed (ΔC_{VOC}). The ON molar yield ($\Delta C_{ON,tot}/\Delta C_{VOC,tot}$) is expressed in Eq. 4.2.

The total ON formed ($\Delta C_{ON,tot}$ in ppb) was calculated by subtracting the total ON prior the VOC injection from the total ON concentration when the maximum SOA concentration has been reached (assumed to represent steady state). A visualization of these periods is shown in Fig. S5 in the Supplement of Nursanto et al. (2026). The percentage of VOC concentration that was consumed was calculated by observing the signal intensity difference of various VOCs detected by the MR-CIMS-$C_6H_6^+$ or NH_4^+-Vocus measurements between the moment of VOC injection and the steady state. The expected injected concentration of each VOC was then multiplied by the decrease in signal intensity for each compound (or compound family) to obtain the mixing ratio of consumed VOCs ($\Delta C_{VOC,tot}$ in ppb). The expected mixing ratios of injected and consumed VOCs are calculated based on the injected volume and are not verified concentration by measurements.

$$\text{ON molar yield (\%)} = \frac{\Delta C_{ON,tot}}{\Delta C_{VOC,tot}} \cdot 100\% \tag{4.2}$$

Presumably, ON species with different volatilities, and whether they are in the gas phase or the particle phase, would have different losses. For instance, it is likely that more volatile gON will have lower losses than less volatile gON. Here, we acknowledge this challenge which can lead to potential uncertainties in the calculation. Measured gON and pON mixing ratios are treated as bulk species. To calculate the yields, the bulk pON and bulk gON mixing ratios were corrected for dilution and wall loss. In this work,

the particle phase concentrations are corrected for wall loss and dilution by using the equation $C_t = 9.01 \cdot exp((1.22 \cdot 10^{-4}) \cdot t)$, based on the observed $(NH_4)_2SO_4$ decay. Gas phase wall losses are known to be negligible (except for highly oxygenated molecules (HOMs), see Zhao et al. (2018)), and thus, we only applied dilution correction to the gas phase mixing ratios. The gas phase concentrations were corrected for a dilution ranging from $4 \cdot 10^{-4}$ min^{-1} to $6 \cdot 10^{-4}$ min^{-1} (chamber volume of 270 m^3 and inflow rate of 7–10 $m^3 \cdot h^{-1}$ depending on the experiment).

We estimate the uncertainty (as one standard deviation) of the ON molar yield by propagating the uncertainties from the determination of the total ON mixing ratio. The uncertainties include the half of detection limits of instruments measuring NO_y ($\pm$25 ppt), NO_x ($\pm$40 ppt), and HONO ($\pm$40 ppt), the uncertainty from calibration of HNO_3 measured by MR-CIMS ($\pm$15 %), the uncertainty of pNO_3 determination from AMS ($\pm$20 %), the uncertainty from NO_x^+ ratio method to obtain pON from AMS ($\pm$23 %, Takeuchi et al. (2024)), and the uncertainty from VOC signal decrease ($\pm$15 %, assuming the maximum uncertainty is similar to MR-CIMS). The description of the uncertainty propagation is detailed in Section S3.1 (Supplement of Nursanto et al. (2026)).

4.2.4 Determination of molecular weight and SOA mass fraction of particulate organic nitrates

The molecular weight of bulk particulate $RONO_2$ (MW_{pRONO_2}, includes organic moiety and nitrate functional group of pON) for each experiment was determined using the signal intensity of compounds detected by WALL-E. Similar to the approach in the previous section, only peaks with chemical formula containing at least one nitrogen and three oxygen atoms ($C_xH_yO_{\geq 3}N_{\geq 1}$) were included. The percentage or ratio of the signal of each peak to the summed signal intensity is multiplied by the corresponding nominal mass of each peak, and then summed for all peaks to obtain the molecular weight of bulk pON (see Eq. 4.3),

$$\mathrm{MW}_{\mathrm{pRONO_2}} = \sum_{k=1}^{n} \frac{A_k}{A_{\mathrm{C_xH_yO_{\geq 3}N_{\geq 1}}}} \cdot MW_k \tag{4.3}$$

where MW_{pRONO_2} is the average molecular weight of bulk particulate organic nitrate as $pRONO_2$ (in $g \cdot mol^{-1}$), A_k is the signal intensity of compound k, $A_{C_xH_yO_{\geq 3}N_{\geq 1}}$ is the total signal intensity of organic compounds with formula $C_xH_yO_{\geq 3}N_{\geq 1}$ (in $g \cdot mol^{-1}$).

This approach, however, may include other organic nitrogen compounds such as nitro aromatic compounds, which is also detected by WALL-E. However, we assume that their contribution is minimal due to the low percentages of aromatic VOCs in the precursor mixture (0–16 %).

Using this bulk molecular weight, we can calculate the contribution of pON to the total organic aerosol (OA), which is expressed as the mass fraction of the concentration of

formed $pRONO_2$ (ΔC_{pRONO_2}) to the total concentration of formed OA (ΔC_{OA}). The $pRONO_2$ mass fraction is expressed in Eq. 4.5. The mass concentration of $pRONO_2$, which includes both organic and nitrate moiety of ON, is calculated from C_{pON} using the molecular weight of bulk organic nitrate (MW_{pRONO_2}, in $g \cdot mol^{-1}$) in each experiment using Eq. 4.4. The total mass of OA includes the concentrations of AMS Org and pON (as $-NO_2$, not $-ONO_2$ since one of the oxygen is accounted as the AMS Org mass; see Takeuchi et al. (2024)).

$$C_{pRONO_2} = C_{pON} \cdot \frac{MW_{pRONO_2}}{62\ g \cdot mol^{-1}} \tag{4.4}$$

$$pRONO_2\ \text{mass fraction}\ (\%) = \frac{\Delta C_{pRONO_2}}{\Delta C_{OA}} \cdot 100\% \tag{4.5}$$

We estimate the uncertainty (as one standard deviation) of the $pRONO_2$ mass fraction from the uncertainty of the determination of pNO_3 and Org in AMS (each contributes $\pm$20 %), the NO_x^+ ratio method to obtain pON from AMS ($\pm$23 %, Takeuchi et al. (2024)), and the standard deviation of the average MW_{pRONO_2}. The uncertainty propagation is detailed in Section S2.2 (Supplement of Nursanto et al. (2026)).

4.2.5 Gas-particle partitioning of organic nitrates

Every compound in the atmosphere can partition between the gas and particle phase according to its properties (e.g., chemical structure, volatility, functional groups). This partitioning reaches an equilibrium or steady state for a given compound at a given temperature and a given total aerosol mass. Therefore, calculating the bulk equilibrium partitioning in an atmospheric mixture can help us understand the average bulk organic species that are produced in the atmosphere.

The partitioning of a compound *i* between the gas and particle phases can be described by the sorption of organic compounds into existing particles, which leads to the condensation of low-volatility organic compounds (LVOCs) into the particle phase. This mechanism can be defined using the partitioning coefficient based on the volatility of the compound *i* ($K_{p,i}$ in $m^3 \cdot \mu g^{-1}$), as expressed in Eq. 4.6 (Pankow, 1994; Pankow and Asher, 2008). It is proportional to the particle-to-gas concentration ratio ($C_{p,i}/C_{g,i}$) and inversely proportional to the total absorptive mass (m_{tot} in $\mu g \cdot m^{-3}$),

$$K_{p,i} = \frac{C_{p,i}}{C_{g,i}} \cdot \frac{1}{m_{tot}} \tag{4.6}$$

When expressed thermodynamically in Eq. 4.7, $K_{p,i}$ is a function of the average temperature (T in K) and the pure liquid vapor pressure of *i* at a given T ($p^o_{L,i}$ in atm), as well as of the composition of the the organic matter (expressed as the molecular weight, MW_{om} in $g \cdot mol^{-1}$), absorptive organic fraction of the PM (f_{om}), and the activity coefficient in the organic fraction of the PM (ζ). The ideal gas constant (R) equal to 0.082

$L \cdot atm \cdot K^{-1} \cdot mol^{-1}$) is used. By estimating the pure liquid vapor pressure of i with a given MW_{om} and ζ, $K_{p,i}$ can be theoretically calculated for a given chemical structure using a group contribution method, for example, SIMPOL.1 from Pankow and Asher (2008). The theoretically derived value of $K_{p,i}$ calculated for different organic compound structures using Eq. 4.7 can be compared to the observed bulk value of $K_{p,i}$ calculated using Eq. 4.6 to deduce the average volatility of the organic compounds formed (thus related to some possible chemical structures) and to characterize the bulk properties of the SOA mixture (Brownwood et al., 2021).

$$K_{p,i} = \frac{760 \cdot R \cdot T \cdot f_{om}}{10^6 \cdot MW_{om} \cdot \zeta \cdot p^o_{L,i}} \tag{4.7}$$

In this study, we characterize the bulk ON in the gas phase and the particle phase under equilibrium conditions using the particle-to-gas ratio of ON (C_{pON}/C_{gON}) and the gas-particle partitioning of ON ($K_{p,ON}$). The equilibrium condition refers to the state in which the rate of mass transfer of a compound from the gas phase to the particle phase is equal to the reverse rate. We identify this equilibrium condition as when the maximum SOA concentration is reached and remains stable over time (ranging from 0.5–5 h), based on the AMS measurements. There is minimal exchange between the two phases under this condition, and thus the system can be considered in steady state. Further reactions within the particle phase and thermal decomposition, however, are not considered in this assumption. For limonene and nighttime Los Angeles experiments, we also describe the partitioning that happens just before a new injection is performed in the chamber (when SOA is still increasing) to compare it with the equilibrium condition.

We evaluated the trend in ON partitioning by differentiating the chamber experiments by daytime and nighttime conditions, as well as VOC precursor mixtures. We compare the observed values of $K_{p,ON}$ (Eq. 4.6) to the theoretical values of $K_{p,ON}$ for various ON structures at a given temperature (Eq. 4.7). The chemical structures are interpreted based on the key m/Q identified by gas-phase and particle-phase CIMS. Through this comparison, we can assess whether the gas-particle partitioning of the bulk ON reflects the ON composition formed from each experiment.

To determine C_{pON}/C_{gON} and $K_{p,ON}$, we performed two sets of calculations, using the loss corrected concentrations and the instantaneous measured concentrations (not loss corrected). We compare the results from the two calculation methods, but the calculation using the instantaneous measured concentrations is the main result presented in this chapter since they represent the actual equilibrium occurring in the chamber. Furthermore, we also need to consider the uncertainty of $K_{p,ON}$ (as one standard deviation). This uncertainty is propagated from C_{pON}, C_{gON}, and m_{tot}, detailed in Section S2.3 in the Supplement of Nursanto et al. (2026).

4.3 Results and discussion

4.3.1 Estimating organic nitrate yields

The consumed VOC mixing ratio in each chamber experiment is presented in Table 4.2. A detailed list of the consumed VOCs are provided in Tables S1, S2, S3, S4, and S5 in the Supplement of Nursanto et al. (2026). In general, we observed a higher consumption of VOCs under daytime conditions compared to nighttime conditions. We observed across experiments a decrease by 96 % in average of isoprene signal/concentration under daytime conditions and 61 % under nighttime conditions. For monoterpenes, limonene is completely consumed (98–100 %) for both daytime and nighttime conditions, while the consumption of α-pinene and β-pinene varied from 63 % up to 100 %. Saturated and unsaturated aldehydes (carbon number ≥ 5; i.e., pentenal, hexadienal, heptanal, octenal, nonanal, decanal) showed a decrease of signal/concentration by 20 % to 99 % under daytime conditions and by 22 % to 59 % under nighttime conditions. Aromatic VOCs (i.e., toluene and xylenes) were consumed from 39 % to 87 % under daytime conditions and 22 % to 51 % under nighttime conditions.

With the percentage of VOCs consumed varying depending on the compound and the oxidation conditions (daytime vs. nighttime), the ON molar yields range between 2–21 % (see Table 4.2). Higher yields are observed for the experiments using only limonene and source-specific emission profiles as precursors (i.e., cooking, gasoline, diesel). The source-specific emission profiles contain a high percentage of unsaturated compounds such as isoprene, monoterpenes, sesquiterpenes, unsaturated aldehydes, and alkenes (see Fig. 4.2), which are susceptible to addition reactions, thereby increasing the likelihood of ON formation. The daytime and nighttime limonene experiments both show 19 % yields, 11–15 % lower compared to the 34 % yield from $OH^{\bullet}$+limonene experiment reported by Pang et al. (2022) and 30 % yield from $NO_3^{\bullet}$+limonene experiment reported by Fry et al. (2011). The cooking emission replicas show 14 % and 11 % yield for low and medium NO conditions, respectively. The traffic-related emission replicas show a yield range of 13–21 %.

In contrast, experiments replicating VCPs and more complex urban emission profiles (i.e., the replica of Los Angeles city, global city, and future city emission profiles) have 2–7 % yields, lower compared to the experiments replicating other source-specific emission profiles. Since complex urban emission replicas also contain VCPs, we suggest that VCP emissions may drive the suppression of ON yields. They contain a higher percentage of lighter VOCs that do not contribute significantly to the mass of ON formed in these experiments. Lower amounts of consumed VOCs are observed for these compounds from compound families such as alkanes (e.g., 17–36 % for isobutane) and alcohols (e.g., 17–38 % for ethanol and 24–32 % for isopropyl alcohol).

Table 4.2: List of ON yields (and their uncertainty) from experiments in the SAPHIR-CHANEL 2024 campaign included in this work, which were grouped based on volatile organic compound (VOC) precursors and arranged in ascending order from low NO to high NO levels, including nighttime conditions. The yields are presented as the molar ratio of total ON formed in the gas and particle phases to the expected consumed VOC concentrations ($\Delta C_{ON,tot}/\Delta C_{VOC}$, in %). The molecular weight of $pRONO_2$ (MW_{pRONO_2}, in $g \cdot mol^{-1}$) and $pRONO_2$ mass fraction to the total organic aerosol mass (OA) ($\Delta C_{pRONO_2}/\Delta C_{OA}$, in %) are also listed. The particle phase concentrations are wall loss and dilution corrected, while the gas phase concentrations are dilution corrected.

VOC precursor	Oxidation and NO conditions	Injected VOC ($C_{VOC,i}$, ppb)	Consumed VOC (ΔC_{VOC}, ppb)[a]	Total ON formed ($\Delta C_{ON,tot}$, ppb)	MW_{pRONO_2} ($g \cdot mol^{-1}$)	$pRONO_2$ formed (ΔC_{pRONO_2}, $\mu g \cdot m^{-3}$)	Total OA formed (ΔC_{OA}, $\mu g \cdot m^{-3}$)	% Molar yield[b] ($\frac{\Delta C_{ON,tot}}{\Delta C_{VOC}}$)	% Mass fraction[c] ($\frac{\Delta C_{pRONO_2}}{\Delta C_{OA}}$)
Single-compound precursor									
limonene[b]	daytime, low NO	23	23	4.3	258.4	3.9	31.9	19 ± 3	9 ± 3
	nighttime	9	8	1.6	336.7	4.5	8.6	19 ± 4	32 ± 11
Source-specific emission mixture									
VCPs	daytime, low NO	207	62	4.3	241.7	0.8	4.5	7 ± 4	11 ± 5
	daytime, medium NO	205	62	3.6	241.2	0.7	3.3	6 ± 3	12 ± 6
	daytime, high NO	200	59	2.8	245.9	0.7	2.9	5 ± 3	15 ± 8
	nighttime	101	27	1.7	311.6	3.6	5.2	6 ± 4	49 ± 17
diesel emission	daytime, medium NO	31	14	1.8	295.8	0.5	1.1	13 ± 5	32 ± 12
	daytime, high NO	31	14	3.1	320.0	0.7	2.4	21 ± 8	23 ± 10
gasoline emission	daytime, medium NO	43	20	3.2	260.9	0.4	0.8	16 ± 6	34 ± 17
	daytime, high NO	43	21	4.4	274.6	0.9	1.5	21 ± 8	44 ± 17
cooking emission	daytime, low NO	43	24	3.3	214.7	0.5	2.1	14 ± 4	18 ± 5
	daytime, medium NO	43	28	3.1	248.7	0.6	1.7	11 ± 3	26 ± 8

Continues next page

Table 4.2: (continued)

VOC precursor	Oxidation and NO conditions	Injected VOC ($C_{VOC,i}$, ppb)	Consumed VOC (ΔC_{VOC}, ppb)[a]	Total ON formed ($\Delta C_{ON,tot}$, ppb)	MW_{pRONO_2} ($g \cdot mol^{-1}$)	$pRONO_2$ formed (ΔC_{pRONO_2}, $\mu g \cdot m^{-3}$)	Total OA formed (ΔC_{OA}, $\mu g \cdot m^{-3}$)	% Molar yield[b] ($\frac{\Delta C_{ON,tot}}{\Delta C_{VOC}}$)	% Mass fraction[c] ($\frac{\Delta C_{pRONO_2}}{\Delta C_{OA}}$)
Complex urban mixture									
Los Angeles anthr. emiss.	daytime, medium NO	247	95	3.2	242.4	0.6	1.9	3 ± 2	20 ± 11
	nighttime	247	78	2.5	341.5	2.1	1.6	3 ± 2	53 ± 42
Los Angeles anthr. +biogenic emission	daytime, low NO	234	113	3.4	262.4	1.0	6.2	3 ± 1	10 ± 4
	daytime, medium NO	234	103	2.5	253.9	0.8	6.4	2 ± 1	9 ± 3
	daytime, high NO	234	98	5.7	268.1	1.7	12.7	6 ± 2	11 ± 3
	nighttime[c]	234	82	4.4	336.1	5.6	8.4	5 ± 3	37 ± 15
global city anthr. emission	daytime, medium NO	241	104	4.3	246.2	0.5	1.5	4 ± 2	20 ± 9
future city anthr. +biogenic emission	daytime, low NO	232	107	2.4	260.2	1.2	10.8	2 ± 1	8 ± 3

[a] The consumed VOC mixing ratio is calculated based on the percentage of signal decrease of individual precursor compound, observed by various instruments, multiplied by the expected injected VOC mixing ratio (see Tables S1, S2, S3, S4, and S5 in the Supplement of Nursanto et al. (2026)).
[b] Limonene was injected several times at three distinct time period (interval 1–1.5 h each).
[c] NO_2+O_3 were added at two distinct times (interval 4 h).

4.3.2 Estimating molecular weight and mass fraction of particulate organic nitrate

Although the VOCs consumed under daytime conditions are higher than those under nighttime conditions, the ON molar yields are not higher for the daytime experiments compared to their nighttime counterparts. The different chemical mechanism of ON formation under daytime conditions ($OH^{\bullet}$ chemistry is prevalent) compared to nighttime conditions ($NO_3^{\bullet}$ chemistry is prevalent) likely explains this difference. The impact of the difference in chemistry is observed on the molecular weights of bulk pON as shown in Fig. 4.3a for composition when the SOA formation has peaked. The summary of the molecular weights can be found in Table 4.2. This is based on WALL-E observations assuming the same sensitivity for all masses detected. It is rather a comparative approach between different experiments and the discussion below is not affected by the fact that we are not quantifying everything with WALL-E. An average molecular weight of 331 $\pm$ 13 g $\cdot$ mol^{-1} is observed for nighttime experiments, higher compared to the average molecular weight of 258 $\pm$ 24 g $\cdot$ mol^{-1} for daytime experiments. The increase in dimer formation ($C_{>10}$ compounds) and less fragmentation ($C_{\leq 5}$ compounds) under nighttime conditions accounts for this difference. In Fig. 4.3b, we see higher contributions of heavier compounds with $C_{>10}$ (e.g., dimers) to the bulk pON under nighttime conditions, 56 % for the single-compound limonene experiment, 36 % for the VCP experiment, 51 % for the Los Angeles anthropogenic emission replica experiment, and 57 % for the Los Angeles anthropogenic+biogenic emission replica. On the other hand, experiments under daytime conditions only report 0–22 % contribution of $C_{>10}$ compounds.

To further show the contribution of ON to the total organic species, we determine the $pRONO_2$ mass fraction to the total OA of each chamber experiment in Table 4.2 and visualize them in Fig. 4.3c. We observe that the nighttime conditions for each VOC-NO_x mixture have a higher $pRONO_2$ mass fraction compared to their daytime counterparts. The percentage of $pRONO_2$ mass fraction under $NO_3^{\bullet}$ oxidation at nighttime conditions varies from 32–53 %, a factor of 2.6 to 4.5 higher than its daytime counterparts (9–20 %). VOCs from traffic and cooking emissions show varying $pRONO_2$ mass fractions ranging from 18–44 %. The difference can be partially explained by lower temperature and higher RH during nighttime experiments, which promote the condensation of ON that increases its mass fraction. Associated with their molecular weight, nighttime $NO_3^{\bullet}$ chemistry results in higher ON production with heavier compounds compared to daytime $OH^{\bullet}$ chemistry, thus converting a larger fraction of the organic precursor to organonitrates, leading to a higher contribution of $pRONO_2$ to the total SOA mass concentration. This shows that despite VOCs consumption under $OH^{\bullet}$ chemistry, more ON is formed in the particle phase under $NO_3^{\bullet}$ chemistry. This could also be caused by the reduction in SOA formation due to interactions between the products of different VOC precursors present in complex urban mixtures (McFiggans et al., 2019).

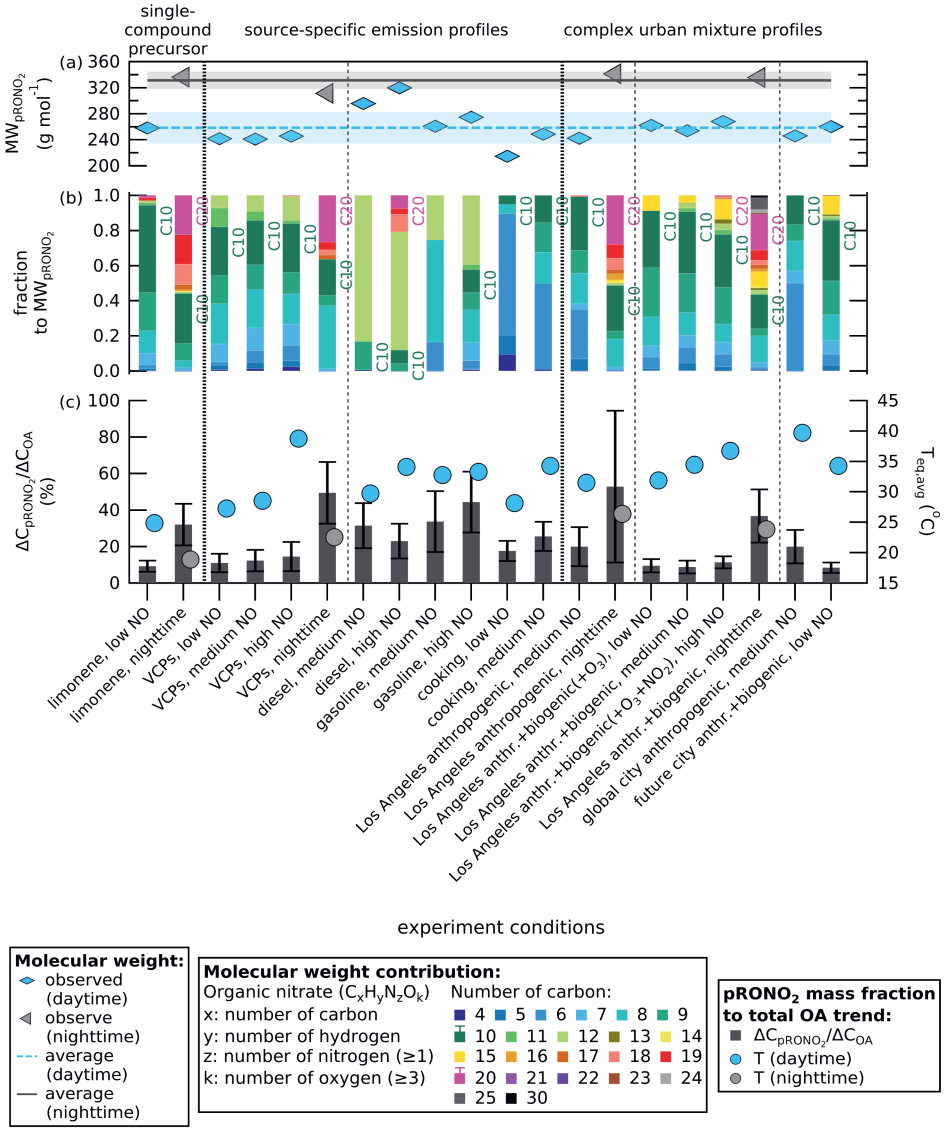


Figure 4.3: **(a)** Molecular weights of bulk pON as $pRONO_2$ ($g \cdot mol^{-1}$) determined using signals from WALL-E measurements when the SOA formation has peaked, sorted first by daytime versus nighttime conditions, and then by the complexity of the VOC precursor mixture. The plot shows an average of 331 ± 13 $g \cdot mol^{-1}$ for nighttime experiments and an average of 258 ± 24 $g \cdot mol^{-1}$ for daytime experiments (color shading represents one standard deviation of the average). **(b)** Contribution fraction of organic compounds color coded by the carbon atom number to the molecular weight of bulk pON. **(c)** $pRONO_2$ mass fraction over total OA (left y-axis, bars in %) and temperature (right y-axis, in °C). The whiskers represent the uncertainty of the mass fraction (one standard deviation).

4.3.3 Trends of gas-particle partitioning of bulk organic nitrate

Influence of oxidation and NO conditions

The particle-to-gas ratio of ON at equilibrium conditions can be used to compare the volatility of the bulk ON aerosol produced from different VOC precursor compositions in a reaction mixture, regardless of the total absorptive mass. We show in Fig. S7 in the Supplement of Nursanto et al. (2026) that differences in the partitioning are not driven by differences in the total aerosol mass. A summary of the concentrations or mixing ratios used for the calculation can be found in Tables S6 and S7 in the Supplement of Nursanto et al. (2026). We show only the results calculated using instantaneous observed gas and particle phase concentrations to represent the actual equilibrium in the chamber. The wall loss and dilution corrected concentrations have similar partitioning behavior compared to the instantaneous concentrations. They are found to systematically increase $C_{\mathrm{pON}}/C_{\mathrm{gON}}$ by 0.001–0.021, and systematically decrease $K_{\mathrm{p,ON}}$ by up to $3 \cdot 10^{-3}$ $\mathrm{m^3 \cdot \mu g^{-1}}$ (see Table S7 in the Supplement of Nursanto et al. (2026)).

For visualization, we use a particle-to-gas ratio scatter plot (see Fig. 4.4), where the y-axis is C_{pON} and the x-axis is C_{gON}. Scatter points falling on a line drawn from the origin point (0,0) to any coordinate $(x, y = (C_{\mathrm{gON}}, C_{\mathrm{pON}}))$ in the plot (shown as dashed grey lines) will have the same $C_{\mathrm{pON}}/C_{\mathrm{gON}}$ slope, and thus a similar profile but differ in concentrations. Scatter points falling on a larger slope have larger $C_{\mathrm{pON}}/C_{\mathrm{gON}}$, and thus higher species concentration in the particle phase. The plot shows the experiments classified based on the presence of light (daytime) and absence of light (nighttime) conditions (light blue and dark grey, respectively).

We observe that SOA formation under nighttime conditions is characterized by larger $C_{\mathrm{pON}}/C_{\mathrm{gON}}$ values (0.030–0.137) than under daytime conditions (0.007–0.045). This daytime and nighttime difference can be partially explained by the temperature and RH differences in the chamber. The temperature during nighttime experiments was systematically lower (18–26 °C) compared to the daytime experiments (24–40 °C) after SOA formation has been reached, which is also representative of real-world temperatures. This temperature drop also affected the nighttime RH (18–51 %) versus the daytime RH (13–42 %); see Table S7 in the Supplement of Nursanto et al. (2026) for details. Lower temperatures and higher RHs in this study are likely associated with higher $C_{\mathrm{pON}}/C_{\mathrm{gON}}$ values, which promote the condensation of low-volatility compounds into the particle phase to form SOA.

The availability of light also modifies the oxidation mechanism of organic species in the chamber. The presence of sunlight in daytime experiments enhances photolytic reactions that lead to $OH^{\bullet}$ formation, promoting oxidation reactions of organic compounds, forming ON (if terminated with NO_x) and non-ON species. In contrast, the absence of light favors a longer lifetime of the $NO_3^{\bullet}$ formed from NO_2 and O_3, which results in

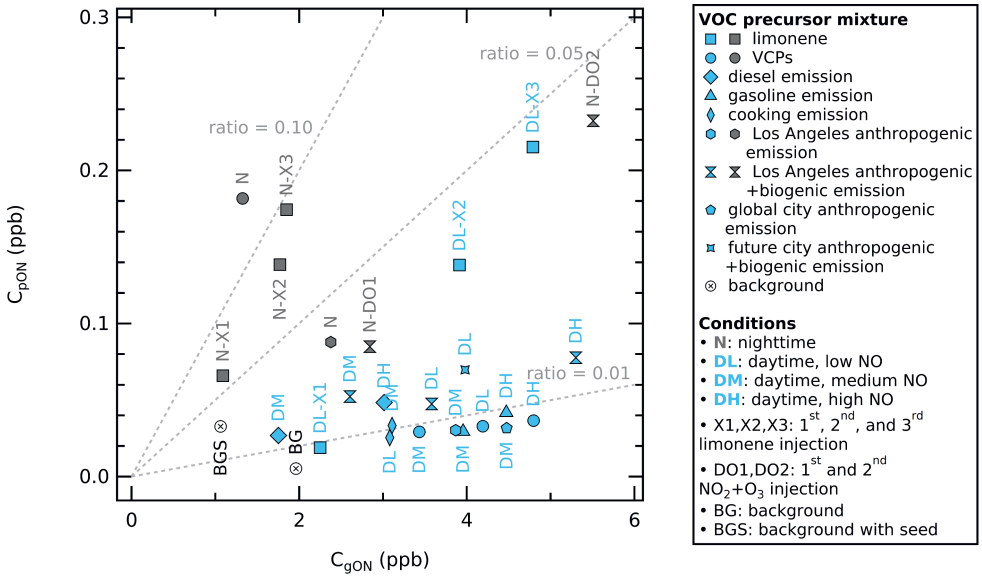


Figure 4.4: Scatter plot of particle phase ON (y-axis) vs. gas phase ON (x-axis) mixing ratio in ppb from different VOC-NO_x mixtures, color-coded by daytime conditions (light blue) and nighttime conditions (dark grey). The total absorptive mass of each experiment at equilibrium varies from 13 to 38 $\mu g \cdot m^{-3}$. The concentrations are the averages under equilibrium conditions. The dotted lines visualize different C_{pON}/C_{gON} values (0.01, 0.05, and 0.10).

the nighttime $NO_3^\bullet$ oxidation of organic compounds that will lead to the formation of ON. This is in line with several laboratory and chamber studies, which have shown that SOA formation from $NO_3^\bullet$ oxidation of BVOCs is larger compared to SOA formed from $OH^\bullet$ or O_3 oxidation (Hallquist et al., 1997; Griffin et al., 1999; Spittler et al., 2006; Ng et al., 2008; Fry et al., 2009; Fry et al., 2011; Rollins et al., 2009; Boyd et al., 2015; Ng et al., 2017). Ozonolysis reactions also contribute to SOA formation during daytime and nighttime conditions, but we expect the differences are by the differences in $OH^\bullet$ and $NO_3^\bullet$ chemistry.

The different C_{pON}/C_{gON} values are thus inferred to be related to differences in temperature and RH in the daytime and nighttime conditions, as well as ON volatilities in SOA formation caused by daytime $OH^\bullet$ versus nighttime $NO_3^\bullet$ chemistry. A higher C_{pON}/C_{gON} value implies a preference for species to condense into the particle phase, which is associated with lower-volatility species. The daytime and nighttime difference in average molecular weight is also consistent with the different chemical mechanisms and species volatility. However, the NO condition in this study does not seem to influence the particle-to-gas ratio of ON. This suggests that changes in the average NO

mixing ratio in the chamber (0.07–1.05 ppb) do not modify the chemical mechanism of ON formation and the volatility distribution of bulk ON.

Relationship between VOC precursor, particle-to-gas ratio, and ON composition distribution

We observe the clustering of certain urban VOC-NO_x mixtures in the particle-to-gas ratio scatter plot in Fig. 4.4 (see Fig. S6 in the Supplement of Nursanto et al. (2026) for the same plot but color-coded by the VOC precursor mixture). The VOC-NO_x mixtures from VCPs, cooking emission, diesel emission, and gasoline emission under daytime conditions have some of the lowest C_{pON}/C_{gON} values (0.007–0.016) compared to other experiments. VCPs and limonene VOC-NO_x mixtures under nighttime conditions have C_{pON}/C_{gON} values (0.061–0.137) up to 10 times higher than in the other experiments. The rest of the experiments are scattered in low and moderate C_{pON}/C_{gON} values (between 0.007–0.042), which are mainly complex urban VOC-NO_x mixtures (i.e., the Los Angeles emission, global city emission, and future city emission).

The differences in C_{pON}/C_{gON} across ON formation with different VOC precursors can be explained by looking further at the specific ON compounds measured in the bulk gas and particle phases. Each VOC precursor mixture contains different compounds with varying reactivities (i.e., functional groups, number of carbon atoms, hydrocarbon saturation; see Fig. 4.2), which affect the ON species formed in gas and particle phases. In Fig. 4.5, we plot the signal intensity of organic compounds containing at least one nitrogen and three oxygens (which is the minimum number for an ON species), detected by various chemical ionization mass spectrometer instruments in the gas phase (by NH_4^+-Vocus and amine-ToF) and in the particle phase (by WALL-E), to show the ON composition. We choose to show the ON composition from the experiment of limonene for the single-compound precursor, the experiment with VCP mixture for the urban emission mixture, and the experiment of Los Angeles anthropogenic+biogenic emission replica for the complex urban mixture. Profiles for experiments with other VOC precursors are shown in Fig. S6 in the Supplement of Nursanto et al. (2026).

We acknowledge that the composition profile may include other organic nitrogen compounds such as oxygenated amines or nitro compounds. The ON composition distribution shown here is an estimate of how the ON species signal is distributed across carbon and oxygen atom numbers, rather than the actual concentrations, as each detected species may have a different sensitivity in each instrument.

In general, both in Figs. 4.5 and S6 in the Supplement of Nursanto et al. (2026), we see that ON species are formed across varying numbers of carbon atoms in the gas phase. However, the distribution of carbon number of ON in the particle phase does not always match that in the gas phase. The ON species in the particle phase tend to be compounds with carbon numbers skewed around 10 (6–10) and 20 (15–20), which

are largely associated with the carbon backbone of monoterpenes (either whole or fragmented into smaller compounds) and their dimers. In terms of oxygen atom number, ON tends to have fewer oxygen atoms (3–8) in the gas phase, while ON tends to be more oxygenated (more than 6 atoms) in the particle phase. This is intuitive from the point of view of volatility-driven gas-particle partitioning, where more oxygenated species have lower volatility and are therefore more likely to partition to the particle phase than less oxygenated species. The further oxidation of the ON species starting from the gas phase until they condense into the particle phase is part of SOA formation and aerosol aging, which shapes the ON composition distribution.

The difference between the ON profiles of the daytime experiments (Figs. 4.5a–c and S6d in the Supplement of Nursanto et al. (2026)) and the nighttime experiments (Figs. 4.5d–f and S6e in the Supplement of Nursanto et al. (2026)) of limonene precursor, VCP mixtures, Los Angeles anthropogenic emission, Los Angeles anthropogenic+biogenic emission, and future city anthropogenic+biogenic emission profile is the most recognizable for the particle phase profile. In addition to species related to monoterpene compounds (carbon number 6–10), substantial signal fraction is observed for monoterpene dimers (carbon number 15–20) in the particle phase, where it represents 15–48 % of the total signal (difference in sensitivity is not yet considered). This result shows that photooxidation promotes the formation of monoterpene nitrates with lower carbon atom numbers (6–10), while oxidation processes under nighttime conditions in the chamber may favor $RO_2^{\bullet}$ production that leads to more dimer formation. Since dimers have lower volatility than their monomer counterparts, they are more likely to condense into the particle phase, possibly driving the higher $C_{\mathrm{pON}}/C_{\mathrm{gON}}$ values for the nighttime experiments.

In contrast, the daytime experiments using VOC precursors from diesel, gasoline, and cooking emissions show less species diversity in the particle phase (Fig. S6a–c in the Supplement of Nursanto et al. (2026)). These VOC precursor mixtures do not contain any or only trace amounts of biogenic compounds (2 % or less), and instead more anthropogenic VOCs from the alkane, alkenes, aromatic, and/or aldehyde compound family. This suggests that although these compounds may react to form ON in the gas phase and in the particle phase, they mostly produce high-volatility compounds that are less likely to condense into the particle phase and form SOA.

These interpretations require further analysis, as the ratio between the signals can change dramatically depending on the sensitivity of each compound or m/Q, and how they fragment. Additionally, thermal decomposition may also affect the measured particle phase, and thus the species distribution profile of ON. Nevertheless, these findings give some insight that even in a very complex urban emission and changing urban emission composition (for instance Los Angeles anthropogenic+biogenic emission

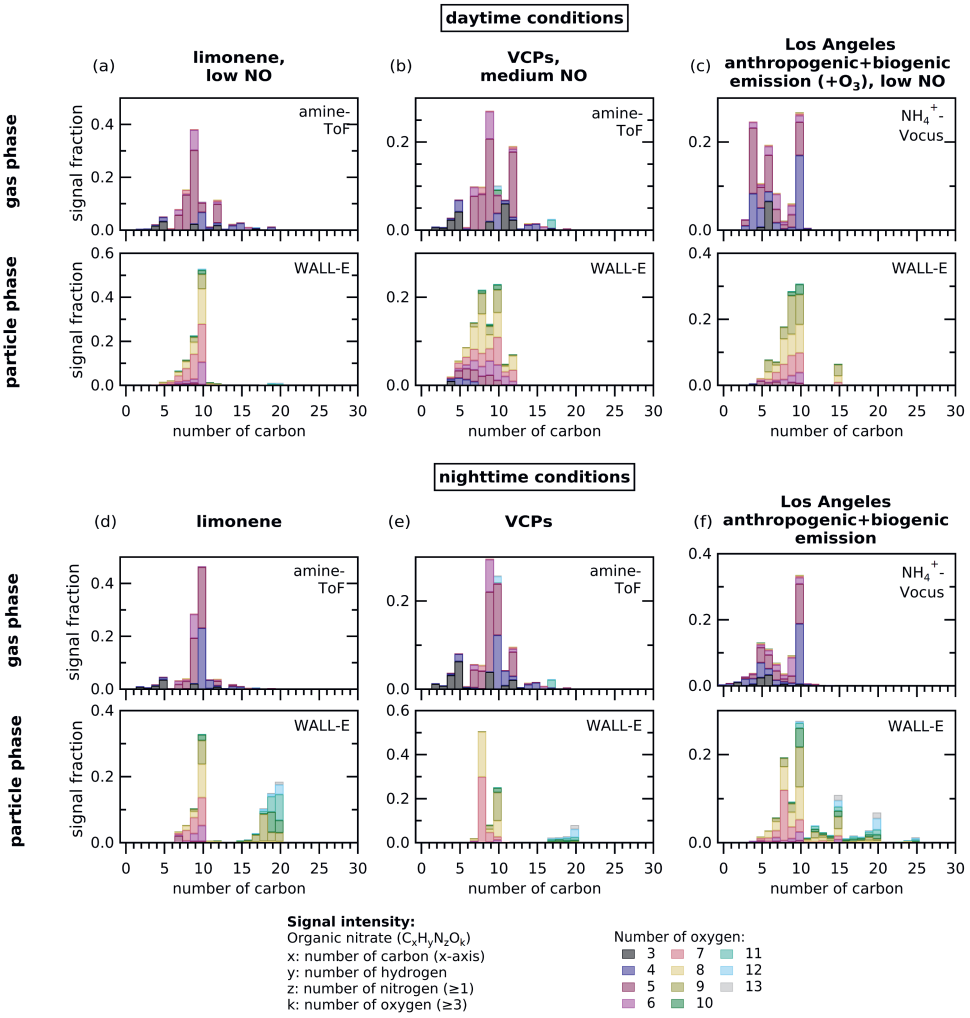


Figure 4.5: (a-f) The ON composition profiles in the gas phase and particle phase for selected chamber experiments (i.e., limonene, VCPs, and Los Angeles anthropogenic+biogenic emission experiments in daytime and nighttime conditions) when SOA formation has been reached. Experiments replicating diesel, gasoline, and cooking emission profiles are not compared since the nighttime experiments were not conducted for these profiles. The profiles show the signal fraction from the total signal intensity of detected species (y-axis) from either amine-ToF or NH_4^+-Vocus measurements in the gas phase and WALL-E measurements in the particle phase as function of the number of carbon (x-axis). The plots only include compounds with at least one nitrogen atom and three oxygen atoms. The color of the bars represents the signal fraction of compounds with a given number of oxygen atoms for each carbon number to all considered species in an individual experiment.

scenario vs. future city anthropogenic+biogenic emission scenario), BVOCs have a large impact shaping the ON species distribution in the bulk aerosol composition.

Observed vs. theoretical gas-particle partitioning coefficient ($K_{p,ON}$)

We compare the observed $K_{p,ON}$ at equilibrium (calculated using Eq. 4.6) for the different chamber experiments as a function of the average temperature in the chamber under equilibrium conditions ($T_{eq,avg}$) in Fig. 4.6. We visualize the results in this way because $K_{p,ON}$ depends on temperature. A summary of $K_{p,ON}$ values, concentrations, and temperatures used for the calculations for all experiments can be found in Tables S6 and S7 in the Supplement of Nursanto et al. (2026).

We found that the nighttime experiments of limonene precursor, VCP mixtures, Los Angeles emission profile, and Los Angeles anthropogenic+biogenic emission profile have higher $K_{p,ON}$ values compared to the daytime experiments with the same precursor. Similarly to the trend of the particle-to-gas ratio, lower chamber temperatures and higher RHs under nighttime conditions enhance the condensation of chemical species to the particle phase. This may seem biased since the daytime experiments are never done at lower temperature (and vice versa). However, we highlight that nighttime temperatures are lower than daytime temperatures in the real world as well, so that these results represent realistic scenarios. Furthermore, when we examine the $K_{p,ON}$ values at temperatures between 24 ^{o}C and 27 °C, for which both daytime and nighttime experiments were conducted, we see that the trend of higher $K_{p,ON}$ for nighttime experiments compared to daytime experiments still holds for similar temperatures. The uncertainty range also overlaps minimally between the $K_{p,ON}$ values. This indicates that the difference in $K_{p,ON}$ between nighttime and daytime conditions is due not only to temperature differences, but also to actual differences in chemical pathways, leading to the production of lower volatility and more oxygenated ON compounds under nighttime conditions.

The ON species shown in Fig. 4.6 to calculate the theoretical $K_{p,ON}$ values using the SIMPOL.1 group contribution method (Eq. 4.7) are chosen as a comparison with the observed $K_{p,ON}$ (calculated using Eq. 4.6). It should be noted that the ON compounds presented in Fig. 4.6 could not be specifically identified with the analytical techniques employed in this study; but are associated with the predominant m/Q values detected by the instruments (see Fig. 4.5). Most of the chemical structures were taken from the Master Chemical Mechanism, MCM v3.3.1 (Jenkin et al., 1997; Saunders et al., 2003; Jenkin et al., 2003; Bloss et al., 2005; Jenkin et al., 2015), via `www.mcm.york.ac.uk` (last accessed: 30 October 2025). Higher $K_{p,ON}$ values are typically associated with more oxygenated compounds and higher molecular weight, which lowers the compound's volatility. The purpose of showing the compounds is to contextualize the $K_{p,ON}$ values to the chemical structures, such as the bulk ON volatility, the oxygen number, and

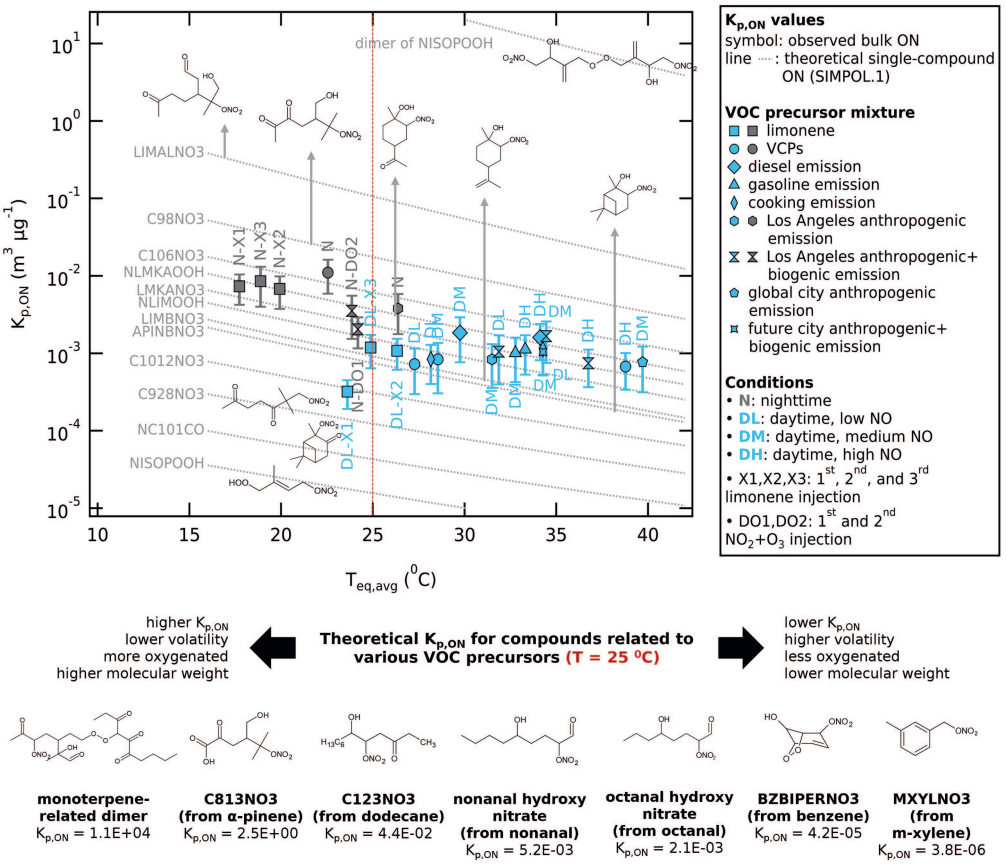


Figure 4.6: Scatter plot of $K_{p,ON}$ against the average chamber temperature at equilibrium ($T_{eq,avg}$) for various urban VOC-NO_x mixture experiments, color-coded by daytime and nighttime conditions. The whiskers represent ±46 % uncertainty (one standard deviation) of the bulk $K_{p,ON}$. The grey dashed lines show temperature-dependent theoretical $K_{p,ON}$ calculated using SIMPOL.1 method for various ON compounds, mostly from isoprene (e.g., NISOPOOH and dimer of NISOPOOH), α-pinene (e.g., NC101CO, APINBNO3), and limonene (e.g., C928NO3, C1012NO3, LIMBNO3, NLIMOOH, LMKANO3, NLMKAOOH). The chemical structures are not observed from the measurements but based on the m/Q detected by the instruments as comparison to the observed bulk $K_{p,ON}$. Chemical structures of selected ON compounds are shown in and below the plot.

the molecular weight. The estimation of volatility to calculate $K_{p,ON}$ using group contribution methods is not without uncertainty, as different computational methods provide a wide range of vapor pressures (Kurtén et al., 2016; Peräkylä et al., 2020). Kurtén et al. (2016) pointed out the limited ability of group contribution methods to distinguish between positional isomers, since the model only takes into account the

presence of functional groups in the structure. The volatility of compounds with a larger number of functional groups is likely to be overestimated (Peräkylä et al., 2020; Räty et al., 2021); increasing oxygenation of organic compounds was found to correspond to a more gradual decrease in volatility than expected based on many existing models, such as SIMPOL.

The range of observed $K_{p,ON}$ of the bulk ON is found to be in the same magnitude as theoretical $K_{p,ON}$ values calculated using the SIMPOL.1 method for many ON species formed from monoterpenes (e.g., LIMALNO3, C98NO3, C106NO3, NLMKAOOH, LMKANO3, NLIMOOH, LIMBNO3, C1012NO3, C928NO3, APINBNO3; notations from MCM) and ON species formed from long-chain aldehydes such as octanal and nonanal (e.g., octanal hydroxy nitrate, nonanal hydroxy nitrate), known to also be an important urban VOC precursor (Bowman et al., 2003; Coggon et al., 2024). These compounds have $K_{p,ON}$ values that range between those of isoprene-related species (e.g., NISOPOOH, more volatile) and their dimers (e.g., dimer of NISOPOOH, less volatile).

The match between the observed $K_{p,ON}$ values and the theoretical bulk ON structure is especially clear for the single-compound experiment using limonene, as limonene nitrate products are expected (see their ON profiles in Fig. 4.5a,d). The nighttime limonene experiment shows higher average $K_{p,ON}$ values compared to the daytime limonene experiment due to monoterpene dimers that have higher $K_{p,ON}$ values. In experiments with cooking emission profile, the observed $K_{p,ON}$ values of the bulk ON are similar to the theoretical $K_{p,ON}$ values for the long-chain aldehyde nitrates and the monoterpene nitrates. This likely occurs because the replicated VOC mixture from cooking emission contains 66 % of aldehydes and 1 % of limonene, which are oxidized into ON compounds.

The $K_{p,ON}$ values for the bulk ON in the experiments with VOCs originating from gasoline and diesel emissions are also comparable to that of monoterpene-related ON species. This is interesting even though these emission profiles do not contain any monoterpenes in the VOC precursor mixture ($\sim$50 % is alkene, and alkanes are the second highest component). Fig. S6a,b in the Supplement of Nursanto et al. (2026) also shows that the ON profiles of the experiment with diesel and gasoline emission replicas do not match the ON profiles of the limonene precursor experiment. Thus, the bulk $K_{p,ON}$ is most likely determined by the mixture of higher volatility ON species (e.g., MXYLNO3 from m-xylene, BZBIPERNO3 from benzene) and lower volatility ON species (e.g., C123NO3 from dodecane) that average to a volatility similar to monoterpene nitrates.

The VCP mixture and complex urban mixtures (Los Angeles emission replicas) also have similar average $K_{p,ON}$ values to the monoterpene-related nitrates, but the ON profiles (see Fig. 4.5b,c,e,f and Fig. S6e,f in the Supplement of Nursanto et al. (2026)) resemble more the ON profile from the limonene experiments despite having only 1–6

% monoterpenes in the precursor mixture. This can be related to the high reactivity of limonene and α-pinene in the mixture. A higher contribution from C_8 compounds can also be observed in the nighttime ON profiles of these experiments (see Fig. 4.5e,f and Fig. S6f in the Supplement of Nursanto et al. (2026)). This increase could be attributed to the secondary oxidation products of pinene with very low volatility (e.g., C813NO3), formed from pinene precursors that are present exclusively in VCPs and complex urban precursor mixtures.

The above results indicate that the bulk volatility of total ON broadly agrees with the individually detected chemical species using high-resolution chemical ionization mass spectrometers. With the calibration and determination of compounds' sensitivity for each instrument, it may be possible to directly validate the agreement between the bulk partitioning and a weighted average of the partitioning coefficients calculated for the major species. These results also underscore the importance of monoterpenes in the formation of pON during SOA formation in a complex urban mixture, where the bulk volatility of ON behaves similar to monoterpenes.

We have presented the molar yield, molecular weight, and the gas-particle partitioning of bulk organic nitrate in different VOC-NO_x precursor mixtures in the SAPHIR-CHANEL chamber experiments. We observe the importance of unsaturated VOCs (e.g., monoterpenes, isoprene, aldehydes, alkenes) in modifying the organic nitrate molar yield, where higher yields are found in experiments with a higher percentage of unsaturated VOC precursors in the precursor mixture. The yield is found to be 19 % for experiments using limonene precursor, 11–21 % for experiments using VOCs from traffic and cooking emission, and 2–7 % for experiments with VCPs and complex urban mixture as precursors.

Regarding the particle phase organic nitrate, the characterization of the molecular weight of bulk particulate organic nitrate based on signal intensity of chemical ionization mass spectrometer shows that the average molecular weight is 258 $g \cdot mol^{-1}$ under daytime conditions and 331 $g \cdot mol^{-1}$ under nighttime conditions. This difference is mainly caused by the higher contribution of heavier compounds such as dimers and lower contribution of lighter compounds from fragmentations during nighttime organic nitrate formation. The mass fraction of particulate organic nitrate to the total organic aerosol is enhanced by nighttime conditions (32–53 %) when the nitrate radical chemistry is dominant, a factor of 2.6 to 4.5 higher compared to daytime conditions (9–20 %) when the hydroxyl radical chemistry is dominant. The ozonolysis chemistry may also have influence on these differences, but we expect the differences are due to contrasting hydroxyl radical and nitrate radical chemistry. Overall, this finding provides new insights in the average molecular weight of organic nitrate and its contribution to SOA formation in realistic urban atmospheric mixtures. However, further analysis is required that considers the instrument's sensitivity across different organic nitrate

compounds when determining the precise composition and molecular weight of bulk particulate organic nitrate.

In gas-particle partitioning, we observe that the nighttime conditions (lower temperature, high relative humidity, and nitrate radical chemistry) enhance the formation of low-volatility organic nitrates that partition to the particle phase, which has been observed in previous studies (Hallquist et al., 1997; Griffin et al., 1999; Spittler et al., 2006; Ng et al., 2008; Fry et al., 2009; Fry et al., 2011; Rollins et al., 2009; Boyd et al., 2015; Ng et al., 2017). This is represented by higher particle-to-gas ratios for experiments under nighttime conditions (0.030–0.137) compared to daytime conditions (0.007–0.045). From the organic nitrate profiles, we highlight that organic nitrate formation occurs across a wide range of gas phase species for every VOC precursor mixture, mainly with lower oxygenation (3–8 oxygen atoms). However, only species with a volatility similar to or lower than that of monoterpene nitrates mainly with higher oxygenation (>6 oxygen atoms) are observed to partition into the particle phase. The observed gas-particle partitioning coefficient, when treated as a bulk compound at equilibrium, shows that the bulk organic nitrate is comparable to the calculated values of monoterpene-related species using SIMPOL.1 method (10^{-4} to 10^{-2} $m^3 \cdot \mu g^{-1}$ at 18–40 °C), regardless of the complexity of the mixture. However, future studies should further investigate the specific particulate organic nitrate composition. The observed partitioning does not consider the thermal decomposition of organic nitrate compounds, and the chemical speciation measurements by the chemical ionization mass spectrometers only report signal intensity, not the concentration (sensitivity of each compound is uncertain). The group contribution method also typically overestimates the volatilities of compounds with higher oxygen numbers and is unable to distinguish positional isomers.

This work highlights the importance of biogenic VOCs and nighttime chemistry in shaping the molecular weight and bulk volatility of ON in complex urban mixtures with changing emission profiles (comparing Los Angeles, global cities, and future city emission scenario). In general, these findings can help us to model organic nitrate aerosol in complex urban atmospheres. This work provides the empirical information regarding the diurnal contrast of bulk organic nitrate yield, molecular weight, SOA mass fraction, and volatility, which can improve the accuracy of chemical transport models. This information is needed for better predictions of how nitrogen reservoir species will respond to a warming climate, which can affect urban air quality and nitrate deposition on ecosystems.

4.4 Conclusions

We have presented the molar yield, molecular weight, and the gas-particle partitioning of bulk organic nitrate in different VOC-NO_x precursor mixtures in the SAPHIR-CHANEL chamber experiments. We observe the importance of unsaturated VOCs

(e.g., monoterpenes, isoprene, aldehydes, alkenes) in modifying the organic nitrate molar yield, where higher yields are found in experiments with a higher percentage of unsaturated VOC precursors in the precursor mixture. The yield is found to be 19 % for experiments using limonene precursor, 11–21 % for experiments using VOCs from traffic and cooking emission, and 2–7 % for experiments with VCPs and complex urban mixture as precursors.

Regarding the particle phase organic nitrate, the characterization of the molecular weight of bulk particulate organic nitrate based on signal intensity of chemical ionization mass spectrometer shows that the average molecular weight is 258 $g \cdot mol^{-1}$ under daytime conditions and 331 $g \cdot mol^{-1}$ under nighttime conditions. This difference is mainly caused by the higher contribution of heavier compounds such as dimers and lower contribution of lighter compounds from fragmentations during nighttime organic nitrate formation. The mass fraction of particulate organic nitrate to the total organic aerosol is enhanced by nighttime conditions (32–53 %) when the nitrate radical chemistry is dominant, a factor of 2.6 to 4.5 higher compared to daytime conditions (9–20 %) when the hydroxyl radical chemistry is dominant. The ozonolysis chemistry may also have influence on these differences, but we expect the differences are due to contrasting hydroxyl radical and nitrate radical chemistry. Overall, this finding provides new insights in the average molecular weight of organic nitrate and its contribution to SOA formation in realistic urban atmospheric mixtures. However, further analysis is required that considers the instrument's sensitivity across different organic nitrate compounds when determining the precise composition and molecular weight of bulk particulate organic nitrate.

In gas-particle partitioning, we observe that the nighttime conditions (lower temperature, high relative humidity, and nitrate radical chemistry) enhance the formation of low-volatility organic nitrates that partition to the particle phase, which has been observed in previous studies (Hallquist et al., 1997; Griffin et al., 1999; Spittler et al., 2006; Ng et al., 2008; Fry et al., 2009; Fry et al., 2011; Rollins et al., 2009; Boyd et al., 2015; Ng et al., 2017). This is represented by higher particle-to-gas ratios for experiments under nighttime conditions (0.030–0.137) compared to daytime conditions (0.007–0.045). From the organic nitrate profiles, we highlight that organic nitrate formation occurs across a wide range of gas phase species for every VOC precursor mixture, mainly with lower oxygenation (3–8 oxygen atoms). However, only species with a volatility similar to or lower than that of monoterpene nitrates mainly with higher oxygenation (>6 oxygen atoms) are observed to partition into the particle phase. The observed gas-particle partitioning coefficient, when treated as a bulk compound at equilibrium, shows that the bulk organic nitrate is comparable to the calculated values of monoterpene-related species using SIMPOL.1 method (10^{-4} to 10^{-2} $m^3 \cdot \mu g^{-1}$ at 18–40 °C), regardless of the complexity of the mixture. However, future studies should further investigate the specific particulate organic nitrate composition. The observed partitioning does not

consider the thermal decomposition of organic nitrate compounds, and the chemical speciation measurements by the chemical ionization mass spectrometers only report signal intensity, not the concentration (sensitivity of each compound is uncertain). The group contribution method also typically overestimates the volatilities of compounds with higher oxygen numbers and is unable to distinguish positional isomers.

This work highlights the importance of biogenic VOCs and nighttime chemistry in shaping the molecular weight and bulk volatility of ON in complex urban mixtures with changing emission profiles (comparing Los Angeles, global cities, and future city emission scenario). In general, these findings can help us to model organic nitrate aerosol in complex urban atmospheres. This work provides the empirical information regarding the diurnal contrast of bulk organic nitrate yield, molecular weight, SOA mass fraction, and volatility, which can improve the accuracy of chemical transport models. This information is needed for better predictions of how nitrogen reservoir species will respond to a warming climate, which can affect urban air quality and nitrate deposition on ecosystems.



Chapter 5

How do the chemical composition of emissions and meteorology influence inorganic and organic nitrate aerosol formation in the Netherlands?

Abstract

In an atmosphere dominated by high concentrations of nitrogen oxides (NO_x = $NO+NO_2$) and ammonia (NH_3), it is important to determine the lifetime of reactive nitrogen, which determines its transport distance before deposition. This lifetime is expected to depend on the speciation of inorganic/organic nitrate and gas-particle partitioning of organic nitrate (ON). By combining continuous measurements of meteorological parameters and ambient gas-phase and particle-phase compounds, we address the variability in reactive nitrogen composition of nitrate aerosol pollution episodes observed in Cabauw, a centrally located rural research station that receives airmasses from across the Netherlands. The volatility differences of semi-volatile ammonium nitrate and less-volatile ON to changing seasons are shown to play a key role in modifying the inorganic/organic nitrate aerosol speciation and the total particulate nitrate concentrations. The high frequency of pollution episodes with nitrate concentration $>0.8\ \mu g \cdot m^{-3}$ during winter (Oct–Feb) is accompanied by lower total ON mixing ratios (2–4 ppb) and lower particulate ON fraction of total nitrate (14–43 %) compared to summer (Mar–Sep; 7–11 ppb; 30–58 %). This trend is associated with a nitric acid (HNO_3)-dominated regime in winter. Weaker solar radiation limits ON formation. In contrast, lower temperatures favor condensation of semi-volatile ON and ammonium nitrate. An organic nitrate ($RONO_2$) regime becomes more important in summer in addition to HNO_3, due to higher temperatures and solar radiation. Slightly over 50% of the nitrate pollution episodes are associated with urban coastal airmasses that have lower particulate ON fractions but higher total nitrate concentrations due to the shorter transport distance from the NO_x emission hotspot to the west. Continental plumes transported from the east are characterized by aged aerosols with higher particulate ON fractions but lower total nitrate concentrations. With this study, we show that in order to assess the impact of emission reduction strategies that target nitrate aerosol reduction, seasonality of the chemical regime should be considered. The varying influence of emissions from different source regions highlights the importance of international cooperation in emission reduction strategies.

5.1 Introduction

Northwestern Europe is a major hotspot for reactive nitrogen emissions. As the main reduced nitrogen species, ammonia (NH_3) is emitted from agricultural fertilizer use, livestock, industries, and exhaust from vehicles with catalytic converters (Groot Koerkamp et al., 1998; Galloway et al., 2003; Erisman et al., 2007; Skjøth and Hertel, 2013; Wen et al., 2023). Oxidized nitrogen species come mainly from vehicles and industry through oxidation of N_2 during fuel combustion, emitting nitrogen oxides (NO_x = NO + NO_2) (Eyring et al., 2010; Johansson et al., 2017; Crippa et al., 2018; Fortems-Cheiney et al., 2021). Some of the major ports in Europe are located in this region (e.g., port of Rotterdam, port of Antwerp, Schiphol Airport, and Frankfurt Airport), contributing substantially to NO_x emissions (Valastro et al., 2023; Tokaya et al., 2024). In the Netherlands, NH_3 accounted for emissions of 100 $Gg \cdot N \cdot y^{-1}$ in 2022, with 87 % originating from agricultural activities (CBS, 2024; Staats et al., 2025). For NO_x, emissions reached 49 $Gg \cdot N \cdot y^{-1}$ in 2022, with the transportation sector accounting for 57 % of the emissions (CBS, 2024; Staats et al., 2025).

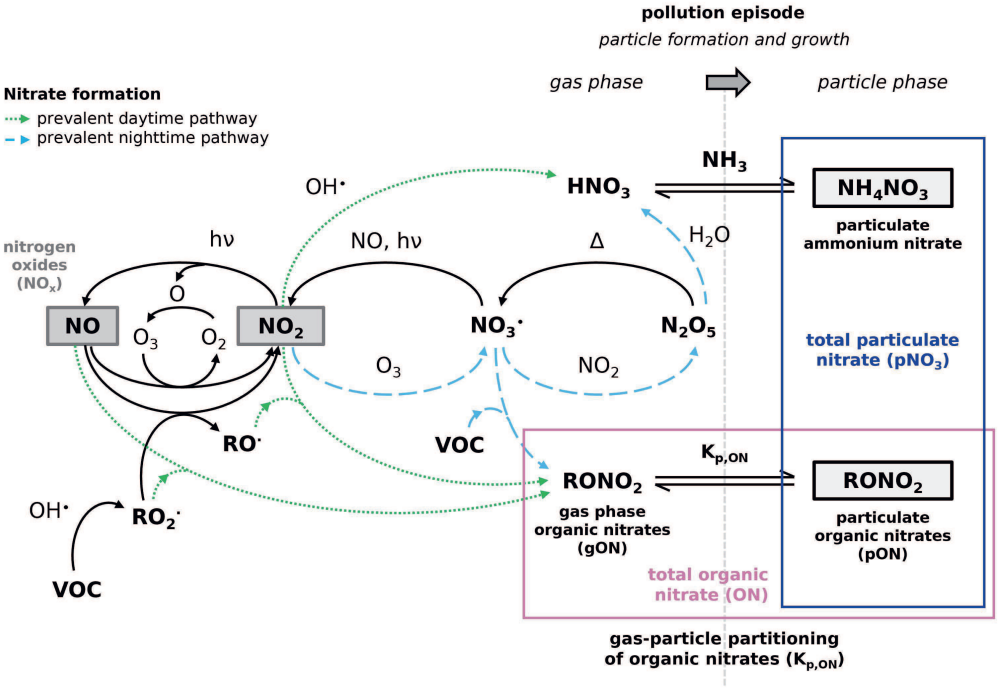


Figure 5.1: Chemical reactions showing the dominant fates of NO_x as NH_4NO_3 and $RONO_2$ in the atmosphere during daytime and nighttime.

NO_x has several fates, as shown in Fig. 5.1. The reaction of NO_2 with $OH^\bullet$ converts NO_x emissions to nitric acid (HNO_3) that can then form ammonium nitrate (NH_4NO_3) with NH_3 in equilibrium as secondary inorganic aerosol (SIA). Due to the decrease in sulfur oxide (SO_x) emissions in the Netherlands (Velders et al., 2011), this pathway is increasingly important relative to ammonium sulfate ($(NH_4)_2SO_4$) formation. Reductions in both SO_x and NO_x emissions also result in the increase of gas-phase NH_3 concentration in the atmosphere, modifying its chemistry, lifetime, and deposition (Fagerli and Aas, 2008; Huang et al., 2011; Saylor et al., 2015; Lawal et al., 2018; Chen et al., 2019; Davuliene et al., 2021). Under nighttime conditions, nitrate radical ($NO_3^\bullet$) formed from NO_2 build up due to lack of photolysis, which is then further transformed into nitrogen pentoxide (N_2O_5) which can be hydrolyzed into HNO_3 to form NH_4NO_3. NO_x can also react with organic radicals ($RO_x^\bullet$) from the oxidation of volatile organic compounds (VOCs) to form organic nitrates ($RONO_2$ or ONs) as a gas-phase species, which can subsequently condense to become a component of secondary organic aerosol (SOA). At night, the ON formation pathway from the reaction between $NO_3^\bullet$ and VOCs is more prevalent. Both NH_4NO_3 and ONs are reservoir species that allow efficient reactive nitrogen transport away from source regions followed by (wet) deposition to remote ecosystems or potential re-release of gas-phase NO_x.

Although the gas-particle partitioning of NH_4NO_3 is well established in simulations (Fountoukis and Nenes, 2007; Aan de Brugh et al., 2012; Aan de Brugh et al., 2013; Barbaro et al., 2015; Kelly et al., 2018; Lin et al., 2024), there is less knowledge about the gas-particle partitioning of ONs, since ONs encompass many different compounds with high temporal and spatial variability. Studies have shown that the average fraction of particulate organic nitrate (pON) in the total nitrate aerosol (pNO_3) in Europe is 34–44 % (Kiendler-Scharr et al., 2016), reaching up to ∼60 % in the Netherlands (Nursanto et al., 2025). Studies in the United States have shown that as NO_x declines with emission reduction efforts, the NO_x sink to ON is becoming more important compared to NH_4NO_3 due to the abundance of biogenic VOCs (Browne and Cohen, 2012; Hidy et al., 2014; Simon et al., 2015). A study shows that NO_x loss and atmospheric composition in the southeastern United States over recent decades generally shifted from HNO_3-dominated regime towards $RONO_2$-dominated regime due to higher VOC reactivity and low NO_2 reactivity (Romer Present et al., 2020). We expect similar processes to shift gas-particle partitioning of nitrate compounds in the Netherlands.

When an ON compound has low volatility or is soluble in water, it can condense in the particle or aqueous phase and extend the multiphase chemical lifetime ranging up to 97 h (González-Sánchez et al., 2023), longer than the lifetime of gas-phase NO_x of 2–8 h in polluted areas (Singh, 1987; Lange et al., 2022). With the increasing importance of the $RONO_2$ chemical regime, ON compounds can transport NO_x further downwind from dense urban or port areas to nature areas (Romer et al., 2016; Xiong et al., 2016; Romer Present et al., 2020), impacting remote ecosystems and human populations. This

includes destructive effects on natural habitats (Erisman et al., 2011; Swaluw et al., 2011; Wamelink et al., 2013; Le Moal et al., 2019) and the deterioration of public health due to pollution or haze episodes (Erisman et al., 2015; Pope et al., 2020; De Vries, 2021; Hang et al., 2022).

The conversion of NH_3 and NO_x to NH_4NO_3 has been the focus of most nitrogen deposition studies, while the chemistry of ONs is less well established. The LOTOS-EUROS (v1.8) chemical transport model with missing process descriptions for reactive nitrogen species and SOA showed 40 % underestimation of total particulate matter $<$10 μm (PM_{10}) and 20 % underestimation of particulate nitrate concentration (assumed to be inorganic nitrate) in the Netherlands (Kranenburg et al., 2013). Some of these missing descriptions are addressed in the later version of LOTOS-EUROS (v2.0), which reduces the underestimation but still needs improvements (Manders et al., 2017). This discrepancy likely stems from a simplified representation of ON gas-particle partitioning that involves diverse VOC precursors. Controlled chamber experiments using replicas of urban air mixture conducted during the CHANEL (Household Chemicals Amplifying Urban Aerosol Pollution) campaign in the SAPHIR (Simulation of Atmospheric Photochemistry in a Large Reaction Chamber) revealed that the gas-particle partitioning of organic nitrates is dynamic. The study demonstrated that the bulk volatility of organic nitrates resembles the volatility of monoterpene-related nitrates and varies depending on the VOC precursor composition and oxidation chemistry taking place (e.g., daytime vs. nighttime conditions) (Nursanto et al., 2026).

To address the knowledge gap in nitrate gas-particle partitioning, we aim to characterize the ambient atmospheric composition of nitrate aerosol in the Netherlands. We evaluate the formation pathways of particulate nitrate at a central Netherlands rural site (Cabauw) as a function of season, time of the day, and wind direction. We investigate the gas-particle partitioning of organic nitrate to understand how much organic nitrate contributes to SOA formation. By using a bulk ON gas-particle partitioning coefficient ($K_{p,ON}$), we can identify candidate organic nitrate species in the bulk composition, based on comparison with theoretical group contribution theory estimates of $K_{p,ON}$. We focus on the gas-particle partitioning of ON during pollution events due to their role in air quality degradation. This focus on pollution events is also convenient because it ensures that we are well above the detection limit of instruments, and that we are representing the partitioning equilibrium under stable atmospheric conditions. Using year-long field measurements of total oxidized nitrogen species (NO_y = NO_x + NO_z), gas and aerosol chemical composition, alongside the Copernicus Atmospheric Monitoring Service (CAMS) data set, we aim to capture the variability in pathways of nitrate aerosol formation in the Netherlands and how other chemical species affect its formation. With this, we hope to bridge the observational knowledge gap and to support improved nitrogen deposition simulations (e.g., Operational Priority Substance (OPS) model (Sauter et al., 2025)).

5.2 Methods

5.2.1 Site description

Measurements were performed at the Cabauw tower (51.97 °N, 4.93 °E), managed and operated by the Royal Netherlands Meteorological Institute (KNMI; the Netherlands) (see Fig. 5.2). The tower is located near Cabauw, the Netherlands, approximately 18 km southwest of city of Utrecht city, 31 km east of the city of Rotterdam, 45 km south of Amsterdam, and 45 km southeast of the Dutch North Sea coast. East and south of the site are regions that consist mainly of forests, agricultural lands, and animal farms (CBS, 2022). The Cabauw site itself is rural and is surrounded by agricultural lands, located in the center of the country. Air composition at Cabauw is influenced by different emission mixtures, making it advantageous to study nitrate aerosol formation as a function of different precursors. Airmasses from the coastal region bring emissions from urban centers known as the Randstad, which includes the port of Rotterdam (Europoort-Maasvlakte, the largest in Europe), industrial areas, and an international airport (Schiphol), that are hotspots of NO_x emissions. Since these emission areas are nearby, it is more likely for NO_x from the coastal region to reach the Cabauw measurement site. In contrast, trajectories from inland bring airmasses from continental Europe (with cities and industries further away) as well as traveling over nature areas that have higher biogenic VOC emissions such as isoprene and monoterpenes (Oomen et al., 2024).

Table 5.1: Summary of meteorological conditions categorized into summer (Mar–Sep) and winter (Oct–Feb) periods.

Season	Period	Length	Temperature (°C)	Global radiation ($W \cdot m^{-2}$)	Precipitation (mm)
Summer	Apr–Jul 2023 Mar–Apr 2025 Jul–Sep 2025	207 d (∼7 mo)	Mean: 15 Min: -4 Max: 32	Mean: 206 Max: 914	Monthly mean: 41
Winter	Oct 2024– Feb 2025	117 d (∼4 mo)	Mean: 6 Min: -5 Max: 19	Mean: 39 Max: 492	Monthly mean: 67

The data set in this study contains overlapping observations of aerosol chemical speciation monitor (ACSM) and total NO_y from 18 April 2023 to 23 July 2023, 21 October 2024 to 27 April 2025, and 11 July 2025 and 4 September 2025 (total 324 d excluding measurement gaps). Weather data were retrieved from the Royal Netherlands Meteorological Institute (KNMI; `https://www.knmi.nl/home`, last access: 8 October 2025), which includes net radiation, wind parameters, and temperatures. The data set is divided into two seasons, consisting of March–September for summer and October–February

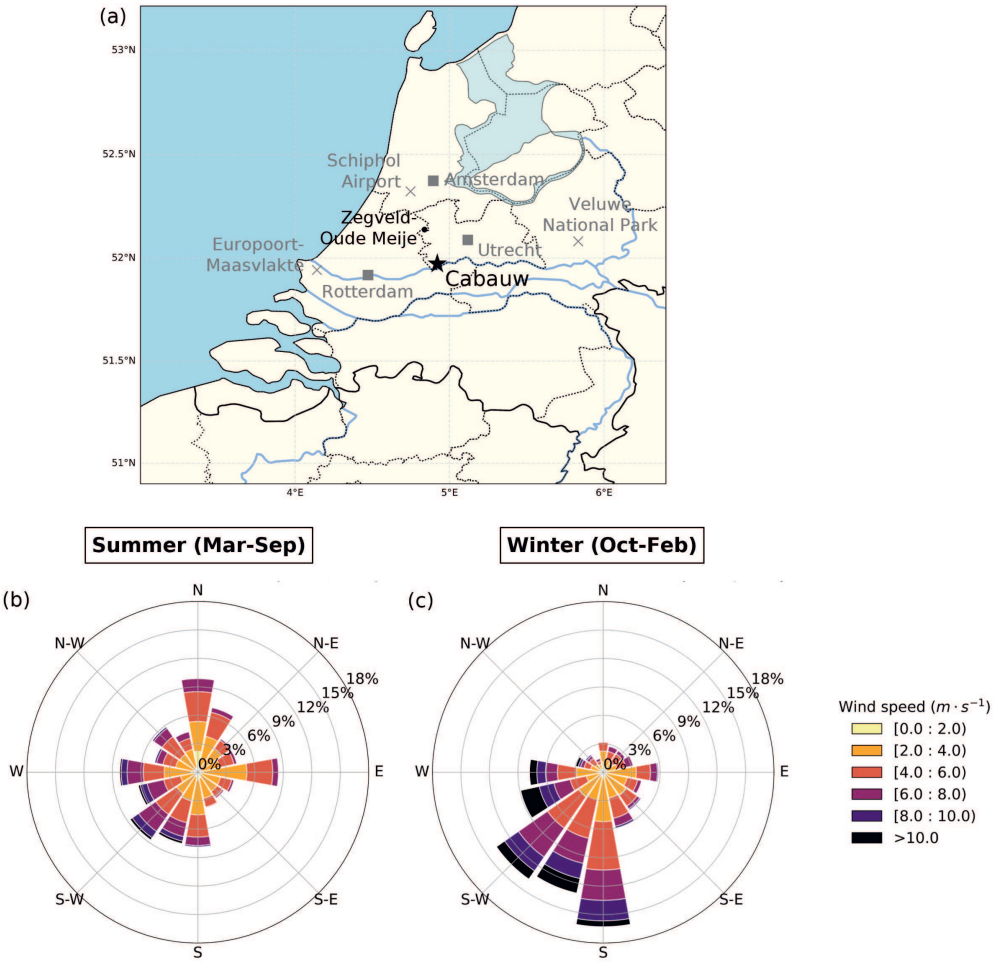


Figure 5.2: Plot **(a)** shows the locations of the Cabauw site (main site, star symbol) and Zegveld-Oude Meije site (NH_3 measurements, full black dot) in central Netherlands, and plots **(b)** and **(c)** show average wind roses for summer and winter months (2023–2025 with gaps). The big cities and ports, i.e., Amsterdam, Rotterdam, Europoort-Maasvlakte, Schiphol Airport, are situated within the Randstad, a region where most urban and industrial activities take place in the country. Coastal airmasses from the North Sea pass over the Randstad, bringing pollutants from urban and shipping emissions. In contrast, the inland Dutch regions contain more nature areas, agricultural lands, and animal farms. The continental airmasses are associated with more BVOC emissions and bring pollutants transported from neighboring countries and other inland regions.

for winter, providing seasonal variations. These periods are considered to match the trend of higher NH_3 concentration during summer, related to agricultural activities

(Vendel et al., 2023) and the authorization of manure applications during this period. The diurnal variability is also considered, where the nighttime and daytime conditions are differentiated based on radiation. Temperatures, global radiation, precipitation, and average wind frequency are shown in Table 5.1. The summer and winter had mean temperatures of 15 and 6 °C, respectively, while the mean global radiation is 206 $W \cdot m^{-2}$ and 492 $W \cdot m^{-2}$, respectively. The average monthly precipitation was the highest in winter (67 mm as monthly mean), and the lowest in summer (41 mm as monthly mean). The wind direction was distributed more evenly into different wind sectors in summer, while southwesterly and southerly wind sectors were more frequent during winter.

5.2.2 Aerosol chemical speciation monitor (ACSM)

The Aerodyne time-of-flight aerosol chemical speciation monitor (ToF-ACSM) measures non-refractory organics, ammonium, nitrate, sulfate, and chloride in the particle phase. The details of the instrument are described in Fröhlich et al. (2013). Ambient air is sampled at 4.5 m height through a stainless-steel inlet system equipped with a $PM_{2.5}$ size-cut cyclone (URG-2000-30ED) and a Nafion dryer, with a flow rate of $\sim$2 $L \cdot min^{-1}$. The intermediate-pressure lens (IPL) is used as an aerodynamic lens, which allows the transmission of particles in the $PM_{2.5}$ fraction (Xu et al., 2017). The instrument is equipped with a capture vaporizer (CV) instead of a standard vaporizer (SV) to increase the particle collection efficiency (CE) (Jayne and Worsnop, 2016). The CV increases particle collision by having a narrow entrance and therefore increases contact with the hot vaporizer surface, minimizing non-evaporated particles and resulting in CE = 1 (Hu et al., 2017). However, it causes fragmentation patterns to shift towards smaller ion masses due to additional thermal decomposition (Hu et al., 2017; Xu et al., 2017; Zheng et al., 2020). The combination of the $PM_{2.5}$ size-cut cyclone, the $PM_{2.5}$ aerodynamic lens, and the CV allows the ToF-ACSM to be a $PM_{2.5}$ measurement (Xu et al., 2017).

The ToF-ACSM provides unit mass resolution (UMR) mass spectra with a 10 min time resolution, which are analyzed using Tofware v3.3 in Igor Pro 8. The fractions of measured UMR signals were assigned to individual aerosol species using the fragmentation table (Allan et al., 2004). The fragmentation table entry for selected Org and NO_3 masses (Org_[30], NO_3_[30], Org_[46], and NO_3_[46]) are updated according to the general fragmentation table adapted for CV-UMR-ToF-ACSM (Nursanto et al., 2025). Several calibrations were performed throughout the deployment of the instrument to determine the ionization efficiencies of the chemical species. The calibrations of the ionization efficiency (IE) and relative IE (RIE) were performed using 300–350 nm diameter particles from pure ammonium nitrate (NH_4NO_3) and ammonium sulfate ($(NH_4)_2SO_4$) dissolved in aqueous solutions. Since the data set encompasses a long period and the instrument's detector has been replaced, different calibration parameters and detection

limits are used for two periods, 2023 and 2024–2025 (see Table A.1 and Table A.2 in the Appendices).

5.2.3 Total NO_y and other gas phase species measurements

A trace-level chemiluminescent NO_x monitor (Thermo 42iQTL) equipped with a modified NO_y inlet was deployed to measure the total NO_y concentration in the experiments. The instrument and the custom inlet setup have been described in detail in previous work (Marsavin et al., 2023; Nursanto et al., 2026). The chamber air is sampled through a 1.2 m Teflon tube (1/4" or 6.4 mm outer diameter, 4.0 mm inner diameter), as short as possible to prevent wall losses of adsorbed NO_y species (Neuman et al., 1999). The sampled air then enters the external NO_y inlet box, which consists of a NO_2-to-NO molybdenum converter (scavenged from Thermo 17i) and a temperature controller (Omega CN616A) to adjust the converter temperature. Through the converter, the NO_y species are pre-reduced into NO which then flows through a longer inlet line to the chemiluminescence detector. The converter is operated at 350 °C. The line then goes to the instrument through a 3 m Teflon tube (same diameters as the previous one) and passes through a filter paper (PTFE (polytetrafluoroethylene), TE 38, Whatman^{TM}) to filter out residual particles. The instrument uses an external pump to draw air sample at a flow rate of 1 $L \cdot min^{-1}$. The chemiluminescence NO_x instrument measures NO_y as NO with 1 min time resolution. The instrument was calibrated with and without the NO_y inlet using a standard NO_x cylinder, where the instrument's sensitivity remains relatively stable ($\pm$8 %) (Nursanto et al., 2026). The conversion efficiencies at 350 °C are (104 $\pm$ 5)% for $RONO_2$, (94 $\pm$ 2)% for NH_4NO_3, and no $(NH_4)_2SO_4$ formed through spurious conversion of NH_4^+ to NO_x was detected. Total NO_y may include some other NO_z species such as HNO_3 (Baylon et al. (2015) reported 95 % conversion efficiency) and HONO (Fehsenfeld et al., 1987). However, the detection efficiency of HNO_3 also depends on the inlet line because it can be absorbed by the tubing (Neuman et al., 1999; Day et al., 2002; Keehan et al., 2020).

In addition to the total NO_y measurements, the mixing ratios of NO_x, O_3, and sulfur dioxide (SO_2) in Cabauw were acquired from the open-source data of *Landelijk Meetnet Luchtkwaliteit* (LML; `https://www.luchtmeetnet.nl`, last access: 19 January 2026). The mixing ratios of NH_3), also obtained from LML, were from the Zegveld-Oude Meije station, 20 km to the north of the Cabauw station (see Fig. 5.2a).

5.2.4 Extraction of organic nitrate concentrations from NO_y and ACSM

The co-located and simultaneous total NO_y and ACSM measurements allow the determination of gas phase ON (gON) mixing ratio and particle phase ON (pON) concentration, allowing direct determination of bulk gas/aerosol partitioning of ON. The mixing ratio of gON is obtained by subtracting NO_x and total pNO_3 from the measured total NO_y

mixing ratio as hourly averages, described in Eq. 5.1. The NO_x data was obtained from LML and the total pNO_3 is from the ACSM observation (which includes NH_4NO_3 and pON but not refractory nitrates such as sodium nitrate ($NaNO_3$) and calcium nitrate ($Ca(NO_3)_2$)).

$$C_{gON} = C_{NO_y} - C_{NO_x} - C_{pNO_3,ACSM} \tag{5.1}$$

C_{gON} : mixing ratio of gas phase ON

C_{NO_y} : mixing ratio of total NO_y (converter temperature at 350 °C)

C_{NO_x} : mixing ratio of NO_x

C_{pNO_3} : mixing ratio of total pNO_3 (inorganic+organic), measured by ACSM

We assume that the contributions of species other than NO_x, gON, and pNO_3 contribute negligibly to the total NO_y. As mentioned previously, HNO_3 and HONO should be included as NO_z in the total observed NO_y, but there were no continuous overlapping measurements of these compounds and total NO_y. However, comparison of the mixing ratio of total NO_y with HNO_3 and HONO from SAPHIR-CHANEL chamber experiments in Nursanto et al. (2026) suggests that the concentrations of HNO_3 and HONO are (7±6) % and (3±2) % of the total NO_y during SOA formation (mean±standard deviation), negligible compared to NO_x and pNO_3. However, we state this with caution, as the concentrations of HNO_3 and HONO may be lower or higher than the mean. Hence, the reported ON concentration represent the upper limit concentration of gas-phase ONs.

The NO_x^+ ratio method is used to speciate the nitrate signal into particulate ammonium nitrate (NH_4NO_3) and particulate organic nitrate (pON) from an ACSM (Nursanto et al., 2025). This method is based on the difference in the fragmentation patterns between $RONO_2$ and NH_4NO_3 in the mass spectrometer's vaporizer and ionizer (Farmer et al., 2010; Day et al., 2022a), which results in different NO_2^+/NO^+ ratios (referred to as NO_x^+ ratios, or R_ν in Eq. 5.2). The NO_x^+ ratio of the observed ambient air (R_{obs}) varies between the NO_x^+ ratios of pure NH_4NO_3 (R_{pAmN}) and pure pON (R_{pON}). The temporal variations of pON mass fraction to the total particulate nitrate (f_{pON}) can be determined from R_{obs} using Eq. 5.3, which is used to calculate the concentration of pON (C_{pON}) from the concentration of total pNO_3 ($C_{pNO_3,tot}$) in Eq. 5.4.

$$R_\nu = \frac{(C_{NO_2^+})_\nu}{(C_{NO^+})_\nu} \tag{5.2}$$

$$f_{pON} = \frac{(R_{obs} - R_{pAmN})(1 + R_{pON})}{(R_{pON} - R_{pAmN})(1 + R_{obs})} \tag{5.3}$$

$$C_{pON} = f_{pON} \cdot C_{pNO_3,tot} \tag{5.4}$$

ν: nitrate compound or mixture measured
$C_{NO_2^+}$: signal intensity of NO_2^+
C_{NO^+}: signal intensity of NO^+

The adapted NO_x^+ ratio method for CV-UMR-ToF-ACSM has been described in detail in Chapter 3 (Nursanto et al., 2025). The method is applied for 60 min time averaging, to match the time resolution of the rest of the data set from LML, as well as to decrease the uncertainty of the NO_x^+ ratio method. The adapted NO_x^+ ratio for CV-UMR-ToF-ACSM, has been shown to analyze organic nitrate composition with uncertainty of f_{pON} <10 % for total pNO_3 concentration $> 4\ \mu g \cdot m^{-3}$ and ∼30 % for total pNO_3 concentration $< 1\ \mu g \cdot m^{-3}$ by performing data filtering and averaging to 60 min (Nursanto et al., 2025).

5.2.5 Defining pollution episodes and airmass origins

In this study, a nitrate pollution episode is defined as an increase of particulate nitrate concentration, which leads to a pollution peak or a plateau of high concentrations that can last from several hours to days. A pollution episode begins with a low concentration of pollutants, followed by a growth period due to pollutant transport and/or accumulation in the nocturnal boundary layer, and ends with a meteorological condition that removes the pollution (Luo et al., 2022). In addition to its impact on the environment, pollution episodes are periods when the signal-to-noise ratio of the measurements is adequate for analysis. We use total pNO_3 concentration as a selection parameter to indicate a pollution episode, where a minimum of $0.8\ \mu g \cdot m^{-3}$ pNO_3 as peak or plateau (relative to pre-episode) is considered as an episode. The minimum pNO_3 concentration is decided from the signal limit of NO^+ used for NO_x^+ ratio method in this study (calculation is described in Table A.2 in the Appendices).

To assign the airmass origin of each nitrate pollution episode, we used the NOAA (National Oceanic and Atmospheric Administration) HYSPLIT (Hybrid Single-Particle Lagrangian Integrated Trajectory) v5.4.2 model (Stein et al., 2015) by running 48 h backward trajectories. Back trajectories were calculated in reference to meters above model ground level (a.m.g.l.) using $0.25^o \times 0.25^o$ resolution meteorological data from the Global Forecast System (GFS) containing sigma-pressure hybrid level forecast model output. The ambient air was sampled at ∼5 m height, and thus the trajectories were initiated at a starting height of 100 m above ground level (assumed within a well-mixed boundary layer) and when the peak of the nitrate pollution episode is reached. Furthermore, clustering analysis was performed on the back trajectories to cluster individual nitrate pollution episode origin into different wind sectors. The last 12 h of the back trajectories were used in the clustering to capture airmass inside the Dutch border and the region surrounding it.

5.2.6 Gas-particle partitioning of organic nitrate

The partitioning of an organic compound i between the gas and particle phases is defined by the absorption of organic compounds into existing particles. The partitioning occurs in a certain proportion according to the compound's properties (e.g., chemical structure, functional groups), where the low-volatility organic compounds (LVOCs) are more favorable to condense onto the particle-phase. The proportion in the gas and particle phases is expected to reach an equilibrium for a given compound at a given temperature. Therefore, calculating this equilibrium constant in an atmospheric mixture can help us understand the typical organic species that are present in the atmosphere. This gas-particle partitioning can be quantified using the partitioning coefficient based on the volatility of the compound i ($K_{p,i}$), as expressed in Eq. 5.5 (Pankow, 1994; Pankow and Asher, 2008). The partitioning coefficient is proportional to the particle-to-gas concentration ratio ($C_{p,i}/C_{g,i}$) and inversely proportional to the absorptive mass of PM (the total mass concentration of $PM_{2.5}$ is determined from the total ACSM species mass concentration).

$$K_{p,i} = \frac{C_{p,i}}{C_{g,i}} \cdot \frac{1}{m_{\text{tot}}} \tag{5.5}$$

$K_{p,i}$: gas-particle partitioning coefficient by volatility ($\text{m}^3 \cdot \mu\text{g}^{-1}$)
$C_{p,i}$: concentration/mixing ratio of i in the particle-phase
$C_{g,i}$: concentration/mixing ratio of i in the gas-phase
m_{tot}: total absorptive mass of PM ($\mu\text{g} \cdot \text{m}^{-3}$)

When expressed thermodynamically in Eq. 5.6, $K_{p,i}$ is a function of the temperature (T), the vapor pressure of i ($p^o_{L,i}$), and the composition of the organic matter, expressed as the molecular weight (MW_{om}) and the activity coefficient (ζ). By estimating the pure liquid vapor pressure of i at temperature T with a given MW_{om} and ζ, $K_{p,i}$ can be theoretically calculated using a group contribution method, for example, SIMPOL.1 from Pankow and Asher (2008). Then, this theoretical $K_{p,i}$ can be compared to the observed $K_{p,i}$ to deduce the typical organic compounds formed and characterize the aggregate properties of the SOA mixture (Brownwood et al., 2021).

$$K_{p,i} = \frac{760 \cdot R \cdot T \cdot f_{om}}{10^6 \cdot MW_{om} \cdot \zeta \cdot p^o_{L,i}} \tag{5.6}$$

R: ideal gas constant ($0.082\ \mathrm{L \cdot atm \cdot K^{-1} \cdot mol^{-1}}$)
T: temperature (K)
f_{om}: absorptive organic fraction of the PM
MW_{om}: average molecular weight of the organic matter ($\mathrm{g \cdot mol^{-1}}$)
ζ: activity coefficient of compound i in the organic matter
$p^0_{L,i}$: pure liquid vapor pressure of i at T (atm)
conversion factors: $760 \cdot \mathrm{Torr \cdot atm^{-1}}$ and $10^6 \cdot \mu\mathrm{g \cdot g^{-1}}$

During a pollution episode, we characterize the volatility of the total ON at the maximum pON concentration (assumed to be an equilibrium condition) using $K_{\mathrm{p,ON}}$. This is described as the condition when the maximum concentration during a pollution has reached its peak or plateau (the concentration is stable). With hourly time resolution, this equilibrium can last for 1–3 h for each pollution episode. We compare the observed partitioning coefficients to the theoretical $K_{\mathrm{p,ON}}$ (as a function of temperature), based on an educated guess of ON structures from known VOC precursors that have been identified in other studies. Through this comparison, we aim to assess what chemical structures are consistent with the observed bulk gas-particle partitioning of ON.

5.3 Results and discussion

5.3.1 Seasonal and diurnal variability of episode frequency

We summarize the identified particulate nitrate episodes in Table 5.2, categorized by season and time of day. The total pNO_3 concentration during a nitrate pollution episode varies between 0.8–19 $\mu\mathrm{g \cdot m^{-3}}$. Nitrate pollution episodes occur more frequently during the winter period with a frequency of 37 episodes $\mathrm{mo^{-1}}$, in contrast to 17 episodes $\mathrm{mo^{-1}}$ in the summer.

We interpret the seasonal variability of the episode number frequency as arising from varying meteorological conditions and precursor emissions (BVOCs and reactive nitrogen), which modify the rates of formation of ammonium nitrate and ONs. In addition, longer days and warmer temperatures during summer allow more convection, thus distributing emissions over a deeper boundary layer, which reduces the likelihood of a pollution episode (fewer episodes in summer).

In winter, despite lower photochemical activity, the frequency of nitrate pollution episodes is higher. As days are shorter and nights are colder, nitrate radical chemistry, an important pathway of organic nitrate formation that is associated with a high SOA yield (Ng et al., 2017), is more prevalent during this period. The meteorological and radiation conditions lead to longer lifetimes of nitrate radicals, thus increasing the chance of ON formation, especially during night. Lower average temperatures also

Table 5.2: Summary of particulate nitrate episodes in Cabauw, Netherlands, in terms of episode number and monthly episode frequency, categorized by season and the time of the day.

Season	Summer (Mar–Sep)	Winter (Oct–Feb)
Length of data (h)	4970	2808
Number of nitrate episodes	118	144
Episode frequency (mo^{-1})	17	37
Daytime occurrence[a]	50 %	41 %
Nighttime occurrence[a]	50 %	59 %

[a] Frequency of hours during nitrate pollution episode at given daytime/nighttime over all studied episodes where the nitrate concentration has reached its maximum and/or relatively constant for several hours during an episode.

favor the condensation of both HNO_3 and oxidized organic vapors, increasing the fraction of particulate nitrate and thus the number of pollution episodes. This seasonal trend is also in line with the trend found when the episodes are categorized into nighttime and daytime conditions. The nitrate episodes are more frequent at night with more stable and shallower boundary layers (50–59 %) compared to day conditions when more convection takes place (41–50 %).

5.3.2 Seasonal and diurnal variability of chemical species

While the episode frequency describes the chance of having a particulate nitrate episode, the chemical composition is helpful to understand the underlying processes driving those episodes that will impact the reactive nitrogen atmospheric lifetime and transport distance from the source. We highlight the diurnal variability of different ambient chemical species in Cabauw as seasonal averages in Fig. 5.3, which encompasses both episode and non-episode periods (see Fig. A.1 in the Appendices for the standard deviations). Average total $PM_{2.5}$ concentrations (Fig. 5.3c–d) are found to be higher during winter (8–10 $\mu g \cdot m^{-3}$, right axes) compared to concentrations during summer (6–8 $\mu g \cdot m^{-3}$, right axes). During winter, less atmospheric mixing and a shallower boundary layer lead to concentrated ground-level particulate matter pollution. The trends of individual chemical species in the gas phase (expressed in mixing ratio, ppb) and in the particle phase (expressed in mass concentration, $\mu g \cdot m^{-3}$) are shown in the following sections.

Total oxidized nitrogen species (NO_y) and ozone (O_3)

The NO_y mixing ratio, which includes NO_x and reservoir species, has higher maximum mixing ratio in summer (10–19 ppb), compared to winter (12–17 ppb) (Fig. 5.3a–b). This seasonal trend is driven by greater conversion of NO_x to various reservoir species in

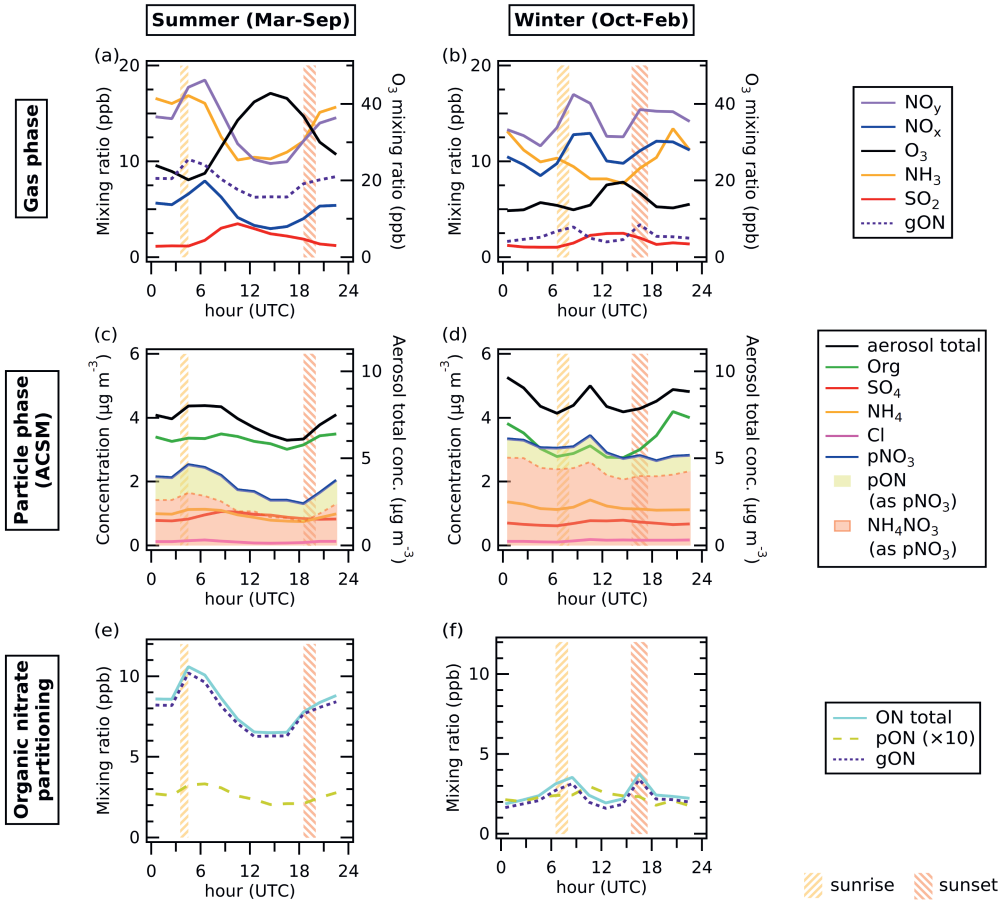


Figure 5.3: **(a–b)** Seasonal average (summer vs. winter) for the mixing ratios of various gas-phase species (NO_y, NO_x, O_3, NH_3, and SO_2) presented as diurnal cycle plots. **(c–d)** Seasonal average for the mass concentration of particle phase species measured by ACSM ($PM_{2.5}$, including Org, SO_4, NH_4, Cl, and NO_3) presented as diurnal cycle plots. **(e–f)** Seasonal average for the mixing ratios of bulk ON in the gas-phase (gON), particle-phase (pON), and sum of both phases (ON total). All species were measured at the Cabauw site except NH_3 which was measured at the Zegveld-Oude Meije site.

summer like ON due to the increase of BVOC availability. This results in higher NO_y mixing ratio and lower NO_x mixing ratio during summer (3–8 ppb) compared to winter (9–13 ppb). The diurnal variability of NO_x is mainly driven by the NO_x photostationary state cycling rate, which increases after sunrise and then decreases later during the day, followed by rising O_3 at noon (Fig. 5.3a–b). The morning peak is associated with vehicular emission from the rush hour.

Ammonia (NH_3), particulate ammonium (NH_4), sulfur dioxide (SO_2), and particulate sulfate (SO_4)

NH_3 shows relatively higher mixing ratios in summer (10–17 ppb) compared to winter (8–13 ppb). The higher NH_3 mixing ratios are associated with the time of year when manure spreading is authorized in the Netherlands (March–September, depending on the type of agricultural soil), and stronger NH_3 evaporation at warmer temperatures (Van Zanten et al., 2017; Liu et al., 2018; Vendel et al., 2023). We observe a diurnal pattern of NH_3 in Zegveld since the site is surrounded by agricultural lands that act as NH_3 sources (similar to Cabauw). For comparison, in Solleveld, a coastal site in the Netherlands surrounded by sand dunes, Vendel et al. (2023) only observed NH_3 increase during the summer months when the wind came from the east (inland NH_3 sources). The dependence of NH_3 concentration on its distance to the point sources and the prevailing regional meteorology has been shown by Schulte et al. (2021).

In contrast to NH_3, the concentrations of particulate NH_4 are only slightly higher during winter (2.0–2.8 $\mu g \cdot m^{-3}$) compared to summer (0.8–1.7 $\mu g \cdot m^{-3}$). The higher concentrations during winter occur due to lower temperatures that promotes particle-phase condensation, as well as to maintain the ionic balance with increasing particulate NO_3 concentrations. This concentration trend demonstrates that NH_3 is available in an excess amount regardless of the season and does not act as a limiting reagent in SO_x and NO_x sink. The diurnal variability of particulate NH_4 follows rather the pattern of particulate NO_3 than particulate SO_4 due to the low particulate SO_4 to particulate NO_3 concentration ratio. Moreover, it is likely that the relatively weak diurnal patterns of NH_4 and SO_4 are driven by the excess NH_3, which has been similarly observed by Lan et al. (2024) in an urban site. SO_2 mixing ratios are generally low throughout the year; the mixing ratio varies between 0.1–0.4 ppb, slightly higher during summer. Like its precursor (SO_2), the concentrations of particulate SO_4 remain low throughout the year (0.6–1.1 $\mu g \cdot m^{-3}$) with a slightly higher concentrations during summer.

Total organic aerosol (OA), total organic nitrate (ON), and total particulate nitrate (pNO_3)

The diurnal variation of the seasonal average of total Org concentrations in Cabauw ranges from 3.0–3.5 $\mu g \cdot m^{-3}$ for summer and 2.8–4.2 $\mu g \cdot m^{-3}$ for winter (Fig. 5.3c–d). The daytime OA concentrations are the highest during the summer period, which is driven by the higher availability of BVOC precursors, stronger solar radiation, and more active photooxidation. Meanwhile, the nocturnal OA concentrations are higher because of the shallow boundary layer and lower temperatures, optimal for the accumulation and condensation of low-volatility organic vapors into the particle phase. This effect is more pronounced during winter due to the colder nights and the generally more stable boundary layer.

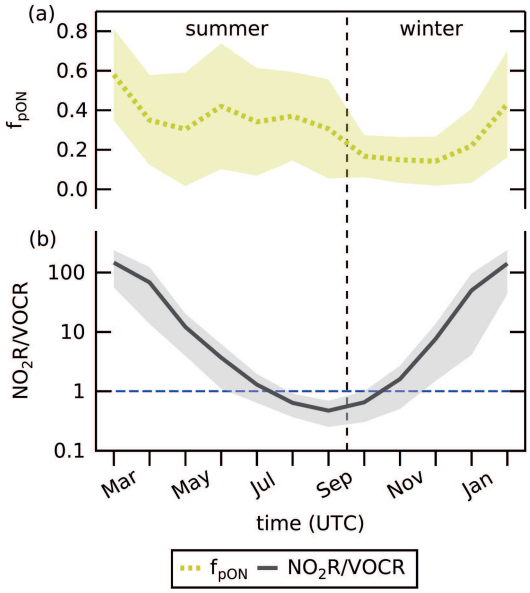


Figure 5.4: (a) The monthly average of pON fraction to total pNO_3 (f_{pON}) from Cabauw observations. **(b)** Monthly average of NO_2-to-VOC reactivity in logarithmic scale, calculated using CAMS global reanalysis (European Centre for Medium-Range Weather Forecasts Atmospheric Composition Reanalysis 4 or EAC4) dataset (Inness et al., 2019; Copernicus Atmosphere Monitoring Service, 2020). Isoprene and monoterpenes are considered in the calculation. The rate constants of NO_2+$OH^{\bullet}$ and isoprene+$OH^{\bullet}$ are obtained from Burkholder et al. (2019), while the rate constant of α-pinene+$OH^{\bullet}$ (for monoterpenes) is taken from the Master Chemical Mechanism, MCM v.3.3.1 (Jenkin et al., 1997; Saunders et al., 2003) via `www.mcm.york.ac.uk` (last accessed: 30 October 2025). See Section A.2 in the Appendices for the details of the calculation. Panel **(b)** covers data set from Jan 2023 to Dec 2024, different but with some overlaps with the ground-based measurements in panel **(a)** (see Table A.1 for measurement periods in the Appendices).

While the range of total OA concentrations are similar during the summer compared to the winter, we observe a larger seasonal difference for the total ON mixing ratio. During winter, the diurnal variation of total ON mixing ratios ranges from 2–4 ppb, while in summer, total ON mixing ratios vary from 7–11 ppb with a larger contrast between daytime and nighttime. The highest mixing ratios of ON are observed during the summer period, which is driven by the higher availability of BVOC precursors, stronger solar radiation, and more active photooxidation. There is a strong summertime overnight ON production, which is indicative of nighttime ($NO_3^{\bullet}$+BVOC) chemistry in a shallow nocturnal boundary layer. We observe that ON is more abundant in the gas phase than in the particle phase, and does not strongly partition into the particle phase during summer (Fig. 5.3e–f). The larger mixing ratio of gas phase ON relative to

particle phase ON occurs in the summer because the average temperature is higher and therefore, less sink of NO_x exists in the form of pON compared to gON due to a stronger evaporation. However, given the small the particulate fraction of ON for both summer and winter periods, the larger mixing ratio of gas phase ON during summer is likely contributed more by a stronger chemical production due to BVOC availability.

The range of total pNO_3 concentrations in the winter period, 2.7–3.4 $\mu g \cdot m^{-3}$, is higher than the concentrations in the summer period, 1.3–2.5 $\mu g \cdot m^{-3}$, as shown in Fig. 5.3c–d. The diurnal pattern of pNO_3 in each season is driven by the variability of NO_x and the semi-volatile properties of NH_4NO_3 (Huffman et al., 2009; Xu et al., 2015). The concentrations of NH_4NO_3 (as pNO_3) are higher during winter (2.0–2.7 $\mu g \cdot m^{-3}$) than summer (1.3–2.1 $\mu g \cdot m^{-3}$). The enhancement of NH_4NO_3 formation in winter is associated with a higher NO_x mixing ratio and lower temperatures compared to summer, causing less evaporation of NH_4NO_3 compared to the evaporation of pON. Diurnally, NH_4NO_3 strongly contributes to the morning rush hour peak after sunrise, around 6–9 UTC depending on the season. During this period, NH_4NO_3 is rapidly produced from the photooxidation of NO_x to HNO_3 and reaction with NH_3, and lost around noon due to evaporation and the growth of the boundary layer height (Weber et al., 2003; Hennigan et al., 2008; Xu et al., 2015).

Fig. 5.4a shows a lower monthly average of f_{pON} (from Cabauw measurements) during the winter period (14–43 %) compared to the summer months (30–58 %), indicating that during the summer organic nitrates contribute more strongly to the total particulate nitrate. The higher f_{pON} in summer is related to the combination of enhanced ON formation, as well as less evaporation of pON compared to NH_4NO_3 as discussed earlier. These phenomena make the pNO_3 formation by pON more dominant in summer compared to in winter. In general, pON contributes less to the variability of total pNO_3, consistent with NH_4NO_3 typically being the more semi-volatile component. The concentrations of pON (as pNO_3) are also generally similar for summer and winter (0.5–0.9 $\mu g \cdot m^{-3}$ or 0.2–0.3 ppb). We interpret this as being due to the compensating balance between having a stronger source of BVOC as a precursor but also less partitioning of ONs into the particle phase (Xu et al., 2015).

These phenomena demonstrate how the preference for inorganic and organic nitrate formation modifies the amount of NO_x sink as ON or NH_4NO_3, and how these nitrates are partitioned between the gas phase and particle phase. The seasonal changes in chemical composition are consistent with the ratio of NO_2-to-VOC reactivity to $OH^{\bullet}$ (NO_2R/VOCR) shown in Fig. 5.4b (see Fig. A.2 for the time series of NO_2 and VOCs in the Appendices). We used the CAMS data set to calculate the reactivity ratio since it covers a longer observation period that is not available from these measurements. Thus, we conclude that the atmospheric NO_x sink in Cabauw is under a HNO_3-dominated regime during winter ($NO_2R/VOCR >> 1$) and the $RONO_2$ sink is becoming more

important in summer ($NO_2R/VOCR < 1$). The abundance of BVOC emission causes this trend, shifting the NO_x sink towards the formation of ON instead of HNO_3, which is in line with the higher mixing ratio of total ON, higher pON concentration, and higher f_{pON} observed in summertime. In the context of the nitrogen crisis in the Netherlands, it suggests that ONs, as part of the NO_x sink, play more significant role in nitrogen deposition especially in summer. While HNO_3 readily deposit locally, ONs (in addition to NH_4NO_3) can transport NO_x further from their sources, spreading nitrogen deposition over larger areas.

5.3.3 Gas-particle partitioning of ON during pollution episodes

We discussed the seasonal and diurnal variations of the total ON, gON, and pON as shown in Fig. 5.3e–f in Section 5.3.2. Here, we further elaborate on how the partitioning occurs specifically during the peak of nitrate pollution episodes. We can visualize seasonal and diurnal variabilities for the bulk ON gas-particle partitioning by plotting $K_{p,ON}$ on the y-axis (see Fig. 5.5) against the temperature on the x-axis to show its dependence on temperature.

Higher theoretical $K_{p,ON}$ values (dotted grey line traces in Fig. 5.5, calculation based on SIMPOL.1 method according to Pankow and Asher (2008)) typically correspond to heavier molecules that have more carbon and oxygen atoms. These include compounds such as dimers and highly oxidized organic nitrates containing several hydroperoxy or carbonyl function groups with monoterpene backbone (e.g., NLIMALOOH, LMKANO3, APINBNO3) or long-chain alkanes and aldehydes (e.g., C123NO3 from dodecane, NONALOHNO3 from nonanal). Lower $K_{p,ON}$ values include compounds that have fewer carbon and oxygen atoms, such as isoprene nitrates and aromatic nitrates (e.g., BZBIPERNO3 from benzene, NISOPOOH from isoprene, and MXYLNO3 from m-xylene). Most of these structures are listed in the Master Chemical Mechanism, MCM v3.3.1 (Jenkin et al., 1997; Saunders et al., 2003; Jenkin et al., 2003; Bloss et al., 2005; Jenkin et al., 2015), via `www.mcm.york.ac.uk` (last accessed: 30 October 2025). Note that these structures are an educated guess of what ON compounds may be expected in this region; characterizing the actual ON products would require additional observations using high-resolution mass spectrometers.

Representative organic nitrate structures from theoretical calculations are shown in Fig. 5.5. For a given structure, the $K_{p,ON}$ value decreases with the increase of temperature (dashed grey lines). We note that group contribution method has uncertainties since it uses the number of specific functional groups to calculate volatility and is thus unable to distinguish positional isomers. Previous studies have pointed out that this method is likely to overestimate the volatility of compounds with a larger number of functional groups (Kurtén et al., 2016; Peräkylä et al., 2020). The goal of showing the structures is to give a general idea of what type of organic nitrate structure corresponds to observed

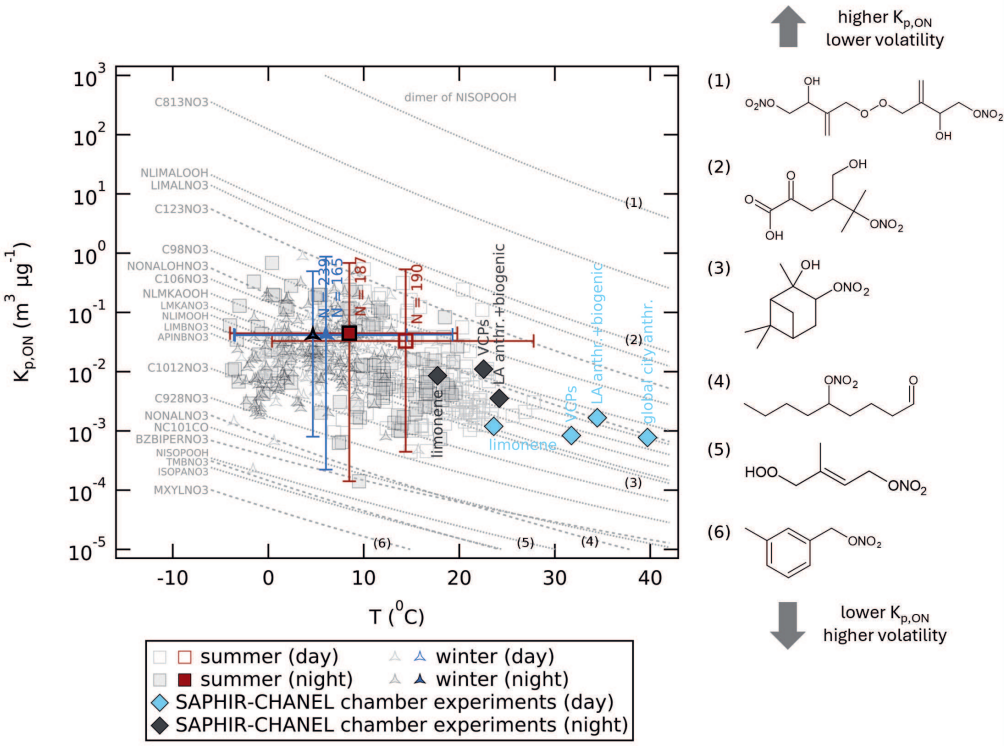


Figure 5.5: Bulk organic nitrate gas-particle partitioning coefficient ($K_{p,ON}$) as function of temperature (T) during nitrate pollution episodes, categorized by season and time of the day. The grey line traces indicate the theoretical $K_{p,ON}$ values of organic nitrate compounds to help the readers scale the $K_{p,ON}$ values with structures and species volatility. Most of the compounds are listed in the MCM v3.3.1 (see Table A.3 in the Appendices for the complete list of the compounds shown in the plot). The red square and blue triangle markers are the means of grey data points categorized by seasons and time of day. The whiskers represent the lower and upper limit of the mean $K_{p,ON}$ and T values. The diamond markers are selected $K_{p,ON}$ values of organic nitrate compounds formed from various urban emission mixture replicated in an atmospheric chamber during SAPHIR-CHANEL campaign (Nursanto et al., 2026). The light blue and black diamond markers represent chamber experiments under daytime and nighttime conditions, respectively. These mixtures include single-compound limonene, volatile chemical products (VCPs), replica of anthropogenic+biogenic emissions of Los Angeles (LA), and replica of anthropogenic emission from global/European cities.

$K_{p,ON}$ values. The complete list of the chemical structures is available in Table A.3 in the Appendices. These compounds are chosen based on their relevance to VOC emissions that have the potential to form SOA, as shown by field observations and chamber experiments (Hallquist et al., 1999; Bowman et al., 2003; Perring et al., 2009; Fry et al., 2009; Bahreini et al., 2012; Warneke et al., 2012; Gordon et al., 2014; Misztal et al., 2014; Ayres et al., 2015; Liu et al., 2017; Gentner et al., 2017; Ng et al., 2017; McDonald et al., 2018; Brownwood et al., 2021; Coggon et al., 2021; Gkatzelis et al., 2021a; Gkatzelis et al., 2021b; Wernis et al., 2022; Pfannerstill et al., 2023; Coggon et al., 2024; Rivellini et al., 2024).

The observed values of $K_{p,ON}$ in Fig. 5.5 (grey triangle and square markers) vary from 10^{-4} to 10^{-1} $m^3 \cdot \mu g^{-1}$ (n = 781), with a large temperature range from -4 to 28 °C. Although the observed $K_{p,ON}$ values fluctuate per pollution event, we can see that these partitioning coefficients always correspond to a similar average organic nitrate structure, even when the points are distinguished diurnally and seasonally. The seasonal and diurnal average of $K_{p,ON}$ values in Cabauw (colored triangle and square symbols) shows no clear seasonal or day/night difference ($K_{p,ON} \sim 4 \cdot 10^{-2}$ $m^3 \cdot \mu g^{-1}$), with the whiskers representing the lower and upper limit of the mean $K_{p,ON}$ and T values. This similarity shows that the bulk ON composition matches the volatility of many monoterpene-derived organic nitrate compounds, despite the wide range of temperature.

The trend of ON gas-particle partitioning coefficient shown here is unlike the gas-particle partitioning trend we found in the diurnal seasonal averages (Fig. 5.3e–f) where there is a larger gas-phase ON fraction in the ON phase partitioning during summer compared to winter. The gas-particle partitioning described here occurs during nitrate pollution episodes, which cover only 10 % of the hours used to obtain the diurnal averages over a season shown in Fig. 5.3. These pollution episodes also were selected based on being above a threshold concentration of particulate nitrate, and thus have higher pON concentrations, which leads to higher particle-to-gas mass concentration ratio and $K_{p,ON}$ values, even in summer.

The observed K_{pON} values are similar to the range of K_{pON} values from the SAPHIR-CHANEL chamber experiments (see the diamond symbols in Fig.5.5 for selected experiments, and more in Nursanto et al. (2026)). These average structures arise for two possible reasons. Since biogenic VOCs account for most of the SOA formation potential in an ambient mixture (Gu et al., 2021; Pfannerstill et al., 2023) and for the most of the ON formation (Beaver et al., 2012), the average volatility of ON is likely driven by biogenic organic nitrates (i.e., monoterpene-related nitrates). The average $K_{p,ON}$ value is therefore similar to ONs derived from terpenes and terpenoids. A second potential explanation is that VOCs other than BVOCs with low or high reactivity and SOA formation potentials (i.e., aromatic compounds, aldehydes, alcohols, alkanes, alkenes) can

also form compounds with a wide range of volatility and oxidation level. They can produce either highly oxygenated molecules or dimers with very low-volatility ONs, or less-oxidized organic nitrates with very high volatility. These contributions combine to give an average $K_{p,ON}$ value that is similar to the values for monoterpene-related nitrates. However, it is an interesting finding that the range of $K_{p,ON}$ values stay within the volatility range of monoterpene-related nitrates, which may indicate that these compounds are broadly representative of average ON in the atmosphere.

The day/night averages of the ambient $K_{p,ON}$ values (Fig. 5.5) are observed to be similar, unlike the $K_{p,ON}$ values of chamber experiments under daytime/nighttime conditions (Nursanto et al., 2026). This is likely because some of the chamber experiments include single-compound limonene experiments, which are not representative of the actual atmosphere. The ambient observations in this study resemble the day/night variability of complex urban mixture experiments, where a diverse VOC precursor ranging from biogenic and volatile chemical products (VCPs), fuel combustion, and cooking emissions are used to replicate the complexity of ambient air. In addition, regional transport, which brings fresh emissions and allows the mixing of different air mixtures from day to night, introduces a more complex loss and production of ON species that may mean that the sampled ONs are representative of a mixture of many days of sources and reaction products, a timescale not explored in Nursanto et al. (2026).

5.3.4 Influence of coastal vs. continental airmass sources

As mentioned in Section 5.2.1, emission profiles of the coastal Netherlands and continental Europe are different. Thus, separating spatially the upwind sector associated with pollution episodes can help us to better understand the influence of each particulate nitrate precursor in its formation. The airmass origin of each episode was categorized based on the clusters determined by HYSPLIT shown in Fig. 5.6a–b. Two clusters with average wind sectors coming from the eastern and southern sector are considered continental airmass, while three clusters with average wind sectors from southwesterly, westerly, and northwesterly directions are classified as coastal. We found that the number of pollution episodes related to coastal airmass and continental airmass are relatively equal, where coastal airmasses contributed slightly more particulate nitrate episodes in Cabauw throughout the year compared to continental airmasses (53 % vs. 47 %, see Table 5.3). This is expected because from the 5 m horizontal wind rose (Fig. 5.6c), we observe that the coastal wind sector and continental wind sector are distributed roughly equally throughout the year. When comparing the hours of pollution episodes to the total hours of all episodes, the coastal and continental wind sectors both cover $\sim$50 % of total hours of the pollution episodes. A nitrate pollution episode in Cabauw lasts around 12–13 h on average regardless of the origin of airmass and the season, ranging from 4–39 h.

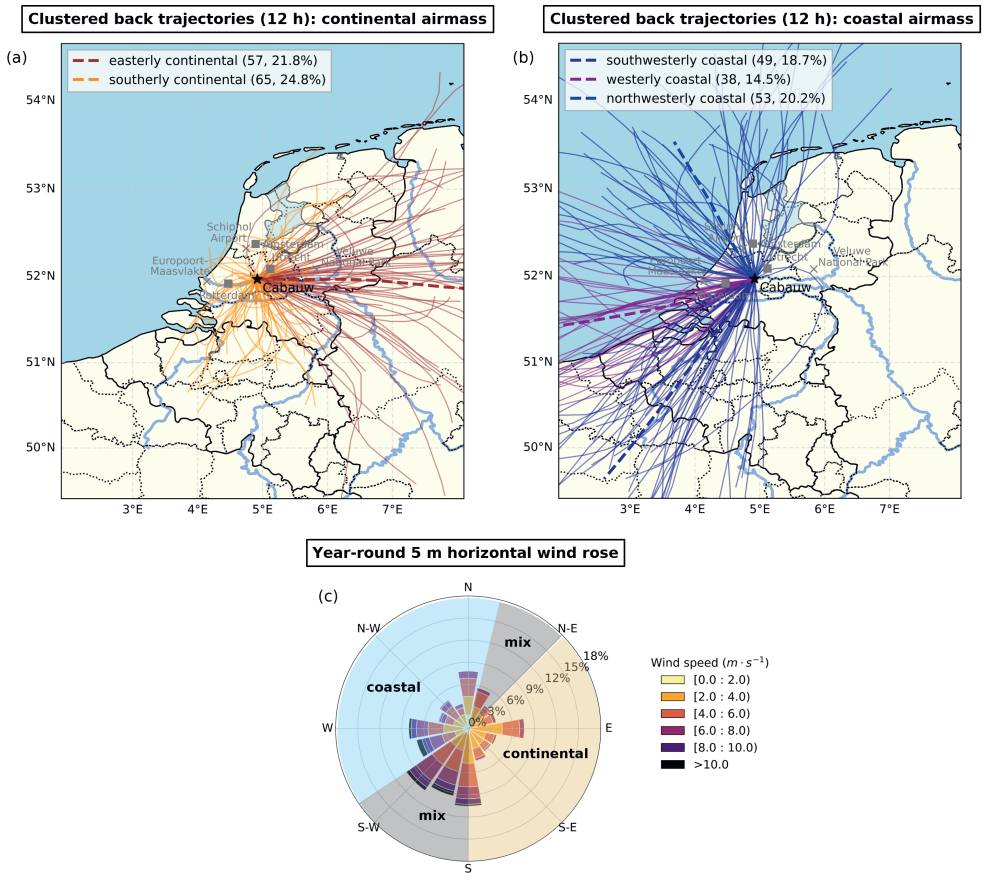


Figure 5.6: Maps of the Netherlands showing the clustering of back trajectories of airmasses coming to Cabauw during nitrate pollution episodes (12 h backward, based on 48 h back trajectories) into **(a)** continental airmass related episodes and **(b)** coastal airmass related episodes. The continental airmass origin is attributed to 47 % of observed nitrate episodes, while the coastal airmass origin is attributed to 53 % of observed nitrate episodes. Plot **(c)** shows the horizontal wind rose at 5 m height throughout the year.

To understand the influence of airmass origin on the variability of chemical composition during particulate nitrate episodes, the normalized pollution roses for total pNO_3, NH_4NO_3, pON, f_{pON}, and $K_{p,ON}$ in Cabauw are shown in Fig. 5.7. The pollution rose in Fig. 5.7a shows that somewhat higher concentrations of total pNO_3 are associated with coastal airmasses. In Fig. 5.7b–c, when the total pNO_3 is speciated as NH_4NO_3 and pON, we see somewhat higher inorganic nitrate contributions originated from the western sector associated with coastal airmasses, and higher organic nitrate contribu-

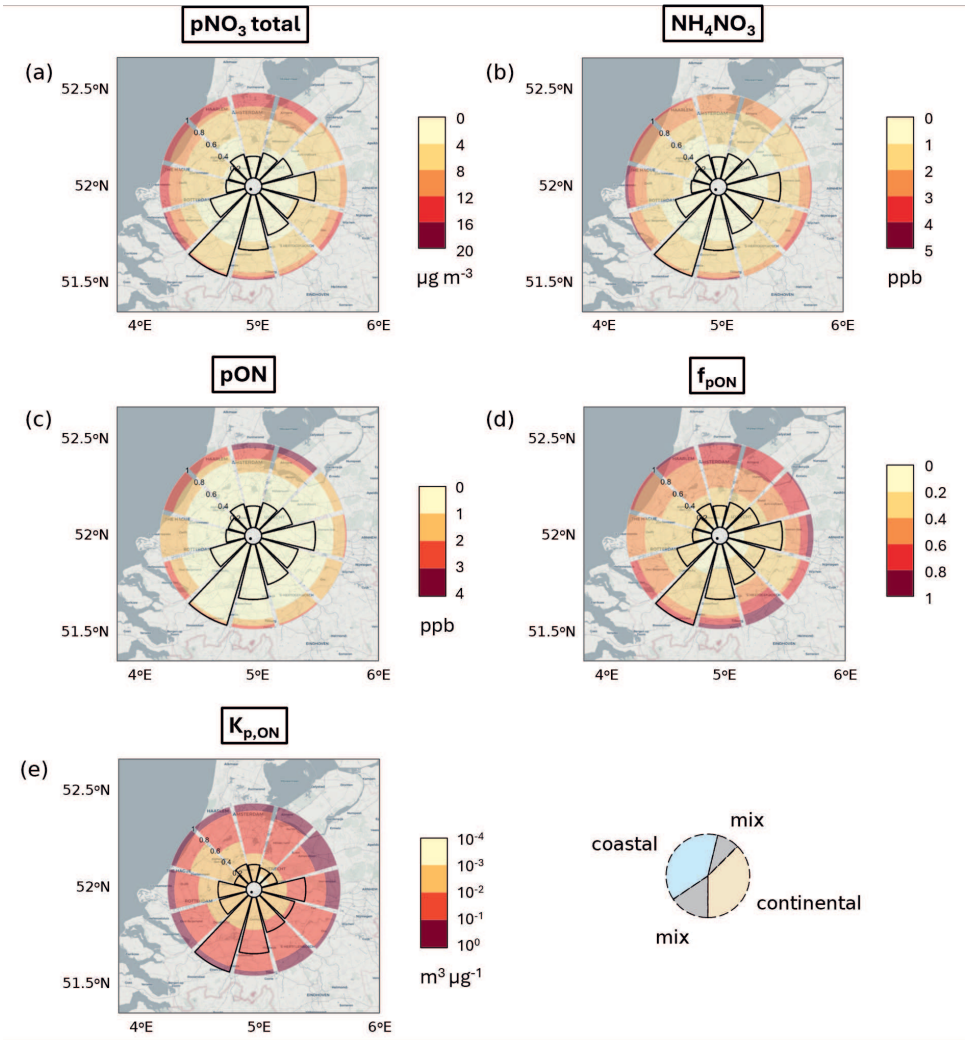


Figure 5.7: Normalized pollution roses of **(a)** pNO_3 total mass concentration (in $\mu g \cdot m^{-3}$), **(b)** NH_4NO_3 mixing ratio (in ppb), **(c)** pON mixing ratio (in ppb), **(d)** f_{pON}, and **(e)** $K_{p,ON}$ in Cabauw, Netherlands during nitrate pollution episodes only. The colored wedges represent the normalized distribution of the variable, while the black outline inside the pollution rose shows the wind direction frequency distribution. The small pie chart of airmass origins shows the wind direction sectors related to continental or coastal airmass during the episodes according to the cluster analysis of HYSPLIT back trajectories in Fig. 5.6.

tions from the northwest-northeast sector associated with both coastal and continental airmasses.

The lower total nitrate concentrations for episodes associated with airmass from continental Europe may be attributed to fewer nitrate sources inland compared to the coast of the Netherlands. A second possibility is that the loss (e.g., evaporation, chemical degradation, and deposition) of nitrate aerosol from continental European airmasses is larger because travel times between source and receptor location are longer compared to coastal airmasses. The short lifetime of NH_4NO_3 due to its local evaporation to HNO_3 and susceptibility to wet deposition result in the loss of NH_4NO_3 during long-range transport, therefore decreasing the nitrate aerosol concentration.

In contrast, we observe that higher f_{pON} are associated with continental airmasses (0–180^o) that have lower total pNO_3 concentrations. In Fig. 5.7d, the wind sector 0–180^o has a mean f_{pON} value of (36$\pm$22) % (mean $\pm$ standard deviation), slightly higher than the wind sector 180–360^o that has an average f_{pON} value of (31$\pm$17) %. Day et al. (2022a) have similarly shown that f_{pON} shows an inverse relationship to the total pNO_3, where f_{pON} approaches 100 % when the total particulate nitrate mass loading (inorganic and organic) is low. This suggests that when the airmass is strongly influenced by urban areas (i.e., coastal region in the Netherlands), more pNO_3 is produced as inorganic nitrate. The higher f_{pON} from the continental airmass is associated with higher BVOC emissions from mainland Europe, as shown in Oomen et al. (2024) for the emission profile of isoprene and monoterpenes over Europe from satellite data in 2018–2021. The higher BVOC emissions increase the availability of precursors for more production of ON, and thus increasing f_{pON}.

The transported organic nitrates are likely to be related to aged organic aerosols. This is shown by the ratio of m/Q 44 (CO_2^+) to m/Q 43 (CH_3CO^+ and $C_3H_7^+$) fragment signals in the CV-ACSM Org mass spectra (f_{44}/f_{43}). The value of f_{44}/f_{43} is a proxy of organic aerosol oxidation level. The continental plumes have a slightly higher oxidation level and age (f_{44}/f_{43} = 6.5$\pm$2.7; mean $\pm$ standard deviation) compared to the coastal plumes (f_{44}/f_{43} = 5.6$\pm$3.7). This is indicative that continental plumes bring photochemically-aged and long-range transported organic aerosols, similar to the finding of higher oxygenated organic aerosol coming from continental Europe (Nursanto et al., 2023).

We also expected higher f_{pON} for continental airmass related episodes to be associated with how inorganic and organic nitrates are lost during transport. The bulk pON also undergoes evaporation, chemical degradation, and deposition during transport, but (depending on their structure) there are ON compounds with lifetimes longer than NH_4NO_3.

Fig. 5.7e shows slightly higher $K_{\mathrm{p,ON}}$ values for pollution episodes associated with the continental airmass. However, when taking the average $K_{\mathrm{p,ON}}$ values, they are not drastically different when categorized by airmass origin ($\sim 4 \cdot 10^{-2}$ m$^3 \cdot \mu$g^{-1}). Similarly, the higher $K_{\mathrm{p,ON}}$ can also be attributed to the continental airmass bringing more BVOCs

Table 5.3: Summary of the number and the hour of nitrate pollution episodes categorized based on airmass origin determined from the cluster analysis of HYSPLIT back trajectories of the entire dataset in this study.

Wind sector	Year-round		Summer (Mar–Sep)		Winter (Oct–Feb)	
	Number of episode	Hour of episode	Number of episode	Hour of episode	Number of episode	Hour of episode
Continental	**122 (47 %)**	**1641 (49 %)**	**51 (43 %)**	**768 (47 %)**	**71 (49 %)**	**873 (51 %)**
Easterly	57	889	28	476	29	413
Southerly	65	752	23	292	42	460
Coastal	**140 (53 %)**	**1695 (51 %)**	**67 (57 %)**	**849 (53 %)**	**73 (51 %)**	**846 (49 %)**
Southwesterly	49	588	13	146	36	442
Westerly	38	490	22	317	16	173
Northwesterly	53	617	32	386	21	231
Sum	**262 (100%)**	**3336 (100%)**	**118 (100%)**	**1617 (100%)**	**144 (100%)**	**1719 (100%)**

that have higher volatility compounds, which are mostly ONs from BVOC precursors with higher reactivity, molecular weight (e.g., terpenes), and SOA formation potentials compared to other VOC precursors (Fry et al., 2011; Beaver et al., 2012; Gu et al., 2021; Pfannerstill et al., 2023).

5.4 Conclusion

We have shown that co-located continuous measurements of total NO_y, aerosol composition, related and meteorological parameters allow us to determine the origins of nitrate pollution episodes and their relationship to other chemical species and meteorological parameters in the Netherlands. These measurements help us to identify the dominant chemical regime for each season. With excess NH_3 throughout the year, it does not limit nitrate aerosol formation, making NO_x, VOCs, solar radiation and temperature the determining factors for the formation of nitrate aerosol in the Netherlands. The speciation of organic and inorganic nitrate is of great importance, as particulate nitrate lifetime is affected by the difference in inorganic vs. organic nitrate volatility. A summary of the underlying processes discussed in this chapter is shown in Fig. 5.8, which is an updated version of Fig. 5.1.

The NO_2-to-VOC reactivity ratio below unity during summer reveals that Cabauw is in a regime in which the $RONO_2$ pathway becomes increasingly important chemical sink of NO_x during pollution episode events in addition to main HNO_3 pathway compared to winter. The nitrate pollution episodes occur most frequently during winter period

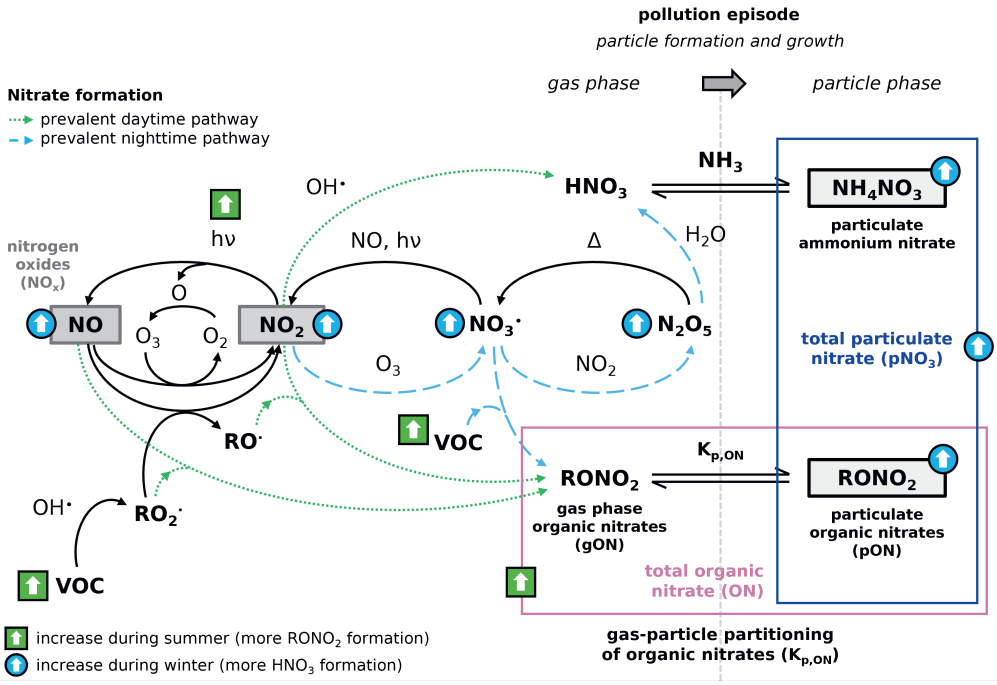


Figure 5.8: Summary of the influence of seasonal fluctuations in summer vs. winter (e.g., length of the day and night, solar radiation, temperature) to the chemical reactions, species concentrations, and partitioning of different reactive nitrogen species between the gas phase and particle phase. Increase of concentrations in summer pollution episodes (more $RONO_2$ formation in addition to the main HNO_3 formation) is shown by green and square-outlined up arrow, while increase of concentrations during more HNO_3-dominated regime in winter is shown by blue and circle-outlined up arrow.

(Oct–Feb, 37 episodes monthly) and at night (50–59 %). However, the higher episode frequency during winter is associated with smaller ON mixing ratio (2–4 ppb) and lower pON fraction (14–43 %) than in summer. In summer, on the other hand, nitrate pollution episodes are associated with stronger ON formation (7–11 ppb) and higher pON fraction (30–58 %). The higher pON fraction is also related to the stronger evaporation of semi-volatile ammonium nitrate compared to the evaporation of less volatile organic nitrate at elevated temperatures during summer.

The bulk ON gas-particle partitioning coefficient ($K_{p,ON}$), describing the average volatility of organic nitrate and how organic nitrates are partitioned between the gas phase and the particle phase, shows a range of 10^{-4} to 10^{-1} $m^3 \cdot \mu g^{-1}$. Although we expect an increase of $K_{p,ON}$ value as the temperature decreases from day to night and from summer to winter for the same compound, $K_{p,ON}$ shows no clear seasonal and diurnal patterns. This is likely caused by the complex loss and production of species from day

to night (and vice versa) that results in the volatility being averaged out. However, it is an interesting finding that the range of partitioning coefficient remains within the volatility of monoterpene-related nitrates, perhaps showing the optimal volatility for organic nitrates condense into the particle phase in general. We recommend this value range when modeling ON formation as bulk in the atmosphere.

Analysis of nitrate pollution episodes based on back trajectories and pollution roses shows different chemical species profiles between episodes associated with continental airmass and coastal airmass. Given the average wind rose profile in Cabauw that brings relatively equal frequency of wind from the coastal and the continental regions, number of episodes associated with coastal airmass and continental airmass are also relatively equal, with slightly importance of coastal airmass (53 %) that is associated with higher total particulate nitrate concentrations. These findings are explained by the abundance of NO_x emission hotspots and less chemical losses during the shorter transport distance. Continental airmasses produce slightly fewer nitrate episodes (47 %) with lower total particulate nitrate concentration but higher pON fractions and more aged organic aerosol. We conclude that continental airmasses bring higher pON fractions due to higher biogenic emissions in the continental wind sector.

Unfortunately, this study lacks measurements of VOCs. Although the concentrations of some VOCs are available from model data reanalysis, in-situ measurements would help us constrain the VOC composition (which includes gas phase ON) and better interpret trends in gON and pON. This would provide a higher resolution of concentrations for NO_2-to-VOC reactivity ratio and wind-dependency of BVOC emission rather than using data assimilation or satellite observation to define better the chemical regimes for NO_x sinks. Online or offline measurements would also help us validate the major ON compounds that are formed, thus constraining the average ambient ON compound interpreted from the gas-particle partitioning coefficient.

With this knowledge, the evaluation for nitrate aerosol reduction strategies should consider the seasonal shift of prevalent NO_x loss regime. The difference in pollution profiles sourced from the continental region and the coastal region also calls for regional cooperation for emission reductions in collaboration with neighboring countries. Further research integrating new knowledge of inorganic/organic nitrate speciation and ON volatility in the Netherlands can improve the NO_x lifetime estimates in chemical transport models to capture better nitrogen transport and deposition, for better emission reduction strategies.

A Appendices

A.1 Data set processing and analysis

Table A.1: Coverage of total NO_y, ACSM measurements (Org, NH_4, SO_4, pNO_3, and Cl), LML observations (NO_x, O_3, NH_3, SO_2) and CAMS EAC4 data set used in this study, shown by the colored shading at available periods. The complete dates (yyyy.mm.dd) indicate the beginning or the end of the data set of a given month. Smaller data gaps within a month are not shown here.

Year-month	NO_y, ACSM, LML	CAMS EAC4
2023		
Jan		2023.01.01–
Feb		
Mar	2023.04.18–	
Apr		
May		
Jun		
Jul	–2023.07.22	
Aug		
Sep		
Oct		
Nov		
Dec		
2024		
Jan		
Feb		
Mar		
Apr		
May		
Jun		
Jul		
Aug		
Sep		
Oct	2024.10.21–	
Nov		
Dec		–2024.12.31
2025		
Jan		
Feb		
Mar		
Apr	–2025.04.27	
May		
Jun		
Jul	2025.07.11–	
Aug		
Sep	–2025.09.04	

Table A.2: Summary of calibration parameters, detection limits, and NO_x^+ ratios method parameters of the CV-ToF-ACSM instrument deployed in this study. Two sets of calibration parameters and detection limits are used for two periods of data set from 2023 and from 2024–2025, due to the replacement of the instrument's detector.

Parameters	2023		2024–2025	
Calibration parameters				
NO_3 ionization efficiency (IE) (ions $\cdot$ pg^{-1})	168.9		163.6	
Relative IE Org	1.40		1.40	
Relative IE NH_4	3.36		3.38	
Relative IE SO_4	1.58		1.71	
Relative IE Cl	1.30		1.30	
Average flow rate (cm$^3\cdot$s^{-1})	1.23		1.56	
Detection limits (μg $\cdot$ m^{-3})	10 min averaging	60 min averaging	10 min averaging	60 min averaging
Org	0.38	0.16	0.10	0.04
NH_4	0.12	0.05	0.07	0.03
NO_3	0.07	0.03	0.03	0.01
SO_4	0.11	0.05	0.05	0.01
Cl	0.09	0.04	0.04	0.01
m/z 30	0.07	0.03	0.02	0.01
m/z 46	0.04	0.02	0.01	0.01
NO_x^+ ratio method parameters (60 min averaging)				
R_{pAmN}	0.0237		0.0360	
R_{pON}[a]	0.0008		0.0011	
C_{DL,NO_2^+}(μg $\cdot$ m^{-3})	0.018		0.005	
$C_{NO^+,\,lim} = \frac{C_{DL,NO_2^+}}{R_{pAmN}}$ (μg $\cdot$ m^{-3})	0.77		0.14	

[a] The geometric mean of the upper and lower limits as described in Nursanto et al. (2025).

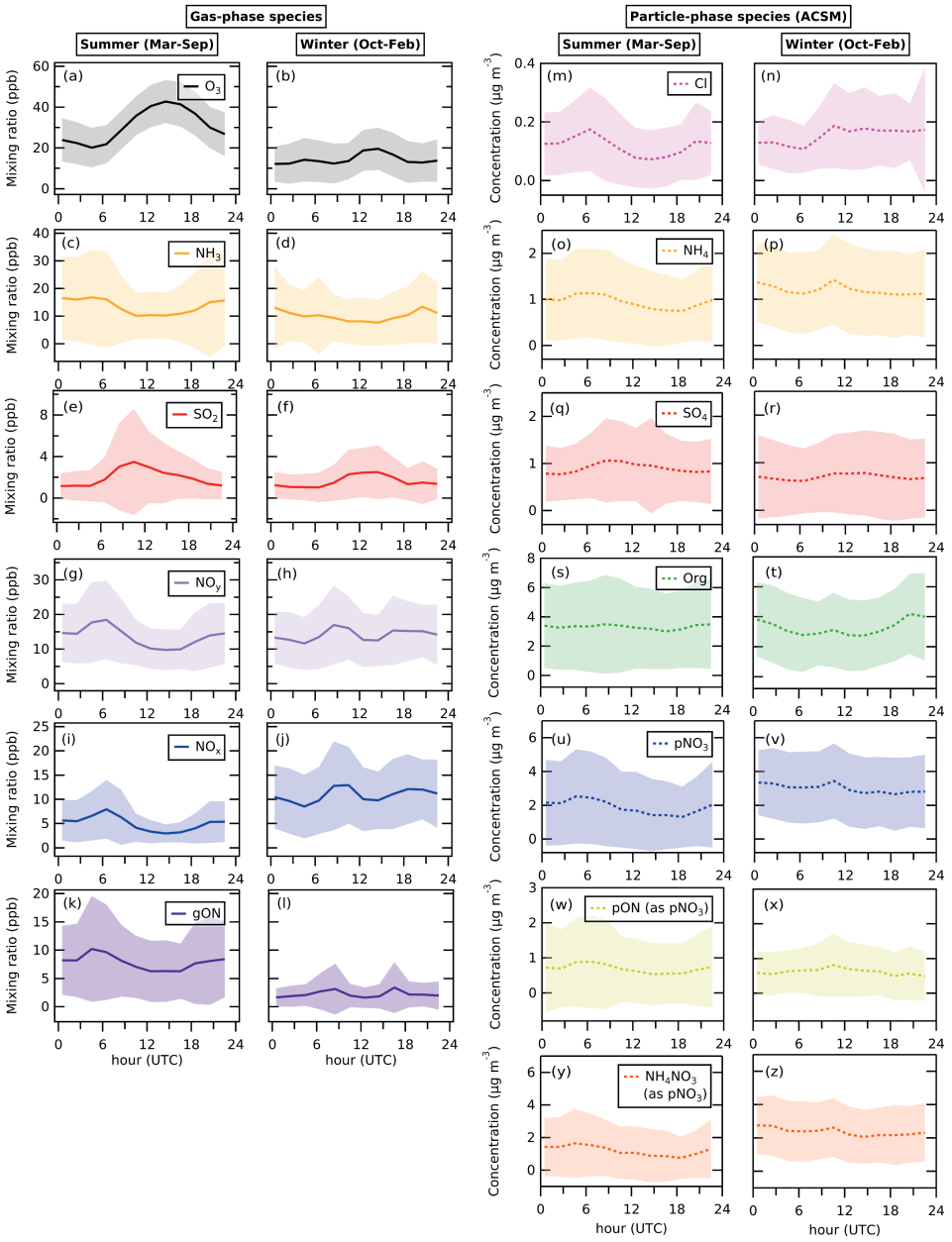


Figure A.1: (a–l) Seasonal average (summer vs. winter) for the mixing ratios of various gas-phase species presented as diurnal cycle plots (appeared in Fig. 5.3), and **(m–z)** Seasonal average for the mass concentration of particle phase species measured by ACSM presented as diurnal cycle plots (appeared in Fig. 5.3). The colored shading represents one standard deviation.

A.2 Calculating NO_2-to-VOC reactivity ratio (NO_2R/VOCR)

The NO_2-to-VOC reactivity ratio (NO_2R/VOCR) shown in Fig. 5.4 is calculated using the Copernicus Atmospheric Monitoring Service (CAMS) global reanalysis (European Centre for Medium-Range Weather Forecasts Atmospheric Composition Reanalysis 4 or EAC4) data set from 1 January 2023 to 31 December 2024. The mixing ratios of NO_2, isoprene, and monoterpenes (in $kg \cdot kg^{-1}$air) were retrieved from the CAMS global reanalysis EAC4 (51.9 °N, 4.9 °E; grid resolution of $0.75^o \times 0.75^o$) and time resolution of 3 h (Inness et al., 2019; Copernicus Atmosphere Monitoring Service, 2020).

To obtain the reactivity for each species, the concentration unit is converted into molecules $\cdot$ cm^{-3}, then multiplied with its reaction rate constant with hydroxyl radicals ($OH^\bullet$). The reaction rate constants (in $cm^3 \cdot molecules^{-1} \cdot s^{-1}$) are calculated using formulas and recombination rate constants from Burkholder et al. (2019) for NO_2 and isoprene (C_5H_8). The recombination rate constants refer to the termolecular reaction between A and B that is pressure dependent (shown in Eq. A.1), forming an intermediate $[AB]^*$ that further collides with a third body (M, gas molecules) to form the product AB. The effective second-order rate constant for a given temperature and pressure ($k_f(T,[M])$) is calculated using Eq. A.2 (the details can be found in Burkholder et al. (2019)), which gives the rate constants of NO_2+$OH^\bullet$ ($k_{NO_2+OH^\bullet}$) and isoprene+$OH^\bullet$ ($k_{ISOP+OH^\bullet}$).

$$A + B \longleftrightarrow [AB]^* \xrightarrow{M} AB \tag{A.1}$$

$$k_f(T,[M]) = \left\{ \frac{k_\infty(T) \cdot k_0(T) \cdot [M]}{k_\infty(T) + k_0(T) \cdot [M]} \right\} \cdot 0.6^{\left\{ 1 + \left[log_{10}\left(\frac{k_0(T)[M]}{k_\infty(T)} \right)^2 \right] \right\}^{-1}} \tag{A.2}$$

$k_f(T,[M])$: effective second-order rate constant of A+B ($cm^3 \cdot molecules^{-1} \cdot s^{-1}$)

$k_\infty(T)$: limiting high-pressure rate constant ($cm^3 \cdot molecules^{-1} \cdot s^{-1}$)

$k_0(T)$: limiting low-pressure rate constant ($cm^6 \cdot molecules^{-2} \cdot s^{-1}$)

T : temperature (K)

$[M]$: total gas concentration (10^{19} molecules $\cdot$ cm^{-3})

To calculate the second-order rate constant for monoterpenes ($C_{10}H_{16}$), the reaction rate constant for α-pinene and $OH^\bullet$ was taken from the Master Chemical Mechanism, MCM v.3.3.1 (Jenkin et al., 1997; Saunders et al., 2003) via `www.mcm.york.ac.uk` (last accessed: 30 October 2025). The formula is given in Eq. A.3.

$$k_{APIN+OH^\bullet}(T) = 1.2 \times 10^{-11} \cdot \exp\left(\frac{440}{T} \right) \cdot 0.572 \tag{A.3}$$

$k_{APIN+OH^\bullet}$: second-order rate constant of α-pinene+$OH^\bullet$ ($cm^3 \cdot molecules^{-1} \cdot s^{-1}$)

T : temperature (K)

The total reactivity of NO_2 (NO_2R, in s^{-1}) is defined as the product of the concentration of NO_2 and its recombination rate constant with hydroxyl radicals ($OH^{\bullet}$). The total reactivity of VOC (VOCR, in s^{-1}) is the sum of the reactivity of isoprene and monoterpenes (reaction for isoprene and α-pinene were used, respectively). The ratio is calculated for each time step as shown in Eq. A.4, then averaged monthly.

$$\frac{NO_2R}{VOCR} = \frac{k_{NO_2 \equiv OH^{\bullet}} \cdot [NO_2]}{(k_{ISOP+OH^{\bullet}} \cdot [\text{isoprene}]) + (k_{APIN+OH^{\bullet}} \cdot [\text{monoterpenes}])} \tag{A.4}$$

The variability of $NO_2R/VOCR$ and the mixing ratios of NO_2, isoprene, and monoterpenes (in ppb or ppt) from the CAMS EAC4 data set are shown in Fig. A.2a–c. To compare the model-derived data set from CAMS, we also provide a snippet of ground-based observation of isoprene (C_5H_8) and monoterpenes ($C_{10}H_{16}$) measured using a proton-transfer-reaction time-of-flight mass spectrometer (PTR-ToF-MS) in Cabauw (see Fig. A.2d–e). The comparison shows that the magnitude of mixing ratios from the CAMS EAC4 data set for isoprene and monoterpenes is within the range of ground-based measurements.

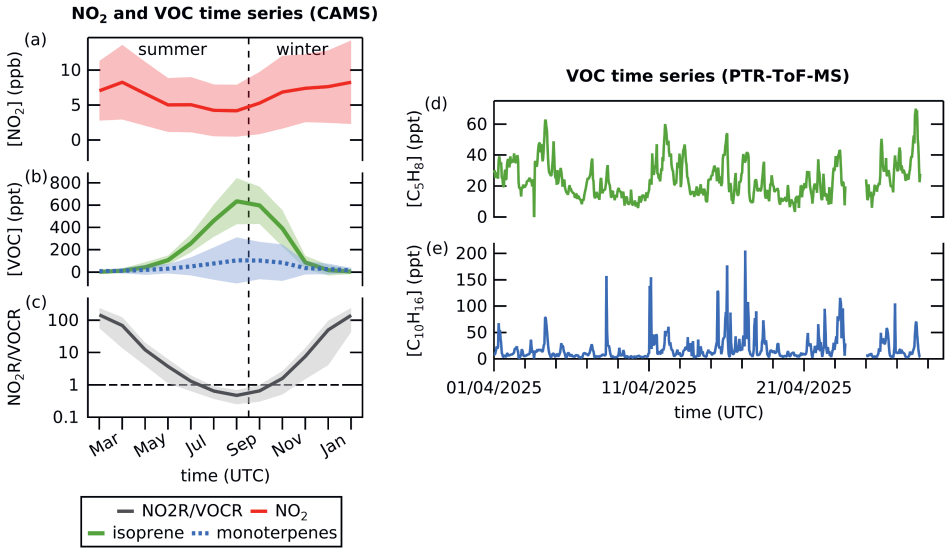
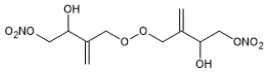
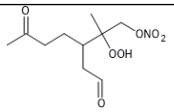
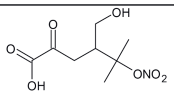
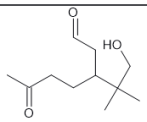
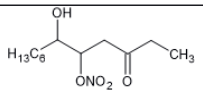
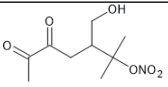
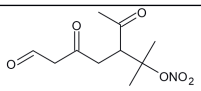
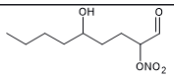
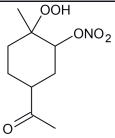


Figure A.2: Monthly average (Jan 2023–Dec 2024) of **(a)** NO_2 vs. VOC reactivity in logarithmic scale, **(b)** NO_2 mixing ratio, **(c)** isoprene and monoterpene mixing ratios determined using CAMS EAC4 data set (Inness et al., 2019; Copernicus Atmosphere Monitoring Service, 2020). **(d–e)** Snippets of isoprene (C_5H_8) and monoterpenes ($C_{10}H_{16}$) mixing ratios observed by a ground-based PTR-ToF-MS measurements in Cabauw (April 2025) as comparison.

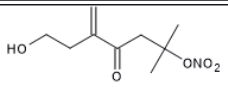
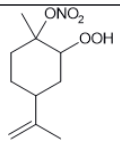
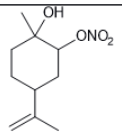
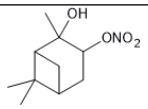
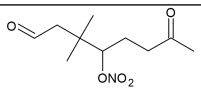
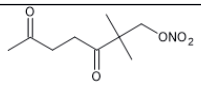
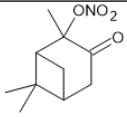
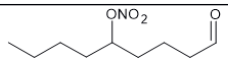
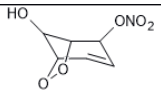
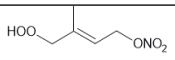
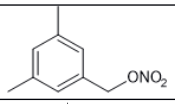
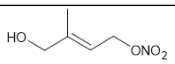
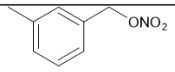
A.3 Theoretical gas-particle partitioning coefficient of organic nitrates ($K_{p,ON}$)

Table A.3: List of organic nitrate compounds named in Fig. 5.5 with their chemical structure, molecular weight, theoretical gas-particle partitioning coefficients ($K_{p,ON}$) calculated using the SIMPOL.1 group contribution method (Pankow and Asher, 2008), and from which precursor(s) they are derived. The list is sorted from high to low based on the $K_{p,ON}$ values at 20 ^{o}C ($m^3 \cdot \mu g^{-1}$), meaning lower volatility compounds with higher particle-to-gas ratio are higher up in the list. The compound names are from MCM v.3.3.1 unless indicated with asterisk (*).

Compound name	Chemical structure	Molecular weight ($g \cdot mol^{-1}$)	$K_{p,ON}$ at 20 ^{o}C ($m^3 \cdot \mu g^{-1}$)	Precursor(s)
dimer of NISOPOOH*		324.24	9.3E+01	isoprene
C813NO3		235.19	5.1E+00	limonene
NLIMALOOH		263.25	3.6E-01	limonene
LIMALNO3		247.25	2.1E-01	limonene
C123NO3		203.26	8.7E-02	dodecane
C98NO3		233.22	3.2E-02	limonene
C106NO3		245.23	1.1E-02	limonene
NONALOHNO3*		219.24	1.0E-02	nonanal
NLMKAOOH		233.22	6.6E-03	limonene

Continues next page

Table A.3: (continued)

Compound name	Chemical structure	Molecular weight ($g \cdot mol^{-1}$)	$K_{p,ON}$ at 20 ^{o}C ($m^3 \cdot \mu g^{-1}$)	Precursor(s)
LMKANO3		217.22	4.1E-03	limonene
NLIMOOH		231.25	2.8E-03	limonene
LIMBNO3		215.25	1.7E-03	limonene
APINBNO3		215.25	1.3E-03	α-pinene
C1012NO3		231.25	5.1E-04	limonene
C928NO3		217.22	2.0E-04	limonene
NC101CO		213.23	6.8E-05	pinene
NONALNO3*		203.28	6.4E-05	nonanal
BZBIPERNO3		189.12	6.2E-05	benzene
NISOPOOH		163.13	2.5E-05	isoprene
TMBNO3		181.19	1.5E-05	1,3,5-trimethylbenzene
ISOPANO3		147.13	1.5E-05	isoprene
MXYLNO3		167.16	6.0E-06	m-xylene



Chapter 6

Synthesis and outlook

6.1 Summary

Throughout this thesis, we investigated the role of nitrate in the reactive nitrogen cycle in a nitrogen-dominated atmosphere by integrating ground-based measurements, chamber experiments, and global reanalysis of atmospheric composition data. In **Chapter 2**, we combined aerosol composition and particle number size distribution observations using a novel hybrid PMF analysis. We aimed to identify the chemical composition responsible for new particle formation (NPF) and growth. While we initially hypothesized that the role of sulfate was diminishing in a nitrogen-dominated atmosphere in the Netherlands, we demonstrated that ammonium sulfate and oxidized organics remain key for NPF, whereas nitrate plays a dominant role in particle growth. The newly formed particles correlate with air masses from the westerly sector, areas with high SO_2 emissions (sulfate precursor), while the growing particles correlate with air masses from the westerly and southerly sectors, areas with higher NH_3 and NO_x emissions (NH_4NO_3 precursors).

In **Chapter 3**, we described for the first time an adapted NO_x^+ ratio method to speciate the nitrate signal in ACSM into ammonium nitrate and organic nitrate. We detailed the data pre-treatment required to overcome the poor detection limit of the ACSM, including data filtering and time averaging. We also provided an updated fragmentation table adapted for the capture vaporizer to determine NO_2^+ and NO^+ signals, along with the method's uncertainty. This method allowed us to quantify the inorganic/organic nitrate speciation at 60 min time averaging using ambient data from Cabauw. Co-located measurements in a controlled chamber experiment showed that this adapted NO_x^+ ratio method for CV-ACSM data agrees well with the method applied to SV-AMS data and PMF results.

In **Chapter 4**, we explored organic nitrate formation in the SAPHIR-CHANEL chamber campaign using realistic urban emission mixtures. We examined how unsaturated VOCs (e.g., monoterpenes, isoprene, and aldehydes) drive the molar yields of organic nitrates. Furthermore, we characterized the differences in molecular weight, volatility, and gas-particle partitioning of organic nitrates formed under daytime ($OH^\bullet$) versus nighttime ($NO_3^\bullet$) oxidation conditions. The average molecular weight of particulate organic nitrate produced under nighttime conditions is found to be higher than that produced under daytime conditions because of the higher mass contribution from oligomers and reduced fragmentation. Similarly, the mass fraction of particulate organic nitrate within the total organic aerosol is up to $\sim$5 times higher under nighttime conditions. This is likely due to differences in both average nitrate molecular weight and lower temperatures affecting gas-particle partitioning. The gas-particle partitioning coefficient of organic nitrates appeared similar to the modeled volatility of oxidized monoterpene nitrates calculated using the SIMPOL.1 method (10^{-4} to 10^{-2} $m^3 \cdot \mu g^{-1}$ at 18–40 °C), regardless

of the complexity of the precursor mixture or the variability in the average molecular weight.

In **Chapter 5**, we analyzed the seasonal variability of nitrate pollution. We investigated the high frequency of winter pollution episodes dominated by nitric acid (HNO_3) versus the summer regime where organic nitrates ($RONO_2$) become more abundant. The high frequency of nitrate pollution episodes during winter (Oct–Feb) is accompanied by lower total concentrations of ON (2–4 ppb) and a lower particulate ON fraction of total nitrate (14–43 %) compared to summer (Mar–Sep; 7–11 ppb; 30–58 %). By categorizing episodes based on air mass origin, we also linked these chemical regimes to specific source regions and emission profiles. When categorizing pollution episodes based on air mass origin, urban coastal air masses and continental air masses contribute roughly equal numbers of episodes. However, slightly more episodes are associated with urban coastal air masses (53 %), which exhibit lower particulate ON fractions but higher total nitrate concentrations, most likely due to the shorter transport distance from the NO_x emission hotspots in the west.

In this synthesis, we integrate the findings from the four preceding chapters, in order to pinpoint the remaining knowledge gaps and outline directions for future research. The main themes include: the influence of emission sources on aerosol chemical composition, the importance of organic nitrate in the aerosol mass, and the influence of seasons and daytime/nighttime conditions on nitrogen sink (inorganic vs. organic nitrate). Lastly, we formulate several recommendations related to the main findings of the investigation by providing an approach to evaluate emission reduction strategies, as well as recommendations for future observations and modeling.

6.2 Main findings and conclusions

6.2.1 Influence of emission sources on aerosol chemical composition

In **Chapter 2** and **Chapter 5**, we found that the airmass origin fundamentally dictates the aerosol chemical profile in the Netherlands. The central location of the Cabauw monitoring site captures the intersection of two distinct regional emission regimes. The change in aerosol chemical composition occurs because of the spatial difference in the emission profiles between the coastal region and the continental region of the Netherlands.

The coastal region (180–360^o wind sector in Cabauw) is dominated by the Randstad metropolitan area and major industrial hubs (e.g., port of Rotterdam). This sector serves as the major source of SO_2 emissions from the port and industrial activities in Rotterdam (western portion of the sector) and NO_x emissions from the urban areas in the Randstad, and some NH_3 emissions from agricultural activities (southwestern and

southern portion of the sector). These precursors facilitate new particle formation (SO_2, NH_3) and growth (NO_x, NH_3; also locally sourced in Cabauw). Coastal airmass origin is associated with 53% of nitrate pollution episodes, characterized by high total nitrate concentrations but a lower organic nitrate fraction due to the abundance of inorganic precursors.

The continental region (0–180^o wind sector in Cabauw) is characterized by long-range transport from mainland Europe, containing higher BVOC emissions, as well as NH_3 and NO_x from agricultural and industrial regions in mainland Europe. We observe that the aerosol chemical composition changes toward more aged organic aerosols coming from long-range transported particles from Europe rather than locally formed particles, although a mixture of inorganic and organic aerosols is also observed. This is also in line with the observations, showing that continental airmasses bring a higher organic nitrate fraction and more oxidized organic aerosols, which represent 47% of the observed nitrate pollution episodes.

6.2.2 Importance of organic nitrate to the aerosol mass

Variability of the particulate organic nitrate fraction

Using the NO_x^+ ratio method established in **Chapter 3**, we revealed that organic nitrates make up a significant portion of the nitrate aerosol mass in the Netherlands, ranging from 14–58 % during pollution episodes (**Chapter 5**). This is different from early assumptions that nitrate in the Netherlands is almost exclusively ammonium nitrate (Schaap et al., 2003; Schaap et al., 2004). More recent studies have found 34–44% of the nitrate aerosol mass loading is particulate organic nitrate in Europe (Kiendler-Scharr et al., 2016). We observed a clear seasonal trend (**Chapter 5**) where the particulate organic nitrate fraction is higher in summer (30–58%) than in winter (14–43%). We attribute this seasonality to larger BVOC availability and solar radiation during summer.

Chamber experiments (**Chapter 4**) demonstrate a significant nighttime enhancement of the organic nitrate mass fraction within the total organic aerosol. Nighttime mass fractions (32–53 %) are higher compared to the daytime values (9–20 %) by a factor of 2.6–4.5, a diurnal shift primarily governed by the properties of organic nitrates detailed in the following section.

Bulk organic nitrate properties

Since only ammonium nitrate has historically been considered in nitrate aerosol deposition modules, there is a sink pathway of NO_x through the formation of organic nitrate aerosol that is not yet included in standard models of nitrogen deposition, likely leading to a misrepresentation of nitrogen deposition. **Chapter 4** measured the chemical composition of organic nitrate in the atmosphere in large detail, to bridge the gap when

interpreting observations or modeling a typical bulk atmospheric composition, which includes nitrate from anthropogenic and biogenic emissions.

For example, we estimated the bulk molecular weight of organic nitrate (**Chapter 4**), which is 258±24 $g \cdot mol^{-1}$ for organic nitrates under daytime conditions and 331±13 $g \cdot mol^{-1}$ under nighttime conditions. These bulk molecular weights are around the commonly used range of average molecular weights of 200–300 $g \cdot mol^{-1}$ (Rollins et al., 2012; Rollins et al., 2013), but this study characterizes for the first time the bulk molecular weight of a realistic replica of the ambient mixture and its diurnal variability. Nighttime conditions promote a significantly higher contribution of high molecular weight compounds ($C_{>10}$, e.g., dimers) to the bulk particulate organic nitrate. Specifically, $C_{>10}$ contributions reached 56 % for the limonene precursor, 36 % for the VCPs precursor, and 51—57 % for the replica of Los Angeles emissions. In contrast, daytime experiments reported substantially lower contributions (0–22 %). These results underscore the need to represent more details of the chemical mechanisms when accounting for organic nitrates in secondary organic aerosol formation models.

The bulk volatility and chemical structure of organic nitrates consistently resemble monoterpene-derived nitrates, regardless of the origin of the air mass or the time of day (**Chapter 4**). The observed gas-particle partitioning coefficients ($K_{p,ON}$) averaged $4 \cdot 10^{-2}$ $m^3 \cdot \mu g^{-1}$ with a range of 10^{-4}–10^{-2} $m^3 \cdot \mu g^{-1}$, a value that aligns with the semi-volatile and low-volatility ranges typically represented in volatility basis set (VBS) frameworks, such as implemented in the LOTOS-EUROS model (Segers et al., 2025). Variation in $K_{p,ON}$ is primarily driven by temperature and the oxidative regime, with lower $K_{p,ON}$ values observed at higher temperatures reflecting the thermodynamic shift toward the gas phase. In contrast, higher $K_{p,ON}$ values are attributed to a synergistic effect of nighttime $NO_3^{\bullet}$ radical chemistry and lower temperatures, which promote the formation of low-volatility oligomers and enhance the condensation of organic nitrates to the particle phase. This is supported by the increased signal intensity of the oligomers observed in BVOC (monoterpene)-rich chamber experiments under nighttime conditions (**Chapter 4**). Such conditions are particularly relevant during winter, characterized by lower average temperatures and prolonged nighttime chemistry, although there are less biogenic monoterpene emissions during winter (but may be emitted from anthropogenic sources like VCPs or cooking).

6.2.3 Influence of seasons and daytime/nighttime conditions on the NO_x sink as inorganic/organic nitrate

The relative contribution of organic nitrate vs. ammonium nitrate to the total nitrate aerosol mass is governed by the prevailing chemical regime of the NO_x sink (**Chapter 5**). A higher particulate organic nitrate fraction is associated with a regime where the reactivity of VOCs towards $OH^{\bullet}$ exceeds that of NO_2 (reactivity ratio < 1), a condition

observed primarily during the summer in the Netherlands. In contrast, the winter period is characterized by reactivity ratios significantly greater than unity, resulting in a lower particulate organic nitrate fraction to the total nitrate aerosol mass and the dominance of HNO_3 formation. This seasonal shift is further modulated by the divergent influences of $OH^{\bullet}$ and $NO_3^{\bullet}$ oxidation pathways and the strong temperature dependence of organic nitrate volatility. The interplay between oxidative chemistry and gas-particle partitioning determines the diurnal and seasonal evolution of the nitrogen sink in the condensed phase.

Seasonal and diurnal cycle of nitrate aerosol formation pathways

The oxidative pathways of NO_x vary significantly by diurnal cycle and season, dictating the ratio of inorganic to organic nitrate. During the day, $OH^{\bullet}$ acts as the primary oxidant, initiating two competing pathways: the direct formation of HNO_3 (Eq. 6.1) and the multi-step formation of alkyl organic nitrates ($RONO_2$) via peroxy radicals ($RO_2^{\bullet}$) (Eqs. 6.2–6.3). Given that these initial reactions (Eqs. 6.1 and 6.2) share similar rate constants ($\approx 10^{-11}$ cm^3·molecules^{-1}·s^{-1} at standard conditions), the dominant sink is primarily determined rather by precursor concentrations. While $RO_2^{\bullet}$ can also form peroxyalkyl nitrates (RO_2NO_2), these species, which include peroxyacyl nitrates (PANs), are not included here in the discussion as they rarely partition into the particle phase and were found to be negligible in the bulk organic nitrate composition (**Chapter 4**).

$$OH^{\bullet} + NO_2 \longrightarrow HNO_3 \tag{6.1}$$

$$OH^{\bullet} + VOC \longrightarrow RO_2^{\bullet} \tag{6.2}$$

$$RO_2^{\bullet} + NO \longrightarrow RONO_2 \tag{6.3}$$

Unlike $OH^{\bullet}$ that reacts with NO_2 to directly form HNO_3, $NO_3^{\bullet}$ exists in a temperature-dependent equilibrium with N_2O_5 (Eq. 6.4). Low temperatures favor the exothermic formation of N_2O_5, which undergoes heterogeneous hydrolysis on aqueous surfaces to form HNO_3 (Eq. 6.5), subsequently yielding NH_4NO_3 in the presence of NH_3. Alternatively, $NO_3^{\bullet}$ reacts directly with VOCs to form $RONO_2$ without branching (Eq. 6.6).

$$NO_3^{\bullet} + NO_2 \rightleftharpoons N_2O_5 \tag{6.4}$$

$$N_2O_5 + H_2O \rightleftharpoons HNO_3 \tag{6.5}$$

$$NO_3^{\bullet} + VOC \longrightarrow RONO_2 \tag{6.6}$$

The seasonal shift in the composition of the nitrate is driven by these competing mechanisms. During summer, extended daytime and elevated BVOC emissions favor organic nitrate formation through $OH^{\bullet}$ chemistry. Warm nights lead the N_2O_5 equilibrium to move towards its decompostion, suppressing the inorganic nocturnal sink and leaving $NO_3^{\bullet}$ available for VOC consumption. This regime promotes $RONO_2$ buildup and contributes to tropospheric ozone accumulation by sequestering NO_2 without O_3 titration.

During winter, shorter days and reduced BVOC emissions favor HNO_3 formation via both $OH^{\bullet}+NO_2$ reaction and N_2O_5 hydrolysis. The combination of lower temperatures (favoring N_2O_5 stability) and higher relative humidity (facilitating hydrolysis) results in a regime dominated by NH_4NO_3, significantly reducing the particulate organic nitrate fraction.

Temperature dependence on nitrate gas-particle partitioning

The shift between HNO_3 and $RONO_2$ regimes is significantly influenced by the divergent gas-particle partitioning behaviors of inorganic and organic nitrates across seasonal and diurnal scales. As established in **Chapter 5**, the diurnal variability of particulate nitrate is primarily governed by NO_x availability and the semi-volatile nature of NH_4NO_3 (Huffman et al., 2009; Xu et al., 2015). During winter, particulate nitrate concentrations peak due to higher NO_x levels and thermodynamically favored partitioning. Low temperatures suppress NH_4NO_3 evaporation more effectively than that of organic nitrates, in line with the inorganic-dominant regime described in Section 6.2.3.

In contrast, the increase in the fraction of particulate organic nitrate in summer is the result of the increased biogenic organic nitrate formation coupled with the relatively lower volatility of these organic nitrate compounds compared to NH_4NO_3 at elevated temperatures. Despite the seasonal variability of the particulate organic nitrate fraction, absolute particulate organic nitrate concentrations remain relatively constant in all seasons. This stability comes from a compensating balance: while summer provides stronger BVOC precursor sources, the concurrent warmer temperatures inhibit gas-to-particle partitioning, effectively counteracting the increase in production (Xu et al., 2015).

Differences in organic nitrate molar yield for varying VOC precursors

The resulting organic nitrate molar yields ranged from 2 % to 21 %, with formation efficiency primarily governed by the percentage of unsaturated compounds in the precursor mixture, such as isoprene, monoterpenes, sesquiterpenes, alkenes, and unsaturated aldehydes. These species are highly susceptible to radical addition reactions, which facilitate organic nitrate production. These compounds are present in higher percentages in the source-specific emission mixtures such as cooking, gasoline, and diesel VOCs. A single-compound limonene precursor exhibited a high yield of 19 % under both oxidative regimes. Cooking emission replicas showed yields of 11–14 %, while traffic-related emissions exhibited the highest yields, ranging from 13–21 %. The complex urban emission mixture as precursor, which contains many low molecular weight alcohols, yielded the lowest ON production (2–7 %). This variability demonstrates that while urban environments provide the necessary NO_x for nitrate formation, the specific

chemical composition of the VOC mix, particularly the fraction of unsaturated biogenic and anthropogenic compounds, determines the degree to which nitrogen is sequestered into the aerosol phase.

6.3 Perspectives and future directions

6.3.1 Evaluating emission reduction strategies

In the context of the Dutch nitrogen crisis, these findings demonstrate that organic nitrates represent a seasonally and diurnally variable fraction of the NO_x sink, altering nitrogen lifetimes and deposition patterns. Unlike HNO_3, the main sink that leads to localized nitrogen deposition, the $RONO_2$ regime, together with the formation of longer-lived NH_4NO_3, facilitates a pathway that enables longer-range transport of reactive nitrogen. By sequestering NO_x as longer-lived organic nitrates, these species distribute nitrogen deposition over broader geographical scales, thereby complicating local mitigation efforts. Consequently, in order to assess the impact of emission reduction strategies that target nitrate aerosol reduction, the seasonal (summer vs. winter) and spatial (coastal vs. continental) variability of nitrate aerosol formation must be considered. In the Netherlands, where NH_3 remains in excess and SO_2 emissions are relatively low, $PM_{2.5}$ formation is almost exclusively governed by the availability of acid precursors, especially HNO_3 and organic acids, rather than alkaline precursors like NH_3. Generally, control of NO_x emissions has been recommended in other studies (Guo et al., 2018; Clappier et al., 2021). Here, we propose a more nuanced approach taking into account the seasons in evaluating the consequences of emission reduction strategies.

As revealed in **Chapter 5**, the Netherlands has an increased formation of NH_4NO_3 during winter, where aerosol formation is NO_x-limited and hydrolysis of N_2O_5 is favored. Low temperatures and high humidity favor the partitioning of HNO_3 into the particle phase. Since there is an abundance of NH_3 to neutralize HNO_3, reducing NH_3 will have a negligible effect on $PM_{2.5}$ mass concentrations. To immediately reduce winter smog and nitrate pollution episodes during winter, NO_x emissions from transport and industry must be the primary target in order to lower HNO_3 production, which is the limiting reagent for NH_4NO_3 formation and particle growth.

Summer in the Netherlands is characterized by a higher organic nitrate production due to high BVOC emissions. In summer, the $OH^{\bullet}$ chemistry is fast and NO_x reacts with BVOC-derived $RO_2^{\bullet}$ to form $RONO_2$. While biogenic emissions from forests and nature areas cannot be controlled, we can control the NO_x emission that reacts with them. The NO_x emission reduction in summer is effective not only in reducing organic nitrate and $PM_{2.5}$ formation, but also in reducing tropospheric O_3 buildup because NO_2 are consumed by $RO_2^{\bullet}$ without consuming O_3, leading to smog production. Although

reducing NO_x emission is the main target, reducing anthropogenic VOC emissions may also lower organic nitrate production, especially in the urban coastal region. In **Chapter 5** we show that anthropogenic source-specific VOC emissions such as VCPs and cooking have a high organic nitrate molar yield due to the unsaturated compounds such as monoterpenes and unsaturated aldehydes emitted from these sources.

Although NO_x emission reduction is the most efficient for immediate $PM_{2.5}$ reduction in an NH_3-rich atmopshere, the mitigation of NH_3 remains a critical long-term priority for both environmental and public health. In the current era of historically low SO_2 emissions, a higher fraction of NH_3 remains free in the atmosphere, leaving it available to either react with HNO_3 or undergo direct dry deposition in natural habitats. Consequently, sustained efforts to reduce NH_3 emissions, which have been pivotal in the Dutch nitrogen policy, must be maintained to decrease the total nitrogen burden on nature reserves and prevent degradation of the ecosystem.

Finally, the distinct pollution profiles associated with continental vs. coastal air masses underscore the need for regional and international cooperation. Because the Netherlands serves as both a source and a receptor for long-range transported reactive nitrogen, localized Dutch policy must be synchronized with broader European emission reduction frameworks. Future research using chemical transport models should simulate these seasonally differentiated strategies to quantify their specific impacts on Dutch nitrogen deposition targets. These models must be able to correctly simulate the formation of inorganic and organic nitrate and its associated seasonal variations.

6.3.2 Recommendations for future modeling and observations

Lagrangian box modeling

Lagrangian box models (e.g., Framework for 0-D Atmospheric Modeling or F0AM) are helpful in simulating the chemical evolution of reactive nitrogen as it is transported downwind from emission sources. In the Netherlands, measurements can be made along a transect using the Ruisdael Observatory network, tracking air mass trajectories between monitoring sites in the Rotterdam port/city (urban site), Cabauw (rural site), Loobos (forest site), and Lutjewad (coastal site). By co-analyzing measurements from these sites (Fig. 6.1), we can simulate the transport of pollutants (e.g., from Rotterdam to Cabauw and onward to Lutjewad) to determine temporal and spatial concentrations of reactive nitrogen. The findings in Section 6.2.3 provide the necessary constraints on inorganic/organic nitrate transformations across different chemical regimes (daytime vs. nighttime, summer vs. winter), allowing for more accurate prediction of NO_x lifetimes, which can then be tested using these transect measurements.

Existing models like F0AM (Wolfe et al., 2016) with the WAM (Washington Aerosol Module) extension (D'Ambro et al., 2017) use gas-particle partitioning modules to

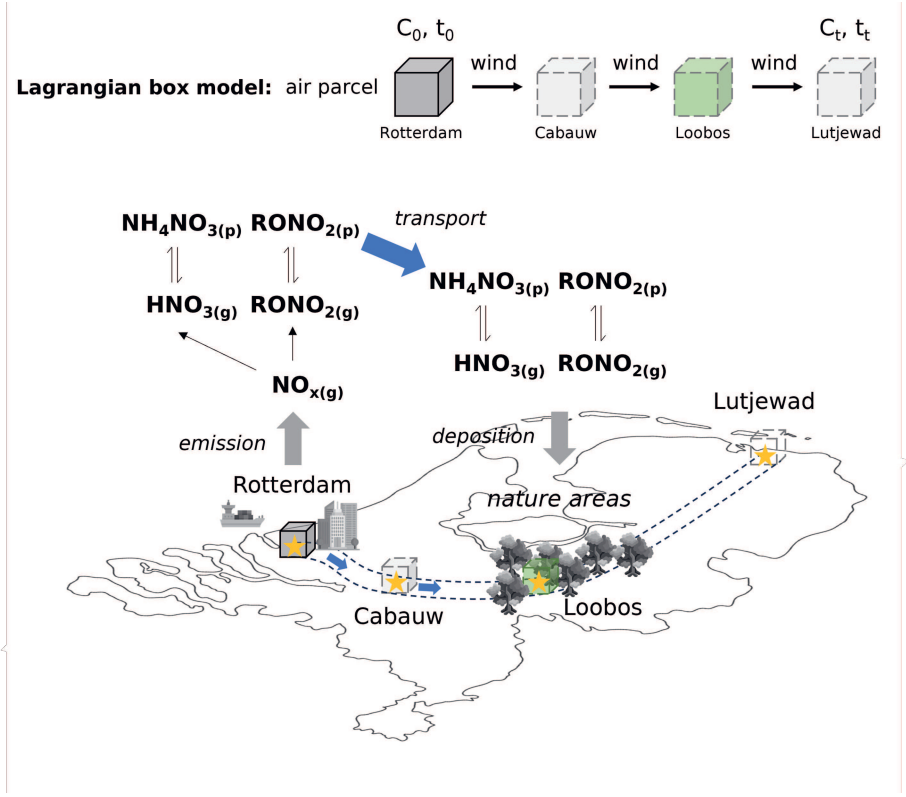


Figure 6.1: Illustration of Lagrangian box model being displaced between existing measurement sites in the Netherlands.

account for the volatility of organic nitrates in the SOA formation. While this model relies on established mechanisms such as MCM v3.2 (Saunders et al., 2003), CB6r2 (Hildebrandt Ruiz and Yarwood, 2013), RACM2 (Goliff et al., 2013), and GEOS-Chem v9.02 (Kim et al., 2025; Fisher et al., 2016; Marais et al., 2016; Travis et al., 2016), they primarily focus on the gas-phase precursors of VOCs. To improve the representation of organic nitrate in complex atmospheric mixtures without overcomplicating the model, we recommend treating organic nitrate as a bulk entity for its initial partitioning and transport. As demonstrated in **Chapter 4**, one can use the established mechanisms of monoterpenes (e.g., limonene or α-pinene) as surrogates, as they share similar bulk volatilities with complex organic nitrate mixtures. However, the molar yield of ON must be tuned to reflect experimental observations in **Chapter 4**, for instance a 2–7 % yield for complex urban air mixtures compared to the 19 % typically used for single-compound limonene precursors.

A critical gap in the current F0AM-WAM model architecture is the representation of organic nitrate oligomers. This thesis, alongside other works in the literature (Nguyen et al., 2011; Mohr et al., 2017; Molteni et al., 2019; DeVault and Ziemann, 2021; Bates et al., 2022; Kenseth et al., 2023; Peräkylä et al., 2023; Zhao et al., 2026), highlights that oligomerization contributes significantly to SOA mass and growth. **Chapter 4** indicates that these oligomers exist primarily in the particulate phase, particularly under nighttime conditions. Once organic nitrate monomers condense, they undergo accretion reactions such as esterification between alcohols and organic acids (Nguyen et al., 2011) or peroxyhemiacetal formation from hydroperoxy organics and aldehydes (Tobias and Ziemann, 2000). Integrating these particle-phase mechanism into F0AM-WAM would significantly improve the model's ability to predict the organic nitrate mass, especially for biogenic VOCs where the base mechanism for the gas-phase is already available.

In addition to particle-phase oligomerization, studies have shown that oligomer formation also occurs in the gas phase. Bates et al. (2022) have shown that gas-phase accretion during the experiment of α-pinene oxidation with $NO_3^{\bullet}$ under nighttime conditions is the primary mechanism for SOA production. While gas-phase accretion is a known source of dimers, this thesis found their gas-phase contribution to be minimal. This is likely due to the extremely low volatility of these accretion products, leading to near-instantaneous partitioning or complete condensation to the particle phase (Molteni et al., 2019; Peräkylä et al., 2023). Another potential explanation for this observation can also be the sensitivity limits of gas-phase instrumentation for high-molecular-weight species. Consequently, we suggest that particle-phase oligomerization be prioritized in future model updates, with gas-phase accretion of secondary priority.

Chemical transport modeling

For chemical transport models such as LOTOS-EUROS, the current volatility base set (VBS) approach to simulating SOA formation can be supplemented, integrating the results from this thesis. For a more simplified approach, we propose including a bulk organic nitrate tracer formed from different kinds of VOC available in the model. We introduce volatility, molecular weight, and yield specific to organic nitrate when treated as bulk, which can be used to estimate organic nitrate formation as a nitrogen sink in the model. In **Chapter 4** and **Chapter 5**, we learned that the $K_{p,ON}$ ranges from 10^{-4}–10^{-1} $m^3 \cdot \mu g^{-1}$ when including both chamber experiments and ambient observation (temperature range -4 to 40 °C). This can be used as a basis in the VBS to determine which volatility range (C^*, inverse of $K_{p,ON}$, equivalent to 10^1–10^4 $\mu g \cdot m^{-3}$) has to be used for organic nitrate compounds.

However, since LOTOS-EUROS already differentiates VOCs based on compound families, another approach is possible. In **Chapter 4**, we have described the consumption of

VOCs in detail for specific compounds in chamber experiments in a realistic ambient air mixture. We also have the volatility, molecular weight, and yield of organic nitrate for limonene and different source-specific emissions, which can be used to estimate the organic nitrate formed from each VOC group. This can be applied to improve the SOA formation in the model. The limonene experiment can be used as a basis to predict organic nitrate formation from biogenic VOCs (isoprene and monoterpenes), while gasoline and diesel experiments can be used to estimate nitrate formation from anthropogenic VOCs (for xylene, toluene, alkanes, and alkenes).

Deposition module

The DEPAC (DEPosition of Acidifying Compounds) module (Zanten et al., 2010) is used in many nitrogen models in the Netherlands (such as LOTOS-EUROS and OPS) to simulate dry deposition. However, the module does not explicitly incorporate organic nitrates into its deposition processes. This thesis underscores the importance of organic nitrate formation in the gas phase and its significant contribution to the total nitrate aerosol budget. Consequently, it is increasingly important to include both gas-phase and particle-phase organic nitrates in deposition models.

While inorganic nitrates like NH_4NO_3 are often dominated by wet deposition due to their high solubility and existence in the fine particle mode, organic nitrates behave differently. A study by Zare et al. (2018) has shown that dry deposition is the most important deposition mechanism for second generation organic nitrate aerosol, especially for highly functionalized nitrates (Fisher et al., 2016). Modeling studies by Knote et al. (2015) using WRF-Chem found that the dry deposition of gas-phase semi-volatile organic compounds, which include organic nitrates, reduced SOA concentrations by 40—52 %. In contrast, wet deposition only contributed to a reduction of 8—11 %.

Unlike the gas-phase organic nitrates, wet deposition remains the dominant sink for the particle-phase organic nitrates. However, efficient deposition of gas-phase precursors may remove the organic nitrates before they can condense to the particles. This is particularly relevant given the observations in this work in which organic nitrates are more abundant in the gas phase in the summer. The observed differences in the deposition patterns are likely related to the molecular properties of organic nitrates, which are generally less polar and less soluble in water than HNO_3.

Integration of organic nitrates into deposition frameworks can be a first step to introduce the complex chemical transformation of nitrogen emission before its deposition. However, it currently faces limitations because the surface resistance (R_c) is not yet characterized for bulk organic nitrate. Since R_c describes how easily a gas-phase molecule is captured by a surface (e.g., canopy, water, soil), it can be parameterized based on the effective Henry's law constant (H^*, in $\text{mol} \cdot \text{L}^{-1} \cdot \text{atm}^{-1}$) denoting solubility, scaled to other chemical species like SO_2 and O_3 (Wesely, 1989). The experimental insights gained

in **Chapter 4** regarding the volatility and gas-particle partitioning of organic nitrates can be exploited as a first step to parameterize these H^* values as bulk properties, providing a feasible path to include organic nitrates in operational deposition models.

Proposed measurement campaign and data exploitation

The expansion of monitoring instrumentation at the Ruisdael Observatory sites (as illustrated in Fig. 6.1) is essential. Deploying longer term measurements for NO_x, NO_y, NH_3, VOCs and aerosol species across the Rotterdam–Cabauw–Lutjewad transect would provide the high-fidelity data needed to validate Lagrangian box models or chemical transport models. Another measurement site in the eastern part of the country, which receives the continental air mass before arriving at Cabauw (**Chapter 5**), can help assess the transboundary contribution of reactive nitrogen species in the Netherlands. This point-to-point measurement allows for an assessment of how nitrogen species transform as air masses traverse the Dutch landscape. Since the Cabauw site is the focal point in the monitoring network, it should ideally host more high mass resolution speciated measurements. Using a co-located long term observation of PTR-MS (for speciated VOCs), mini-DOAS (for NH_3), and MARGA (for NH_3 and HNO_3), NO_y monitor, ACSM (for speciated aerosol phase), and particle sizer (for particle size distribution) will enable seasonal characterization of both gas and particle phase chemical species. It can capture the shift in NO_x sink regimes across seasons to validate data assimilation and satellite products, and to elucidate ways to accomplish seasonal nitrogen deposition mitigation. High mass resolution measurements from VOCs and organic aerosol can be further used to characterize the gas-particle partitioning of organic nitrates in the Netherlands, providing the empirical basis for the bulk properties of organic nitrate in ambient air that have been discussed in **Chapters 4 and 5**.

It is critical to determine whether $RONO_2$ and NH_4NO_3 share similar size distributions. Given the lower volatility of organic nitrate oligomers compared to the highly semi-volatile NH_4NO_3, they may be distributed in different size ranges. We have successfully demonstrated the hybrid PMF approach to provide knowledge on new particle formation and growth in **Chapter 2**. However, the study has not included any distinction between inorganic and organic nitrate composition. We recommend applying a similar approach by integrating gas-phase precursors, gas-phase organic nitrates, and inorganic/organic nitrate aerosol fraction on top of the aerosol composition and particle number size distributions. This approach can be applied to the ongoing CAINA research project, which also focuses on understanding the gas-particle partitioning of nitrogenous compounds and cloud formation in the Netherlands. Attributing these species to specific size bins is a prerequisite for improving aerosol microphysics in chemical transport models that can predict the nitrate transport range and deposition pattern. This integrated approach not only resolves the source origins, but also fills a gap between chemical speciation and physical aerosol dynamics.

Regarding the modeling of nitrogen deposition, height-resolved aerosol composition (canopy vs. aloft) during the intensive field campaign within the CAINA project can directly quantify the deposition velocities of particulate organic nitrates needed for the DEPAC module. For wet scavenging of organic nitrates, integrating ground-based aerosol data with cloud water sampling and more complete analysis of rainwater samples will allow the determination of the scavenging efficiency of organic nitrates. Ideally, measurements of NH_3, NO_x, and NO_y fluxes in future campaigns or research infrastructure, for instance in Loobos (forest site where nitrogen may deposit), should also be prioritized to provide a more complete budget for total nitrogen removal in the atmosphere.

6.3.3 Final words

This thesis refines our fundamental understanding of the fate of reactive nitrogen in the atmosphere. This more accurate simulation of chemical processes involving reactive nitrogen, from emission to deposition, can be used to improve the modeled nitrogen deposition map that we have seen in Fig. 1.2. Through the proposal of emission reduction strategies and recommendations for modeling, measurements, and data exploitation, this work invites the scientific community and policymakers to further explore and resolve open questions regarding the nitrogen budget. Our proposed strategy would allow more accurate estimates of nitrogen deposition patterns for better policymaking to mitigate the nitrogen crisis and protect our ecosystem and health.



References

Aan de Brugh, J. M. J., J. S. Henzing, M. Schaap, W. T. Morgan, C. C. Van Heerwaarden, E. P. Weijers, H. Coe, and M. C. Krol (2012). "Modelling the partitioning of ammonium nitrate in the convective boundary layer". en. *Atmospheric Chemistry and Physics* 12 (6), 3005–3023. DOI: 10.5194/acp-12-3005-2012.

Aan de Brugh, J. M. J., H. G. Ouwersloot, J. Vilà-Guerau de Arellano, and M. C. Krol (2013). "A large-eddy simulation of the phase transition of ammonium nitrate in a convective boundary layer". *Journal of Geophysical Research: Atmospheres* 118 (2), 826–836. DOI: 10.1002/jgrd.50161.

Adams, P. J., J. H. Seinfeld, D. Koch, L. Mickley, and D. Jacob (2001). "General circulation model assessment of direct radiative forcing by the sulfate-nitrate-ammonium-water inorganic aerosol system". *Journal of Geophysical Research: Atmospheres* 106 (D1), 1097–1111. DOI: 10.1029/2000JD900512.

Adams, P. J., J. H. Seinfeld, and D. M. Koch (1999). "Global concentrations of tropospheric sulfate, nitrate, and ammonium aerosol simulated in a general circulation model". *Journal of Geophysical Research: Atmospheres* 104 (D11), 13791–13823. DOI: 10.1029/1999JD900083.

Alfarra, M. (2004). *Insights into atmospheric organic aerosols using an aerosol mass spectrometer*.

Allan, J. D., A. E. Delia, H. Coe, K. N. Bower, M. Alfarra, J. L. Jimenez, A. M. Middlebrook, F. Drewnick, T. B. Onasch, M. R. Canagaratna, J. T. Jayne, and D. R. Worsnop (2004). "A generalised method for the extraction of chemically resolved mass spectra from Aerodyne aerosol mass spectrometer data". *Journal of Aerosol Science* 35 (7), 909–922. DOI: 10.1016/j.jaerosci.2004.02.007.

Amaral, S., J. de Carvalho, M. Costa, and C. Pinheiro (2015). "An Overview of Particulate Matter Measurement Instruments". *Atmosphere* 6 (9), 1327–1345. DOI: 10.3390/atmos6091327.

Andreae, M. O. and P. J. Crutzen (1997). "Atmospheric Aerosols: Biogeochemical Sources and Role in Atmospheric Chemistry". *Science* 276 (5315), 1052–1058. DOI: 10.1126/science.276.5315.1052.

Apel, E. C., T. Brauers, R. Koppmann, B. Bandowe, J. Boßmeyer, C. Holzke, R. Tillmann, A. Wahner, R. Wegener, A. Brunner, M. Jocher, T. Ruuskanen, C. Spirig, D. Steigner, R. Steinbrecher, E. Gomez Alvarez, K. Müller, J. P. Burrows, G. Schade, S. J. Solomon, A. Ladstätter-Weißenmayer, P. Simmonds, D. Young, J. R. Hopkins, A. C. Lewis, G. Legreid, S. Reimann, A. Hansel, A. Wisthaler, R. S. Blake, A. M. Ellis, P. S. Monks, and K. P. Wyche (2008). "Intercomparison of oxygenated volatile organic compound measurements at the SAPHIR atmosphere simu-

lation chamber". *Journal of Geophysical Research: Atmospheres* 113 (D20), 2008JD009865. DOI: 10.1029/2008JD009865.

Asmi, E., N. Kivekäs, V.-M. Kerminen, M. Komppula, A.-P. Hyvärinen, J. Hatakka, Y. Viisanen, and H. Lihavainen (2011). "Secondary new particle formation in Northern Finland Pallas site between the years 2000 and 2010". *Atmospheric Chemistry and Physics* 11 (24), 12959–12972. DOI: 10.5194/acp-11-12959-2011.

Ayala, A., M. Brauer, J. L. Mauderly, and J. M. Samet (2012). "Air pollutants and sources associated with health effects". *Air Quality, Atmosphere & Health* 5 (2), 151–167. DOI: 10.1007/s11869-011-0155-2.

Ayres, B. R., H. M. Allen, D. C. Draper, S. S. Brown, R. J. Wild, J. L. Jimenez, D. A. Day, P. Campuzano-Jost, W. Hu, J. de Gouw, A. Koss, R. C. Cohen, K. C. Duffey, P. Romer, K. Baumann, E. Edgerton, S. Takahama, J. A. Thornton, B. H. Lee, F. D. Lopez-Hilfiker, C. Mohr, P. O. Wennberg, T. B. Nguyen, A. Teng, A. H. Goldstein, K. Olson, and J. L. Fry (2015). "Organic nitrate aerosol formation via NO_3 + biogenic volatile organic compounds in the southeastern United States". *Atmospheric Chemistry and Physics* 15 (23), 13377–13392. DOI: 10.5194/acp-15-13377-2015.

Bahreini, R., B. Ervens, A. M. Middlebrook, C. Warneke, J. A. de Gouw, P. F. DeCarlo, J. L. Jimenez, C. A. Brock, J. A. Neuman, T. B. Ryerson, H. Stark, E. Atlas, J. Brioude, A. Fried, J. S. Holloway, J. Peischl, D. Richter, J. Walega, P. Weibring, A. G. Wollny, and F. C. Fehsenfeld (2009). "Organic aerosol formation in urban and industrial plumes near Houston and Dallas, Texas". *Journal of Geophysical Research: Atmospheres* 114 (D7). DOI: https://doi.org/10.1029/2008JD011493. eprint: https://agupubs.onlinelibrary.wiley.com/doi/pdf/10.1029/2008JD011493.

Bahreini, R., A. M. Middlebrook, J. A. De Gouw, C. Warneke, M. Trainer, C. A. Brock, H. Stark, S. S. Brown, W. P. Dube, J. B. Gilman, K. Hall, J. S. Holloway, W. C. Kuster, A. E. Perring, A. S. H. Prevot, J. P. Schwarz, J. R. Spackman, S. Szidat, N. L. Wagner, R. J. Weber, P. Zotter, and D. D. Parrish (2012). "Gasoline emissions dominate over diesel in formation of secondary organic aerosol mass". *Geophysical Research Letters* 39 (6). Publisher: American Geophysical Union (AGU). DOI: 10.1029/2011gl050718.

Barbaro, E., M. Krol, and J. Vilà-Guerau De Arellano (2015). "Numerical simulation of the interaction between ammonium nitrate aerosol and convective boundary-layer dynamics". *Atmospheric Environment* 105. Publisher: Elsevier BV, 202–211. DOI: 10.1016/j.atmosenv.2015.01.048.

Barsanti, K. C., J. H. Kroll, and J. A. Thornton (2017). "Formation of Low-Volatility Organic Compounds in the Atmosphere: Recent Advancements and Insights". *The Journal of Physical Chemistry Letters* 8 (7), 1503–1511. DOI: 10.1021/acs.jpclett.6b02969.

Bates, K. H., G. J. P. Burke, J. D. Cope, and T. B. Nguyen (2022). "Secondary organic aerosol and organic nitrogen yields from the nitrate radical (NO_3) oxidation of alpha-pinene from various RO_2 fates". *Atmospheric Chemistry and Physics* 22 (2), 1467–1482. DOI: 10.5194/acp-22-1467-2022.

Bauer, S. E., D. Koch, N. Unger, S. M. Metzger, D. T. Shindell, and D. G. Streets (2007). "Nitrate aerosols today and in 2030: a global simulation including aerosols and tropospheric ozone". *Atmospheric Chemistry and Physics* 7 (19), 5043–5059. DOI: 10.5194/acp-7-5043-2007.

Baylon, P., D. Jaffe, N. Wigder, H. Gao, and J. Hee (2015). "Ozone enhancement in western US wildfire plumes at the Mt. Bachelor Observatory: The role of NOx". *Atmospheric Environment* 109, 297–304. DOI: 10.1016/j.atmosenv.2014.09.013.

Beaver, M. R., J. M. S. Clair, F. Paulot, K. M. Spencer, J. D. Crounse, B. W. LaFranchi, K. E. Min, S. E. Pusede, P. J. Wooldridge, G. W. Schade, C. Park, R. C. Cohen, and P. O. Wennberg (2012). "Importance of biogenic precursors to the budget of organic nitrates: observations of multifunctional organic nitrates by CIMS and TD-LIF during BEARPEX 2009". *Atmospheric Chemistry and Physics* 12 (13). Publisher: Copernicus GmbH, 5773–5785. DOI: 10.5194/acp-12-5773-2012.

Berkemeier, T., M. Ammann, T. F. Mentel, U. Pöschl, and M. Shiraiwa (2016). "Organic Nitrate Contribution to New Particle Formation and Growth in Secondary Organic Aerosols from α-Pinene Ozonolysis". *Environmental Science & Technology* 50 (12), 6334–6342. DOI: 10.1021/acs.est.6b00961.

Berndt, T. (2021). "Peroxy Radical Processes and Product Formation in the OH Radical-Initiated Oxidation of α-Pinene for Near-Atmospheric Condition". *The Journal of Physical Chemistry A* 125 (41), 9151–9160. DOI: 10.1021/acs.jpca.1c05576.

Bian, H., M. Chin, D. A. Hauglustaine, M. Schulz, G. Myhre, S. E. Bauer, M. T. Lund, V. A. Karydis, T. L. Kucsera, X. Pan, A. Pozzer, R. B. Skeie, S. D. Steenrod, K. Sudo, K. Tsigaridis, A. P. Tsimpidi, and S. G. Tsyro (2017). "Investigation of global particulate nitrate from the AeroCom phase III experiment". *Atmospheric Chemistry and Physics* 17 (21), 12911–12940. DOI: 10.5194/acp-17-12911-2017.

Bianchi, F., J. Tröstl, H. Junninen, C. Frege, S. Henne, C. R. Hoyle, U. Molteni, E. Herrmann, A. Adamov, N. Bukowiecki, X. Chen, J. Duplissy, M. Gysel, M. Hutterli, J. Kangasluoma, J. Kontkanen, A. Kürten, H. E. Manninen, S. Münch, O. Peräkylä, T. Petäjä, L. Rondo, C. Williamson, E. Weingartner, J. Curtius, D. R. Worsnop, M. Kulmala, J. Dommen, and U. Baltensperger (2016). "New particle formation in the free troposphere: A question of chemistry and timing". *Science* 352 (6289), 1109–1112. DOI: 10.1126/science.aad5456.

Bloss, C., V. Wagner, M. E. Jenkin, R. Volkamer, W. J. Bloss, J. D. Lee, D. E. Heard, K. Wirtz, M. Martin-Reviejo, G. Rea, J. C. Wenger, and M. J. Pilling (2005). "Development of a detailed chemical mechanism (MCMv3.1) for the atmospheric oxidation of aromatic hydrocarbons". *Atmospheric Chemistry and Physics* 5 (3), 641–664. DOI: 10.5194/acp-5-641-2005.

Bobbink, R. and W. K. Hicks (2014). "Factors Affecting Nitrogen Deposition Impacts on Biodiversity: An Overview". In: *Nitrogen Deposition, Critical Loads and Biodiversity*. Ed. by M. A. Sutton, K. E. Mason, L. J. Sheppard, H. Sverdrup, R. Haeuber, and W. K. Hicks. Dordrecht: Springer Netherlands, 127–138. DOI: 10.1007/978-94-007-7939-6_14.

Bossmeyer, J., T. Brauers, C. Richter, F. Rohrer, R. Wegener, and A. Wahner (2006). "Simulation chamber studies on the NO_3 chemistry of atmospheric aldehydes". *Geophysical Research Letters* 33 (18), 2006GL026778. DOI: 10.1029/2006GL026778.

Bowman, J. H., D. J. Barket, and P. B. Shepson (2003). "Atmospheric Chemistry of Nonanal". *Environmental Science & Technology* 37 (10). _eprint: https://doi.org/10.1021/es026220p, 2218–2225. DOI: 10.1021/es026220p.

Boyd, C. M., J. Sanchez, L. Xu, A. J. Eugene, T. Nah, W. Y. Tuet, M. I. Guzman, and N. L. Ng (2015). "Secondary organic aerosol formation from the -pinene+NO_3 system: effect of humidity and peroxy radical fate". *Atmospheric Chemistry and Physics* 15 (13), 7497–7522. DOI: 10.5194/acp-15-7497-2015.

Brean, J., M. Dall'Osto, R. Simó, Z. Shi, D. C. S. Beddows, and R. M. Harrison (2021). "Open ocean and coastal new particle formation from sulfuric acid and amines around the Antarctic Peninsula". *Nature Geoscience* 14 (6), 383–388. DOI: 10.1038/s41561-021-00751-y.

Browne, E. C. and R. C. Cohen (2012). "Effects of biogenic nitrate chemistry on the NO_x lifetime in remote continental regions". *Atmospheric Chemistry and Physics* 12 (24). Publisher: Copernicus GmbH, 11917–11932. DOI: 10.5194/acp-12-11917-2012.

Brownwood, B., A. Turdziladze, T. Hohaus, R. Wu, T. F. Mentel, P. T. M. Carlsson, E. Tsiligiannis, M. Hallquist, S. Andres, L. Hantschke, D. Reimer, F. Rohrer, R. Tillmann, B. Winter, J. Liebmann, S. S. Brown, A. Kiendler-Scharr, A. Novelli, H. Fuchs, and J. L. Fry (2021). "Gas-Particle Partitioning and SOA Yields of Organonitrate Products from NO_3-Initiated Oxidation of Isoprene under Varied Chemical Regimes". *ACS Earth and Space Chemistry* 5 (4), 785–800. DOI: 10.1021/acsearthspacechem.0c00311.

Burkholder, J. B., S. P. Sander, J. Abbat, J. R. Barker, C. Cappa, J. D. Crounse, T. S. Dibble, R. E. Huie, C. E. Kolb, M. J. Kurylo, V. L. Orkin, C. J. Percival, D. M. Wilmouth, and P. H. Wine (2019). *Chemical Kinetics and Photochemical Data for Use in Atmospheric Studies, Evaluation No. 19*.

Canagaratna, M., J. Jayne, J. Jimenez, J. Allan, M. Alfarra, Q. Zhang, T. Onasch, F. Drewnick, H. Coe, A. Middlebrook, A. Delia, L. Williams, A. Trimborn, M. Northway, P. DeCarlo, C. Kolb, P. Davidovits, and D. Worsnop (2007). "Chemical and microphysical characterization of ambient aerosols with the aerodyne aerosol mass spectrometer". *Mass Spectrometry Reviews* 26 (2), 185–222. DOI: 10.1002/mas.20115.

Cape, J. N., Y. S. Tang, J. M. González-Beníez, M. Mitošinková, U. Makkonen, M. Jocher, and A. Stolk (2012). "Organic nitrogen in precipitation across Europe". *Biogeosciences* 9 (11), 4401–4409. DOI: 10.5194/bg-9-4401-2012.

Carlton, A. G., J. De Gouw, J. L. Jimenez, J. L. Ambrose, A. R. Attwood, S. Brown, K. R. Baker, C. Brock, R. C. Cohen, S. Edgerton, C. M. Farkas, D. Farmer, A. H. Goldstein, L. Gratz, A. Guenther, S. Hunt, L. Jaeglé, D. A. Jaffe, J. Mak, C. McClure, A. Nenes, T. K. Nguyen, J. R. Pierce, S. De Sa, N. E. Selin, V. Shah, S. Shaw, P. B. Shepson, S. Song, J. Stutz, J. D. Surratt, B. J. Turpin, C. Warneke, R. A. Washenfelder, P. O. Wennberg, and X. Zhou (2018). "Synthesis of the Southeast Atmosphere Studies: Investigating Fundamental Atmospheric Chemistry Questions". *Bulletin of the American Meteorological Society* 99 (3), 547–567. DOI: 10.1175/BAMS-D-16-0048.1.

Carslaw, D. C. and K. Ropkins (2012). "openair — An R package for air quality data analysis". *Environmental Modelling & Software* 27-28, 52–61. DOI: 10.1016/j.envsoft.2011.09.008.

Castro, A., E. Alonso-Blanco, M. González-Colino, A. I. Calvo, M. Fernández-Raga, and R. Fraile (2010). "Aerosol size distribution in precipitation events in León, Spain". *Atmospheric Research* 96 (2-3), 421–435. DOI: 10.1016/j.atmosres.2010.01.014.

CBS (2022). *Agriculture; crops, livestock and land use by general farm type, region*. Tech. rep. CBS.

– (2024). *Nitrogen emissions into the atmosphere*. Tech. rep. CBS.

Chen, G., F. Canonaco, A. Tobler, W. Aas, A. Alastuey, J. Allan, S. Atabakhsh, M. Aurela, U. Baltensperger, A. Bougiatioti, J. F. De Brito, D. Ceburnis, B. Chazeau, H. Chebaicheb, K. R. Daellenbach, M. Ehn, I. El Haddad, K. Eleftheriadis, O. Favez, H. Flentje, A. Font, K. Fossum, E. Freney, M. Gini, D. C. Green, L. Heikkinen, H. Herrmann, A.-C. Kalogridis, H. Keernik, R. Lhotka, C. Lin, C. Lunder, M. Maasikmets, M. I. Manousakas, N. Marchand, C. Marin, L. Marmureanu, N. Mihalopoulos, G. Močnik, J. Nęcki, C. O'Dowd, J. Ovadnevaite, T. Peter, J.-E. Petit, M. Pikridas, S. Matthew Platt, P. Pokorná, L. Poulain, M. Priestman, V. Riffault, M. Rinaldi, K. Różański, J. Schwarz, J. Sciare, L. Simon, A. Skiba, J. G. Slowik, Y. Sosedova, I. Stavroulas, K. Styszko, E. Teinemaa, H. Timonen, A. Tremper, J. Vasilescu, M. Via, P. Vodička, A. Wiedensohler, O. Zografou, M. Cruz Minguillón, and A. S. Prévôt (2022). "European aerosol phenomenology 8: Harmonised source apportionment of organic aerosol using 22 Year-long ACSM/AMS datasets". *Environment International* 166, 107325. DOI: 10.1016/j.envint.2022.107325.

Chen, Y., H. Shen, and A. G. Russell (2019). "Current and Future Responses of Aerosol pH and Composition in the U.S. to Declining SO_2 Emissions and Increasing NH_3 Emissions". *Environmental Science & Technology* 53 (16). Publisher: American Chemical Society (ACS), 9646–9655. DOI: 10.1021/acs.est.9b02005.

Clappier, A., P. Thunis, M. Beekmann, J. Putaud, and A. De Meij (2021). "Impact of SOx, NOx and NH3 emission reductions on PM2.5 concentrations across Europe: Hints for future measure development". *Environment International* 156. Publisher: Elsevier BV, 106699. DOI: 10.1016/j.envint.2021.106699.

CLO (2025). *Nitrogen deposition, 1990-2025 (indicator 0189, version 19, 9 October 2025)*.

Clough, P. N. and B. A. Thrush (1967). "Mechanism of chemiluminescent reaction between nitric oxide and ozone". *Transactions of the Faraday Society* 63, 915. DOI: 10.1039/tf9676300915.

Coggon, M. M., G. I. Gkatzelis, B. C. McDonald, J. B. Gilman, R. H. Schwantes, N. Abuhassan, K. C. Aikin, M. F. Arend, T. A. Berkoff, S. S. Brown, T. L. Campos, R. R. Dickerson, G. Gronoff, J. F. Hurley, G. Isaacman-VanWertz, A. R. Koss, M. Li, S. A. McKeen, F. Moshary, J. Peischl, V. Pospisilova, X. Ren, A. Wilson, Y. Wu, M. Trainer, and C. Warneke (2021). "Volatile chemical product emissions enhance ozone and modulate urban chemistry". *Proceedings of the National Academy of Sciences* 118 (32). Publisher: Proceedings of the National Academy of Sciences. DOI: 10.1073/pnas.2026653118.

Coggon, M. M., C. E. Stockwell, L. Xu, J. Peischl, J. B. Gilman, A. Lamplugh, H. J. Bowman, K. Aikin, C. Harkins, Q. Zhu, R. H. Schwantes, J. He, M. Li, K. Seltzer, B. McDonald, and C. Warneke (2024). "Contribution of cooking emissions to the urban volatile organic compounds in Las Vegas, NV". *Atmospheric Chemistry and Physics* 24 (7). Publisher: Copernicus GmbH, 4289–4304. DOI: 10.5194/acp-24-4289-2024.

Copernicus Atmosphere Monitoring Service (2020). *CAMS global reanalysis (EAC4)*. DOI: 10.24381/D58BBF47.

Cowan, N., E. Nemitz, J. T. Walker, D. Fowler, J. J. Finnigan, H. N. Webster, P. Levy, M. Twigg, S. Y. Tang, N. Bachiller-Jareno, P. Trembath, R. P. Kinnersley, and C. F. Braban (2022). "Review of methods for assessing deposition of reactive nitrogen pollutants across complex terrain with focus on the UK". *Environmental Science: Atmospheres* 2 (5), 829–851. DOI: 10.1039/D2EA00012A.

Crippa, M., D. Guizzardi, M. Muntean, E. Schaaf, F. Dentener, J. A. Van Aardenne, S. Monni, U. Doering, J. G. J. Olivier, V. Pagliari, and G. Janssens-Maenhout (2018). "Gridded emissions of air pollutants for the period 1970–2012 within EDGAR v4.3.2". *Earth System Science Data* 10 (4). Publisher: Copernicus GmbH, 1987–2013. DOI: 10.5194/essd-10-1987-2018.

D'Ambro, E. L., K. H. Møller, F. D. Lopez-Hilfiker, S. Schobesberger, J. Liu, J. E. Shilling, B. H. Lee, H. G. Kjaergaard, and J. A. Thornton (2017). "Isomerization of Second-Generation Isoprene Peroxy Radicals: Epoxide Formation and Implications for Secondary Organic Aerosol Yields". *Environmental Science & Technology* 51 (9), 4978–4987. DOI: 10.1021/acs.est.7b00460.

Dada, L., P. Paasonen, T. Nieminen, S. Buenrostro Mazon, J. Kontkanen, O. Peräkylä, K. Lehtipalo, T. Hussein, T. Petäjä, V.-M. Kerminen, J. Bäck, and M. Kulmala (2017). "Long-term analysis of clear-sky new particle formation events and nonevents in Hyytiälä". *Atmospheric Chemistry and Physics* 17 (10), 6227–6241. DOI: 10.5194/acp-17-6227-2017.

Dall'Osto, M., D. C. S. Beddows, A. Asmi, L. Poulain, L. Hao, E. Freney, J. D. Allan, M. Canagaratna, M. Crippa, F. Bianchi, G. de Leeuw, A. Eriksson, E. Swietlicki, H. C. Hansson, J. S. Henzing, C. Granier, K. Zemankova, P. Laj, T. Onasch, A. Prevot, J. P. Putaud, K. Sellegri, M. Vidal, A. Virtanen, R. Simo, D. Worsnop, C. O'Dowd, M. Kulmala, and R. M. Harrison (2018). "Novel insights on new particle formation derived from a pan-european observing system". *Scientific Reports* 8 (1), 1482. DOI: 10.1038/s41598-017-17343-9.

Davuliene, L., D. Jasineviciene, I. Garbariene, J. Andriejauskiene, V. Ulevicius, and S. Bycenkiene (2021). "Long-term air pollution trend analysis in the South-eastern Baltic region, 1981–2017". *Atmospheric Research* 247. Publisher: Elsevier BV, 105191. DOI: 10.1016/j.atmosres.2020.105191.

Day, D. A., P. J. Wooldridge, M. B. Dillon, J. A. Thornton, and R. C. Cohen (2002). "A thermal dissociation laser-induced fluorescence instrument for in situ detection of NO_2, peroxy nitrates, alkyl nitrates, and HNO_3". *Journal of Geophysical Research: Atmospheres* 107 (D6), ACH 4–1–ACH 4–14. DOI: 10.1029/2001JD000779.

Day, D. A., P. Campuzano-Jost, B. A. Nault, B. B. Palm, W. Hu, H. Guo, P. J. Wooldridge, R. C. Cohen, K. S. Docherty, J. A. Huffman, S. S. de Sá, S. T. Martin, and J. L. Jimenez (2022a). "A systematic re-evaluation of methods for quantification of bulk particle-phase organic nitrates using real-time aerosol mass spectrometry". *Atmospheric Measurement Techniques* 15 (2), 459–483. DOI: 10.5194/amt-15-459-2022.

Day, D. A., J. L. Fry, H. G. Kang, J. E. Krechmer, B. R. Ayres, N. I. Keehan, S. L. Thompson, W. Hu, P. Campuzano-Jost, J. C. Schroder, H. Stark, M. P. DeVault, P. J. Ziemann, K. J. Zarzana, R. J. Wild, W. P. Dubè, S. S. Brown, and J. L. Jimenez (2022b). "Secondary Organic Aerosol

Mass Yields from NO_3 Oxidation of α-Pinene and Δ-Carene: Effect of RO_2 Radical Fate". *The Journal of Physical Chemistry A* 126 (40), 7309–7330. DOI: 10.1021/acs.jpca.2c04419.

Day, D. A., B. A. Nault, P. Campuzano-Jost, and J. L. Jimenez (2023). "Evaluation of Uncertainties and Introduction of Tools for Quantification of Bulk Particle-phase Organic Nitrates Using Real-time Aerosol Mass Spectrometry". In: Portland, Oregon.

De Vries, W. (2021). "Impacts of nitrogen emissions on ecosystems and human health: A mini review". *Current Opinion in Environmental Science & Health* 21, 100249. DOI: 10.1016/j.coesh.2021.100249.

DeCarlo, P. F., J. R. Kimmel, A. Trimborn, M. J. Northway, J. T. Jayne, A. C. Aiken, M. Gonin, K. Fuhrer, T. Horvath, K. S. Docherty, D. R. Worsnop, and J. L. Jimenez (2006). "Field-Deployable, High-Resolution, Time-of-Flight Aerosol Mass Spectrometer". *Analytical Chemistry* 78 (24), 8281–8289. DOI: 10.1021/ac061249n.

DeVault, M. P. and P. J. Ziemann (2021). "Gas- and Particle-Phase Products and Their Mechanisms of Formation from the Reaction of -3-Carene with NO_3 Radicals". *The Journal of Physical Chemistry A* 125 (47), 10207–10222. DOI: 10.1021/acs.jpca.1c07763.

Drewnick, F., J.-M. Diesch, P. Faber, and S. Borrmann (2015). "Aerosol mass spectrometry: particle–vaporizer interactions and their consequences for the measurements". *Atmospheric Measurement Techniques* 8 (9), 3811–3830. DOI: 10.5194/amt-8-3811-2015.

Drewnick, F., S. S. Hings, M. R. Alfarra, A. S. H. Prevot, and S. Borrmann (2009). "Aerosol quantification with the Aerodyne Aerosol Mass Spectrometer: detection limits and ionizer background effects". *Atmospheric Measurement Techniques* 2 (1), 33–46. DOI: 10.5194/amt-2-33-2009.

Drewnick, F., S. S. Hings, P. DeCarlo, J. T. Jayne, M. Gonin, K. Fuhrer, S. Weimer, J. L. Jimenez, K. L. Demerjian, S. Borrmann, and D. R. Worsnop (2005). "A New Time-of-Flight Aerosol Mass Spectrometer (TOF-AMS)—Instrument Description and First Field Deployment". *Aerosol Science and Technology* 39 (7), 637–658. DOI: 10.1080/02786820500182040.

Drugé, T., P. Nabat, M. Mallet, and S. Somot (2019). "Model simulation of ammonium and nitrate aerosols distribution in the Euro-Mediterranean region and their radiative and climatic effects over 1979–2016". *Atmospheric Chemistry and Physics* 19 (6), 3707–3731. DOI: 10.5194/acp-19-3707-2019.

Drummond, J. W., A. Volz, and D. H. Ehhalt (1985). "An optimized chemiluminescence detector for tropospheric NO measurements". *Journal of Atmospheric Chemistry* 2 (3), 287–306. DOI: 10.1007/BF00051078.

Ehn, M., J. A. Thornton, E. Kleist, M. Sipilä, H. Junninen, I. Pullinen, M. Springer, F. Rubach, R. Tillmann, B. Lee, F. Lopez-Hilfiker, S. Andres, I.-H. Acir, M. Rissanen, T. Jokinen, S. Schobesberger, J. Kangasluoma, J. Kontkanen, T. Nieminen, T. Kurtén, L. B. Nielsen, S. Jørgensen, H. G. Kjaergaard, M. Canagaratna, M. D. Maso, T. Berndt, T. Petäjä, A. Wahner, V.-M. Kerminen, M. Kulmala, D. R. Worsnop, J. Wildt, and T. F. Mentel (2014). "A large source of low-volatility secondary organic aerosol". *Nature* 506 (7489), 476–479. DOI: 10.1038/nature13032.

Eisele, F. L. and D. J. Tanner (1993). "Measurement of the gas phase concentration of H_2SO_4 and methane sulfonic acid and estimates of H_2 SO_4 production and loss in the atmosphere". *Journal of Geophysical Research: Atmospheres* 98 (D5), 9001–9010. DOI: 10.1029/93JD00031.

Erisman, J., A. Bleeker, J. Galloway, and M. Sutton (2007). "Reduced nitrogen in ecology and the environment". *Environmental Pollution* 150 (1). Publisher: Elsevier BV, 140–149. DOI: 10.1016/j.envpol.2007.06.033.

Erisman, J. W., E. Dammers, V. Damme, and N. Soudzilovskaia (2015). "Trends in EU nitrogen deposition and impacts on ecosystems". *EM Air and Waste Management Association's Magazine for Environmental Managers* 65, 31–35.

Erisman, J. W., J. Galloway, S. Seitzinger, A. Bleeker, and K. Butterbach-Bahl (2011). "Reactive nitrogen in the environment and its effect on climate change". *Current Opinion in Environmental Sustainability* 3 (5), 281–290. DOI: 10.1016/j.cosust.2011.08.012.

Eurostat (2022). *Country level - gross weight of goods handled in all ports*. DOI: 10.2908/MAR_MG_AA_CWH.

Eyring, V., I. S. Isaksen, T. Berntsen, W. J. Collins, J. J. Corbett, O. Endresen, R. G. Grainger, J. Moldanova, H. Schlager, and D. S. Stevenson (2010). "Transport impacts on atmosphere and climate: Shipping". *Atmospheric Environment* 44 (37). Publisher: Elsevier BV, 4735–4771. DOI: 10.1016/j.atmosenv.2009.04.059.

Fagerli, H. and W. Aas (2008). "Trends of nitrogen in air and precipitation: Model results and observations at EMEP sites in Europe, 1980–2003". *Environmental Pollution* 154 (3). Publisher: Elsevier BV, 448–461. DOI: 10.1016/j.envpol.2008.01.024.

Fan, J., D. Rosenfeld, Y. Zhang, S. E. Giangrande, Z. Li, L. A. T. Machado, S. T. Martin, Y. Yang, J. Wang, P. Artaxo, H. M. J. Barbosa, R. C. Braga, J. M. Comstock, Z. Feng, W. Gao, H. B. Gomes, F. Mei, C. Pöhlker, M. L. Pöhlker, U. Pöschl, and R. A. F. de Souza (2018). "Substantial convection and precipitation enhancements by ultrafineaerosol particles". *Science* 359 (6374), 411–418. DOI: 10.1126/science.aan8461.

Farmer, D. K., A. Matsunaga, K. S. Docherty, J. D. Surratt, J. H. Seinfeld, P. J. Ziemann, and J. L. Jimenez (2010). "Response of an aerosol mass spectrometer to organonitrates and organosulfates and implications for atmospheric chemistry". *Proceedings of the National Academy of Sciences* 107 (15), 6670–6675. DOI: 10.1073/pnas.0912340107.

Farmer, D. K. and J. L. Jimenez (2010). "Real-time Atmospheric Chemistry Field Instrumentation". *Analytical Chemistry* 82 (19), 7879–7884. DOI: 10.1021/ac1010603.

Fehsenfeld, F. C., R. R. Dickerson, G. Hübler, W. T. Luke, L. J. Nunnermacker, E. J. Williams, J. M. Roberts, J. G. Calvert, C. M. Curran, A. C. Delany, C. S. Eubank, D. W. Fahey, A. Fried, B. W. Gandrud, A. O. Langford, P. C. Murphy, R. B. Norton, K. E. Pickering, and B. A. Ridley (1987). "A ground-based intercomparison of NO, NO_x, and NO_y measurement techniques". *Journal of Geophysical Research: Atmospheres* 92 (D12). Publisher: American Geophysical Union (AGU), 14710–14722. DOI: 10.1029/jd092id12p14710.

Feng, Y. and J. E. Penner (2007). "Global modeling of nitrate and ammonium: Interaction of aerosols and tropospheric chemistry". *Journal of Geophysical Research: Atmospheres* 112 (D1), 2005JD006404. DOI: 10.1029/2005JD006404.

Fields, S. (2004). "Global Nitrogen: Cycling out of Control". *Environmental Health Perspectives* 112 (10), A556–A563. DOI: 10.1289/ehp.112-a556.

Fioletov, V. E., C. A. McLinden, N. Krotkov, C. Li, J. Joiner, N. Theys, S. Carn, and M. D. Moran (2016). "A global catalogue of large SO_2 sources and emissions derived from the Ozone Monitoring Instrument". *Atmospheric Chemistry and Physics* 16 (18), 11497–11519. DOI: 10.5194/acp-16-11497-2016.

Fisher, J. A., D. J. Jacob, K. R. Travis, P. S. Kim, E. A. Marais, C. Chan Miller, K. Yu, L. Zhu, R. M. Yantosca, M. P. Sulprizio, J. Mao, P. O. Wennberg, J. D. Crounse, A. P. Teng, T. B. Nguyen, J. M. St. Clair, R. C. Cohen, P. Romer, B. A. Nault, P. J. Wooldridge, J. L. Jimenez, P. Campuzano-Jost, D. A. Day, W. Hu, P. B. Shepson, F. Xiong, D. R. Blake, A. H. Goldstein, P. K. Misztal, T. F. Hanisco, G. M. Wolfe, T. B. Ryerson, A. Wisthaler, and T. Mikoviny (2016). "Organic nitrate chemistry and its implications for nitrogen budgets in an isoprene- and monoterpene-rich atmosphere: constraints from aircraft (SEAC^{4}RS) and ground-based (SOAS) observations in the Southeast US". *Atmospheric Chemistry and Physics* 16 (9). Publisher: Copernicus GmbH, 5969–5991. DOI: 10.5194/acp-16-5969-2016.

Fontijn, A., A. J. Sabadell, and R. J. Ronco (1970). "Homogeneous chemiluminescent measurement of nitric oxide with ozone. Implications for continuous selective monitoring of gaseous air pollutants". *Analytical Chemistry* 42 (6), 575–579. DOI: 10.1021/ac60288a034.

Fortems-Cheiney, A., G. Broquet, I. Pison, M. Saunois, E. Potier, A. Berchet, G. Dufour, G. Siour, H. Denier Van Der Gon, S. N. C. Dellaert, and K. F. Boersma (2021). "Analysis of the Anthropogenic and Biogenic NO_x Emissions Over 2008–2017: Assessment of the Trends in the 30 Most Populated Urban Areas in Europe". *Geophysical Research Letters* 48 (11). Publisher: American Geophysical Union (AGU). DOI: 10.1029/2020gl092206.

Fountoukis, C. and A. Nenes (2007). "ISORROPIA II: a computationally efficient thermodynamic equilibrium model for K^+–Ca^{2+}–Mg^{2+}–NH_4^+–Na^+–SO_4^{2-}–NO_3^-–Cl^-–H_2O aerosols". *Atmospheric Chemistry and Physics* 7 (17), 4639–4659. DOI: 10.5194/acp-7-4639-2007.

Francisco, M. A. and J. Krylowski (2005). "Chemistry of Organic Nitrates: Thermal Chemistry of Linear and Branched Organic Nitrates". *Industrial & Engineering Chemistry Research* 44 (15), 5439–5446. DOI: 10.1021/ie049380d.

Fröhlich, R., M. J. Cubison, J. G. Slowik, N. Bukowiecki, A. S. H. Prévôt, U. Baltensperger, J. Schneider, J. R. Kimmel, M. Gonin, U. Rohner, D. R. Worsnop, and J. T. Jayne (2013). "The ToF-ACSM: a portable aerosol chemical speciation monitor with TOFMS detection". *Atmospheric Measurement Techniques* 6 (11), 3225–3241. DOI: 10.5194/amt-6-3225-2013.

Fry, J. L., H. Allen, B. Ayres, D. C. Draper, A. Steinbach, and S. Kappes (2014). *On-line Monitoring of Atmospheric Inorganic Gases and Aerosols in the Southeastern and Northwestern U.S.* The Applications Book.

Fry, J. L., D. C. Draper, K. J. Zarzana, P. Campuzano-Jost, D. A. Day, J. L. Jimenez, S. S. Brown, R. C. Cohen, L. Kaser, A. Hansel, L. Cappellin, T. Karl, A. Hodzic Roux, A. Turnipseed, C. Cantrell, B. L. Lefer, and N. Grossberg (2013). "Observations of gas- and aerosol-phase organic nitrates at BEACHON-RoMBAS 2011". *Atmospheric Chemistry and Physics* 13 (17), 8585–8605. DOI: 10.5194/acp-13-8585-2013.

Fry, J. L., A. Kiendler-Scharr, A. W. Rollins, T. Brauers, S. S. Brown, H.-P. Dorn, W. P. Dubé, H. Fuchs, A. Mensah, F. Rohrer, R. Tillmann, A. Wahner, P. J. Wooldridge, and R. C. Cohen (2011). "SOA from limonene: role of NO_3; in its generation and degradation". *Atmospheric Chemistry and Physics* 11 (8), 3879–3894. DOI: 10.5194/acp-11-3879-2011.

Fry, J. L., A. Kiendler-Scharr, A. W. Rollins, P. J. Wooldridge, S. S. Brown, H. Fuchs, W. Dubé, A. Mensah, M. Dal Maso, R. Tillmann, H.-P. Dorn, T. Brauers, and R. C. Cohen (2009). "Organic nitrate and secondary organic aerosol yield from NO_3 oxidation of -pinene evaluated using a gas-phase kinetics/aerosol partitioning model". *Atmospheric Chemistry and Physics* 9 (4), 1431–1449. DOI: 10.5194/acp-9-1431-2009.

Fry, J. L., S. S. Brown, A. M. Middlebrook, P. M. Edwards, P. Campuzano-Jost, D. A. Day, J. L. Jimenez, H. M. Allen, T. B. Ryerson, I. Pollack, M. Graus, C. Warneke, J. A. de Gouw, C. A. Brock, J. Gilman, B. M. Lerner, W. P. Dubé, J. Liao, and A. Welti (2018). "Secondary organic aerosol (SOA) yields from NO_3 radical + isoprene based on nighttime aircraft power plant plume transects". *Atmospheric Chemistry and Physics* 18 (16), 11663–11682. DOI: 10.5194/acp-18-11663-2018.

Galloway, J. N., J. D. Aber, J. W. Erisman, S. P. Seitzinger, R. W. Howarth, E. B. Cowling, and B. J. Cosby (2003). "The Nitrogen Cascade". *BioScience* 53 (4). Publisher: Oxford University Press (OUP), 341. DOI: 10.1641/0006-3568(2003)053[0341:tnc]2.0.co;2.

Gao, L., J. Song, C. Mohr, W. Huang, M. Vallon, F. Jiang, T. Leisner, and H. Saathoff (2022). "Kinetics, SOA yields, and chemical composition of secondary organic aerosol from -caryophyllene ozonolysis with and without nitrogen oxides between 213 and 313 K". *Atmospheric Chemistry and Physics* 22 (9), 6001–6020. DOI: 10.5194/acp-22-6001-2022.

Gao, L., I. Zgheib, E. Stergiou, C. Carstens, F. Sari Doré, M. Dupanloup, F. Bourgain, S. Perrier, and M. Riva (2025). "Characterization of the newly designed wall-free particle evaporator (WALL-E) for online measurements of atmospheric particles". en. *Atmospheric Measurement Techniques* 18 (19), 5087–5101. DOI: 10.5194/amt-18-5087-2025.

Gentner, D. R., S. H. Jathar, T. D. Gordon, R. Bahreini, D. A. Day, I. El Haddad, P. L. Hayes, S. M. Pieber, S. M. Platt, J. De Gouw, A. H. Goldstein, R. A. Harley, J. L. Jimenez, A. S. H. Prévôt, and A. L. Robinson (2017). "Review of Urban Secondary Organic Aerosol Formation from Gasoline and Diesel Motor Vehicle Emissions". *Environmental Science & Technology* 51 (3). Publisher: American Chemical Society (ACS), 1074–1093. DOI: 10.1021/acs.est.6b04509.

Gkatzelis, G. I., M. M. Coggon, B. C. McDonald, J. Peischl, K. C. Aikin, J. B. Gilman, M. Trainer, and C. Warneke (2021a). "Identifying Volatile Chemical Product Tracer Compounds in U.S. Cities". *Environmental Science & Technology* 55 (1). Publisher: American Chemical Society (ACS), 188–199. DOI: 10.1021/acs.est.0c05467.

Gkatzelis, G. I., M. M. Coggon, B. C. McDonald, J. Peischl, J. B. Gilman, K. C. Aikin, M. A. Robinson, F. Canonaco, A. S. H. Prevot, M. Trainer, and C. Warneke (2021b). "Observations Confirm that Volatile Chemical Products Are a Major Source of Petrochemical Emissions in U.S. Cities". *Environmental Science & Technology* 55 (8). Publisher: American Chemical Society (ACS), 4332–4343. DOI: 10.1021/acs.est.0c05471.

Goliff, W. S., W. R. Stockwell, and C. V. Lawson (2013). "The regional atmospheric chemistry mechanism, version 2". *Atmospheric Environment* 68, 174–185. DOI: 10.1016/j.atmosenv.2012.11.038.

González-Sánchez, J. M., N. Brun, J. Wu, J. Morin, B. Temime-Roussel, S. Ravier, C. Mouchel-Vallon, J.-L. Clément, and A. Monod (2021). "On the importance of atmospheric loss of organic nitrates by aqueous-phase OH oxidation". *Atmospheric Chemistry and Physics* 21 (6), 4915–4937. DOI: 10.5194/acp-21-4915-2021.

González-Sánchez, J. M., N. Brun, J. Wu, S. Ravier, J.-L. Clément, and A. Monod (2023). "On the importance of multiphase photolysis of organic nitrates on their global atmospheric removal". *Atmospheric Chemistry and Physics* 23 (10), 5851–5866. DOI: 10.5194/acp-23-5851-2023.

Gordon, H., K. Sengupta, A. Rap, J. Duplissy, C. Frege, C. Williamson, M. Heinritzi, M. Simon, C. Yan, J. Almeida, J. Tröstl, T. Nieminen, I. K. Ortega, R. Wagner, E. M. Dunne, A. Adamov, A. Amorim, A.-K. Bernhammer, F. Bianchi, M. Breitenlechner, S. Brilke, X. Chen, J. S. Craven, A. Dias, S. Ehrhart, L. Fischer, R. C. Flagan, A. Franchin, C. Fuchs, R. Guida, J. Hakala, C. R. Hoyle, T. Jokinen, H. Junninen, J. Kangasluoma, J. Kim, J. Kirkby, M. Krapf, A. Kürten, A. Laaksonen, K. Lehtipalo, V. Makhmutov, S. Mathot, U. Molteni, S. A. Monks, A. Onnela, O. Peräkylä, F. Piel, T. Petäjä, A. P. Praplan, K. J. Pringle, N. A. D. Richards, M. P. Rissanen, L. Rondo, N. Sarnela, S. Schobesberger, C. E. Scott, J. H. Seinfeld, S. Sharma, M. Sipilä, G. Steiner, Y. Stozhkov, F. Stratmann, A. Tomé, A. Virtanen, A. L. Vogel, A. C. Wagner, P. E. Wagner, E. Weingartner, D. Wimmer, P. M. Winkler, P. Ye, X. Zhang, A. Hansel, J. Dommen, N. M. Donahue, D. R. Worsnop, U. Baltensperger, M. Kulmala, J. Curtius, and K. S. Carslaw (2016). "Reduced anthropogenic aerosol radiative forcing caused by biogenic new particle formation". *Proceedings of the National Academy of Sciences* 113 (43), 12053–12058. DOI: 10.1073/pnas.1602360113.

Gordon, T. D., A. A. Presto, N. T. Nguyen, W. H. Robertson, K. Na, K. N. Sahay, M. Zhang, C. Maddox, P. Rieger, S. Chattopadhyay, H. Maldonado, M. M. Maricq, and A. L. Robinson (2014). "Secondary organic aerosol production from diesel vehicle exhaust: impact of aftertreatment, fuel chemistry and driving cycle". *Atmospheric Chemistry and Physics* 14 (9). Publisher: Copernicus GmbH, 4643–4659. DOI: 10.5194/acp-14-4643-2014.

Grantz, D., J. Garner, and D. Johnson (2003). "Ecological effects of particulate matter". *Environment International* 29 (2-3), 213–239. DOI: 10.1016/S0160-4120(02)00181-2.

Griffin, R. J., D. R. Cocker, R. C. Flagan, and J. H. Seinfeld (1999). "Organic aerosol formation from the oxidation of biogenic hydrocarbons". *Journal of Geophysical Research: Atmospheres* 104 (D3), 3555–3567. DOI: 10.1029/1998JD100049.

Groot Koerkamp, P., J. Metz, G. Uenk, V. Phillips, M. Holden, R. Sneath, J. Short, R. White, J. Hartung, J. Seedorf, M. Schröder, K. Linkert, S. Pedersen, H. Takai, J. Johnsen, and C. Wathes (1998). "Concentrations and Emissions of Ammonia in Livestock Buildings in Northern Europe". *Journal of Agricultural Engineering Research* 70 (1). Publisher: Elsevier BV, 79–95. DOI: 10.1006/jaer.1998.0275.

Gu, S., A. Guenther, and C. Faiola (2021). "Effects of Anthropogenic and Biogenic Volatile Organic Compounds on Los Angeles Air Quality". *Environmental Science & Technology* 55 (18). PMID: 34495669, 12191–12201. DOI: 10.1021/acs.est.1c01481.

Guo, H., R. Otjes, P. Schlag, A. Kiendler-Scharr, A. Nenes, and R. J. Weber (2018). "Effectiveness of ammonia reduction on control of fine particle nitrate". *Atmospheric Chemistry and Physics* 18 (16), 12241–12256. DOI: 10.5194/acp-18-12241-2018.

Hallquist, M., I. Wängberg, and E. Ljungström (1997). "Atmospheric Fate of Carbonyl Oxidation Products Originating from α-Pinene and Δ^3 -Carene: Determination of Rate of Reaction with OH and NO_3 Radicals, UV Absorption Cross Sections, and Vapor Pressures". *Environmental Science & Technology* 31 (11), 3166–3172. DOI: 10.1021/es970151a.

Hallquist, M., I. Wängberg, E. Ljungström, I. Barnes, and K.-H. Becker (1999). "Aerosol and Product Yields from NO_3 Radical-Initiated Oxidation of Selected Monoterpenes". *Environmental Science & Technology* 33 (4). Publisher: American Chemical Society (ACS), 553–559. DOI: 10.1021/es980292s.

Hamed, A., J. Joutsensaari, S. Mikkonen, L. Sogacheva, M. Dal Maso, M. Kulmala, F. Cavalli, S. Fuzzi, M. C. Facchini, S. Decesari, M. Mircea, K. E. J. Lehtinen, and A. Laaksonen (2007). "Nucleation and growth of new particles in Po Valley, Italy". *Atmospheric Chemistry and Physics* 7 (2), 355–376. DOI: 10.5194/acp-7-355-2007.

Hang, Y., X. Meng, T. Li, T. Wang, J. Cao, Q. Fu, S. Dey, S. Li, K. Huang, F. Liang, H. Kan, X. Shi, and Y. Liu (2022). "Assessment of long-term particulate nitrate air pollution and its health risk in China". *iScience* 25 (9), 104899. DOI: 10.1016/j.isci.2022.104899.

Haywood, J. (2016). "Atmospheric Aerosols and Their Role in Climate Change". In: *Climate Change*. Elsevier, 449–463. DOI: 10.1016/B978-0-444-63524-2.00027-0.

He, L.-Y., Y. Lin, X.-F. Huang, S. Guo, L. Xue, Q. Su, M. Hu, S.-J. Luan, and Y.-H. Zhang (2010). "Characterization of high-resolution aerosol mass spectra of primary organic aerosol emissions from Chinese cooking and biomass burning". *Atmospheric Chemistry and Physics* 10 (23), 11535–11543. DOI: 10.5194/acp-10-11535-2010.

Heer, M. d., F. Roozen, and R. Maas (2017). "The Integrated Approach to Nitrogen in the Netherlands: A preliminary review from a societal, scientific, juridical and practical perspective". *Journal for Nature Conservation* 35, 101–111. DOI: 10.1016/j.jnc.2016.11.006.

Heinritzi, M., L. Dada, M. Simon, D. Stolzenburg, A. C. Wagner, L. Fischer, L. R. Ahonen, S. Amanatidis, R. Baalbaki, A. Baccarini, P. S. Bauer, B. Baumgartner, F. Bianchi, S. Brilke, D. Chen, R. Chiu, A. Dias, J. Dommen, J. Duplissy, H. Finkenzeller, C. Frege, C. Fuchs, O. Garmash, H. Gordon, M. Granzin, I. El Haddad, X. He, J. Helm, V. Hofbauer, C. R. Hoyle, J. Kangasluoma, T. Keber, C. Kim, A. Kürten, H. Lamkaddam, T. M. Laurila, J. Lampilahti, C. P. Lee, K. Lehtipalo, M. Leiminger, H. Mai, V. Makhmutov, H. E. Manninen, R. Marten, S. Mathot, R. L. Mauldin, B. Mentler, U. Molteni, T. Müller, W. Nie, T. Nieminen, A. Onnela, E. Partoll, M. Passananti, T. Petäjä, J. Pfeifer, V. Pospisilova, L. L. J. Quéléver, M. P. Rissanen, C. Rose, S. Schobesberger, W. Scholz, K. Scholze, M. Sipilä, G. Steiner, Y. Stozhkov, C. Tauber, Y. J. Tham, M. Vazquez-Pufleau, A. Virtanen, A. L. Vogel, R. Volkamer, R. Wagner, M. Wang, L. Weitz, D. Wimmer, M. Xiao, C. Yan, P. Ye, Q. Zha, X. Zhou, A. Amorim, U. Baltensperger, A. Hansel, M. Kulmala, A. Tomé, P. M. Winkler, D. R. Worsnop, N. M. Donahue, J. Kirkby, and J. Curtius (2020). "Molecular understanding of the suppression of new-particle formation by isoprene". *Atmospheric Chemistry and Physics* 20 (20), 11809–11821. DOI: 10.5194/acp-20-11809-2020.

Heintzenberg, J., B. Wehner, and W. Birmili (2007). "How to find bananas in the atmospheric aerosol?: new approach for analyzing atmospheric nucleation and growth events". *Tellus B* 59 (2), 273–282. DOI: 10.1111/j.1600-0889.2007.00249.x.

Hennigan, C. J., A. P. Sullivan, C. I. Fountoukis, A. Nenes, A. Hecobian, O. Vargas, R. E. Peltier, A. T. Case Hanks, L. G. Huey, B. L. Lefer, A. G. Russell, and R. J. Weber (2008). "On the volatility and production mechanisms of newly formed nitrate and water soluble organic aerosol in Mexico City". *Atmospheric Chemistry and Physics* 8 (14). Publisher: Copernicus GmbH, 3761–3768. DOI: 10.5194/acp-8-3761-2008.

Henschel, S., X. Querol, R. Atkinson, M. Pandolfi, A. Zeka, A. Le Tertre, A. Analitis, K. Katsouyanni, O. Chanel, M. Pascal, C. Bouland, D. Haluza, S. Medina, and P. G. Goodman (2013). "Ambient air SO_2 patterns in 6 European cities". *Atmospheric Environment* 79, 236–247. DOI: 10.1016/j.atmosenv.2013.06.008.

Hidy, G. M., C. L. Blanchard, K. Baumann, E. Edgerton, S. Tanenbaum, S. Shaw, E. Knipping, I. Tombach, J. Jansen, and J. Walters (2014). "Chemical climatology of the southeastern United States, 1999–2013". *Atmospheric Chemistry and Physics* 14 (21). Publisher: Copernicus GmbH, 11893–11914. DOI: 10.5194/acp-14-11893-2014.

Hildebrandt Ruiz, L. and G. Yarwood (2013). *Interactions between Organic Aerosol and NO_y: Influence of Oxidant Production*. Tech. rep. , Final report for AQRP project 12-012. Austin, TX.

Hodshire, A. L., M. J. Lawler, J. Zhao, J. Ortega, C. Jen, T. Yli-Juuti, J. F. Brewer, J. K. Kodros, K. C. Barsanti, D. R. Hanson, P. H. McMurry, J. N. Smith, and J. R. Pierce (2016). "Multiple new-particle growth pathways observed at the US DOE Southern GreatPlains field site". *Atmospheric Chemistry and Physics* 16 (14), 9321–9348. DOI: 10.5194/acp-16-9321-2016.

Höpfner, M., J. Ungermann, S. Borrmann, R. Wagner, R. Spang, M. Riese, G. Stiller, O. Appel, A. M. Batenburg, S. Bucci, F. Cairo, A. Dragoneas, F. Friedl-Vallon, A. Hünig, S. Johansson, L. Krasauskas, B. Legras, T. Leisner, C. Mahnke, O. Möhler, S. Molleker, R. Müller, T. Neubert, J. Orphal, P. Preusse, M. Rex, H. Saathoff, F. Stroh, R. Weigel, and I. Wohltmann (2019). "Ammonium nitrate particles formed in upper troposphere from ground ammonia sources during Asian monsoons". *Nature Geoscience* 12 (8), 608–612. DOI: 10.1038/s41561-019-0385-8.

Horbanski, M., D. Pöhler, J. Lampel, and U. Platt (2019). "The ICAD (iterative cavity-enhanced DOAS) method". *Atmospheric Measurement Techniques* 12 (6), 3365–3381. DOI: 10.5194/amt-12-3365-2019.

Hu, W., A. Handschy, and J. L. Jimenez (n.d.). *AMS Capture Vaporizer Spectral Database*. (last access: 9 July 2025), [dataset].

Hu, W., P. Campuzano-Jost, D. A. Day, P. Croteau, M. R. Canagaratna, J. T. Jayne, D. R. Worsnop, and J. L. Jimenez (2016a). *Evaluation of the new capture vaporizer for Aerosol Mass Spectrometers (AMS) through laboratory studies of inorganic species*. DOI: 10.5194/amt-2016-337.

– (2017). "Evaluation of the new capture vaporizer for aerosol mass spectrometers (AMS) through field studies of inorganic species". *Aerosol Science and Technology* 51 (6), 735–754. DOI: 10.1080/02786826.2017.1296104.

Hu, W., D. A. Day, P. Campuzano-Jost, B. A. Nault, T. Park, T. Lee, P. Croteau, M. R. Canagaratna, J. T. Jayne, D. R. Worsnop, and J. L. Jimenez (2018a). "Evaluation of the New Capture Vaporizer for Aerosol Mass Spectrometers (AMS): Elemental Composition and Source Apportionment of Organic Aerosols (OA)". *ACS Earth and Space Chemistry* 2 (4), 410–421. DOI: 10.1021/acsearthspacechem.8b00002.

– (2018b). "Evaluation of the new capture vaporizer for aerosol mass spectrometers: Characterization of organic aerosol mass spectra". *Aerosol Science and Technology* 52 (7), 725–739. DOI: 10.1080/02786826.2018.1454584.

Hu, W., M. Hu, W. Hu, J. L. Jimenez, B. Yuan, W. Chen, M. Wang, Y. Wu, C. Chen, Z. Wang, J. Peng, L. Zeng, and M. Shao (2016b). "Chemical composition, sources, and aging process of submicron aerosols in Beijing: Contrast between summer and winter". *Journal of Geophysical Research: Atmospheres* 121 (4), 1955–1977. DOI: https://doi.org/10.1002/2015JD024020. eprint: https://agupubs.onlinelibrary.wiley.com/doi/pdf/10.1002/2015JD024020.

Huang, W., H. Saathoff, X. Shen, R. Ramisetty, T. Leisner, and C. Mohr (2019a). "Chemical Characterization of Highly Functionalized Organonitrates Contributing to Night-Time Organic Aerosol Mass Loadings and Particle Growth". *Environmental Science & Technology* 53 (3), 1165–1174. DOI: 10.1021/acs.est.8b05826.

– (2019b). "Seasonal characteristics of organic aerosol chemical composition and volatility in Stuttgart, Germany". *Atmospheric Chemistry and Physics* 19 (18), 11687–11700. DOI: 10.5194/acp-19-11687-2019.

Huang, X., R. Qiu, C. K. Chan, and P. Ravi Kant (2011). "Evidence of high PM2.5 strong acidity in ammonia-rich atmosphere of Guangzhou, China: Transition in pathways of ambient ammonia to form aerosol ammonium at [NH4+]/[SO42–] = 1.5". *Atmospheric Research* 99 (3-4). Publisher: Elsevier BV, 488–495. DOI: 10.1016/j.atmosres.2010.11.021.

Huffman, J. A., K. S. Docherty, A. C. Aiken, M. J. Cubison, I. M. Ulbrich, P. F. DeCarlo, D. Sueper, J. T. Jayne, D. R. Worsnop, P. J. Ziemann, and J. L. Jimenez (2009). "Chemically-resolved aerosol volatility measurements from two megacity field studies". *Atmospheric Chemistry and Physics* 9 (18), 7161–7182. DOI: 10.5194/acp-9-7161-2009.

Hussein, T., A. Puustinen, P. P. Aalto, J. M. Mäkelä, K. Hämeri, and M. Kulmala (2004). "Urban aerosol number size distributions". *Atmospheric Chemistry and Physics* 4 (2), 391–411. DOI: 10.5194/acp-4-391-2004.

Inness, A., M. Ades, A. Agustí-Panareda, J. Barré, A. Benedictow, A.-M. Blechschmidt, J. J. Dominguez, R. Engelen, H. Eskes, J. Flemming, V. Huijnen, L. Jones, Z. Kipling, S. Massart, M. Parrington, V.-H. Peuch, M. Razinger, S. Remy, M. Schulz, and M. Suttie (2019). "The CAMS reanalysis of atmospheric composition". *Atmospheric Chemistry and Physics* 19 (6), 3515–3556. DOI: 10.5194/acp-19-3515-2019.

Jayne, J. T. and D. R. Worsnop (2016). "Particle Capture Device". US 20150040689 A1.

Jenkin, M. E., S. M. Saunders, V. Wagner, and M. J. Pilling (2003). "Protocol for the development of the Master Chemical Mechanism, MCM v3 (Part B): tropospheric degradation of aromatic volatile organic compounds". *Atmospheric Chemistry and Physics* 3 (1), 181–193. DOI: 10.5194/acp-3-181-2003.

Jenkin, M. E., J. C. Young, and A. R. Rickard (2015). "The MCM v3.3.1 degradation scheme for isoprene". *Atmospheric Chemistry and Physics* 15 (20), 11433–11459. DOI: 10.5194/acp-15-11433-2015.

Jenkin, M. E., S. M. Saunders, and M. J. Pilling (1997). "The tropospheric degradation of volatile organic compounds: a protocol for mechanism development". *Atmospheric Environment* 31 (1), 81–104. DOI: 10.1016/S1352-2310(96)00105-7.

Jickells, T., A. R. Baker, J. N. Cape, S. E. Cornell, and E. Nemitz (2013). "The cycling of organic nitrogen through the atmosphere". *Philosophical Transactions of the Royal Society B: Biological Sciences* 368 (1621), 20130115. DOI: 10.1098/rstb.2013.0115.

Jimenez, J. L., M. R. Canagaratna, N. M. Donahue, A. S. H. Prevot, Q. Zhang, J. H. Kroll, P. F. DeCarlo, J. D. Allan, H. Coe, N. L. Ng, A. C. Aiken, K. S. Docherty, I. M. Ulbrich, A. P. Grieshop, A. L. Robinson, J. Duplissy, J. D. Smith, K. R. Wilson, V. A. Lanz, C. Hueglin, Y. L. Sun, J. Tian, A. Laaksonen, T. Raatikainen, J. Rautiainen, P. Vaattovaara, M. Ehn, M. Kulmala, J. M. Tomlinson, D. R. Collins, M. J. Cubison, E., J. Dunlea, J. A. Huffman, T. B. Onasch, M. R. Alfarra, P. I. Williams, K. Bower, Y. Kondo, J. Schneider, F. Drewnick, S. Borrmann, S. Weimer, K. Demerjian, D. Salcedo, L. Cottrell, R. Griffin, A. Takami, T. Miyoshi, S. Hatakeyama, A. Shimono, J. Y. Sun, Y. M. Zhang, K. Dzepina, J. R. Kimmel, D. Sueper, J. T. Jayne, S. C. Herndon, A. M. Trimborn, L. R. Williams, E. C. Wood, A. M. Middlebrook, C. E. Kolb, U. Baltensperger, and D. R. Worsnop (2009). "Evolution of Organic Aerosols in the Atmosphere". *Science* 326 (5959), 1525–1529. DOI: 10.1126/science.1180353. eprint: https://www.science.org/doi/pdf/10.1126/science.1180353.

Johansson, L., J.-P. Jalkanen, and J. Kukkonen (2017). "Global assessment of shipping emissions in 2015 on a high spatial and temporal resolution". *Atmospheric Environment* 167. Publisher: Elsevier BV, 403–415. DOI: 10.1016/j.atmosenv.2017.08.042.

Jokinen, T., K. Lehtipalo, R. C. Thakur, I. Ylivinkka, K. Neitola, N. Sarnela, T. Laitinen, M. Kulmala, T. Petäjä, and M. Sipilä (2022). "Measurement report: Long-term measurements of aerosol precursor concentrations in the Finnish subarctic boreal forest". *Atmospheric Chemistry and Physics* 22 (4), 2237–2254. DOI: 10.5194/acp-22-2237-2022.

Joo, T., Y. Chen, W. Xu, P. Croteau, M. R. Canagaratna, D. Gao, H. Guo, G. Saavedra, S. S. Kim, Y. Sun, R. Weber, J. Jayne, and N. L. Ng (2021). "Evaluation of a New Aerosol Chemical Speciation Monitor (ACSM) System at an Urban Site in Atlanta, GA: The Use of Capture Vaporizer and $PM_{2.5}$ Inlet". *ACS Earth and Space Chemistry* 5 (10), 2565–2576. DOI: 10.1021/acsearthspacechem.1c00173.

Junninen, H., M. Ehn, T. Petäjä, L. Luosujärvi, T. Kotiaho, R. Kostiainen, U. Rohner, M. Gonin, K. Fuhrer, M. Kulmala, and D. R. Worsnop (2010). "A high-resolution mass spectrometer to measure atmospheric ion composition". *Atmospheric Measurement Techniques* 3 (4), 1039–1053. DOI: 10.5194/amt-3-1039-2010.

Keehan, N. I., B. Brownwood, A. Marsavin, D. A. Day, and J. L. Fry (2020). "A thermal-dissociation–cavity ring-down spectrometer (TD-CRDS) for the detection of organic nitrates in gas and particle phases". *Atmospheric Measurement Techniques* 13 (11), 6255–6269. DOI: 10.5194/amt-13-6255-2020.

Kelly, J. T., C. L. Parworth, Q. Zhang, D. J. Miller, K. Sun, M. A. Zondlo, K. R. Baker, A. Wisthaler, J. B. Nowak, S. E. Pusede, R. C. Cohen, A. J. Weinheimer, A. J. Beyersdorf, G. S. Tonnesen, J. O. Bash, L. C. Valin, J. H. Crawford, A. Fried, and J. G. Walega (2018). "Modeling NH_4 NO_3 Over the San Joaquin Valley During the 2013 DISCOVER-AQ Campaign". en. *Journal of Geophysical Research: Atmospheres* 123 (9), 4727–4745. DOI: 10.1029/2018JD028290.

Kenagy, H. S., T. L. Sparks, C. J. Ebben, P. J. Wooldrige, F. D. Lopez-Hilfiker, B. H. Lee, J. A. Thornton, E. E. McDuffie, D. L. Fibiger, S. S. Brown, D. D. Montzka, A. J. Weinheimer, J. C. Schroder, P. Campuzano-Jost, D. A. Day, J. L. Jimenez, J. E. Dibb, T. Campos, V. Shah, L. Jaeglé, and R. C. Cohen (2018). "NO_x Lifetime and NO_y Partitioning During WINTER". *Journal of Geophysical Research: Atmospheres* 123 (17), 9813–9827. DOI: 10.1029/2018JD028736.

Kenseth, C. M., N. J. Hafeman, S. P. Rezgui, J. Chen, Y. Huang, N. F. Dalleska, H. G. Kjaergaard, B. M. Stoltz, J. H. Seinfeld, and P. O. Wennberg (2023). "Particle-phase accretion forms dimer esters in pinene secondary organic aerosol". *Science* 382 (6672), 787–792. DOI: 10.1126/science.adi0857.

Kerminen, V.-M., X. Chen, V. Vakkari, T. Petäjä, M. Kulmala, and F. Bianchi (2018). "Atmospheric new particle formation and growth: review of field observations". *Environmental Research Letters* 13 (10), 103003. DOI: 10.1088/1748-9326/aadf3c.

Kiendler-Scharr, A., A. A. Mensah, E. Friese, D. Topping, E. Nemitz, A. S. H. Prevot, M. Äijälä, J. Allan, F. Canonaco, M. Canagaratna, S. Carbone, M. Crippa, M. Dall Osto, D. A. Day, P. De Carlo, C. F. Di Marco, H. Elbern, A. Eriksson, E. Freney, L. Hao, H. Herrmann, L. Hildebrandt, R. Hillamo, J. L. Jimenez, A. Laaksonen, G. McFiggans, C. Mohr, C. O'Dowd, R. Otjes, J. Ovadnevaite, S. N. Pandis, L. Poulain, P. Schlag, K. Sellegri, E. Swietlicki, P. Tiitta, A. Vermeulen, A. Wahner, D. Worsnop, and H.-C. Wu (2016). "Ubiquity of organic nitrates from nighttime chemistry in the European submicron aerosol". *Geophysical Research Letters* 43 (14), 7735–7744. DOI: 10.1002/2016GL069239.

Kim, J., Y. Chang, T. K. Hwang, D.-G. Kim, and K. Park (2025). "Potential influence of ammonia reduction on particulate nitrate concentration in South Korea". *Journal of Hazardous Materials* 494, 138675. DOI: 10.1016/j.jhazmat.2025.138675.

Knote, C., A. Hodzic, and J. L. Jimenez (2015). "The effect of dry and wet deposition of condensable vapors on secondary organic aerosols concentrations over the continental US". *Atmospheric Chemistry and Physics* 15 (1), 1–18. DOI: 10.5194/acp-15-1-2015.

Kodros, J. K., D. K. Papanastasiou, M. Paglione, M. Masiol, S. Squizzato, K. Florou, K. Skyllakou, C. Kaltsonoudis, A. Nenes, and S. N. Pandis (2020). "Rapid dark aging of biomass burning as an overlooked source of oxidized organic aerosol". *Proceedings of the National Academy of Sciences* 117 (52), 33028–33033. DOI: 10.1073/pnas.2010365117.

Kolesar, K. R., J. Cellini, P. K. Peterson, A. Jefferson, T. Tuch, W. Birmili, A. Wiedensohler, and K. A. Pratt (2017). "Effect of Prudhoe Bay emissions on atmospheric aerosol growth events observed in Utqiaġvik (Barrow), Alaska". *Atmospheric Environment* 152, 146–155. DOI: 10.1016/j.atmosenv.2016.12.019.

Kranenburg, R., A. J. Segers, C. Hendriks, and M. Schaap (2013). "Source apportionment using LOTOS-EUROS: module description and evaluation". *Geoscientific Model Development* 6 (3), 721–733. DOI: 10.5194/gmd-6-721-2013.

Krechmer, J., F. Lopez-Hilfiker, A. Koss, M. Hutterli, C. Stoermer, B. Deming, J. Kimmel, C. Warneke, R. Holzinger, J. Jayne, D. Worsnop, K. Fuhrer, M. Gonin, and J. De Gouw (2018). "Evaluation of a New Reagent-Ion Source and Focusing Ion–Molecule Reactor for Use in Proton-Transfer-Reaction Mass Spectrometry". *Analytical Chemistry* 90 (20), 12011–12018. DOI: 10.1021/acs.analchem.8b02641.

Kroll, J. H. and J. H. Seinfeld (2008). "Chemistry of secondary organic aerosol: Formation and evolution of low-volatility organics in the atmosphere". *Atmospheric Environment* 42 (16), 3593–3624. DOI: 10.1016/j.atmosenv.2008.01.003.

Kulmala, M., J. Kontkanen, H. Junninen, K. Lehtipalo, H. E. Manninen, T. Nieminen, T. Petäjä, M. Sipilä, S. Schobesberger, P. Rantala, A. Franchin, T. Jokinen, E. Järvinen, M. Äijälä, J. Kangasluoma, J. Hakala, P. P. Aalto, P. Paasonen, J. Mikkilä, J. Vanhanen, J. Aalto, H. Hakola, U. Makkonen, T. Ruuskanen, R. L. Mauldin, J. Duplissy, H. Vehkamäki, J. Bäck, A. Kortelainen, I. Riipinen, T. Kurtén, M. V. Johnston, J. N. Smith, M. Ehn, T. F. Mentel, K. E. J. Lehtinen, A. Laaksonen, V.-M. Kerminen, and D. R. Worsnop (2013). "Direct Observations of Atmospheric Aerosol Nucleation". *Science* 339 (6122), 943–946. DOI: 10.1126/science.1227385. eprint: https://www.science.org/doi/pdf/10.1126/science.1227385.

Kürten, A. (2019). "New particle formation from sulfuric acid and ammonia: nucleation and growth model based on thermodynamics derived from CLOUD measurements for a wide range of conditions". *Atmospheric Chemistry and Physics* 19 (7), 5033–5050. DOI: 10.5194/acp-19-5033-2019.

Kurtén, T., K. Tiusanen, P. Roldin, M. Rissanen, J.-N. Luy, M. Boy, M. Ehn, and N. Donahue (2016). "α-Pinene Autoxidation Products May Not Have Extremely Low Saturation Vapor Pressures Despite High O:C Ratios". *The Journal of Physical Chemistry A* 120 (16), 2569–2582. DOI: 10.1021/acs.jpca.6b02196.

Lan, Z., X. Zhang, W. Lin, X. Xu, Z. Ma, J. Jin, L. Wu, and Y. Zhang (2024). "Atmospheric NH_3 in urban Beijing: long-term variations and implications for secondary inorganic aerosol control". *Atmospheric Chemistry and Physics* 24 (16). Publisher: Copernicus GmbH, 9355–9368. DOI: 10.5194/acp-24-9355-2024.

Lange, K., A. Richter, and J. P. Burrows (2022). "Variability of nitrogen oxide emission fluxes and lifetimes estimated from Sentinel-5P TROPOMI observations". *Atmospheric Chemistry and Physics* 22 (4), 2745–2767. DOI: 10.5194/acp-22-2745-2022.

Lanz, V. A., M. R. Alfarra, U. Baltensperger, B. Buchmann, C. Hueglin, and A. S. H. Prévôt (2007). "Source apportionment of submicron organic aerosols at an urban site by factor analytical modelling of aerosol mass spectra". *Atmospheric Chemistry and Physics* 7 (6), 1503–1522. DOI: 10.5194/acp-7-1503-2007.

Lawal, A. S., X. Guan, C. Liu, L. R. Henneman, P. Vasilakos, V. Bhogineni, R. J. Weber, A. Nenes, and A. G. Russell (2018). "Linked Response of Aerosol Acidity and Ammonia to SO_2 and

NO_x Emissions Reductions in the United States". *Environmental Science & Technology* 52 (17). Publisher: American Chemical Society (ACS), 9861–9873. DOI: 10.1021/acs.est.8b00711.

Le Moal, M., C. Gascuel-Odoux, A. Ménesguen, Y. Souchon, C. Étrillard, A. Levain, F. Moatar, A. Pannard, P. Souchu, A. Lefebvre, and G. Pinay (2019). "Eutrophication: A new wine in an old bottle?" *Science of The Total Environment* 651, 1–11. DOI: 10.1016/j.scitotenv.2018.09.139.

Ledoux, F., C. Roche, F. Cazier, C. Beaugard, and D. Courcot (2018). "Influence of ship emissions on NOx, SO_2, O3 and PM concentrations in a North-Sea harbor in France". *Journal of Environmental Sciences* 71, 56–66. DOI: 10.1016/j.jes.2018.03.030.

Lee, B. H., C. Mohr, F. D. Lopez-Hilfiker, A. Lutz, M. Hallquist, L. Lee, P. Romer, R. C. Cohen, S. Iyer, T. Kurtén, W. Hu, D. A. Day, P. Campuzano-Jost, J. L. Jimenez, L. Xu, N. L. Ng, H. Guo, R. J. Weber, R. J. Wild, S. S. Brown, A. Koss, J. de Gouw, K. Olson, A. H. Goldstein, R. Seco, S. Kim, K. McAvey, P. B. Shepson, T. Starn, K. Baumann, E. S. Edgerton, J. Liu, J. E. Shilling, D. O. Miller, W. Brune, S. Schobesberger, E. L. D'Ambro, and J. A. Thornton (2016). "Highly functionalized organic nitrates in the southeast United States: Contribution to secondary organic aerosol and reactive nitrogen budgets". *Proceedings of the National Academy of Sciences* 113 (6), 1516–1521. DOI: 10.1073/pnas.1508108113.

Lee, S.-H., H. Gordon, H. Yu, K. Lehtipalo, R. Haley, Y. Li, and R. Zhang (2019). "New Particle Formation in the Atmosphere: From Molecular Clusters to Global Climate". *Journal of Geophysical Research: Atmospheres* 124 (13), 7098–7146. DOI: https://doi.org/10.1029/2018JD029356. eprint: https://agupubs.onlinelibrary.wiley.com/doi/pdf/10.1029/2018JD029356.

Lehtipalo, K., C. Yan, L. Dada, F. Bianchi, M. Xiao, R. Wagner, D. Stolzenburg, L. R. Ahonen, A. Amorim, A. Baccarini, P. S. Bauer, B. Baumgartner, A. Bergen, A.-K. Bernhammer, M. Breitenlechner, S. Brilke, A. Buchholz, S. B. Mazon, D. Chen, X. Chen, A. Dias, J. Dommen, D. C. Draper, J. Duplissy, M. Ehn, H. Finkenzeller, L. Fischer, C. Frege, C. Fuchs, O. Garmash, H. Gordon, J. Hakala, X. He, L. Heikkinen, M. Heinritzi, J. C. Helm, V. Hofbauer, C. R. Hoyle, T. Jokinen, J. Kangasluoma, V.-M. Kerminen, C. Kim, J. Kirkby, J. Kontkanen, A. Kürten, M. J. Lawler, H. Mai, S. Mathot, R. L. Mauldin, U. Molteni, L. Nichman, W. Nie, T. Nieminen, A. Ojdanic, A. Onnela, M. Passananti, T. Petäjä, F. Piel, V. Pospisilova, L. L. J. Quéléver, M. P. Rissanen, C. Rose, N. Sarnela, S. Schallhart, S. Schuchmann, K. Sengupta, M. Simon, M. Sipilä, C. Tauber, A. Tomé, J. Tröstl, O. Väisänen, A. L. Vogel, R. Volkamer, A. C. Wagner, M. Wang, L. Weitz, D. Wimmer, P. Ye, A. Ylisirniö, Q. Zha, K. S. Carslaw, J. Curtius, N. M. Donahue, R. C. Flagan, A. Hansel, I. Riipinen, A. Virtanen, P. M. Winkler, U. Baltensperger, M. Kulmala, and D. R. Worsnop (2018). "Multicomponent new particle formation from sulfuric acid, ammonia, and biogenic vapors". *Science Advances* 4 (12), eaau5363. DOI: 10.1126/sciadv.aau5363.

Liao, H., P. J. Adams, S. H. Chung, J. H. Seinfeld, L. J. Mickley, and D. J. Jacob (2003). "Interactions between tropospheric chemistry and aerosols in a unified general circulation model". *Journal of Geophysical Research: Atmospheres* 108 (D1), AAC 1–1–AAC 1–23. DOI: 10.1029/2001JD001260.

Lin, C., R. Ooka, H. Kikumoto, Y. Kim, Y. Zhang, C. Flageul, and K. Sartelet (2024). "Impact of gas dry deposition parameterization on secondary particle formation in an urban canyon". en. *Atmospheric Environment* 333, 120633. DOI: 10.1016/j.atmosenv.2024.120633.

Liu, J., P. J. A. Kleinman, H. Aronsson, D. Flaten, R. W. McDowell, M. Bechmann, D. B. Beegle, T. P. Robinson, R. B. Bryant, H. Liu, A. N. Sharpley, and T. L. Veith (2018). "A review of

regulations and guidelines related to winter manure application". *Ambio* 47 (6). Publisher: Springer Science and Business Media LLC, 657–670. DOI: 10.1007/s13280-018-1012-4.

Liu, T., Z. Li, M. Chan, and C. K. Chan (2017). "Formation of secondary organic aerosols from gas-phase emissions of heated cooking oils". *Atmospheric Chemistry and Physics* 17 (12). Publisher: Copernicus GmbH, 7333–7344. DOI: 10.5194/acp-17-7333-2017.

Liu, X., D. Alves Gouveia, B. Henzing, A. Apituley, A. Hensen, D. Van Dinther, R. Huang, and U. Dusek (2024). "Aerosol optical properties within the atmospheric boundary layer predicted from ground-based observations compared to Raman lidar retrievals during RITA-2021". *Atmospheric Chemistry and Physics* 24 (16), 9597–9614. DOI: 10.5194/acp-24-9597-2024.

Lohle, J. (2021). "Modelling the Dutch nitrogen crisis". PhD thesis. Delft University of Technology.

Lohmann, U. and J. Feichter (2005). "Global indirect aerosol effects: a review". *Atmospheric Chemistry and Physics* 5 (3), 715–737. DOI: 10.5194/acp-5-715-2005.

Lu, Z., X. Liu, R. A. Zaveri, R. C. Easter, S. Tilmes, L. K. Emmons, F. Vitt, B. Singh, H. Wang, R. Zhang, and P. J. Rasch (2021). "Radiative Forcing of Nitrate Aerosols From 1975 to 2010 as Simulated by MOSAIC Module in CESM2-MAM4". *Journal of Geophysical Research: Atmospheres* 126 (17), e2021JD034809. DOI: 10.1029/2021JD034809.

Luo, S., Y. Zhu, and S. X. Chen (2022). "Episode based air quality assessment". *Atmospheric Environment* 285. Publisher: Elsevier BV, 119242. DOI: 10.1016/j.atmosenv.2022.119242.

Mahowald, N., D. S. Ward, S. Kloster, M. G. Flanner, C. L. Heald, N. G. Heavens, P. G. Hess, J.-F. Lamarque, and P. Y. Chuang (2011). "Aerosol Impacts on Climate and Biogeochemistry". *Annual Review of Environment and Resources* 36 (1), 45–74. DOI: 10.1146/annurev-environ-042009-094507.

Manders, A. M. M., P. J. H. Builtjes, L. Curier, H. A. C. Denier Van Der Gon, C. Hendriks, S. Jonkers, R. Kranenburg, J. J. P. Kuenen, A. J. Segers, R. M. A. Timmermans, A. J. H. Visschedijk, R. J. Wichink Kruit, W. A. J. Van Pul, F. J. Sauter, E. Van Der Swaluw, D. P. J. Swart, J. Douros, H. Eskes, E. Van Meijgaard, B. Van Ulft, P. Van Velthoven, S. Banzhaf, A. C. Mues, R. Stern, G. Fu, S. Lu, A. Heemink, N. Van Velzen, and M. Schaap (2017). "Curriculum vitae of the LOTOS–EUROS (v2.0) chemistry transport model". *Geoscientific Model Development* 10 (11), 4145–4173. DOI: 10.5194/gmd-10-4145-2017.

Marais, E. A., D. J. Jacob, J. L. Jimenez, P. Campuzano-Jost, D. A. Day, W. Hu, J. Krechmer, L. Zhu, P. S. Kim, C. C. Miller, J. A. Fisher, K. Travis, K. Yu, T. F. Hanisco, G. M. Wolfe, H. L. Arkinson, H. O. T. Pye, K. D. Froyd, J. Liao, and V. F. McNeill (2016). "Aqueous-phase mechanism for secondary organic aerosol formation from isoprene: application to the southeast United States and co-benefit of SO_2 emission controls". *Atmospheric Chemistry and Physics* 16 (3), 1603–1618. DOI: 10.5194/acp-16-1603-2016.

Marrero-Ortiz, W., M. Hu, Z. Du, Y. Ji, Y. Wang, S. Guo, Y. Lin, M. Gomez-Hermandez, J. Peng, Y. Li, J. Secrest, M. L. Zamora, Y. Wang, T. An, and R. Zhang (2019). "Formation and Optical Properties of Brown Carbon from Small α-Dicarbonyls and Amines". *Environmental Science & Technology* 53 (1), 117–126. DOI: 10.1021/acs.est.8b03995.

Marsavin, A., R. Van Gageldonk, N. Bernays, N. W. May, D. A. Jaffe, and J. L. Fry (2023). "Optical properties of biomass burning aerosol during the 2021 Oregon fire season: comparison between wild and prescribed fires". *Environmental Science: Atmospheres* 3 (3), 608–626. DOI: 10.1039/D2EA00118G.

Maso, M. D., M. Kulmala, I. Riipinen, R. Wagner, T. Hussein, P. P. Aalto, and K. E. J. Lehtinen (2005). "Formation and growth of fresh atmospheric aerosols: eight years of aerosol size distribution data from SMEAR II, Hyytiälä, Finland". *Boreal Environment Research* 10 (5), 323–336.

McDonald, B. C., J. A. De Gouw, J. B. Gilman, S. H. Jathar, A. Akherati, C. D. Cappa, J. L. Jimenez, J. Lee-Taylor, P. L. Hayes, S. A. McKeen, Y. Y. Cui, S.-W. Kim, D. R. Gentner, G. Isaacman-VanWertz, A. H. Goldstein, R. A. Harley, G. J. Frost, J. M. Roberts, T. B. Ryerson, and M. Trainer (2018). "Volatile chemical products emerging as largest petrochemical source of urban organic emissions". *Science* 359 (6377). Publisher: American Association for the Advancement of Science (AAAS), 760–764. DOI: 10.1126/science.aaq0524.

McFiggans, G., T. F. Mentel, J. Wildt, I. Pullinen, S. Kang, E. Kleist, S. Schmitt, M. Springer, R. Tillmann, C. Wu, D. Zhao, M. Hallquist, C. Faxon, M. Le Breton, Å. M. Hallquist, D. Simpson, R. Bergström, M. E. Jenkin, M. Ehn, J. A. Thornton, M. R. Alfarra, T. J. Bannan, C. J. Percival, M. Priestley, D. Topping, and A. Kiendler-Scharr (2019). "Secondary organic aerosol reduced by mixture of atmospheric vapours". *Nature* 565 (7741), 587–593. DOI: 10.1038/s41586-018-0871-y.

Melillo, J. M. (2021). "Disruption of the global nitrogen cycle: A grand challenge for the twenty-first century". *Ambio* 50 (4), 759–763. DOI: 10.1007/s13280-020-01429-2.

Mensah, A. A., R. Holzinger, R. Otjes, A. Trimborn, T. F. Mentel, H. ten Brink, B. Henzing, and A. Kiendler-Scharr (2012). "Aerosol chemical composition at Cabauw, The Netherlands as observed in two intensive periods in May 2008 and March 2009". *Atmospheric Chemistry and Physics* 12 (10), 4723–4742. DOI: 10.5194/acp-12-4723-2012.

Metzger, S. (2002). "Gas/aerosol partitioning 2. Global modeling results". *Journal of Geophysical Research* 107 (D16), 4313. DOI: 10.1029/2001JD001103.

Metzger, S., F. Dentener, S. Pandis, and J. Lelieveld (2002). "Gas/aerosol partitioning: 1. A computationally efficient model". *Journal of Geophysical Research: Atmospheres* 107 (D16). DOI: 10.1029/2001JD001102.

Middlebrook, A. M., R. Bahreini, J. L. Jimenez, and M. R. Canagaratna (2012). "Evaluation of Composition-Dependent Collection Efficiencies for the Aerodyne Aerosol Mass Spectrometer using Field Data". *Aerosol Science and Technology* 46 (3), 258–271. DOI: 10.1080/02786826.2011.620041.

Misztal, P. K., T. Karl, R. Weber, H. H. Jonsson, A. B. Guenther, and A. H. Goldstein (2014). "Airborne flux measurements of biogenic isoprene over California". *Atmospheric Chemistry and Physics* 14 (19). Publisher: Copernicus GmbH, 10631–10647. DOI: 10.5194/acp-14-10631-2014.

Modini, R. L., Z. D. Ristovski, G. R. Johnson, C. He, N. Surawski, L. Morawska, T. Suni, and M. Kulmala (2009). "New particle formation and growth at a remote, sub-tropical coastal

location". *Atmospheric Chemistry and Physics* 9 (19), 7607–7621. DOI: 10.5194/acp-9-7607-2009.

Mohr, C., P. F. DeCarlo, M. F. Heringa, R. Chirico, J. G. Slowik, R. Richter, C. Reche, A. Alastuey, X. Querol, R. Seco, J. Peñuelas, J. L. Jiménez, M. Crippa, R. Zimmermann, U. Baltensperger, and A. S. H. Prévôt (2012). "Identification and quantification of organic aerosol from cooking and other sources in Barcelona using aerosol mass spectrometer data". *Atmospheric Chemistry and Physics* 12 (4), 1649–1665. DOI: 10.5194/acp-12-1649-2012.

Mohr, C., J. A. Huffman, M. J. Cubison, A. C. Aiken, K. S. Docherty, J. R. Kimmel, I. M. Ulbrich, M. Hannigan, and J. L. Jimenez (2009). "Characterization of Primary Organic Aerosol Emissions from Meat Cooking, Trash Burning, and Motor Vehicles with High-Resolution Aerosol Mass Spectrometry and Comparison with Ambient and Chamber Observations". *Environmental Science & Technology* 43 (7), 2443–2449. DOI: 10.1021/es8011518.

Mohr, C., F. D. Lopez-Hilfiker, T. Yli-Juuti, A. Heitto, A. Lutz, M. Hallquist, E. L. D'Ambro, M. P. Rissanen, L. Hao, S. Schobesberger, M. Kulmala, R. L. Mauldin, U. Makkonen, M. Sipilä, T. Petäjä, and J. A. Thornton (2017). "Ambient observations of dimers from terpene oxidation in the gas phase: Implications for new particle formation and growth". *Geophysical Research Letters* 44 (6), 2958–2966. DOI: 10.1002/2017GL072718.

Mohr, C., J. A. Thornton, A. Heitto, F. D. Lopez-Hilfiker, A. Lutz, I. Riipinen, J. Hong, N. M. Donahue, M. Hallquist, T. Petäjä, M. Kulmala, and T. Yli-Juuti (2019). "Molecular identification of organic vapors driving atmospheric nanoparticle growth". *Nature Communications* 10 (1), 4442. DOI: 10.1038/s41467-019-12473-2.

Molteni, U., M. Simon, M. Heinritzi, C. R. Hoyle, A.-K. Bernhammer, F. Bianchi, M. Breitenlechner, S. Brilke, A. Dias, J. Duplissy, C. Frege, H. Gordon, C. Heyn, T. Jokinen, A. Kürten, K. Lehtipalo, V. Makhmutov, T. Petäjä, S. M. Pieber, A. P. Praplan, S. Schobesberger, G. Steiner, Y. Stozhkov, A. Tomé, J. Tröstl, A. C. Wagner, R. Wagner, C. Williamson, C. Yan, U. Baltensperger, J. Curtius, N. M. Donahue, A. Hansel, J. Kirkby, M. Kulmala, D. R. Worsnop, and J. Dommen (2019). "Formation of Highly Oxygenated Organic Molecules from -Pinene Ozonolysis: Chemical Characteristics, Mechanism, and Kinetic Model Development". *ACS Earth and Space Chemistry* 3 (5), 873–883. DOI: 10.1021/acsearthspacechem.9b00035.

Mooibroek, D., M. Schaap, E. Weijers, and R. Hoogerbrugge (2011). "Source apportionment and spatial variability of PM2.5 using measurements at five sites in the Netherlands". *Atmospheric Environment* 45 (25), 4180–4191. DOI: 10.1016/j.atmosenv.2011.05.017.

Mordas, G., K. Plauškaitė, N. Prokopčiuk, V. Dudoitis, C. Bozzetti, and V. Ulevicius (2016). "Observation of new particle formation on Curonian Spit located between continental Europe and Scandinavia". *Journal of Aerosol Science* 97, 38–55. DOI: 10.1016/j.jaerosci.2016.03.002.

Németh, Z. and I. Salma (2014). "Spatial extension of nucleating air masses in the Carpathian Basin". *Atmospheric Chemistry and Physics* 14 (16), 8841–8848. DOI: 10.5194/acp-14-8841-2014.

Nenes, A., S. N. Pandis, and C. Pilinis (1999). "Continued development and testing of a new thermodynamic aerosol module for urban and regional air quality models". *Atmospheric Environment* 33 (10), 1553–1560. DOI: 10.1016/S1352-2310(98)00352-5.

Neuman, J. A., L. G. Huey, T. B. Ryerson, and D. W. Fahey (1999). "Study of Inlet Materials for Sampling Atmospheric Nitric Acid". *Environmental Science & Technology* 33 (7), 1133–1136. DOI: 10.1021/es980767f.

Ng, N. L., M. R. Canagaratna, Q. Zhang, J. L. Jimenez, J. Tian, I. M. Ulbrich, J. H. Kroll, K. S. Docherty, P. S. Chhabra, R. Bahreini, S. M. Murphy, J. H. Seinfeld, L. Hildebrandt, N. M. Donahue, P. F. DeCarlo, V. A. Lanz, A. S. H. Prévôt, E. Dinar, Y. Rudich, and D. R. Worsnop (2010). "Organic aerosol components observed in Northern Hemispheric datasets from Aerosol Mass Spectrometry". *Atmospheric Chemistry and Physics* 10 (10), 4625–4641. DOI: 10.5194/acp-10-4625-2010.

Ng, N. L., S. C. Herndon, A. Trimborn, M. R. Canagaratna, P. L. Croteau, T. B. Onasch, D. Sueper, D. R. Worsnop, Q. Zhang, Y. L. Sun, and J. T. Jayne (2011). "An Aerosol Chemical Speciation Monitor (ACSM) for Routine Monitoring of the Composition and Mass Concentrations of Ambient Aerosol". *Aerosol Science and Technology* 45 (7), 780–794. DOI: 10.1080/02786826.2011.560211.

Ng, N. L., A. J. Kwan, J. D. Surratt, A. W. H. Chan, P. S. Chhabra, A. Sorooshian, H. O. T. Pye, J. D. Crounse, P. O. Wennberg, R. C. Flagan, and J. H. Seinfeld (2008). "Secondary organic aerosol (SOA) formation from reaction of isoprene with nitrate radicals (NO_3)". *Atmospheric Chemistry and Physics* 8 (14), 4117–4140. DOI: 10.5194/acp-8-4117-2008.

Ng, N. L., S. S. Brown, A. T. Archibald, E. Atlas, R. C. Cohen, J. N. Crowley, D. A. Day, N. M. Donahue, J. L. Fry, H. Fuchs, R. J. Griffin, M. I. Guzman, H. Herrmann, A. Hodzic, Y. Iinuma, J. L. Jimenez, A. Kiendler-Scharr, B. H. Lee, D. J. Luecken, J. Mao, R. McLaren, A. Mutzel, H. D. Osthoff, B. Ouyang, B. Picquet-Varrault, U. Platt, H. O. T. Pye, Y. Rudich, R. H. Schwantes, M. Shiraiwa, J. Stutz, J. A. Thornton, A. Tilgner, B. J. Williams, and R. A. Zaveri (2017). "Nitrate radicals and biogenic volatile organic compounds: oxidation, mechanisms, and organic aerosol". *Atmospheric Chemistry and Physics* 17 (3), 2103–2162. DOI: 10.5194/acp-17-2103-2017.

Nguyen, T. B., J. Laskin, A. Laskin, and S. A. Nizkorodov (2011). "Nitrogen-Containing Organic Compounds and Oligomers in Secondary Organic Aerosol Formed by Photooxidation of Isoprene". *Environmental Science & Technology* 45 (16), 6908–6918. DOI: 10.1021/es201611n.

Nieminen, T., A. Asmi, M. D. Maso, P. P. Aalto, P. Keronen, T. Petäjä, M. Kulmala, and V.-M. Kerminen (2014). "Trends in atmospheric new-particle formation: 16 years of observations in a boreal-forest environment". *Boreal Environment Research* 19 (suppl. B), 191–214.

Nunnermacker, L. J., L. I. Kleinman, D. Imre, P. H. Daum, Y.-N. Lee, J. H. Lee, S. R. Springston, L. Newman, and N. Gillani (2000). "NO_y lifetimes and O_3 production efficiencies in urban and power plant plumes: Analysis of field data". *Journal of Geophysical Research: Atmospheres* 105 (D7), 9165–9176. DOI: 10.1029/1999JD900753.

Nursanto, F. R., D. A. Day, R. Meinen, R. Holzinger, H. Saathoff, J. Fu, J. Mulder, U. Dusek, and J. L. Fry (2025). "Development and validation of a NO_x^+ ratio method for the quantitative separation of inorganic and organic nitrate aerosol using a unit-mass-resolution time-of-flight aerosol chemical speciation monitor equipped with a capture vaporizer (CV-UMR-ToF-ACSM)". *Atmospheric Measurement Techniques* 18 (13). Publisher: Copernicus GmbH, 3051–3072. DOI: 10.5194/amt-18-3051-2025.

Nursanto, F. R., Q. He, S. Van De Wouw, A. Zanders, T. Hohaus, W. S. J. Kroese, R. Wegener, M. G. Adam, B. Winter, R. Dubus, L. Kesper, F. Rohrer, Y. Wang, E. Matthews, A. Voliotis, T. J. Bannan, G. McFiggans, H. Coe, Y. Wu, M. Roska, M. Canagaratna, M. Alton, M. M. Coggon, C. E. Stockwell, K. H. Bates, E. Y. Pfannerstill, S. R. Zorn, H. Wang, M. Riva, S. Perrier, B. Yang, L. Liu, A. Novelli, M. Färber, H. Fuchs, A. C. Marcillo Lara, A. Grasse, C. Wesolek, R. Tillmann, R. Holzinger, M. C. Krol, G. I. Gkatzelis, and J. L. Fry (2026). *Gas-particle partitioning, molecular weight, and yield of organic nitrate under different urban VOC, NO_x, and oxidation conditions during SAPHIR-CHANEL campaign*. DOI: 10.5194/egusphere-2025-6310.

Nursanto, F. R., R. Meinen, R. Holzinger, M. C. Krol, X. Liu, U. Dusek, B. Henzing, and J. L. Fry (2023). "What chemical species are responsible for new particle formation and growth in the Netherlands? A hybrid positive matrix factorization (PMF) analysis using aerosol composition (ACSM) and size (SMPS)". *Atmospheric Chemistry and Physics* 23 (17), 10015–10034. DOI: 10.5194/acp-23-10015-2023.

Olin, M., M. Okuljar, M. P. Rissanen, J. Kalliokoski, J. Shen, L. Dada, M. Lampimäki, Y. Wu, A. Lohila, J. Duplissy, M. Sipilä, T. Petäjä, M. Kulmala, and M. Dal Maso (2022). *Measurement report: Atmospheric new particle formation in a coastal agricultural site explained with binPMF analysis of nitrate CI-APi-TOF spectra*. preprint. DOI: 10.5194/acp-2022-261.

Oomen, G.-M., J.-F. Müller, T. Stavrakou, I. De Smedt, T. Blumenstock, R. Kivi, M. Makarova, M. Palm, A. Röhling, Y. Té, C. Vigouroux, M. M. Friedrich, U. Frieß, F. Hendrick, A. Merlaud, A. Piters, A. Richter, M. Van Roozendael, and T. Wagner (2024). "Weekly derived top-down volatile-organic-compound fluxes over Europe from TROPOMI HCHO data from 2018 to 2021". *Atmospheric Chemistry and Physics* 24 (1), 449–474. DOI: 10.5194/acp-24-449-2024.

Paatero, P. (1999). "The Multilinear Engine—A Table-Driven, Least Squares Program for Solving Multilinear Problems, Including the *n*-Way Parallel Factor Analysis Model". *Journal of Computational and Graphical Statistics* 8 (4), 854–888. DOI: 10.1080/10618600.1999.10474853.

Paatero, P. and U. Tapper (1994). "Positive matrix factorization: A non-negative factor model with optimal utilization of error estimates of data values". *Environmetrics* 5 (2), 111–126. DOI: 10.1002/env.3170050203.

Paglione, M., A. Kiendler-Scharr, A. A. Mensah, E. Finessi, L. Giulianelli, S. Sandrini, M. C. Facchini, S. Fuzzi, P. Schlag, A. Piazzalunga, E. Tagliavini, J. S. Henzing, and S. Decesari (2014). "Identification of humic-like substances (HULIS) in oxygenated organic aerosols using NMR and AMS factor analyses and liquid chromatographic techniques". *Atmospheric Chemistry and Physics* 14 (1), 25–45. DOI: 10.5194/acp-14-25-2014.

Pandolfi, M., X. Querol, A. Alastuey, J. L. Jimenez, O. Jorba, D. Day, A. Ortega, M. J. Cubison, A. Comerón, M. Sicard, C. Mohr, A. S. H. Prévôt, M. C. Minguillón, J. Pey, J. M. Baldasano, J. F. Burkhart, R. Seco, J. Peñuelas, B. L. Van Drooge, B. Artiñano, C. Di Marco, E. Nemitz, S. Schallhart, A. Metzger, A. Hansel, J. Lorente, S. Ng, J. Jayne, and S. Szidat (2014). "Effects of sources and meteorology on particulate matter in the Western Mediterranean Basin: An overview of the DAURE campaign". *Journal of Geophysical Research: Atmospheres* 119 (8), 4978–5010. DOI: 10.1002/2013JD021079.

Pang, J. Y. S., A. Novelli, M. Kaminski, I.-H. Acir, B. Bohn, P. T. M. Carlsson, C. Cho, H.-P. Dorn, A. Hofzumahaus, X. Li, A. Lutz, S. Nehr, D. Reimer, F. Rohrer, R. Tillmann, R. Wegener, A.

Kiendler-Scharr, A. Wahner, and H. Fuchs (2022). "Investigation of the limonene photooxidation by OH at different NO concentrations in the atmospheric simulation chamber SAPHIR (Simulation of Atmospheric PHotochemistry In a large Reaction Chamber)". *Atmospheric Chemistry and Physics* 22 (13), 8497–8527. DOI: 10.5194/acp-22-8497-2022.

Pankow, J. F. and W. E. Asher (2008). "SIMPOL.1: a simple group contribution method for predicting vapor pressures and enthalpies of vaporization of multifunctional organic compounds". *Atmospheric Chemistry and Physics* 8 (10), 2773–2796. DOI: 10.5194/acp-8-2773-2008.

Pankow, J. F. (1994). "An absorption model of gas/particle partitioning of organic compounds in the atmosphere". *Atmospheric Environment* 28 (2), 185–188. DOI: 10.1016/1352-2310(94)90093-0.

Paulot, F., P. Ginoux, W. F. Cooke, L. J. Donner, S. Fan, M.-Y. Lin, J. Mao, V. Naik, and L. W. Horowitz (2016). "Sensitivity of nitrate aerosols to ammonia emissions and to nitrate chemistry: implications for present and future nitrate optical depth". *Atmospheric Chemistry and Physics* 16 (3), 1459–1477. DOI: 10.5194/acp-16-1459-2016.

Peltola, M., C. Rose, J. V. Trueblood, S. Gray, M. Harvey, and K. Sellegri (2022). "New particle formation in coastal New Zealand with a focus on open-ocean air masses". *Atmospheric Chemistry and Physics* 22 (9), 6231–6254. DOI: 10.5194/acp-22-6231-2022.

Peng, Y., X. Liu, J. Dai, Z. Wang, Z. Dong, Y. Dong, C. Chen, X. Li, N. Zhao, and C. Fan (2017). "Aerosol size distribution and new particle formation events in the suburb of Xi'an, northwest China". *Atmospheric Environment* 153, 194–205. DOI: 10.1016/j.atmosenv.2017.01.022.

Peräkylä, O., T. Berndt, L. Franzon, G. Hasan, M. Meder, R. R. Valiev, C. D. Daub, J. G. Varelas, F. M. Geiger, R. J. Thomson, M. Rissanen, T. Kurtén, and M. Ehn (2023). "Large Gas-Phase Source of Esters and Other Accretion Products in the Atmosphere". *Journal of the American Chemical Society* 145 (14), 7780–7790. DOI: 10.1021/jacs.2c10398.

Peräkylä, O., M. Riva, L. Heikkinen, L. Quéléver, P. Roldin, and M. Ehn (2020). "Experimental investigation into the volatilities of highly oxygenated organic molecules (HOMs)". *Atmospheric Chemistry and Physics* 20 (2), 649–669. DOI: 10.5194/acp-20-649-2020.

Perring, A. E., T. H. Bertram, P. J. Wooldridge, A. Fried, B. G. Heikes, J. Dibb, J. D. Crounse, P. O. Wennberg, N. J. Blake, D. R. Blake, W. H. Brune, H. B. Singh, and R. C. Cohen (2009). "Airborne observations of total $RONO_2$: new constraints on the yield and lifetime of isoprene nitrates". *Atmospheric Chemistry and Physics* 9 (4). Publisher: Copernicus GmbH, 1451–1463. DOI: 10.5194/acp-9-1451-2009.

Pfannerstill, E. Y., C. Arata, Q. Zhu, B. C. Schulze, R. Ward, R. Woods, C. Harkins, R. H. Schwantes, J. H. Seinfeld, A. Bucholtz, R. C. Cohen, and A. H. Goldstein (2024). "Temperature-dependent emissions dominate aerosol and ozone formation in Los Angeles". *Science* 384 (6702). Publisher: American Association for the Advancement of Science (AAAS), 1324–1329. DOI: 10.1126/science.adg8204.

Pfannerstill, E. Y., C. Arata, Q. Zhu, B. C. Schulze, R. Woods, C. Harkins, R. H. Schwantes, B. C. McDonald, J. H. Seinfeld, A. Bucholtz, R. C. Cohen, and A. H. Goldstein (2023). "Comparison between Spatially Resolved Airborne Flux Measurements and Emission Inventories of Volatile

Organic Compounds in Los Angeles". *Environmental Science & Technology* 57 (41). Publisher: American Chemical Society (ACS), 15533–15545. DOI: 10.1021/acs.est.3c03162.

Pfeifer, S., W. Birmili, A. Schladitz, T. Müller, A. Nowak, and A. Wiedensohler (2014). "A fast and easy-to-implement inversion algorithm for mobility particle size spectrometers considering particle number size distribution information outside of the detection range". *Atmospheric Measurement Techniques* 7 (1), 95–105. DOI: 10.5194/amt-7-95-2014.

Platt, U., J. Meinen, D. Pöhler, and T. Leisner (2009). "Broadband Cavity Enhanced Differential Optical Absorption Spectroscopy (CE-DOAS) – applicability and corrections". *Atmospheric Measurement Techniques* 2 (2), 713–723. DOI: 10.5194/amt-2-713-2009.

Platt, U., D. Perner, and H. W. Pätz (1979). "Simultaneous measurement of atmospheric CH_2O, O_3 , and NO_2 by differential optical absorption". *Journal of Geophysical Research: Oceans* 84 (C10), 6329–6335. DOI: 10.1029/JC084iC10p06329.

Pope, C. A., N. Coleman, Z. A. Pond, and R. T. Burnett (2020). "Fine particulate air pollution and human mortality: 25+ years of cohort studies". *Environmental Research* 183, 108924. DOI: 10.1016/j.envres.2019.108924.

Pospisilova, V., F. D. Lopez-Hilfiker, D. M. Bell, I. El Haddad, C. Mohr, W. Huang, L. Heikkinen, M. Xiao, J. Dommen, A. S. H. Prevot, U. Baltensperger, and J. G. Slowik (2020). "On the fate of oxygenated organic molecules in atmospheric aerosol particles". *Science Advances* 6 (11), eaax8922. DOI: 10.1126/sciadv.aax8922.

Pushpawela, B., R. Jayaratne, and L. Morawska (2019). "The influence of wind speed on new particle formation events in an urban environment". *Atmospheric Research* 215, 37–41. DOI: 10.1016/j.atmosres.2018.08.023.

Pye, H. O. T., D. J. Luecken, L. Xu, C. M. Boyd, N. L. Ng, K. R. Baker, B. R. Ayres, J. O. Bash, K. Baumann, W. P. L. Carter, E. Edgerton, J. L. Fry, W. T. Hutzell, D. B. Schwede, and P. B. Shepson (2015). "Modeling the Current and Future Roles of Particulate Organic Nitrates in the Southeastern United States". *Environmental Science & Technology* 49 (24), 14195–14203. DOI: 10.1021/acs.est.5b03738.

Qi, X. M., A. J. Ding, W. Nie, T. Petäjä, V.-M. Kerminen, E. Herrmann, Y. N. Xie, L. F. Zheng, H. Manninen, P. Aalto, J. N. Sun, Z. N. Xu, X. G. Chi, X. Huang, M. Boy, A. Virkkula, X.-Q. Yang, C. B. Fu, and M. Kulmala (2015). "Aerosol size distribution and new particle formation in the western Yangtze River Delta of China: 2 years of measurements at the SORPES station". *Atmospheric Chemistry and Physics* 15 (21), 12445–12464. DOI: 10.5194/acp-15-12445-2015.

Räty, M., O. Peräkylä, M. Riva, L. Quéléver, O. Garmash, M. Rissanen, and M. Ehn (2021). "Measurement report: Effects of NO_x and seed aerosol on highly oxygenated organic molecules (HOMs) from cyclohexene ozonolysis". *Atmospheric Chemistry and Physics* 21 (9), 7357–7372. DOI: 10.5194/acp-21-7357-2021.

Riccobono, F., S. Schobesberger, C. E. Scott, J. Dommen, I. K. Ortega, L. Rondo, J. Almeida, A. Amorim, F. Bianchi, M. Breitenlechner, A. David, A. Downard, E. M. Dunne, J. Duplissy, S. Ehrhart, R. C. Flagan, A. Franchin, A. Hansel, H. Junninen, M. Kajos, H. Keskinen, A. Kupc, A. Kürten, A. N. Kvashin, A. Laaksonen, K. Lehtipalo, V. Makhmutov, S. Mathot, T. Nieminen, A. Onnela, T. Petäjä, A. P. Praplan, F. D. Santos, S. Schallhart, J. H. Seinfeld, M. Sipilä, D. V.

Spracklen, Y. Stozhkov, F. Stratmann, A. Tomé, G. Tsagkogeorgas, P. Vaattovaara, Y. Viisanen, A. Vrtala, P. E. Wagner, E. Weingartner, H. Wex, D. Wimmer, K. S. Carslaw, J. Curtius, N. M. Donahue, J. Kirkby, M. Kulmala, D. R. Worsnop, and U. Baltensperger (2014). "Oxidation Products of Biogenic Emissions Contribute to Nucleation of Atmospheric Particles". *Science* 344 (6185), 717–721. DOI: 10.1126/science.1243527.

Riipinen, I., T. Yli-Juuti, J. R. Pierce, T. Petäjä, D. R. Worsnop, M. Kulmala, and N. M. Donahue (2012). "The contribution of organics to atmospheric nanoparticle growth". *Nature Geoscience* 5 (7), 453–458. DOI: 10.1038/ngeo1499.

Riva, M., M. Brüggemann, D. Li, S. Perrier, C. George, H. Herrmann, and T. Berndt (2020). "Capability of CI-Orbitrap for Gas-Phase Analysis in Atmospheric Chemistry: A Comparison with the CI-APi-TOF Technique". *Analytical Chemistry* 92 (12). Publisher: American Chemical Society (ACS), 8142–8150. DOI: 10.1021/acs.analchem.0c00111.

Riva, M., M. Ehn, D. Li, S. Tomaz, F. Bourgain, S. Perrier, and C. George (2019). "CI-Orbitrap: An Analytical Instrument To Study Atmospheric Reactive Organic Species". *Analytical Chemistry* 91 (15). Publisher: American Chemical Society (ACS), 9419–9423. DOI: 10.1021/acs.analchem.9b02093.

Riva, M., V. Pospisilova, C. Frege, S. Perrier, P. Bansal, S. Jorga, P. Sturm, J. A. Thornton, U. Rohner, and F. Lopez-Hilfiker (2024). "Evaluation of a reduced-pressure chemical ion reactor utilizing adduct ionization for the detection of gaseous organic and inorganic species". *Atmospheric Measurement Techniques* 17 (19), 5887–5901. DOI: 10.5194/amt-17-5887-2024.

Rivellini, L.-H., S. Jorga, Y. Wang, A. K. Lee, J. G. Murphy, A. W. Chan, and J. P. Abbatt (2024). "Sources of Wintertime Atmospheric Organic Pollutants in a Large Canadian City: Insights from Particle and Gas Phase Measurements". *ACS ES&T Air* 1 (7), 690–703. DOI: 10.1021/acsestair.4c00039.

Rodriguez, M. A. and D. Dabdub (2004). "IMAGES-SCAPE2: A modeling study of size- and chemically resolved aerosol thermodynamics in a global chemical transport model". *Journal of Geophysical Research: Atmospheres* 109 (D2), 2003JD003639. DOI: 10.1029/2003JD003639.

Rohrer, F., B. Bohn, T. Brauers, D. Brüning, F.-J. Johnen, A. Wahner, and J. Kleffmann (2005). "Characterisation of the photolytic HONO-source in the atmosphere simulation chamber SAPHIR". *Atmospheric Chemistry and Physics* 5 (8), 2189–2201. DOI: 10.5194/acp-5-2189-2005.

Rollins, A. W., E. C. Browne, K.-E. Min, S. E. Pusede, P. J. Wooldridge, D. R. Gentner, A. H. Goldstein, S. Liu, D. A. Day, L. M. Russell, and R. C. Cohen (2012). "Evidence for NO $_x$ Control over Nighttime SOA Formation". *Science* 337 (6099), 1210–1212. DOI: 10.1126/science.1221520.

Rollins, A. W., A. Kiendler-Scharr, J. L. Fry, T. Brauers, S. S. Brown, H.-P. Dorn, W. P. Dubé, H. Fuchs, A. Mensah, T. F. Mentel, F. Rohrer, R. Tillmann, R. Wegener, P. J. Wooldridge, and R. C. Cohen (2009). "Isoprene oxidation by nitrate radical: alkyl nitrate and secondary organic aerosol yields". *Atmospheric Chemistry and Physics* 9 (18), 6685–6703. DOI: 10.5194/acp-9-6685-2009.

Rollins, A. W., S. Pusede, P. Wooldridge, K.-E. Min, D. R. Gentner, A. H. Goldstein, S. Liu, D. A. Day, L. M. Russell, C. L. Rubitschun, J. D. Surratt, and R. C. Cohen (2013). "Gas/particle

partitioning of total alkyl nitrates observed with TD-LIF in Bakersfield". *Journal of Geophysical Research: Atmospheres* 118 (12), 6651–6662. DOI: 10.1002/jgrd.50522.

Romer, P. S., K. C. Duffey, P. J. Wooldridge, H. M. Allen, B. R. Ayres, S. S. Brown, W. H. Brune, J. D. Crounse, J. De Gouw, D. C. Draper, P. A. Feiner, J. L. Fry, A. H. Goldstein, A. Koss, P. K. Misztal, T. B. Nguyen, K. Olson, A. P. Teng, P. O. Wennberg, R. J. Wild, L. Zhang, and R. C. Cohen (2016). "The lifetime of nitrogen oxides in an isoprene-dominated forest". *Atmospheric Chemistry and Physics* 16 (12). Publisher: Copernicus GmbH, 7623–7637. DOI: 10.5194/acp-16-7623-2016.

Romer Present, P. S., A. Zare, and R. C. Cohen (2020). "The changing role of organic nitrates in the removal and transport of NO_x". *Atmospheric Chemistry and Physics* 20 (1), 267–279. DOI: 10.5194/acp-20-267-2020.

Rotterdam, P. of (2025). *Throughput in the port of Rotterdam*. Tech. rep. Rotterdam, the Netherlands: Port of Rotterdam.

Ryerson, T. B., M. P. Buhr, G. J. Frost, P. D. Goldan, J. S. Holloway, G. Hübler, B. T. Jobson, W. C. Kuster, S. A. McKeen, D. D. Parrish, J. M. Roberts, D. T. Sueper, M. Trainer, J. Williams, and F. C. Fehsenfeld (1998). "Emissions lifetimes and ozone formation in power plant plumes". *Journal of Geophysical Research: Atmospheres* 103 (D17), 22569–22583. DOI: 10.1029/98JD01620.

Salimi, F., L. R. Crilley, S. Stevanovic, Z. Ristovski, M. Mazaheri, C. He, G. Johnson, G. Ayoko, and L. Morawska (2015). "Insights into the growth of newly formed particles in a subtropical urban environment". *Atmospheric Chemistry and Physics* 15 (23), 13475–13485. DOI: 10.5194/acp-15-13475-2015.

Saunders, S. M., M. E. Jenkin, R. G. Derwent, and M. J. Pilling (2003). "Protocol for the development of the Master Chemical Mechanism, MCM v3 (Part A): tropospheric degradation of non-aromatic volatile organic compounds". *Atmospheric Chemistry and Physics* 3 (1), 161–180. DOI: 10.5194/acp-3-161-2003.

Sauter, F., M. Sterk, E. van der Swaluw, R. Wichink Kruit, W. de Vries, A. van Pul, H. van Jaarsveld, M. van Zanten, J. Aben, and F. de Leeuw (2025). *The OPS-model: Description of OPS 5.3.1.0*.

Saylor, R., L. Myles, D. Sibble, J. Caldwell, and J. Xing (2015). "Recent trends in gas-phase ammonia and $PM_{2.5}$ ammonium in the Southeast United States". *Journal of the Air & Waste Management Association* 65 (3). Publisher: Informa UK Limited, 347–357. DOI: 10.1080/10962247.2014.992554.

Schaap, M., M. van Loon, H. M. ten Brink, F. J. Dentener, and P. J. H. Builtjes (2003). *The nitrate aerosol field over Europe: simulations with an atmospheric chemistry-transport model of intermediate complexity*. preprint. DOI: 10.5194/acpd-3-5919-2003.

– (2004). "Secondary inorganic aerosol simulations for Europe with special attention to nitrate". *Atmospheric Chemistry and Physics* 4 (3), 857–874. DOI: 10.5194/acp-4-857-2004.

Schiphol (2025). *Traffic review 2024*. Tech. rep. Schiphol Airport.

Schlag, P., A. Kiendler-Scharr, M. J. Blom, F. Canonaco, J. S. Henzing, M. Moerman, A. S. H. Prévôt, and R. Holzinger (2016). "Aerosol source apportionment from 1-year measurements

at the CESAR tower in Cabauw, the Netherlands". *Atmospheric Chemistry and Physics* 16 (14), 8831–8847. DOI: 10.5194/acp-16-8831-2016.

Schneider, J., S. Weimer, F. Drewnick, S. Borrmann, G. Helas, P. Gwaze, O. Schmid, M. Andreae, and U. Kirchner (2006). "Mass spectrometric analysis and aerodynamic properties of various types of combustion-related aerosol particles". *International Journal of Mass Spectrometry* 258 (1-3), 37–49. DOI: 10.1016/j.ijms.2006.07.008.

Schobesberger, S., H. Junninen, F. Bianchi, G. Lönn, M. Ehn, K. Lehtipalo, J. Dommen, S. Ehrhart, I. K. Ortega, A. Franchin, T. Nieminen, F. Riccobono, M. Hutterli, J. Duplissy, J. Almeida, A. Amorim, M. Breitenlechner, A. J. Downard, E. M. Dunne, R. C. Flagan, M. Kajos, H. Keskinen, J. Kirkby, A. Kupc, A. Kürten, T. Kurtén, A. Laaksonen, S. Mathot, A. Onnela, A. P. Praplan, L. Rondo, F. D. Santos, S. Schallhart, R. Schnitzhofer, M. Sipilä, A. Tomé, G. Tsagkogeorgas, H. Vehkamäki, D. Wimmer, U. Baltensperger, K. S. Carslaw, J. Curtius, A. Hansel, T. Petäjä, M. Kulmala, N. M. Donahue, and D. R. Worsnop (2013). "Molecular understanding of atmospheric particle formation from sulfuric acid and large oxidized organic molecules". *Proceedings of the National Academy of Sciences* 110 (43), 17223–17228. DOI: 10.1073/pnas.1306973110.

Scholz, S. M. C., V. A. Karydis, G. I. Gkatzelis, H. Fuchs, S. N. Pandis, and A. P. Tsimpidi (2025). *Incorporation of lumped IVOC emissions into the ORACLE model (V1.1): A multi-product framework for assessing global SOA formation from internal combustion engines*. DOI: 10.5194/egusphere-2025-2510.

Schulte, R., M. van Zanten, S. Rutledge-Jonker, D. Swart, R. Wichink Kruit, M. Krol, W. van Pul, and J. Vilà-Guerau de Arellano (2021). "Unraveling the diurnal atmospheric ammonia budget of a prototypical convective boundary layer". *Atmospheric Environment* 249, 118153. DOI: 10.1016/j.atmosenv.2020.118153.

Segers, A. J., R. Kranenburg, H. J. Jonas, T. L. Hohenberger, L. Geers, and A. M. M. Manders-Groot (2025). *LOTOS-EUROS Reference Guide v3.0.000*. Tech. rep.

Sellegri, K., C. Rose, A. Marinoni, A. Lupi, A. Wiedensohler, M. Andrade, P. Bonasoni, and P. Laj (2019). "New Particle Formation: A Review of Ground-Based Observations at Mountain Research Stations". *Atmosphere* 10 (9), 493. DOI: 10.3390/atmos10090493.

Shao, Y., A. Voliotis, M. Du, Y. Wang, K. Pereira, J. Hamilton, M. R. Alfarra, and G. McFiggans (2022). "Chemical composition of secondary organic aerosol particles formed from mixtures of anthropogenic and biogenic precursors". *Atmospheric Chemistry and Physics* 22 (15), 9799–9826. DOI: 10.5194/acp-22-9799-2022.

Simon, H., A. Reff, B. Wells, J. Xing, and N. Frank (2015). "Ozone Trends Across the United States over a Period of Decreasing NOx and VOC Emissions". *Environmental Science & Technology* 49 (1). Publisher: American Chemical Society (ACS), 186–195. DOI: 10.1021/es504514z.

Singh, H. B. (1987). "Reactive nitrogen in the troposphere". *Environmental Science & Technology* 21 (4), 320–327. DOI: 10.1021/es00158a001.

Skjøth, C. A. and O. Hertel (2013). "Ammonia Emissions in Europe". In: *Urban Air Quality in Europe*. Ed. by M. Viana. Berlin, Heidelberg: Springer Berlin Heidelberg, 141–163. DOI: 10.1007/698_2012_206.

Sobanski, N., J. Thieser, J. Schuladen, C. Sauvage, W. Song, J. Williams, J. Lelieveld, and J. N. Crowley (2017). "Day and night-time formation of organic nitrates at a forested mountain site in south-west Germany". *Atmospheric Chemistry and Physics* 17 (6), 4115–4130. DOI: 10.5194/acp-17-4115-2017.

Song, J., H. Saathoff, L. Gao, R. Gebhardt, F. Jiang, M. Vallon, J. Bauer, S. Norra, and T. Leisner (2022). "Variations of $PM_{2.5}$ sources in the context of meteorology and seasonality at an urban street canyon in Southwest Germany". *Atmospheric Environment* 282, 119147. DOI: 10.1016/j.atmosenv.2022.119147.

Song, J., H. Saathoff, F. Jiang, L. Gao, H. Zhang, and T. Leisner (2024). "Sources of organic gases and aerosol particles and their roles in nighttime particle growth at a rural forested site in southwest Germany". *Atmospheric Chemistry and Physics* 24 (11), 6699–6717. DOI: 10.5194/acp-24-6699-2024.

Spittler, M., I. Barnes, I. Bejan, K. Brockmann, T. Benter, and K. Wirtz (2006). "Reactions of NO_3 radicals with limonene and α-pinene: Product and SOA formation". *Atmospheric Environment* 40, 116–127. DOI: 10.1016/j.atmosenv.2005.09.093.

Spracklen, D. V., K. S. Carslaw, J. Merikanto, G. W. Mann, C. L. Reddington, S. Pickering, J. A. Ogren, E. Andrews, U. Baltensperger, E. Weingartner, M. Boy, M. Kulmala, L. Laakso, H. Lihavainen, N. Kivekäs, M. Komppula, N. Mihalopoulos, G. Kouvarakis, S. G. Jennings, C. O'Dowd, W. Birmili, A. Wiedensohler, R. Weller, J. Gras, P. Laj, K. Sellegri, B. Bonn, R. Krejci, A. Laaksonen, A. Hamed, A. Minikin, R. M. Harrison, R. Talbot, and J. Sun (2010). "Explaining global surface aerosol number concentrations in terms of primary emissions and particle formation". *Atmospheric Chemistry and Physics* 10 (10), 4775–4793. DOI: 10.5194/acp-10-4775-2010.

Staats, N., M. Bolech, S. Dellaert, R. Dröge, E. van Eijk, B. van Huet, J. van Huijstee, S. van Mill, R. te Molder, D. Wever, M. van Zanten, and T. van der Zee (2025). *Informative Inventory Report 2025. Emissions of transboundary air pollutants in the Netherlands 1990-2023*. Tech. rep. Rijksinstituut voor Volksgezondheid en Milieu RIVM. DOI: 10.21945/RIVM-2025-0007.

Stein, A. F., R. R. Draxler, G. D. Rolph, B. J. B. Stunder, M. D. Cohen, and F. Ngan (2015). "NOAA's HYSPLIT Atmospheric Transport and Dispersion Modeling System". *Bulletin of the American Meteorological Society* 96 (12), 2059–2077. DOI: 10.1175/BAMS-D-14-00110.1.

Stockwell, C. E., M. M. Coggon, R. H. Schwantes, C. Harkins, B. Verreyken, C. Lyu, Q. Zhu, L. Xu, J. B. Gilman, A. Lamplugh, J. Peischl, M. A. Robinson, P. R. Veres, M. Li, A. W. Rollins, K. Zuraski, S. Baidar, S. Liu, T. Kuwayama, S. S. Brown, B. C. McDonald, and C. Warneke (2025). "Urban ozone formation and sensitivities to volatile chemical products, cooking emissions, and NO_x upwind of and within two Los Angeles Basin cities". *Atmospheric Chemistry and Physics* 25 (2). Publisher: Copernicus GmbH, 1121–1143. DOI: 10.5194/acp-25-1121-2025.

Stull, R. B., ed. (1988). *An Introduction to Boundary Layer Meteorology*. Dordrecht: Springer Netherlands. DOI: 10.1007/978-94-009-3027-8.

Sun, Y., W. Du, P. Fu, Q. Wang, J. Li, X. Ge, Q. Zhang, C. Zhu, L. Ren, W. Xu, J. Zhao, T. Han, D. R. Worsnop, and Z. Wang (2016). "Primary and secondary aerosols in Beijing in winter:

sources, variations and processes". *Atmospheric Chemistry and Physics* 16 (13), 8309–8329. DOI: 10.5194/acp-16-8309-2016.

Swaluw, E. van der, W. A. Asman, H. van Jaarsveld, and R. Hoogerbrugge (2011). "Wet deposition of ammonium, nitrate and sulfate in the Netherlands over the period 1992–2008". *Atmospheric Environment* 45 (23), 3819–3826. DOI: 10.1016/j.atmosenv.2011.04.017.

Takeuchi, M. and N. L. Ng (2019). "Chemical composition and hydrolysis of organic nitrate aerosol formed from hydroxyl and nitrate radical oxidation of α-pinene and -pinene". *Atmospheric Chemistry and Physics* 19 (19), 12749–12766. DOI: 10.5194/acp-19-12749-2019.

Takeuchi, M., Y. Wang, B. A. Nault, Y. Chen, M. R. Canagaratna, and N. L. Ng (2024). "Evaluating the response of the Aerodyne aerosol mass spectrometer to monoterpene- and isoprene-derived organic nitrate standards". *Aerosol Science and Technology* 58 (12), 1371–1388. DOI: 10.1080/02786826.2024.2389183.

Thornton, J. A., J. E. Shilling, M. Shrivastava, E. L. D'Ambro, M. A. Zawadowicz, and J. Liu (2020). "A Near-Explicit Mechanistic Evaluation of Isoprene Photochemical Secondary Organic Aerosol Formation and Evolution: Simulations of Multiple Chamber Experiments with and without Added NO_x". *ACS Earth and Space Chemistry* 4 (7), 1161–1181. DOI: 10.1021/acsearthspacechem.0c00118.

Tobias, H. J. and P. J. Ziemann (2000). "Thermal Desorption Mass Spectrometric Analysis of Organic Aerosol Formed from Reactions of 1-Tetradecene and O_3 in the Presence of Alcohols and Carboxylic Acids". *Environmental Science & Technology* 34 (11), 2105–2115. DOI: 10.1021/es9907156.

Tokaya, J., R. Kranenburg, R. Timmermans, P. Coenen, B. Kelly, J. Hullegie, T. Megaritis, and G. Valastro (2024). "The impact of shipping on the air quality in European port cities with a detailed analysis for Rotterdam". *Atmospheric Environment: X* 23. Publisher: Elsevier BV, 100278. DOI: 10.1016/j.aeaoa.2024.100278.

Travis, K. R., D. J. Jacob, J. A. Fisher, P. S. Kim, E. A. Marais, L. Zhu, K. Yu, C. C. Miller, R. M. Yantosca, M. P. Sulprizio, A. M. Thompson, P. O. Wennberg, J. D. Crounse, J. M. St. Clair, R. C. Cohen, J. L. Laughner, J. E. Dibb, S. R. Hall, K. Ullmann, G. M. Wolfe, I. B. Pollack, J. Peischl, J. A. Neuman, and X. Zhou (2016). "Why do models overestimate surface ozone in the Southeast United States?" *Atmospheric Chemistry and Physics* 16 (21), 13561–13577. DOI: 10.5194/acp-16-13561-2016.

Tröstl, J., W. K. Chuang, H. Gordon, M. Heinritzi, C. Yan, U. Molteni, L. Ahlm, C. Frege, F. Bianchi, R. Wagner, M. Simon, K. Lehtipalo, C. Williamson, J. S. Craven, J. Duplissy, A. Adamov, J. Almeida, A.-K. Bernhammer, M. Breitenlechner, S. Brilke, A. Dias, S. Ehrhart, R. C. Flagan, A. Franchin, C. Fuchs, R. Guida, M. Gysel, A. Hansel, C. R. Hoyle, T. Jokinen, H. Junninen, J. Kangasluoma, H. Keskinen, J. Kim, M. Krapf, A. Kürten, A. Laaksonen, M. Lawler, M. Leiminger, S. Mathot, O. Möhler, T. Nieminen, A. Onnela, T. Petäjä, F. M. Piel, P. Miettinen, M. P. Rissanen, L. Rondo, N. Sarnela, S. Schobesberger, K. Sengupta, M. Sipilä, J. N. Smith, G. Steiner, A. Tomè, A. Virtanen, A. C. Wagner, E. Weingartner, D. Wimmer, P. M. Winkler, P. Ye, K. S. Carslaw, J. Curtius, J. Dommen, J. Kirkby, M. Kulmala, I. Riipinen, D. R. Worsnop, N. M. Donahue, and U. Baltensperger (2016). "The role of low-volatility organic

compounds in initial particle growth in the atmosphere". *Nature* 533 (7604), 527–531. DOI: 10.1038/nature18271.

Ulbrich, I. M., M. R. Canagaratna, Q. Zhang, D. R. Worsnop, and J. L. Jimenez (2009). "Interpretation of organic components from Positive Matrix Factorization of aerosol mass spectrometric data". *Atmospheric Chemistry and Physics* 9 (9), 2891–2918. DOI: 10.5194/acp-9-2891-2009.

Valastro, G., J. Tokaya, J. Hullegie, R. Kranenburg, R. Timmermans, P. Coenen, and T. Megaritis (2023). *The impact of aviation emissions to urban air quality in Europe – Detailed airport-city analysis*. Tech. rep. 10/23. Concawe Air Quality Management Group.

Valin, L. C., A. R. Russell, and R. C. Cohen (2013). "Variations of OH radical in an urban plume inferred from NO_2 column measurements". *Geophysical Research Letters* 40 (9), 1856–1860. DOI: 10.1002/grl.50267.

Van Zanten, M., R. Wichink Kruit, R. Hoogerbrugge, E. Van Der Swaluw, and W. Van Pul (2017). "Trends in ammonia measurements in the Netherlands over the period 1993–2014". *Atmospheric Environment* 148. Publisher: Elsevier BV, 352–360. DOI: 10.1016/j.atmosenv.2016.11.007.

Vasilakos, P., A. Russell, R. Weber, and A. Nenes (2018). "Understanding nitrate formation in a world with less sulfate". *Atmospheric Chemistry and Physics* 18 (17), 12765–12775. DOI: 10.5194/acp-18-12765-2018.

Velders, G. J., A. Snijder, and R. Hoogerbrugge (2011). "Recent decreases in observed atmospheric concentrations of SO2 in the Netherlands in line with emission reductions". *Atmospheric Environment* 45 (31). Publisher: Elsevier BV, 5647–5651. DOI: 10.1016/j.atmosenv.2011.07.009.

Vendel, K., R. Wichink Kruit, M. Blom, P. Van Den Bulk, B. Van Egmond, A. Frumau, S. Rutledge-Jonker, A. Hensen, and M. Van Zanten (2023). "Dry deposition of ammonia in a coastal dune area: Measurements and modeling". *Atmospheric Environment* 298. Publisher: Elsevier BV, 119596. DOI: 10.1016/j.atmosenv.2023.119596.

Voliotis, A., M. Du, Y. Wang, Y. Shao, M. R. Alfarra, T. J. Bannan, D. Hu, K. L. Pereira, J. F. Hamilton, M. Hallquist, T. F. Mentel, and G. McFiggans (2022). "Chamber investigation of the formation and transformation of secondary organic aerosol in mixtures of biogenic and anthropogenic volatile organic compounds". *Atmospheric Chemistry and Physics* 22 (21), 14147–14175. DOI: 10.5194/acp-22-14147-2022.

Voliotis, A., Y. Wang, Y. Shao, M. Du, T. J. Bannan, C. J. Percival, S. N. Pandis, M. R. Alfarra, and G. McFiggans (2021). "Exploring the composition and volatility of secondary organic aerosols in mixed anthropogenic and biogenic precursor systems". *Atmospheric Chemistry and Physics* 21 (18), 14251–14273. DOI: 10.5194/acp-21-14251-2021.

Voort, M. van der, H. Schoorlemmer, and C. de Visser (2012). *Country Report - The Netherlands: Stakeholder and Driver Analysis on Energy Efficiency in Agriculture*. Tech. rep. Applied Plant Research, Wageningen University & Research.

Wagner, R., C. Yan, K. Lehtipalo, J. Duplissy, T. Nieminen, J. Kangasluoma, L. R. Ahonen, L. Dada, J. Kontkanen, H. E. Manninen, A. Dias, A. Amorim, P. S. Bauer, A. Bergen, A.-K. Bernhammer, F. Bianchi, S. Brilke, S. B. Mazon, X. Chen, D. C. Draper, L. Fischer, C. Frege,

C. Fuchs, O. Garmash, H. Gordon, J. Hakala, L. Heikkinen, M. Heinritzi, V. Hofbauer, C. R. Hoyle, J. Kirkby, A. Kürten, A. N. Kvashnin, T. Laurila, M. J. Lawler, H. Mai, V. Makhmutov, R. L. Mauldin III, U. Molteni, L. Nichman, W. Nie, A. Ojdanic, A. Onnela, F. Piel, L. L. J. Quéléver, M. P. Rissanen, N. Sarnela, S. Schallhart, K. Sengupta, M. Simon, D. Stolzenburg, Y. Stozhkov, J. Tröstl, Y. Viisanen, A. L. Vogel, A. C. Wagner, M. Xiao, P. Ye, U. Baltensperger, J. Curtius, N. M. Donahue, R. C. Flagan, M. Gallagher, A. Hansel, J. N. Smith, A. Tomé, P. M. Winkler, D. Worsnop, M. Ehn, M. Sipilä, V.-M. Kerminen, T. Petäjä, and M. Kulmala (2017). "The role of ions in new particle formation in the CLOUD chamber". *Atmospheric Chemistry and Physics* 17 (24), 15181–15197. DOI: 10.5194/acp-17-15181-2017.

Wamelink, G., B. de Knegt, R. Pouwels, C. Schuiling, R. Wegman, A. Schmidt, H. van Dobben, and M. Sanders (2013). "Considerable environmental bottlenecks for species listed in the Habitats and Birds Directives in the Netherlands". *Biological Conservation* 165, 43–53. DOI: 10.1016/j.biocon.2013.05.012.

Wang, M., W. Kong, R. Marten, X.-C. He, D. Chen, J. Pfeifer, A. Heitto, J. Kontkanen, L. Dada, A. Kürten, T. Yli-Juuti, H. E. Manninen, S. Amanatidis, A. Amorim, R. Baalbaki, A. Baccarini, D. M. Bell, B. Bertozzi, S. Bräkling, S. Brilke, L. C. Murillo, R. Chiu, B. Chu, L.-P. De Menezes, J. Duplissy, H. Finkenzeller, L. G. Carracedo, M. Granzin, R. Guida, A. Hansel, V. Hofbauer, J. Krechmer, K. Lehtipalo, H. Lamkaddam, M. Lampimäki, C. P. Lee, V. Makhmutov, G. Marie, S. Mathot, R. L. Mauldin, B. Mentler, T. Müller, A. Onnela, E. Partoll, T. Petäjä, M. Philippov, V. Pospisilova, A. Ranjithkumar, M. Rissanen, B. Rörup, W. Scholz, J. Shen, M. Simon, M. Sipilä, G. Steiner, D. Stolzenburg, Y. J. Tham, A. Tomé, A. C. Wagner, D. S. Wang, Y. Wang, S. K. Weber, P. M. Winkler, P. J. Wlasits, Y. Wu, M. Xiao, Q. Ye, M. Zauner-Wieczorek, X. Zhou, R. Volkamer, I. Riipinen, J. Dommen, J. Curtius, U. Baltensperger, M. Kulmala, D. R. Worsnop, J. Kirkby, J. H. Seinfeld, I. El-Haddad, R. C. Flagan, and N. M. Donahue (2020). "Rapid growth of new atmospheric particles by nitric acid and ammonia condensation". *Nature* 581 (7807), 184–189. DOI: 10.1038/s41586-020-2270-4.

Wang, M., M. Xiao, B. Bertozzi, G. Marie, B. Rörup, B. Schulze, R. Bardakov, X.-C. He, J. Shen, W. Scholz, R. Marten, L. Dada, R. Baalbaki, B. Lopez, H. Lamkaddam, H. E. Manninen, A. Amorim, F. Ataei, P. Bogert, Z. Brasseur, L. Caudillo, L.-P. De Menezes, J. Duplissy, A. M. L. Ekman, H. Finkenzeller, L. G. Carracedo, M. Granzin, R. Guida, M. Heinritzi, V. Hofbauer, K. Höhler, K. Korhonen, J. E. Krechmer, A. Kürten, K. Lehtipalo, N. G. A. Mahfouz, V. Makhmutov, D. Massabò, S. Mathot, R. L. Mauldin, B. Mentler, T. Müller, A. Onnela, T. Petäjä, M. Philippov, A. A. Piedehierro, A. Pozzer, A. Ranjithkumar, M. Schervish, S. Schobesberger, M. Simon, Y. Stozhkov, A. Tomé, N. S. Umo, F. Vogel, R. Wagner, D. S. Wang, S. K. Weber, A. Welti, Y. Wu, M. Zauner-Wieczorek, M. Sipilä, P. M. Winkler, A. Hansel, U. Baltensperger, M. Kulmala, R. C. Flagan, J. Curtius, I. Riipinen, H. Gordon, J. Lelieveld, I. El-Haddad, R. Volkamer, D. R. Worsnop, T. Christoudias, J. Kirkby, O. Möhler, and N. M. Donahue (2022). "Synergistic HNO_3–H_2SO_4–NH_3 upper tropospheric particle formation". *Nature* 605 (7910), 483–489. DOI: 10.1038/s41586-022-04605-4.

Warneke, C., J. A. De Gouw, J. S. Holloway, J. Peischl, T. B. Ryerson, E. Atlas, D. Blake, M. Trainer, and D. D. Parrish (2012). "Multiyear trends in volatile organic compounds in Los Angeles,

California: Five decades of decreasing emissions". *Journal of Geophysical Research: Atmospheres* 117 (D21). Publisher: American Geophysical Union (AGU). DOI: 10.1029/2012jd017899.

Warneke, C., R. H. Schwantes, P. R. Veres, A. Rollins, S. Baidar, W. A. Brewer, C. Senff, A. Langford, K. Aikin, G. Frost, D. Fahey, L. Judd, B. Lefer, R. B. Pierce, S. Kondragunta, C. Stockwell, D. Gentner, A. T. Lambe, D. B. Millet, D. Farmer, N. L. Ng, J. Kaiser, C. Young, J. E. Mak, G. M. Wolfe, J. Sullivan, K. Mueller, A. Karion, L. Valin, M. Witte, L. M. Russel, X. Ren, R. Dickerson, P. DeCarlo, B. McDonald, and S. S. Brown (2023). *The AEROMMA 2023 experiment (Atmospheric Emissions and Reactions Observed from Megacities to Marine Areas)*. White Paper.

Weber, R., D. Orsini, Y. Duan, K. Baumann, C. S. Kiang, W. Chameides, Y. N. Lee, F. Brechtel, P. Klotz, P. Jongejan, H. Ten Brink, J. Slanina, C. B. Boring, Z. Genfa, P. Dasgupta, S. Hering, M. Stolzenburg, D. D. Dutcher, E. Edgerton, B. Hartsell, P. Solomon, and R. Tanner (2003). "Intercomparison of near real time monitors of PM2.5 nitrate and sulfate at the U.S. Environmental Protection Agency Atlanta Supersite". *Journal of Geophysical Research: Atmospheres* 108 (D7). Publisher: American Geophysical Union (AGU). DOI: 10.1029/2001jd001220.

Wegener, R., T. Brauers, R. Koppmann, S. Rodríguez Bares, F. Rohrer, R. Tillmann, A. Wahner, A. Hansel, and A. Wisthaler (2007). "Simulation chamber investigation of the reactions of ozone with short-chained alkenes". *Journal of Geophysical Research: Atmospheres* 112 (D13), 2006JD007531. DOI: 10.1029/2006JD007531.

Wehner, B., F. Werner, F. Ditas, R. A. Shaw, M. Kulmala, and H. Siebert (2015). "Observations of new particle formation in enhanced UV irradiance zones near cumulus clouds". *Atmospheric Chemistry and Physics* 15 (20), 11701–11711. DOI: 10.5194/acp-15-11701-2015.

Weimer, S., M. R. Alfarra, D. Schreiber, M. Mohr, A. S. H. Prévôt, and U. Baltensperger (2008). "Organic aerosol mass spectral signatures from wood-burning emissions: Influence of burning conditions and wood type". *Journal of Geophysical Research* 113 (D10), D10304. DOI: 10.1029/2007JD009309.

Wen, Y., S. Zhang, Y. Wu, and J. Hao (2023). "Vehicular ammonia emissions: an underappreciated emission source in densely populated areas". *Atmospheric Chemistry and Physics* 23 (6). Publisher: Copernicus GmbH, 3819–3828. DOI: 10.5194/acp-23-3819-2023.

Wernis, R. A., N. M. Kreisberg, R. J. Weber, G. T. Drozd, and A. H. Goldstein (2022). "Source apportionment of VOCs, IVOCs and SVOCs by positive matrix factorization in suburban Livermore, California". *Atmospheric Chemistry and Physics* 22 (22), 14987–15019. DOI: 10.5194/acp-22-14987-2022.

Wesely, M. (1989). "Parameterization of surface resistances to gaseous dry deposition in regional-scale numerical models". *Atmospheric Environment (1967)* 23 (6), 1293–1304. DOI: 10.1016/0004-6981(89)90153-4.

Westervelt, D. M., L. W. Horowitz, V. Naik, J.-C. Golaz, and D. L. Mauzerall (2015). "Radiative forcing and climate response to projected 21st century aerosol decreases". *Atmospheric Chemistry and Physics* 15 (22), 12681–12703. DOI: 10.5194/acp-15-12681-2015.

Whitten, G. Z., H. Hogo, and J. P. Killus (1980). "The carbon-bond mechanism: a condensed kinetic mechanism for photochemical smog". *Environmental Science & Technology* 14 (6), 690–700. DOI: 10.1021/es60166a008.

Wiedensohler, A., W. Birmili, A. Nowak, A. Sonntag, K. Weinhold, M. Merkel, B. Wehner, T. Tuch, S. Pfeifer, M. Fiebig, A. M. Fjäraa, E. Asmi, K. Sellegri, R. Depuy, H. Venzac, P. Villani, P. Laj, P. Aalto, J. A. Ogren, E. Swietlicki, P. Williams, P. Roldin, P. Quincey, C. Hüglin, R. Fierz-Schmidhauser, M. Gysel, E. Weingartner, F. Riccobono, S. Santos, C. Grüning, K. Faloon, D. Beddows, R. Harrison, C. Monahan, S. G. Jennings, C. D. O'Dowd, A. Marinoni, H.-G. Horn, L. Keck, J. Jiang, J. Scheckman, P. H. McMurry, Z. Deng, C. S. Zhao, M. Moerman, B. Henzing, G. De Leeuw, G. Löschau, and S. Bastian (2012). "Mobility particle size spectrometers: harmonization of technical standards and data structure to facilitate high quality long-term observations of atmospheric particle number size distributions". *Atmospheric Measurement Techniques* 5 (3), 657–685. DOI: 10.5194/amt-5-657-2012.

Williams, L. R., L. A. Gonzalez, J. Peck, D. Trimborn, J. McInnis, M. R. Farrar, K. D. Moore, J. T. Jayne, W. A. Robinson, D. K. Lewis, T. B. Onasch, M. R. Canagaratna, A. Trimborn, M. T. Timko, G. Magoon, R. Deng, D. Tang, E. De La Rosa Blanco, A. S. H. Prévôt, K. A. Smith, and D. R. Worsnop (2013). *Characterization of an aerodynamic lens for transmitting particles greater than 1 micrometer in diameter into the Aerodyne aerosol mass spectrometer*. DOI: 10.5194/amtd-6-5033-2013.

Winer, A. M., J. W. Peters, J. P. Smith, and J. N. Pitts (1974). "Response of commercial chemiluminescent nitric oxide-nitrogen dioxide analyzers to other nitrogen-containing compounds". *Environmental Science & Technology* 8 (13), 1118–1121. DOI: 10.1021/es60098a004.

Wolfe, G. M., M. R. Marvin, S. J. Roberts, K. R. Travis, and J. Liao (2016). "The Framework for 0-D Atmospheric Modeling (F0AM) v3.1". *Geoscientific Model Development* 9 (9), 3309–3319. DOI: 10.5194/gmd-9-3309-2016.

Wong, J. P. S., A. Nenes, and R. J. Weber (2017). "Changes in Light Absorptivity of Molecular Weight Separated Brown Carbon Due to Photolytic Aging". *Environmental Science & Technology* 51 (15), 8414–8421. DOI: 10.1021/acs.est.7b01739.

Wu, Z., M. Hu, P. Lin, S. Liu, B. Wehner, and A. Wiedensohler (2008). "Particle number size distribution in the urban atmosphere of Beijing, China". *Atmospheric Environment* 42 (34), 7967–7980. DOI: https://doi.org/10.1016/j.atmosenv.2008.06.022.

Xing, J., J. Wang, R. Mathur, S. Wang, G. Sarwar, J. Pleim, C. Hogrefe, Y. Zhang, J. Jiang, D. C. Wong, and J. Hao (2017). "Impacts of aerosol direct effects on tropospheric ozone through changes in atmospheric dynamics and photolysis rates". *Atmospheric Chemistry and Physics* 17 (16), 9869–9883. DOI: 10.5194/acp-17-9869-2017.

Xiong, F., C. H. Borca, L. V. Slipchenko, and P. B. Shepson (2016). "Photochemical degradation of isoprene-derived 4,1-nitrooxy enal". *Atmospheric Chemistry and Physics* 16 (9). Publisher: Copernicus GmbH, 5595–5610. DOI: 10.5194/acp-16-5595-2016.

Xu, L., S. Suresh, H. Guo, R. J. Weber, and N. L. Ng (2015). "Aerosol characterization over the southeastern United States using high-resolution aerosol mass spectrometry: spatial and

seasonal variation of aerosol composition and sources with a focus on organic nitrates". *Atmospheric Chemistry and Physics* 15 (13), 7307–7336. DOI: 10.5194/acp-15-7307-2015.

Xu, L., M. M. Coggon, C. E. Stockwell, J. B. Gilman, M. A. Robinson, M. Breitenlechner, A. Lamplugh, J. D. Crounse, P. O. Wennberg, J. A. Neuman, G. A. Novak, P. R. Veres, S. S. Brown, and C. Warneke (2022). "Chemical ionization mass spectrometry utilizing ammonium ions (NH_4^+ CIMS) for measurements of organic compounds in the atmosphere". *Atmospheric Measurement Techniques* 15 (24), 7353–7373. DOI: 10.5194/amt-15-7353-2022.

Xu, W., M. Takeuchi, C. Chen, Y. Qiu, C. Xie, W. Xu, N. Ma, D. R. Worsnop, N. L. Ng, and Y. Sun (2021). "Estimation of particulate organic nitrates from thermodenuder–aerosol mass spectrometer measurements in the North China Plain". *Atmospheric Measurement Techniques* 14 (5), 3693–3705. DOI: 10.5194/amt-14-3693-2021.

Xu, W., P. Croteau, L. Williams, M. Canagaratna, T. Onasch, E. Cross, X. Zhang, W. Robinson, D. Worsnop, and J. Jayne (2017). "Laboratory characterization of an aerosol chemical speciation monitor with $PM_{2.5}$ measurement capability". *Aerosol Science and Technology* 51 (1), 69–83. DOI: 10.1080/02786826.2016.1241859.

Yarwood, G., M. Rao, M. Yocke, and G. Whitten (2005). *Updates to the Carbon bond chemical mechanism: CB05*. Tech. rep. RT-04- 00675. ENVIRON Internation Corp.

Yarwood, G., J. Jung, G. Z. Whitten, G. Heo, J. Mellberg, and M. Estes (2010). "Updates to the Carbon Bond Mechanism for Version 6 (CB6)". In: Chapel Hill, NC.

Yarwood, G., Y. Shi, and R. Beardsley (2021). *Develop CB7 Chemical Mechanism for CAMx Ozone Modeling*. Tech. rep.

Yu, X., Q. Li, K. Liao, Y. Li, X. Wang, Y. Zhou, Y. Liang, and J. Z. Yu (2024). "New measurements reveal a large contribution of nitrogenous molecules to ambient organic aerosol". *npj Climate and Atmospheric Science* 7 (1), 72. DOI: 10.1038/s41612-024-00620-6.

Zanten, M. van, F. Sauter, R. Wichink Kruit, J. van Jaarsveld, and W. van Pul (2010). *Description of the DEPAC module. Dry deposition modelling with DEPAC_ GCN2010*. Tech. rep. RIVM Report 680180001/2010. Bilthoven, the Netherlands: RIVM.

Zare, A., P. S. Romer, T. Nguyen, F. N. Keutsch, K. Skog, and R. C. Cohen (2018). "A comprehensive organic nitrate chemistry: insights into the lifetime of atmospheric organic nitrates". *Atmospheric Chemistry and Physics* 18 (20), 15419–15436. DOI: 10.5194/acp-18-15419-2018.

Zhang, Q., J. L. Jimenez, M. R. Canagaratna, I. M. Ulbrich, N. L. Ng, D. R. Worsnop, and Y. Sun (2011). "Understanding atmospheric organic aerosols via factor analysis of aerosol mass spectrometry: a review". *Analytical and Bioanalytical Chemistry* 401 (10), 3045–3067. DOI: 10.1007/s00216-011-5355-y.

Zhang, R., A. Khalizov, L. Wang, M. Hu, and W. Xu (2012). "Nucleation and Growth of Nanoparticles in the Atmosphere". *Chemical Reviews* 112 (3). PMID: 22044487, 1957–2011. DOI: 10.1021/cr2001756.

Zhang, X., R. C. McVay, D. D. Huang, N. F. Dalleska, B. Aumont, R. C. Flagan, and J. H. Seinfeld (2015). "Formation and evolution of molecular products in α-pinene secondary organic aerosol". *Proceedings of the National Academy of Sciences* 112 (46), 14168–14173. DOI:

10.1073/pnas.1517742112. eprint: https://www.pnas.org/doi/pdf/10.1073/pnas.1517742112.

Zhao, D., I. Pullinen, H. Fuchs, S. Schrade, R. Wu, I.-H. Acir, R. Tillmann, F. Rohrer, J. Wildt, Y. Guo, A. Kiendler-Scharr, A. Wahner, S. Kang, L. Vereecken, and T. F. Mentel (2021). "Highly oxygenated organic molecule (HOM) formation in the isoprene oxidation by NO_3 radical". *Atmospheric Chemistry and Physics* 21 (12), 9681–9704. DOI: 10.5194/acp-21-9681-2021.

Zhao, D., S. H. Schmitt, M. Wang, I.-H. Acir, R. Tillmann, Z. Tan, A. Novelli, H. Fuchs, I. Pullinen, R. Wegener, F. Rohrer, J. Wildt, A. Kiendler-Scharr, A. Wahner, and T. F. Mentel (2018). "Effects of NO_x and SO_2 on the secondary organic aerosol formation from photooxidation of α-pinene and limonene". *Atmospheric Chemistry and Physics* 18 (3). Publisher: Copernicus GmbH, 1611–1628. DOI: 10.5194/acp-18-1611-2018.

Zhao, Y., Y. Zhao, C. Wang, Y. Shao, H. Xie, J. Yang, W. Zhang, G. Wu, G. Li, L. Jiang, and X. Yang (2026). "Photooxidation and ozonolysis of -pinene and limonene mixtures: Mechanisms of secondary organic aerosol formation and cross-dimerization". *Journal of Environmental Sciences* 161, 525–535. DOI: 10.1016/j.jes.2025.04.020.

Zheng, Y., X. Cheng, K. Liao, Y. Li, Y. J. Li, R.-J. Huang, W. Hu, Y. Liu, T. Zhu, S. Chen, L. Zeng, D. R. Worsnop, and Q. Chen (2020). "Characterization of anthropogenic organic aerosols by TOF-ACSM with the new capture vaporizer". *Atmospheric Measurement Techniques* 13 (5), 2457–2472. DOI: 10.5194/amt-13-2457-2020.

Authorship statement

The overall research direction of this thesis was developed by Farhan R. Nursanto as part of the WIMEK graduate program. The proposal was developed together with my promotors. Based on the proposal, I conducted the research and formulated the specific research questions presented in this thesis. I wrote the introduction (Chapter 1) and the synthesis (Chapter 6), incorporating feedback from my promotors. Chapters 2–5 are the result of collaborations, for which the contribution is outlined below by chapter.

Chapter 1 Introduction. I developed the specific research questions based on the initial proposal created with my promotors. I conducted the literature review, wrote the introduction, and revised the text following feedback from my promotors.

Chapter 2 Chemistry of new particle formation and growth. I am the lead author of this chapter. I conceptualized the research design alongside my co-promotor. While the data collection was a collaborative effort, I performed the data analysis and interpretation in its entirety. I wrote the first draft of the manuscript and coordinated the revision process with all co-authors.

Chapter 3 NO_x^+ ratio method in CV-UMR-ToF-ACSM. I am the lead author of this chapter. I designed the research with my co-promotor and a collaborator from the United States. I participated in the data collection during the chamber experiments and performed the full data analysis and interpretation. I was responsible for writing the manuscript draft, which was later revised with input from the co-authors.

Chapter 4 Gas-particle partitioning, molecular weight, and yield of organic nitrates. This chapter represents a large-scale collaborative SAPHIR-CHANEL campaign participated by researchers over Europe and the US, led by a coordinator from FZJ. As lead author of the manuscript, I conceptualized the paper's specific focus with my co-promotor. I participated in the NO_y data collection during the chamber experiments. My primary contribution was the synthesis and interpretation of the combined datasets (including AMS, GC, and CIMS provided by the campaign collaborators). I wrote the manuscript and managed the extensive revision process involving the large author consortium.

Chapter 5 Influence of emission signature and meteorology on nitrate aerosol formation. I am the lead author of this chapter. I conceptualized the study and research design with

my co-promotor. I conducted the NO_y data collection with support from other people within the CAINA project for other measurements. I performed all data analysis and interpretation. I wrote the manuscript with my promotors and finalized the text after integrating comments from the co-authors.

Chapter 6 Synthesis and outlook. I am the sole author of the synthesis. I developed the subjects and arguments presented, including the modeling recommendations and future research directions. I wrote the draft independently and performed revisions based on feedback from my promotors.

Finally, artificial intelligence tools (ChatGPT-5 and Google Gemini 3) were used for editorial support to improve text clarity and phrasing in the summary, Chapter 1, and Chapters 4–6. I assume full responsibility for the scientific content and interpretation of the results.

List of publications

Peer-reviewed Journal Publications

Ajith, T. C., E. Windwer, C. Li, Z. Fang, S. K. Kompalli, **Nursanto, Farhan R.**, T. E. Olayemi, J. I. Ese, S. A. L. Sharpe, M. Fraund, R. C. Moffet, A. Laskin, J. L. Fry, and Y. Rudich (2024). "Investigating New Particle Formation and Growth Over an Urban Location in the Eastern Mediterranean". *Journal of Geophysical Research: Atmospheres* 129 (23). e2024JD041802 2024JD041802, e2024JD041802. DOI: https://doi.org/10.1029/2024JD041802. eprint: https://agupubs.onlinelibrary.wiley.com/doi/pdf/10.1029/2024JD041802.

Nursanto, Farhan R., D. A. Day, R. Meinen, R. Holzinger, H. Saathoff, J. Fu, J. Mulder, U. Dusek, and J. L. Fry (2025). "Development and validation of a NO_x^+ ratio method for the quantitative separation of inorganic and organic nitrate aerosol using a unit-mass-resolution time-of-flight aerosol chemical speciation monitor equipped with a capture vaporizer (CV-UMR-ToF-ACSM)". *Atmospheric Measurement Techniques* 18 (13). Publisher: Copernicus GmbH, 3051–3072. DOI: 10.5194/amt-18-3051-2025.

Nursanto, Farhan R., R. Meinen, R. Holzinger, M. C. Krol, X. Liu, U. Dusek, B. Henzing, and J. L. Fry (2023). "What chemical species are responsible for new particle formation and growth in the Netherlands? A hybrid positive matrix factorization (PMF) analysis using aerosol composition (ACSM) and size (SMPS)". *Atmospheric Chemistry and Physics* 23 (17), 10015–10034. DOI: 10.5194/acp-23-10015-2023.

Other Scientific Publications

Nursanto, Farhan R., Q. He, S. Van De Wouw, A. Zanders, T. Hohaus, W. S. J. Kroese, R. Wegener, M. G. Adam, B. Winter, R. Dubus, L. Kesper, F. Rohrer, Y. Wang, E. Matthews, A. Voliotis, T. J. Bannan, G. McFiggans, H. Coe, Y. Wu, M. Roska, M. Canagaratna, M. Alton, M. M. Coggon, C. E. Stockwell, K. H. Bates, E. Y. Pfannerstill, S. R. Zorn, H. Wang, M. Riva, S. Perrier, B. Yang, L. Liu, A. Novelli, M. Färber, H. Fuchs, A. C. Marcillo Lara, A. Grasse, C. Wesolek, R. Tillmann, R. Holzinger, M. C. Krol, G. I. Gkatzelis, and J. L. Fry (2026). *Gas-particle partitioning, molecular weight, and yield of organic nitrate under different urban VOC, NO_x, and oxidation conditions during SAPHIR-CHANEL campaign*. **in review** (preprint in Atmospheric Chemistry and Physics). DOI: 10.5194/egusphere-2025-6310.



Acknowledgements

The past four years have been the most adventurous and life-changing experiences I have ever had. Moving far from my homeland to a third country for my academic years has allowed me to grow both personally and scientifically. I owe this growth to the people I interacted with during my PhD, who made this journey enjoyable and rewarding.

First of all, I would like to thank **Julie**, who has been a kind mentor, teacher, and parent while away from home. You reignited my confidence in science and showed me how vital good communication is for both research goals and personal well-being. I truly enjoyed our weekly discussions, and I appreciate your patience with me. Thank you for the insights into atmospheric science and policymaking, and for the memorable trips to Rotterdam, Paris, Jülich, Vienna, and Kuala Lumpur. I am especially happy you could visit my hometown, Jakarta! I really appreciate all the guidance and support you have given me. I am so proud of the work we have done together on this thesis.

Maarten, although we interacted more during my final year, you have been involved since the very beginning. I enjoyed our discussions about science. Your multidisciplinary approach, bridging meteorology and air quality, is truly inspiring and has given me a more holistic understanding of atmospheric chemistry. Thank you for your support, kindness, and patience; I am glad we are able to finish this thesis!

My thesis was closely linked with the CAINA consortium and other aerosol science researchers in the Netherlands. I would like to thank **Uli** and **Rupert**, whom I consider to be my mentors as well. I enjoyed our discussions and organizing the monthly Dutch Aerosol Club meetings. The instruments would not have run without **Roy** and **Jan**, so I thank you for your hard work in keeping them running! I also enjoyed our van trips to Paris for the ACSM workshops, trips to Cabauw, and the many conversations we had along the way. To **Pascale**, thank you for the fun times and the car trips to Cabauw; I really enjoyed discussing about life, culture, and many other things. To **Laurie**, thank you for the modeling discussions and for always checking in on me and others; we need more people like you in the group! **Willem**, thank you for hosting me every time I am in Utrecht, especially during our instrument intercomparison experiments. To **Marije**, I

enjoyed our discussions whenever I am in Groningen and Cabauw. To all four of you, it was amazing that we made it to the summer school in Finland together in 2023!

I would like to thank **Harald** for hosting me in Karlsruhe during the CAINA AIDA experiments and also **Jinglan** for her help during my visit and our discussions on organic aerosol formation. I also mention **Xinya**, who have been really helpful in the beginning of my PhD with the scientific discussion; also **Namita** for our discussions on the Cabauw data.

Special thanks to **Doug** in Colorado. Despite the time zone difference, you always made time for our online meetings. I learned so much about statistics, aerosol mass spectrometry, and data analysis from you, and I truly appreciate you meeting me during your early mornings and my evenings. Also, thanks to **Delphine** for our discussions during your visit to MAQ. It was a pleasure to discover that you were the author of a paper that I have been citing extensively throughout this thesis!

I am grateful to be part of the MAQ group, which I consider my second home in the Netherlands. I loved working in the office because of the great "atmosphere." Thank you to **Michiel**, **Laurens**, **Folkert**, **Margreet**, **Bert (Heusinkveld)**, and **Mahrooz** for the discussion related to air quality, especially in the Air Quality Working Group meetings. Thanks to **Gert-Jan** who have helped me through your Atmospheric Modelling course. I also would like to express my gratitude to **Henk** and **Reinder**, as well as **Frits** and **Wendy** from the AEW Laboratory, for your technical help and lab supplies. I am also grateful to **Oscar**, **Chiel**, and **Wouter (Peters)** for your willingness to 'test' all my baking experiments, **Ingrid** for bringing vegan cakes, and to **Wiebke** for your kindness of sharing your fresh produce with the group. I also thank **Sandra** and **Chi** for helping me navigate the administrative work of being a foreign PhD student in the Netherlands. To the many staff members I have chatted with over coffee or lunch: there are far too many of you to name individually, but it has been a pleasure getting to know you all!

I have watched MAQ grow significantly over the last four years. To all the PhDs who have come and gone during my time: thank you for the memories and for making the research journey so enjoyable. **Wouter (Mol)**, you were the first PhD student I met when I first enter the office, and we instantly clicked over photography, hiking, and cooking. We even made a photography trip to Zandvoort! **Christoph**, **Ruben (Schulte)**, **Auke (Visser)**, **Sjoerd**, and **Anja**: as fellow nitrogen and/or air quality PhDs, thank you for the discussions and for making me feel less alone early on. I would also like to mention **Auke (van der Woude)** for the jokes you always make, and to **Menno** and **Martin** for the great conversations. Additionally, the last five people I mentioned just made me realize just how many people enjoy MAQ a lot and stay on in new positions!

Next, I would like to thank **Kim** for her contagious laughter and the pizza/movie night, and **Mary Rose**, who has been incredibly helpful and provided so many useful tips during the final stages of my PhD. To everyone who started their PhDs around the end

of "Covid-era": thank you **Raquel** for your cheerful personality and your invitation to your performance; **Anne-Wil**, for the treats and helping me arrange the language quiz during BBOS; and **Mirjam**, **Thomas**, and **Esther**, with whom I shared an office from time to time and many discussions.

I would also like to express my appreciation to my paranymphs, **Marnix** and **Ruben (van 't Loo)**, for your help in arranging my defence. **Marnix**, thank you for your kindness and attentiveness for our many discussions on life, politics, food, and research. You truly live up to your reputation as the MAQ "student president"! The museum trip to Haarlem was also a highlight for me. **Ruben**, thank you for spreading joy in the office with your big smile. I truly enjoyed our conversations and appreciated the chance to share my food with you, especially since you mentioned enjoying it so much.

I would also like to thank **Bianca** and **Lucas** for their bubbly personalities, which always led to such wonderful conversations. My thanks to **Reinaart**, **Sebastiaan**, and **Tristan** for being so kind and thoughtful, and to **Mohamad**, whose good-natured character made our discussions about culture, language, and civilization interesting. To **Firmin**, I enjoyed all our chats (and I know you also prefer our smaller lunch group at MAQ over the bustle of Orion!).

Thank you to **Vincent (de Feiter)** and **Marloes** for the jokes; you were a great match as PhD representatives! I also appreciate **Bernard (Postema)**, **Sarah (Warnau)**, **Robbert**, and **Leander** for their easy-going natures, and **Ewout** for our discussions on nitrogen. Finally, thank you to **Agatha** for the homemade gnocchi invitation, **Vincent** for the pizza baking evening, and to **Jianan** for the delicious hotpot lunch at your place.

The list continues! I also want to mention how much I enjoyed sharing an office and having discussions with many more of you on various occasions. Thanks to **Kevin**, whom I always seemed to randomly bump into in the Wageningen centrum. To **Ashriah**, ***Mas*[1] Nunuk**, and **Fera**, thank you for bringing a bit of Indonesia to MAQ. Thanks also to **Sreehari** for the great Indian food, and to **Francisca**, **Job**, **Juliëtte**, **Indy**, **Robin**, **Daan**, **Anna**, **Ara**, **Peter**, **Ariadna**, and **Vicente**. Thank you to **Alba** and **Isidora** too; it was great to cross paths again after first meeting as teaching assistants during the Air Quality course! And speaking of the Air Quality course, I would also like to express my gratitude to **Antonija**, **Romijn**, **Cassandre**, **Johanna**, **Aude**, **Circe**, **Max (Bouman)**, **Jente**, and **Zhiyu** for your help in the course practicals.

My research journey reached far beyond the borders of Dutch universities. I am grateful to the many people I met within the broader international community during various workshops, symposia, and conferences. I would like to give a big shout-out to the SAPHIR-CHANEL campaign team for introducing me to a new area of atmospheric chemistry. Special thanks to **Georgios** for his warm welcome to Jülich and for his patience in organizing and directing the campaign. I also thank **Yizhen**, with whom I have had many valuable discussions as we navigated the early stages of our campaign

manuscripts. I also thank **Sophia**, who conducted her Master's thesis on modeling the chamber experiments and helped me run the NO_y monitor. Additionally, I thank **Thorsten** and **Quanfu** for our collaboration in the instrument container. I am also thankful to **Robert**, **Max (Gerrit Adam)**, **Benjamin**, **René**, **Lukas**, **Özgür**, and **Franz** for the assistance you provided with instrument calibrations and experiment setup, and **Milan** for your hospitality during my stay in Jülich. Finally, my thanks also go to the many other participants who contributed to this project.

I also acknowledge **Donna** and **Ian** for their help with PMF setup at the beginning of my PhD. I am also thankful to **Janot**, **Enrico**, **Astrid**, **Daniëlle**, **Jan-Pieter**, and **Jessie** from TNO, as well as **Tycho** from Leiden for the wonderful conversation about nitrogen-related topics and atmospheric modeling. Thanks to **Han** and **Hugo** from DCMR; **Bas** for the invitation to guest lecture on his course at TU Delft; and the team at LSCE in Paris and Aerodyne during the ACSM workshop (**Jean-Eudes**, **Anandi**, **Phil**, **Leah**, **Olivier**, **Prodip**, **Evelyn**, **Hasna**, and **Laurent**). To the people I met in Hyytiälä, Finland — **Samuel**, **Mihai**, **Herbert**, **Markus**, **Lauri**, **Vincent (Enders)**, **Merve**, **Boxing**, and many others — thank you for making the summer school memorable. During my attendance at EAC in Málaga and/or IGAC in Kuala Lumpur, I was grateful to be able to meet ***Mbak*[2] Sari**, **Nurzawani**, **Adit**, ***Teh*[3] Windy**, ***Teh* Sheila**, **Ellie (Smith)**, **Flossie**, **Emmie**, **Sherin**, **Jason**, **Facundo**, **Keith**, **Print**, **Bert (Verreyken)**, **Victor**, and many more.

I feel incredibly grateful to have friends from back home in Indonesia who are also living in the Netherlands or elsewhere in Europe. I would like to express my appreciation to my high school friends from SMAN 78 Jakarta. **Putri**, **Salsa** (and **Izzat**), **Adam**, and **Elory**, thank you for the outings, chats, inside jokes, and our travels to visit each other in Germany, Denmark, and Sweden! To my friends from my Bachelor's program in ITB who are (and were) scattered across Europe: thank you **Zaid**, ***Kak*[4] Donny**, **Ica** (and **Alvin**), **Rafi** (and **Dina**), ***Kak* Dhimaz**, ***Kak* Felix**, ***Kak* Ike**, ***Kak* Marvel** (and **Vero**), and **Irish** for being there, visiting me (or me visiting you), dinner invites, and traveling together. Through **Zaid**, I also met a wonderful community in Groningen, including **Wahyu**, **Elysa**, ***Mbak* Angela**, ***Kak* Dina (Maniar)**, ***Kak* Ali**, ***Kak* Liany**, ***Kang*[5] Fajar**, ***Teh* Monik**, ***Mas* Sidqi**, and **Nanda**. To **Zaid**, ***Mbak* Angela**, ***Kak* Dina**, ***Kak* Donny**, **Petros**, **Ica**, and **Alvin**, I would like to mention that our travel adventures were truly memorable, with some of the most breathtaking views I have ever seen in Ireland and Norway. Thank you all for being the best travel buddies! I also want to thank **Zaid** and **Nada** for the cultural exchange and the delicious meals at your home. Also, I thank ***Kak* Felix** for your kind help in giving suggestions to the Indonesian summary of this thesis.

I have also stayed in close contact with friends from my Master's in Strasbourg. Thank you to ***Kak* Ari**, who helped me discover the joy of hiking in the Vosges (which I continued to enjoy during my PhD time), and assisted in proofreading my thesis in

Indonesian and French. To **Joana** and **Carla**, it was wonderful to reconnect with you in Strasbourg during the course of my PhD. To **Dhifa** and **Reza**, thank you for letting me stay with you whenever I visited Strasbourg; and **Dayi** and **Zaki** while exploring Paris. To **Tya** and **Daffa**, whom I met in Strasbourg and who have now ended up in Utrecht: I truly appreciate all the outings, lunches, dinners and board games we shared with **Rafi** and **Dina**. Finally, thank you to **Arzak** and **Della**, with whom I first moved to France for our Master's degrees, for staying in touch all these years.

I want to thank my former housemates — **Bernard (Prasetyo)**, **Ellie (Yu)**, **Aina**, **Foivos**, **Rosie**, **Luuk**, **Pim**, and **Sudhanwa** — for the shared meals and stories. Thanks also to the Avicenna Wageningen community, especially **Mahmoud**, **Ayoub**, **Abubakr**, and **Khushhaal**. To the Indonesian group I started with in Wageningen — **Tessa**, **Sunsun**, **Shinta**, **Oza**, ***Teh*** **Miwa**, **Ditro**, **Wahdan**, **Zaki**, **Onk**, **Fathi**, **Hira**, **Ghufron**, **Putra**, ***Kang*** **Asep**, ***Teh*** **Ayu**, ***Teh*** **Puri**, **Tita**, and **Opik** — thank you for the memorable moments. I also want to thank my ITB friends back home — **Rozi**, **Reren**, **Riri**, **Cucu**, **Vina**, **Hardian**, **Intan**, **Feni**, **Nyimas**, and **Dimitri** — for the wonderful trips and all the catch-ups whenever I return to Indonesia. Also, to **Bobby** and **Dina (Pariata)**, thank you for guiding **Julie** and me exploring Jakarta!

This final paragraph is dedicated to my family in Jakarta. I thank you for giving me the opportunity to study and build a career abroad. To my sister, ***Kak*** **Hani**, my brother-in-law, ***Bang***[6] **Andy**, and my nieces, **Almira** and **Aliyya**: thank you for visiting me in the Netherlands — it was wonderful to show you the country where I do my PhD. To my brother, ***Ubang***[7] **Shadri**, my sister-in-law, ***Kak*** **Rinda**, and my nieces, **Shofi**, **Sarah**, and **Rahil**: thank you for your warmth and for welcoming me home every time I return. Finally, to **Mama** and **Papa**, I hope that what I have learned has a positive impact on the world and helps me grow spiritually, as you have always taught me.

Sincerely,
Farhan R. Nursanto
Wageningen, February 2026

[1] *Mas*: A Javanese masculine honorific meaning 'older brother,' used for someone of an older age.

[2] *Mbak*: A Javanese feminine honorific meaning 'older sister,' used for someone of an older age.

[3] *Teh*: A Sundanese feminine honorific meaning 'older sister,' used for someone of an older age.

[4] *Kak*: An Indonesian gender-neutral honorific meaning 'older sibling,' used for someone of an older age.

[5] *Kang*: A Sundanese masculine honorific meaning 'older brother,' used for someone of an older age.

[6] *Bang*: A Malay/Betawi masculine honorific meaning 'older brother,' used for someone of an older age.

[7] *Ubang*: An Acehnese masculine honorific meaning 'older brother,' used for someone of an older age.

About the cover



The image on the cover of this thesis features the characteristic Dutch landscape and illustrates the primary precursors of nitrate aerosols investigated in this research. The scene depicts the intersection of agricultural emissions (reduced nitrogen), transport emissions (oxidized nitrogen), and the biogenic contributions of the surrounding natural fields (volatile organic compounds). These precursor sources are watched over by the measurement tower in Cabauw, the main site for the data presented in this work. This scene captures the quiet curiosity that the author felt every time he wondered how these different emitters interact to shape our atmosphere. It is a visual reminder of the questions of how these sources combine to form nitrate aerosols and what our observations can reveal about their composition and where they may go.

Netherlands Research School for the
Socio-Economic and Natural Sciences of the Environment

D I P L O M A

for specialised PhD training

The Netherlands research school for the
Socio-Economic and Natural Sciences of the Environment
(SENSE) declares that

Farhan Ramadzan Nursanto

born on 23 January 1998 in Jakarta, Indonesia

has successfully fulfilled all requirements of the
educational PhD programme of SENSE.

Wageningen, 6 July 2026

SENSE coordinator PhD education

Dr Ir Peter Vermeulen

The SENSE Director

Dr Jampel Dell'Angelo

The SENSE Research School declares that **Farhan Ramadzan Nursanto** has successfully fulfilled all requirements of the educational PhD programme of SENSE with a workload of 38.3 EC, including the following activities:

SENSE PhD Courses

- A1: Environmental Research in Context (2022)
- A2 Research in context activity: 'PhD impact incubator: Organizing and leading the Dutch Aerosol Club Meeting' (2024-2025)

Other PhD and Advanced MSc Courses

- INAR Autumn School: Formation and growth of atmospheric aerosols, University of Helsinki (2024)
- IGAC Early Career Short Course (2024)
- Atmospheric Modelling, WUR (2023)

External training at a foreign research institute

- ACMCC-ACTRIS ACSM workshop 2022
- ACMCC-ACTRIS ACSM workshop 2023

Teaching and supervision

- Teaching Assistant BSc course 'Air Quality' (2022-2023)
- Guest Lecturer on “Air pollution meteorology & dispersion” at TU Delft (2024)
- Supervision of MSc student with thesis entitled 'Modelling secondary organic nitrate aerosol formation from atmospheric limonene emissions in daytime and nighttime’ (2024)

Oral Presentations

- *What chemical species are responsible for new particle formation and growth in the Netherlands? A hybrid positive matrix factorization (PMF) analysis using aerosol composition (ACSM) and size (SMPS).* European Aerosol Conference (EAC) 2023, 4-8 Sep 2023, Málaga, ES
- *Development and validation of a NO_x^+ ratio method for the quantitative separation of inorganic and organic nitrate aerosol using CV-UMR-ToF-ACSM.* AMS/ACSM Users Meeting 2024, 31 Aug 2024, Tampere, FI *(online participation)*
- *Gas-particle partitioning and yield of organic nitrate under different VOC, NO_x, and oxidation conditions.* EGU General Assembly, 27 Apr-2 May 2025, Vienna, AT
- *Variability of nitrate aerosol formation in Cabauw, Netherlands.* Ruisdael Science Day, 19 Sep 2025, Utrecht, NL

This research was financially supported by the Meteorology and Air Quality Chair Group, Environmental Science Group, Wageningen University. This work has been accomplished using data generated in the Ruisdael Observatory as part of continuous monitoring, the Ruisdael Land–Atmosphere Interactions Intensive Trace-gas and Aerosol (RITA) 2021 campaign, and the Cloud-Aerosol Interactions in a Nitrogen-dominated Atmosphere (CAINA) project. The Ruisdael Observatory is a scientific infrastructure co-financed by the Dutch Research Council (NWO) under grant no. 184.034.015. The CAINA project is a research consortium supported by NWO under grant no. OCENW.XL21.XL21.112). The SAPHIR (Simulation of Atmospheric PHotochemistry In a large Reaction chamber)-CHANEL (Household Chemicals Amplifying Urban Aerosol Pollution) 2024 campaign is supported by the European Research Council (ERC) under the European Union's Horizon Europe research and innovation program through the Starting Grant CHANEL, grant no. 101076276, which provided the primary funding for the CHANEL campaign. Additional support for SAPHIR chamber operations was provided by the European Commission (EC) ATMO-ACCESS Transnational Access program, grant no. 101008004.

The cover and portraits at the beginning of each chapter are photographs taken by Farhan R. Nursanto.

This thesis is printed by Proefschriftmaken.

